INVESTIGATING THE PH OF ATMOSPHERIC FINE PARTICLES AND IMPLICATIONS FOR ATMOSPHERIC CHEMISTRY

A Dissertation
Presented to
The Academic Faculty

by

Hongyu Guo

In Partial Fulfillment
of the Requirements for the Degree
Doctorate of Philosophy in the
School of Earth & Atmospheric Sciences

Georgia Institute of Technology
August 2017

INVESTIGATING THE PH OF ATMOSPHERIC FINE PARTICLES AND IMPLICATIONS FOR ATMOSPHERIC CHEMISTRY

Approved by:

Dr. Rodney J. Weber, Advisor
School of Earth and Atmospheric Sciences
Georgia Institute of Technology

Dr. Armistead G. Russell
School of Civil and Environmental Engineering
Georgia Institute of Technology

Dr. Athanasios Nenes
School of Earth and Atmospheric Sciences
Georgia Institute of Technology

Dr. Nga Lee (Sally) Ng
School of Chemical and Biomolecular Engineering
Georgia Institute of Technology

Dr. Gregory L. Huey
School of Earth and Atmospheric Sciences
Georgia Institute of Technology

Date Approved: July 17, 2017

ACKNOWLEDGEMENTS

I would like to acknowledge my advisor, Dr. Rodney J. Weber, who gave me invaluable guidance on transformation from a college student to a graduate researcher. First, I'm truly grateful for the opportunity to work with him and his hands-on guidance on experiments, writing, and most importantly critical thinking. During the last six years, I have been learning to think like a scientist like him: logically, scientifically, and cautiously. I'm also truly thankful for the motivation, trust, and freedom that he gave me to conduct field research and explore the unknowns. He has always been fast responsive and very helpful whenever I have questions in research. Without his strong skills, insightful visions, and countless guidance, I would not have been as productive in my graduate research and would not be passionate to become an atmospheric scientist in the future.

I'm highly thankful for a closely collaborated professor, Dr. Athanasios Nenes. Without his expertise in thermodynamic modeling, it would have been more difficult to push forward the particle pH work. Particle pH is a controversial and difficult topic, although seems to be intuitive and simple. I want to truly thank him for the insightful guidance and strong supports in the past few years. During my graduate study, it has been a great opportunity to learn from several atmospheric field outstanding experts, including Dr. Michael Bergin, Dr. Sally Ng, Dr. Armistead G. Russell, and Dr. Gregory L. Huey. A special thank you to Dr. Michael Bergin for his kind help with developing a particle liquid water measurement method.

My graduate research work is made possible by National Science Foundation (NSF) grants 1242258, 1360730, 0931492, 0802237, and U.S. Environmental Protection Agency

(EPA) grant R834799. My work is highly supported by a large suite of data sets collected in several field studies. I have never been alone owning to the kind support from many responsible collaborators. Many thanks to Atmospheric Research & Analysis (ARA) personnel, including Eric S. Edgerton, Karsten Baumann, for their support during the SOAS campaign and Research Aviation Facility (RAF) personnel for their contributions supporting the WINTER field deployments. A special acknowledgement to Dr. Amy P. Sullivan, a former member in Rodney's group and now a research scientist in Colorado State University, for taking care of aboard instruments for me during the WINTER aircraft study. I'm also grateful for the shared high-quality field data from professors and experts in other institutes, not limited to Dr. Shan-Hu Lee, Dr. Jose L. Jimenez, Dr. Joel Thornton, Dr. Karl D. Froyd, and Dr. James M. Roberts.

I have been fortunate to work with several excellent colleagues closely, including Dr. Lu Xu, Dr. Kate M. Cerully, and Dr. Aikaterini Bougiatioti. I am very grateful to my past and current group mates, Dr. Jiumeng Liu, Ting Fang, Dr. Vishal Verma, Dong Gao, Linghan Zeng, Dr. Theodora Nah, Dr. Jenny Wong, Laura E. King, Neel Kotra, Gabby Agostini, Qian Zhang, and Dr. Yuzhong Zhang, for their help with my research from different aspects and for all the joyful moments we spent together. I want to particularly thank Jiumeng and Yuzhong for their kind help to me to accommodate the life in U.S. A special thank you to Ting for her encouragements whenever I was down.

Finally, I want to sincerely thank my parents for their unconditional love and unending support that made all these possible.

TABLE OF CONTENTS

LIST OF TABLES

LIST OF FIGURES

based on T = 20 °C, particle liquid water level = 5 μg m^{-3}, and ideal solution (i.e. $\gamma = 1$). The S curve equations can be found at *Guo et al.* [2017a]. Non-ideality only shifts the S curves but does not change the shapes. The 0.3 unit pH (SOAS) and 0.5 unit pH (WINTER) variations (biases) are the upper limit values based on the difference between zero and inferred Na^+ inputs (Figure 6-8) and indicated by paired red and blue sticks, respectively. The response of $\varepsilon(NH_4^+)$ or $\varepsilon(NO_3^-)$ to pH reaches maximum at 50% $\varepsilon(NH_4^+)$ or $\varepsilon(NO_3^-)$ (i.e., position (2), 0.3 unit pH change causes ~20% or 0.5 unit pH change causes ~30% shift in the particle phase fraction), but down to nearly zero when 100% or 0% $\varepsilon(NH_4^+)$ or $\varepsilon(NO_3^-)$ (e.g. position (1) or (3)).

Figure 6-10 Mean summer (June–August) trends in (a) measured and predicted R_{SO4}, (b) predicted $PM_{2.5}$ pH, and (c) inferred Na^+ (from ion charge balance of Na^+-NH_4^+-SO_4^{2-}-NO_3^- aerosols) concentration and mole fraction at the SEARCH-CTR site. Model input includes the observational $PM_{2.5}$ composition data (NH_4^+, SO_4^{2-}, NO_3^-) and meteorological data (RH, T) at CTR. R_{SO4} and pH were estimated with ISORROPIA-II run in forward mode with an assumed NH_3 level of 0.36 μg m^{-3}, the mean concentration from the SOAS study (CTR site, summer 2013), due to limited NH_3 data before 2008. Historical NH_3 mean summer concentration at CTR were 0.2 μg m^{-3} (2004-2007) [*Blanchard et al.*, 2013] and 0.23 ± 0.14 μg m^{-3} (2008-2013) [*Weber et al.*, 2016]. 41 out of the total 609 (7%) daily mean R_{SO4} were observed above 3 due to measurement error, above the upper limit of $R_{SO4} = 2$, therefore, excluded in the model input. Error bars represent daily data ranges (SD). Linear regression fits are shown and uncertainties in the fits are one SD. In (a), based on regression slope, the observed R_{SO4} trend was –0.021 ± 0.007 at CTR versus a predicted value of –0.017 ± 0.006 unit yr^{-1} for ISORROPIA run with Na^+ from the charge balance, and –0.003 ± 0.001 unit yr^{-1} for a constant Na^+ of 0.03 μg m^{-3}, used by *Weber et al.* [2016]. These results are consistent with the reported R_{SO4} trend of –0.01 to –0.03 yr^{-1} reported by *Hidy et al.* [2014] for SEARCH data set. In (b), the pH predictions with inferred Na^+ or with limited Na^+ of 0.03 μg m^{-3} shows a fairly stable $PM_{2.5}$ pH in the last 15 years. In (c), the inferred Na^+ shows a general decreasing trend while the inferred Na^+ mole fraction stays relatively stable around 15% (± 4%). 183

LIST OF SYMBOLS AND ABBREVIATIONS

SYMBOLS:

D_p	aerosol diameter
e_s	saturated water vapor pressure
E_{NH_3}	ammonia emission rate
f_i	volume fraction of species *i* in particle
f(RH)	aerosol hygroscopic growth factor
gf_D	aerosol diameter-based growth factor
H_{air}^{+}	hydronium ion concentration in air
H_{aq}^{+}	hydronium ion concentration in aqueous solution
H_{HNO_3}	nitric acid Henry's Law constant
$H_{HNO_3}^{*}$	equilibrium constant of $HNO_{3(g)} \leftrightarrow {NO_3}^{-} + H^{+}$
H_{NH_3}	ammonia Henry's Law constant
K_a	acid dissociation constant
K_{n1}	nitric acid dissociation constant
K_w	water dissociation constant
m_{org}	organic mass concentration
m_p	dry aerosol mass concentration
m_r	particle refractive index
$N(D_p)$	particle number distribution function
N_t	particle number concentration
p_{HNO_3}	partial pressure of nitric acid
Q_s	aerosol light scattering coefficiency

R	ammonium-sulfate aerosol ratio
R_{SO4}	ammonium-sulfate aerosol ratio (excluding nitrate)
$V_d^{NH_3}$	ammonia deposition velocity
$V_d^{NH_4^+}$	ammonium deposition velocity
W_i	particle water associated with inorganics
W_o	particle water associated with organics
γ_{H^+}	hydronium ion activity coefficient
$\gamma_{H^+-NO_3^-}$	hydronium ion-nitrate ion pair activity coefficient
$\gamma_{NH_4^+}$	ammonium activity coefficient
$\gamma_{NO_3^-}$	nitrate activity coefficient
Δ	change of any changeable quantity
$\varepsilon(Cl^-)$	particle phase fraction of chloride
$\varepsilon(NH_4^+)$	particle phase fraction of ammonium
$\varepsilon(NO_3^-)$	particle phase fraction of nitrate
ε_{Org}	organic aerosol mass fraction (to dry aerosol mass)
ε_{W_o}	particle water associated with organics fraction (to total particle water)
κ	particle hygroscopic parameter
κ_{org}	organic aerosol hygroscopicity parameter
λ	wavelength
ρ_{org}	organic aerosol density
ρ_p	dry aerosol density
ρ_w	water density
σ_{sp}	aerosol light scattering coefficient

ABBREVIATIONS:

AIOMFAC	Aerosol Inorganic-Organic Mixtures Functional groups Activities Coefficients
AMoN	Ammonia Monitoring Network
AMS	Aerosol Mass Spectrometer
ARA	Atmospheric Research & Analysis
BC	black carbon
BB	biomass burning
BJ	Beijing
BVOC	biogenic volatile organic compound
$Ca(NO_3)_2$	calcium nitrate
Ca^{2+}	calcium ion
CalNex	California Research at the Nexus of Air Quality and Climate Change
CCN	cloud condensation nuclei
Cd	cadmium
CFSTGC or CCNc	Continuous-Flow Streamwise Thermal Gradient Cloud Condensation Nuclei counter
CIMS	Chemical Ionization Mass Spectrometer
Cl^-	chloride ion
CO_2	carbon dioxide
CTM	chemical transport model
CTR	Centreville
E-AIM	Extended Aerosol Inorganics Model
Fe	iron
GA	Georgia

GAS	Georgia Station
GIT	Georgia Institute of Technology
H^+	hydronium ion (short for H_3O^+)
H_2O	water
H_2O_2	hydrogen peroxide
HCl	hydrochloric acid
HEPA	High efficiency particulate-free air
Hg	mercury
HIMIL	HIAPER Modular Inlet
HIAPER	High-Performance Instrumented Airborne Platform for Environmental Research
HNO_3	nitric acid
HR-ToF-AMS	High-Resolution Time-of-Flight Aerosol Mass Spectrometer
HSO_3^-	bisulfite ion
HSO_4^-	bisulfate ion
H_2SO_4	sulfuric acid
HYSPLIT	Hybrid Single-Particle Lagrangian Integrated Trajectory model
I^-	Iodine ion
IC	Ion Chromatograph
inorgNO_3	inorganic nitrate
Isoprene-OA	isoprene derived organic aerosol
ISORROPIA	improved thermodynamic equilibrium aerosol mode; "equilibrium" in Greek
JST	Jefferson Street
K^+	potassium ion
K_2CO_3	potassium carbonate

K_2SO_4	potassium sulfate
KCl	potassium chloride
KNO_3	potassium nitrate
LA	Los Angeles
LiF	lithium fluoride
LOD	limit of detection
LOOOA	less-oxidized oxygenated organic aerosol
LVOOA	lowvolatile oxygenated organic aerosol
LWC	liquid water content
MAAP	Multiangle Absorption Photometer
$Mg(NO_3)_2$	magnesium nitrate
Mg^{2+}	Magnesium ion
$MgSO_4$	magnesium suflate
MILARGO	The Megacity Initiative: Local and Global Research Observations
MOOOA	more-oxidized oxygenated organic aerosol
Na^+	sodium ion
NaCl	sodium chloride
Na_2CO_3	sodium carbonate
$NaHCO_3$	sodium bicarbonate
$NaNO_3$	sodium nitrate
$NaSO_4$	sodium sulfate
NAAQS	National Ambient Air Quality Standard
NCAR	National Center for Atmospheric Research
NE	northeast
NH_3	ammonia

NH_4^+	ammonium ion
NH_4HSO_4	ammonium bisulfate
$(NH_4)_2SO_4$	ammonium sulfate
NI-PT-CIMS	negative-ion proton-transfer chemical ionization mass spectrometer
NO_2	nitrogen dioxide
NO_3^-	nitrate ion
$NO_{3,total}$	sum of nitrate and nitric acid
NOAA	National Oceanic and Atmospheric Administrations
NO_x	nitrogen oxides (NO and NO_2)
NVC	nonvolatile cation
O:C	oxygen to carbon atomic ratio
O_3	ozone
OA	organic aerosol
OAK	Oak Grove
ODR	orthogonal distance regression
PALMS	Particle Analysis by Laser Mass Spectrometry
PFA	perfluoroalkoxy
PILS-IC	Particle-Into-Liquid-Sampler coupled to an Ion Chromatograph
PM_1	particulate matters with aerodynamic diameters within 1.0 μm
$PM_{2.5}$	particulate matters with aerodynamic diameters within 2.5 μm
PM_4	particulate matters with aerodynamic diameters within 4.0 μm
ppbv	parts per billion by volume
QC-TILDAS	Quantum Cascade Tunable Infrared Laser Differential Absorption Spectrometer
RAF	Research Aviation Facility

R	gas constant
R^2 or r^2	coefficient of determination
RH	relative humidity
RS	road-side
SCAPE	Southeastern Center for Air Pollution and Epidemiology
SD	standard deviation
SE	southeast
SEARCH	Southeastern Aerosol Research and Characterization
SENEX	Southeastern Nexus of Air Quality and Climate
SMAI	Submicron Aerosol Inlet
SO_2	sulfur dioxide
SO_4^{2-}	sulfate ion
SOA	secondary organic aerosol
SOAS	Southern Oxidant and Aerosol Study
STP	standard temperature and pressure
SVDMA	Semivolatile Differential Mobility Analyzer
SVOOA	semivolatile oxygenated organic aerosol
SW	southwest
T	temperature
Te	Telluride
TEOM	Tapered Element Oscillating Microbalance
TMI	transition metal ions
U.S. or US	United States
UTC	Coordinated Universal Time
VOC	volatile organic compound

WINTER	Wintertime Investigation of Transport, Emissions, and Reactivity
XA	Xi'an
YRK	Yorkville
ZSR	Zdanovskii-Stokes-Robinson

SUMMARY

Particle acidity is a critical but poorly understood quantity that affects many aerosol processes and properties, including aerosol composition and toxicity. In this study, particle pH and water (which affects pH) are predicted using a thermodynamic model and measurements of RH, T, and inorganic gas and particle species. The method was first developed during the SOAS field campaign conducted in the southeastern U.S. in summer (pH = 0.94 ± 0.59), and then extended to aircraft observations in the northeastern U.S. in winter (WINTER study; pH = 0.77 ± 0.96) and ground observations in the coastal southwestern US in early summer (CalNex study; PM_1 pH = 1.9 ± 0.5 and $PM_{2.5}$ pH = 2.7 ± 0.3). All studies have consistently found highly acidic PM_1 with pH generally below 3. The results are supported by reproducing particle water and gas-particle partitioning of inorganic NH_4^+, NO_3^-, and Cl^-. Nonvolatile cations may increase pH with particle size above 1μm depending on mixing state but have little effect on PM_1 pH. Ion balance or molar ratio, are not accurate pH proxy and highly sensitive to observational uncertainties. Impacts of low particle pH were investigated, including the effects on aerosol nitrate trends and the role of acidity in heterogeneous chemistry. We found that $PM_{2.5}$ remained highly acidic despite a ~70% sulfate reduction in the southeastern U.S. in the last 15 years, due to buffering by semivolatile NH_3; that the bias in molar ratio predictions in past studies is linearly correlated to nonvolatile cations but not organics, challenging the organic film postulation that exclusively limits the gas-particle transfer of NH_3; that recently proposed rapid SO_2 oxidation by NO_2 during China haze events may not be a significant source of sulfate due to relatively low pH (~4); and lastly that pH is also not highly sensitive to NH_3,

a 10-fold increase in NH_3 only increases pH by one unit in various locations and seasons, which has implications for use of NH_3 controls to reduce $PM_{2.5}$ concentrations.

CHAPTER 1. INTRODUCTION

1.1 Importance of atmospheric aerosols

Aerosols, also known as particulate matters, are particles normally in forms of liquid or solid. Aerosols are found to be ubiquitous in atmosphere and often a major contributor to impaired air quality and visibility. Aerosols can suspend in air weeks long and be transported by wind across ocean, making long-lasting impacts on public health and global climate. Therefore, it is essential to understand aerosol chemistry and the links to health and climate, and to support policy making of controlling air pollution.

Aerosols affect climate directly and indirectly. Depending on the chemical composition, particle size, mixture state, and morphology, atmospheric aerosols absorb or scatter solar radiation, altering the radiation balance of the Earth surface. Black carbon and brown carbon heat up atmosphere by absorbing solar radiation, whereas the most aerosol components (both organics and inorganics) cool down atmosphere by scattering solar radiation (e.g. [*Pilinis et al.*, 1995; *Haywood and Boucher*, 2000; *Chung and Seinfeld*, 2002; *IPCC*, 2013]). Aerosols also have an indirect climate effect through modification of cloud properties, such as cloud albedo and lifetime, due to involvement in cloud formation as cloud condensation nuclei [*Lohmann and Feichter*, 2005]. The net radiative forcing from aerosols is estimated to be a cooling effect of 0.9 W m^{-2} [*IPCC*, 2013].

Ambient fine aerosols are a leading and fast-growing mortality risk factor (5^{th} ranking), resulting in more than 4 million deaths in 2015 globally [*Cohen et al.*, 2017]. Back in 2010, $PM_{2.5}$ was the 9^{th} ranking among 67 risk factors, causing 3.1 million deaths [*Lim et al.*,

2012]. After inhalation, $PM_{2.5}$ deposits in lung and may penetrate the alveoli, therefore, raises more health concerns than particles of larger sizes that cannot go as far [*Rostami*, 2009; *Kleinstreuer and Zhang*, 2010]. Numerous epidemiological studies show that aerosols are positively correlated with cardiovascular, respiratory, and allergic diseases [*Pope et al.*, 1995; *Katsouyanni et al.*, 2001; *Gauderman et al.*, 2004; *Pope et al.*, 2004]. The aerosol components that cause varying adverse health outcomes are normally minor mass fractions, such as black carbon (BC), transition metal ions (TMIs), and polycyclic aromatic hydrocarbons (PAHs).

A brief introduction on aerosol composition is followed since it is closely related to the impacts of aerosols on climate and health.

1.2 Composition of atmospheric aerosols

Fine particles ($PM_{2.5}$) are complex mixtures of organic and inorganic species [*Kanakidou et al.*, 2005; *Sardar et al.*, 2005; *Zhang et al.*, 2007a] often mixed with significant amounts of liquid water content (LWC) [*Liao and Seinfeld*, 2005; *Carlton and Turpin*, 2013].

Organic matters make up a large fraction of $PM_{2.5}$ dry mass, typically in the range of 20-60% and up to 90% in pristine forests [*Kanakidou et al.*, 2005; *Zhang et al.*, 2007a]. Organic aerosols (OA) are commonly classified into two groups: nonvolatile species emitted as aerosols (primary organic aerosol, POA), such as BC, and volatile organic compounds (VOCs) oxidized in gas phase and converted to low vapor pressure products, and then partition to the condensed phase (secondary organic aerosol, SOA) [*Chung and Seinfeld*, 2002; *Ervens et al.*, 2011]. SOA is typically a substantial fraction of OA mass,

80% on a global scale [*Kanakidou et al.*, 2005; *Spracklen et al.*, 2011] and 50%-100% depending on season and location [*Xu et al.*, 2015b].

Inorganic species are also significant fractions of $PM_{2.5}$ dry mass. Sulfate (SO_4^{2-}), ammonium (NH_4^+), and nitrate (NO_3^-) are typically the most abundant inorganic ions, with lower levels of sodium (Na^+), chloride (Cl^-), crustal elements (e.g. Ca^{2+}, Mg^{2+}, K^+), and TMIs [*Cabada et al.*, 2004; *Sardar et al.*, 2005; *Peltier et al.*, 2007a; *Zhang et al.*, 2010; *Fang et al.*, 2015; *Guo et al.*, 2015]. Aerosol hydronium ion (H_3O^+, hereafter denoted as H^+, but recognizing that the unhydrated hydrogen ion is rare in aqueous solutions) is difficult to quantify directly and often expressed as a logarithmic scale, pH (discussed further below).

Although LWC is inorganic, it is not routinely measured as other inorganic ions. LWC is the most abundant particle species in the atmosphere, at least 2-3 times of the total aerosol dry mass on a global scale [*Pilinis et al.*, 1995; *Liao and Seinfeld*, 2005]. It is a vital medium for aerosol aqueous chemistry, and it is mainly determined by relative humidity (RH), particle concentration and composition (i.e. hygroscopicity).

1.3 Importance of particle pH

pH is defined as the hydrogen ion activity in an aqueous solution [*Stumm and Morgan*, 1996].

$$pH = -\log_{10} \gamma_{H^+} H^+_{aq} \tag{1-1}$$

where γ_{H^+} is the hydronium ion activity coefficient, H^+_{aq} (mole L^{-1}) is the hydronium ion concentration in particle water. pH varies considerably in natural liquid systems and pH of

7 indicates a neutrality at 25 °C. For examples, pH of seawater is between 7.4 and 9.6 [*Marion et al.*, 2011], pH of human blood is typically limited to a range between 7.34 and 7.45 [*Waugh and Grant*, 2014], pH of normal rain is 5.6, pH of acid rain is usually lower between 3.5 and 5.0 [*Menz and Seip*, 2004], and pH of lemon juice is as low as 2. pH is an important liquid property in many fields, such as chemistry, biology, oceanography, and environmental science. Here we focus on how pH affects aerosol chemical and biochemical properties such as chemical reactions, equilibrium conditions, and biological toxicity.

pH is involved in secondary aerosol formation, for the pH-sensitive aqueous reactions. H^+ catalyzes heterogeneous reactions of organics such as hydration, polymerization, and carbonyl ring opening [*Jang et al.*, 2002] and may play a key role in SOA formation. Laboratory chamber studies have shown the production rates of SOA from some biogenic volatile organic compound (BVOC) precursors, such as isoprene and α-pinene, are enhanced by acidic particle seeds [*Jang et al.*, 2002; *Gao et al.*, 2004; *Edney et al.*, 2005; *Surratt et al.*, 2007; *Eddingsaas et al.*, 2010; *Surratt et al.*, 2010; *Han et al.*, 2016b]. Evidence for enhanced acid-catalyzed SOA formation in the ambient atmosphere have also been reported in several studies [*Chu*, 2004; *Lewandowski et al.*, 2007; *Zhang et al.*, 2007b; *Tanner et al.*, 2009; *Pathak et al.*, 2011; *Lin et al.*, 2012; *Budisulistiorini et al.*, 2013]. Sulfate is a ubiquitous inorganic aerosol species and is produced by aqueous and gas phase oxidation of sulfur dioxide (SO_2) along well-established pathways. The competition between aqueous pathways depends on the pH level; ozone (O_3) dominates under alkaline and hydrogen peroxide (H_2O_2) dominates under acidic conditions [*Seinfeld and Pandis*, 2006].

In addition to controlling certain aqueous reactions, pH affects particle concentrations and compositions directly through partitioning of both semivolatile weak (e.g. formic, acetic, and oxalic) and strong acids (e.g., nitric and hydrochloric). Low pH drives these acids to the protonated and volatile states, and hence into the gas phase. By impacting $PM_{2.5}$ mass concentrations, particle pH can affect emission control priorities aimed at meeting air quality standards to protect human health [*Lelieveld et al.*, 2015]. Furthermore, pH-controlled partitioning of these acids and associated ammonium affects deposition patterns of both acids and nitrogen (nitric acid, ammonia) due to large differences in gas and particle deposition rates [*Huebert and Robert*, 1985; *Duyzer*, 1994; *Schrader and Brummer*, 2014] and particle nitrate potentially affects N_2O_5 heterogeneous reaction rates and NO_x control [*Wahner et al.*, 1998; *Bertram and Thornton*, 2009; *Wagner et al.*, 2013].

pH also affects the solubility of TMIs found in aerosols, such as Fe [*Meskhidze et al.*, 2003; *Oakes et al.*, 2012; *Longo et al.*, 2016]. Although mainly present as insoluble oxides, lower pH can dissolve these metals and convert them to soluble forms, such as metal sulfates [*Oakes et al.*, 2012] and thereby significantly change the aerosol environmental impacts. For example, on global scales, metal mobility affects nutrient distributions [*Duce and Tindale*, 1991; *Meskhidze et al.*, 2003; *Meskhidze et al.*, 2005; *Nenes et al.*, 2011; *Ito and Xu*, 2014; *Myriokefalitakis et al.*, 2015; *Myriokefalitakis et al.*, 2016] with important impacts on productivity [*Meskhidze et al.*, 2005], carbon sequestration and oxygen levels in the ocean [*Ito et al.*, 2016], whereas on regional scales soluble TMIs have been linked to aerosol toxicity or aerosol oxidative potential [*Ghio et al.*, 2012; *Verma et al.*, 2014; *Fang et al.*, 2015]. Synergistic adverse health effects have also been observed between ozone and acidic aerosols [*Last*, 1991; *Enami et al.*, 2008] and many epidemiological

studies have reported adverse health outcomes associated with strong aerosol acidity [*Koutrakis et al.*, 1988; *Thurston et al.*, 1994; *Dockery et al.*, 1996; *Raizenne et al.*, 1996; *Gwynn et al.*, 2000; *Lelieveld et al.*, 2015].

Besides the above effects on aerosol composition, aerosol morphology and phase transitions, including efflorescence and phase separation, is found to be pH-dependent [*Losey et al.*, 2016].

1.4 Current understanding of particle pH

Despite its importance, a direct measurement technique of particle pH is very limited. A recent indirect optical method that infers H^+ activity based on the ratio of SO_4^{2-} and HSO_4^- was developed, but only applicable to determine pH for particle sizes larger than 10 μm and requires activity coefficient predicted by thermodynamic modeling [*Rindelaub et al.*, 2016]. Filter collected aerosols are widely extracted via de-ionized water with follow-up analysis in lab. The pH of the extracted solution measured via a pH probe or a pH test strip (not accurate as a probe) does not necessarily indicate the pH in aerosols for two reasons. First, aerosol water-soluble ions get completed dissociated in the very dilute extracted solution compared to the much more concentrated aerosol water, in which multiple forms of ions are possible and depend on pH (e.g., sulfate can be in the form of H_2SO_4, HSO_4^-, or SO_4^{2-}). Second, some originally water-insoluble ions may dissolve in the extraction and change the ion balance.

The inability to directly measure fine particle pH has led to the use of measurable aerosol properties as acidity proxies, such as aerosol ammonium-sulfate ratio or ion balances (e.g. [*Paulot and Jacob*, 2014; *Wang et al.*, 2016; *Silvern et al.*, 2017]). Use of these pH proxies

may lead to inappropriate conclusions on pH's effect because they do not capture the variability in particle water, ion activity coefficients, or partial dissociation of species in the aerosol phase (as discussed in the thesis).

The method that best constrains aerosol pH is comparison between a thermodynamic analysis and observations of gas-particle partitioning of semivolatile species that are sensitive to pH at the given environmental conditions (i.e., gas-particle concentration ratios near 1:1). Based on this framework, particle pH was reported in the range of 2.5 to 3.5 for deliquesced sea-salts at Bermuda [*Keene and Savoie*, 1998], below 2 for acidified dust over the Yellow Sea [*Meskhidze et al.*, 2003], and 2 to 3 in the northern Colorado U.S. [*Young et al.*, 2013].

1.5 Overview of this study

The scope of this work is to develop a pH prediction method based on a thermodynamic model that calculates ion interactions, gas-particle partitioning, and LWC at the in situ and non-ideal conditions of atmospheric aerosols. Compared to the previous work that predict particle pH, this work extensively evaluates the accuracies of the reported pH with a large suite of observational dataset from several field campaigns conducted in the US. The predicted pH is used for investigating the pH impacts on aerosol chemistry. This work also explains the historical observational trends and provides insights on the particle pH change in the future.

The thesis is organized by the following structure**: Chapter 2** presents a detailed development, validation, and uncertainty analysis of the new pH prediction method. NH_3-NH_4^+ partitioning was used to constrain pH predictions. As LWC is essential for pH

calculation, we compared the modeled and measured LWC and found a good agreement. Although water associated with organics accounted for 35% the total LWC, it is fairly accurate to predict particle pH only by water associated with inorganics, expecting a minor bias of 0.15 to 0.23 for the conditions investigated. In the southeastern (SE) U.S., pH was found in a range of 0.5 to 2 in the summer and 1 to 3 in the winter, showing that aerosols were highly acidic throughout the year. **Chapter 3 and 4** present the extended pH analysis to the northeastern (NE) U.S. and the southwestern (SW) U.S., respectively. A vertical profile of pH was shown for the first time that PM_1 was highly acidic for altitudes up to 5000 m, with a pH of 0.77 ± 0.96 (± SD) in the NE US in winter. The PM_1 pH, 1.9 ± 0.5, in the SW US was about one unit higher than the SE, 0.94 ± 0.59, despite a similar temperature (T) and relative humidity (RH) ranges, and likely caused by much higher total nitrate concentrations relative to sulfate in the Los Angeles city (LA). The internally mixed sea-salts between 1 and 2.5 μm sizes further increase $PM_{2.5}$ in LA to 2.7 ± 0.3. HNO_3-NO_3^- partitioning, LWC, and pH are found to be inter-related in complex ways and can only be captured and resolved with a thermodynamic model. **Chapter 5** presents a sensitivity analysis of $PM_{2.5}$ pH to sulfate and ammonia based on the historical 70% SO_4^{2-} reduction in the SE US from 1998 to 2013. On contrary to the common expectations that aerosols are becoming more neutral and ammonium nitrate will replace ammonium sulfate as the dominant inorganics, we found nearly constant pH (~1) throughout the last 15 years and no increasing sign of ammonium nitrate. **Chapter 6** focuses on the roles of nonvolatile cations (NVC) on model-predicted ammonium-sulfate molar ratio and pH. We found the error in molar ratio prediction is positively correlated with NVC and not organic aerosol, therefore, challenged the postulated ability of organic films to prevent ammonia from

achieving gas-particle equilibrium. We also found that inclusion of NVC resulted in predicted molar ratio agreeable to the 15 years observed decreasing trend as shown in Chapter 5, and the conclusion of consistently strong aerosol acidity despite large sulfate reduction remained robust. **Chapter 7** presents a sensitivity analysis of pH to ammonia for a wide range of ammonia and various locations in U.S. and China. We showed that for a given set of meteorological conditions (T and RH), roughly a 10-fold decrease in NH_3 concentrations is required to drop pH levels by one unit, revealing an inherent consistency between vastly different aerosol systems. Most importantly, the China haze aerosol pH was found below 5, under the condition it is unlikely that NO_2-mediated oxidation of SO_2 is a major sulfate formation route. **Chapter 8** talks about future work following the thesis work.

Some companion works that are not included in the thesis but closely relevant to the topic of pH and pH affected aerosol properties are introduced here briefly. Utilizing the pH and LWC presented in Chapter 2, *Xu et al.* [2015a] found that isoprene derived organic aerosol (Isoprene-OA, 18-36% of OA) in the SE US was not limited by acidity or water, but rather linearly correlated with aerosol sulfate (R = 0.77), since sulfate provides both adequate H^+ and water required in isoprene aqueous phase oxidation. Therefore, controlling sulfate also benefits from reducing Isoprene-OA in the SE US. Further evidence was found as enhanced Isoprene-OA formation in sulfur-rich power plant plumes [*Xu et al.*, 2016]. *Fang et al.* [2017] presented a size-resolved pH analysis and hypothesized a possible link between sulfate and particle oxidative potential (OP) through solubilizing TMIs. Fine particles were found to be SO_4^{2-}-rich with pH generally below 2 and coarse particles (aerodynamic diameters ranging from 2.5 to 10 μm) with pH approaching 7 (neutrality) as size increases. Soluble metals and OP peaked at the intersection of the two particle modes and suggested

that sulfate played a key role in producing highly acidic fine particles capable of dissolving primary TMIs that contribute to aerosol OP.

CHAPTER 2. FINE PARTICLE WATER AND PH IN THE SOUTHEASTERN UNITED STATES

2.1 Abstract

Particle water and pH are predicted using meteorological observations (RH, T), gas/particle composition and thermodynamic modeling (ISORROPIA-II). A comprehensive uncertainty analysis is included, and the model is validated. We investigate mass concentrations of particle water and related particle pH for ambient fine mode aerosols sampled in a relatively remote Alabama forest during the Southern Oxidant and Aerosol Study (SOAS) in summer and at various sites in the southeastern U.S. during different seasons, as part of the Southeastern Center for Air Pollution and Epidemiology (SCAPE) study. Particle water and pH are closely linked; pH is a measure of the particle H^+ aqueous concentration and depends on both the presence of ions and amount of particle liquid water. Levels of particle water, in-turn, are determined through water uptake by both the ionic species and organic compounds. Thermodynamic calculations based on measured ion concentrations can predict both pH and liquid water but may be biased since contributions of organic species to liquid water are not considered. In this study, contributions of both the inorganic and organic fractions to aerosol liquid water were considered and predictions were in good agreement with measured liquid water based on differences in ambient and dry light scattering coefficients (prediction vs. measurement: slope = 0.91, intercept = 0.46 μg m^{-3}, R^2 = 0.75). ISORROPIA-II predictions were confirmed by good agreement between predicted and measured ammonia concentrations (slope = 1.07, intercept = −0.12 μg m^{-3}, R^2 = 0.76). Based on this study, organic species on average contributed 35% to the total water, with a substantially higher contribution (50%) at night. However, not including

contributions of organic water had a minor effect on pH (changes pH by 0.15 to 0.23 units), suggesting that predicted pH without consideration of organic water could be sufficient for the purposes of aqueous SOA chemistry. The mean pH predicted in the Alabama forest (SOAS) was 0.94 ± 0.59 (median 0.93). pH diurnal trends followed liquid water and were driven mainly by variability in RH; during SOAS nighttime pH was near 1.5, while daytime pH was near 0.5. pH ranged from 0.5 to 2 in summer and 1 to 3 in the winter at other sites. The systematically low pH levels in the southeast may have important ramifications, such as significantly influencing acid-catalyzed reactions, gas-aerosol partitioning, and mobilization of redox metals and minerals. Particle ion balances or molar ratios, often used to infer pH, do not consider the dissociation state of individual ions or particle liquid water levels and do not correlate with particle pH.

2.2 Introduction

The concentration of the hydronium ion (H^+) in aqueous aerosols, or pH, is an important aerosol property that drives many processes related to particle composition and gas-aerosol partitioning [*Jang et al.*, 2002; *Meskhidze et al.*, 2003; *Gao et al.*, 2004; *Iinuma et al.*, 2004; *Tolocka et al.*, 2004; *Edney et al.*, 2005; *Czoschke and Jang*, 2006; *Kleindienst et al.*, 2006; *Surratt et al.*, 2007; *Eddingsaas et al.*, 2010; *Surratt et al.*, 2010]. Measurement of pH is highly challenging and so indirect proxies are often used to represent particle acidity. The most common is an ion balance: the charge balance of measurable cations and anions (excluding the hydronium ion). Although correlated with an acidic (net negative balance) or alkaline (net positive balance) aerosol [*Surratt et al.*, 2007; *Tanner et al.*, 2009; *Pathak et al.*, 2011; *Yin et al.*, 2014], an ion balance cannot be used as a measure of the aerosol concentration of H^+ in air (i.e., moles H^+ per volume of air, denoted hereafter as H^+_{air}). This is due to two factors, first, an ion balance assumes all ions are completely dissociated,

but multiple forms are possible, depending on pH (e.g., sulfate can be in the form of H_2SO_4, HSO_4^-, or SO_4^{2-}). Secondly, pH depends on the particle liquid water content (LWC), as pH is the concentration of H^+ in an aqueous solution. LWC can vary considerably over the course of a day and between seasons significantly influencing pH [*Seinfeld and Pandis*, 2006]. Aerosol thermodynamic models, such as ISORROPIA-II [*Nenes et al.*, 1998; *Fountoukis and Nenes*, 2007] and E-AIM [*Clegg et al.*, 1998], are able to calculate LWC and particle pH, based on concentrations of various aerosol species, temperature (T), and relative humidity (RH) and offer a more rigorous approach to obtain aerosol pH [*Pye et al.*, 2013]. ISORROPIA-II calculates the composition and phase state of an NH_4^+-SO_4^{2-}-NO_3^--Cl^--Na^+-Ca^{2+}-K^+-Mg^{2+}-water inorganic aerosol in thermodynamic equilibrium with water vapor and gas phase precursors. The model has been tested with ambient data to predict acidic or basic compounds, such as NH_3, NH_4^+, and NO_3^- [*Meskhidze et al.*, 2003; *Nowak et al.*, 2006; *Fountoukis et al.*, 2009; *Hennigan et al.*, 2015].

LWC is a function of RH, particle concentration and composition, and is the most abundant particle-phase species in the atmosphere, at least 2-3 times the total aerosol dry mass on a global average [*Pilinis et al.*, 1995; *Liao and Seinfeld*, 2005]. At 90% RH, the scattering cross-section of an ammonium sulfate particle can increase by a factor of five or more above that of the dry particle, due to large increases in size from water uptake [*Malm and Day*, 2001]. Because of this, LWC is the most important contributor to direct radiative cooling by aerosols [*Pilinis et al.*, 1995], currently thought to be -0.45 W m^{-2} (-0.95 W m^{-2} to +0.05 W m^{-2}) [*IPCC*, 2013]. LWC plays a large role in secondary aerosol formation for inorganic and possibly organic species by providing a large aqueous surface for increased gas uptake and a liquid phase where aqueous phase chemical reactions can result in products of lower vapor pressures than the absorbed gases [*Ervens et al.*, 2011; *Nguyen et al.*, 2013]. In the eastern U.S., it has been suggested that the potential for organic gases

to partition to LWC is greater than the potential to partition to particle-phase organic matter [*Carlton and Turpin*, 2013], and partitioning of water soluble organic carbon (WSOC) into the particle phase becomes stronger as RH (i.e., LWC) increases [*Hennigan et al.*, 2008a]. Thus LWC enhances particle scattering effects directly by increasing particle cross sections [*Nemesure et al.*, 1995] and indirectly by promoting secondary aerosol formation [*Ervens et al.*, 2011; *Nguyen et al.*, 2013].

The behavior of inorganic salts under variable RH is well established both experimentally and theoretically. It is known that dry inorganic salts (or mixtures thereof) exhibit a phase change, called deliquescence, when exposed to RH above a characteristic value. During deliquescence, the dry aerosol spontaneously transforms (at least partially) into an aqueous solution [*Tang*, 1976; *Wexler and Seinfeld*, 1991; *Tang and Munkelwitz*, 1993]. In contrast, due to its chemical complexity that evolves with atmospheric aging, the relationship of organics to LWC is not well characterized and requires a parameterized approach [*Petters and Kreidenweis*, 2007]. Relationships between volatility, oxidation level, and hygroscopicity are not always straightforward and still remain to be fully understood [*Frosch et al.*, 2011; *Villani et al.*, 2013; *Cerully et al.*, 2015; *Hildebrandt Ruiz et al.*, 2015]. Despite the abundance and importance of LWC, it is not routinely measured. Thus typically, particle total mass concentration (that includes liquid water) is often not characterized. In general, LWC is measured by perturbing the in situ RH. The loss of particle volume when RH is lowered is assumed to be solely due to evaporated water. Approaches for LWC measurements are classified into single particle size probes and bulk size quantification [*Sorooshian et al.*, 2008]. Single size particle probes provide more information (i.e., size resolved hygroscopic growth) and usually tend to be slow due to whole size range scanning. In contrast, bulk size measurements quantify the total water

amount directly. The LWC measurement presented in this paper by nephelometers is a bulk measurement.

As part of the Southern Oxidant and Aerosol Study (SOAS), we made detailed measurements of particle organic and inorganic composition [*Xu et al.*, 2015a], aerosol hygroscopicity [*Cerully et al.*, 2015], and indirect measurements of particle LWC. These data are used to first determine the particle water mass concentrations, which are then utilized in a thermodynamic model for predicting pH. The fine particle LWC and pH data from this analysis are used in our other studies of secondary aerosol formation as part of SOAS and discussed in companion papers to this work [*Cerully et al.*, 2015; *Xu et al.*, 2015a].

2.3 Data collection

2.3.1 Measurement sites

Aerosol measurements were conducted at the Southeastern Aerosol Research and Characterization (SEARCH) Centreville site (CTR; 32.90289 N, 87.24968 W, altitude: 126 m), located in Brent, Alabama, as part of SOAS (Southern Oxidant and Aerosol Study) (http://soas2013.rutgers.edu). SOAS ground measurements were made from June 1 to July 15 in the summer of 2013. CTR is a rural site within a large forested region dominated by biogenic volatile organic compound (VOC) emissions, with minor local anthropogenic emissions and some plumes transported from other locations (coal-fired electrical generating units, urban emissions, biomass burning, mineral dust). It is representative of background conditions in the southeastern U.S. and chosen to investigate biogenic

secondary organic aerosol (SOA) formation and its interaction with anthropogenic pollution transported from other locations.

Additional measurements were also made at various sampling sites in and around the metropolitan Atlanta region from May 2012 to December 2012 as part of a large health study; the Southeastern Center for Air Pollution and Epidemiology (SCAPE). A map of all five sites is shown in Figure 2-1. The SCAPE measurement sites include:

- A road-side (RS) site (33.775602 N, 84.390957 W), situated within 5m from the interstate highway (I75/85) in midtown Atlanta and chosen to capture fresh traffic emissions;
- A near-road site (GIT site, 33.779125 N, 84.395797 W), located on the rooftop of the Ford Environmental Science and Technology (EST) building at Georgia Institute of Technology (GIT), Atlanta, roughly 30 to 40 m above ground level, 840 m from the RS site;
- Jefferson Street (JST) (33.777501 N, 84.416667 W), a central SEARCH site representative of the Atlanta urban environment, located approximately 2000 m west of the GIT site;
- Yorkville (YRK) (33.928528 N, 85.045483 W), the rural SEARCH pair of JST, situated in an agricultural region approximately 70 km west from the JST, GIT and RS sites.

More information on the SEARCH sites can be found elsewhere [*Hansen et al.*, 2003; *Hansen et al.*, 2006]. We first focus on the SOAS campaign data, where wide range of instrumentation was deployed (http://soas2013.rutgers.edu) to develop a comprehensive method of predicting LWC and pH, as well as assessing their uncertainties. The approach

is then applied to the SCAPE site data to provide a broader spatial and temporal assessment of $PM_{2.5}$ pH in the southeastern US.

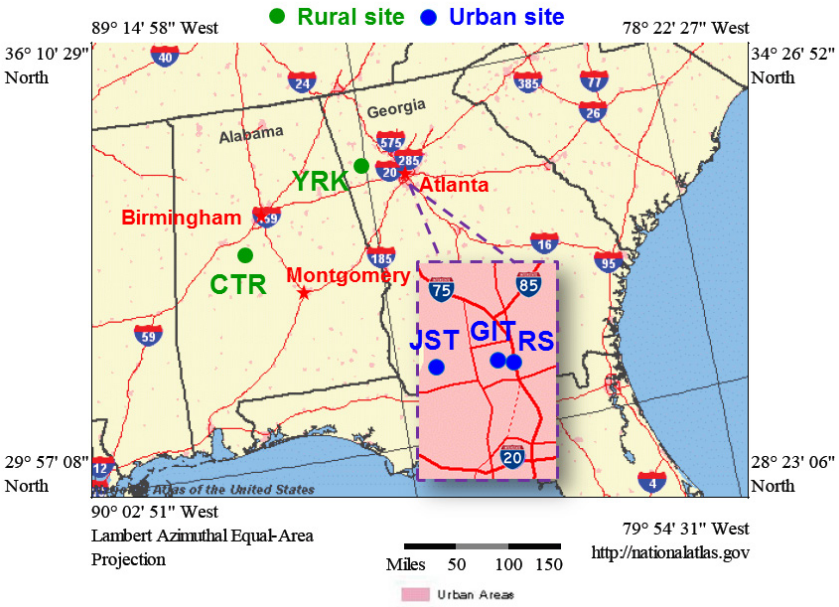

Figure 2-1 Sampling sites in the southeastern U.S., consisting of two rural and three urban sites.

2.3.2 Instrumentation

2.3.2.1 PILS-IC

$PM_{2.5}$ or PM_1 (particles with aerodynamic diameters < 2.5 or 1.0 µm at ambient conditions) water soluble ions were measured by a Particle-Into-Liquid-Sampler coupled to an Ion Chromatograph (PILS-IC; Metrohm 761 Compact IC). Similar setups are described in previous field studies [*Orsini et al.*, 2003; *Liu et al.*, 2012]. Metrosep A Supp-5, 150/4.0 anion column and C 4, 150/4.0 cation column (Metrohm U.S., Riverside, FL) were used to

separate the PILS liquid sample anions (sulfate, nitrate, chloride, oxalate, acetate, formate) and cations (ammonium, sodium, potassium, calcium, magnesium) at a 20 min duty cycle. The PILS sample ambient air flow rate was 16.8 ± 0.4 L min^{-1}. URG (Chapel Hill, North Carolina) cyclones were used to provide PM cut sizes of $PM_{2.5}$ for the 1st half of field study (June 1 to June 22) and PM_1 for the latter half (June 23 to July 15). Honeycomb acid (phosphoric acid)- and base (sodium carbonate)-coated denuders removed interfering gases before entering the PILS. The sample inlet was ~7 m above ground level and ~4 m long. The sampling line was insulated inside the trailer (typical indoor T was 25 °C) and less than 1m in length to minimize possible changes in aerosol composition prior to measurement. Periodic 1-hr blank measurements were made every day by placing a High Efficiency Particulate-Free Air (HEPA) filter (Pall Corp.) on the cyclone inlet. All data were blank corrected. The PILS-IC was only deployed for the SOAS study.

2.3.2.2 AMS

A High-Resolution Time-of-Flight Aerosol Mass Spectrometer (HR-ToF-AMS, Aerodyne Research Inc., hereafter referred to as "AMS") provided real time, quantitative measurements of the non-refractory components of submicron aerosols [*DeCarlo et al.*, 2006; *Canagaratna et al.*, 2007]. In brief, particles were first dried (RH < 20%) and then immediately sampled through an aerodynamic lens into the high vacuum region of the mass spectrometer, then transmitted into a detection chamber where particles impact on a hot surface (600°C). Non-refractory species are flash vaporized and then ionized by 70 eV electron impact ionization. The generated ions are extracted into the time-of-flight mass

spectrometer. Further details on the AMS setup and data processing can be found in *Xu et al.* [2015a].

2.3.2.3 CCNc

The particle hygroscopic parameter, κ [*Petters and Kreidenweis*, 2007], used to infer the hygroscopic properties (liquid water associated with organics), was obtained from size-resolved CCN measurements from a Droplet Measurement Technologies Continuous-Flow Streamwise Thermal Gradient Cloud Condensation Nuclei counter (CFSTGC, referred to hereafter as CCNc) [*Roberts and Nenes*, 2005; *Lance et al.*, 2006]. The CCNc exposes aerosols to a known supersaturation, then counts the activated particles that grow rapidly to droplet size. Theory can be used to parameterize the water phase properties (here, expressed by κ; [*Petters and Kreidenweis*, 2007]) of the organic aerosol, based on the size of particles that form CCN and their composition. A URG PM_1 cyclone was installed for both AMS and CCNc. The details of the CCNc setup and data analysis procedure can be found in *Cerully et al.* [2014].

2.3.2.4 Ambient vs Dry Nephelometers

$PM_{2.5}$ (URG cyclones) aerosol light scattering coefficients (σ_{sp}) were measured online with two different nephelometers (Radiance Research M903) to infer LWC. Both were operated at nominally 3 L min^{-1}. Particle dry scattering was measured with a nephelometer located in the air-conditioned sampling trailer operated with a nafion dryer upstream that maintained an RH of 31.5 ± 1.9 % (study mean ± SD, n = 12464 based on 5-min averages). The other was situated in a small white 3-sided wooden shelter (one side covered by a loose

tarp) located a distance away from all buildings to provide a scattering measurement at ambient T and RH. Both $PM_{2.5}$ cut cyclones were in ambient conditions, and both nephelometers were calibrated by CO_2 prior to the SOAS field campaign. Typical uncertainty is 3% for scattering coefficients [*Mitchell et al.*, 2009]. In addition, the nephelometer RH sensors were calibrated by placing the sensors in a closed container above aqueous saturated salt solutions that had reached equilibrium (measurements made in a thermally insulated container after a period of a few hours). Solution temperatures were monitored. Details on the calibration results are provided in the supporting materials A.1. Recorded RH was corrected by the calibration results.

2.3.3 Determining LWC from nephelometers

Particle water was inferred from the ratio of ambient and dry $PM_{2.5}$ scattering coefficients (σ_{sp}) measured by the two nephelometers (defined here as aerosol hygroscopic growth factor, $f(RH) = \sigma_{sp(ambient)} / \sigma_{sp(dry)}$, where $\sigma_{sp(ambient)}$ and $\sigma_{sp(dry)}$ are particle scattering coefficients at ambient and dry RH conditions, respectively) following the method developed by other investigators [*Carrico et al.*, 1998; *Kotchenruther and Hobbs*, 1998; *Carrico et al.*, 2000; *Malm and Day*, 2001; *Sheridan et al.*, 2002; *Magi and Hobbs*, 2003; *Kim et al.*, 2006]. A difference between ambient and dry scattering coefficients is assumed to be caused solely by loss of water. Detailed derivations are provided in the supporting materials A.2. $f(RH)$ is related to the particle scattering efficiencies (Q_s) and average particle diameter ($\overline{D_p}$) by;

$$\overline{D_{p,ambient}} = \overline{D_{p,dry}} \sqrt{f(RH)\, \overline{Q_{s,dry}} / \overline{Q_{s,ambient}}} \qquad (2\text{-}1)$$

$\overline{Q_{s,ambient}}$, $\overline{D_{p,ambient}}$ are the average scattering efficiency and average particle diameter under ambient conditions, while $\overline{Q_{s,dry}}$, $\overline{D_{p,dry}}$ represent dry conditions. The method is based on fine particle light scattering being mostly due to particles in the accumulation mode and can be related to scattering efficiencies and the diameter of average surface, for both ambient and dry particle size distributions. Assuming $\overline{Q_{s,ambient}} = \overline{Q_{s,dry}}$ (see supporting materials A.2 for justification and uncertainty analysis), it follows that

$$\overline{D_{p,ambient}} = \overline{D_{p,dry}}\sqrt{f(RH)} \quad (2\text{-}2)$$

Since the LWC is equal to the difference between ambient and dry particle volume, we get

$$f(RH)\_water = [f(RH)^{1.5} - 1]m_p\rho_w/\rho_p \quad (2\text{-}3)$$

where m_p and ρ_p are dry particle mass and density, respectively; ρ_w is water density (constant 1 g cm^{-3} is applied). For SOAS, dry $PM_{2.5}$ mass concentrations were measured continuously by a TEOM (tapered element oscillating microbalance, 1400a, Thermo Fisher Scientific Inc., operated by Atmospheric Research & Analysis Inc., referred to hereafter as ARA). Particle density, ρ_p, was computed from the particle composition, including AMS total organics, ammonium, and sulfate, which accounted for 90% of the measured $PM_{2.5}$ (TEOM) dry mass (SOAS study mean). A typical organic density 1.4 g cm^{-3} is assumed [*Turpin and Lim*, 2001; *King et al.*, 2007; *Engelhart et al.*, 2008; *Kuwata et al.*, 2012; *Cerully et al.*, 2014], and the density of ammonium sulfate is assumed to be 1.77 g cm^{-3} [*Sloane et al.*, 1991; *Stein et al.*, 1994]. ρ_p was calculated to be 1.49 ± 0.04 g cm^{-3} (n = 4,393) using mass fractions (ε) to dry particle mass:

$$\rho_p = \frac{1}{\varepsilon_{NH_4^+ + SO_4^{2-}}/1.77 + \varepsilon_{Org}/1.4} \quad (2\text{-}4)$$

The time-resolved composition data shows that dry particle density did not have a significant diurnal variability (± 2.7%, SD/mean, Figure A-2). In the following we refer to the particle water calculated by this method as *f(RH)*_water. The uncertainty of *f(RH*)_water is estimated to be 15%, mainly caused by the calculation of $\overline{Q_{s,ambient}}/\overline{Q_{s,dry}}$ (LWC error of 10% from assuming $\overline{Q_{s,ambient}}/\overline{Q_{s,dry}}$ = 1, see supporting materials A.2), m_p (10%), $\sigma_{sp(ambient)}/\sigma_{sp(dry)}$ (4.2%) (uncertainty for a single σ_{sp} measurement is 3%, *Mitchell et al*. [2009]), and ρ_p (2.7%). Note that LWC error depends on RH, and for SOAS average composition aerosol could increase to 21% for RH > 90% (supporting materials Figure A-6).

The deployment status of the above instruments at the SOAS and SCAPE sites are summarized in Table 2-1.

Table 2-1 Deployment status of instruments at various sites. All the listed instruments or probes were operated at CTR for SOAS.

Site	Period (mm yyyy)	PILS-IC	AMS	CCNc	Nephelometer	TEOM	RH&T
JST	May&Nov 2012	No	Yes	No	No	Yes	Yes
YRK	July&Dec 2012	No	Yes	No	No	Yes	Yes
GIT	July-Aug 2012	No	Yes	No	No	Yes	Yes
RS	Sept 2012	No	Yes	No	No	Yes	Yes
CTR	June-July 2013	Yes	Yes	Yes	Yes	Yes	Yes

2.4 Modeling methods: Predicting LWC and pH from aerosol composition

In most studies, such as SCAPE, particle water was not measured and must be determined based on aerosol composition. Both inorganic and organic components contribute to uptake of water vapor, establishing equilibrium for the ambient RH and T conditions. Thus, LWC is controlled by meteorological conditions and by aerosol concentration and composition. Thermodynamic models, such as ISORROPIA-II, have been extensively used to predict LWC due to inorganic aerosol components [*Fountoukis and Nenes*, 2007]. Contributions to LWC by organic components are typically based on an aerosol hygroscopicity parameter, κ, which is determined by CCN data. Here we refer to particle water associated with inorganics and organics as W_i and W_o, respectively. Total particle water ($W_i + W_o$) is taken as the sum of water associated with individual aerosol chemical components (sum of ions and lumped organics) based on Zdanovskii-Stokes-Robinson (ZSR) relationship [*Zdanovskii*, 1936; *Stokes and Robinson*, 1966], with the assumption that the particles are internally mixed.

2.4.1 LWC from inorganic species

Particle water associated with inorganic species (W_i) were predicted by ISORROPIA-II [*Nenes et al.*, 1998; *Fountoukis and Nenes*, 2007]. ISORROPIA-II calculates the composition and phase state of a K^+-Ca^{2+}-Mg^{2+}-NH_4^+-Na^+-SO_4^{2-}-NO_3^--Cl^--water inorganic aerosol in thermodynamic equilibrium with gas phase precursors. Chemical and meteorological data are necessary inputs. For our analysis at CTR, the inputs to ISORROPIA-II are the inorganic ions measured by the IC or AMS, RH measured by the outside nephelometer, and temperature from the SEARCH site (ARA) meteorological data.

2.4.2 LWC from organic fraction

To determine the contributions to particle water by W_o, in SOAS the organic hygroscopicity parameter (κ_{org}) was calculated based on the observed CCN activities of the organic fraction [*Cerully et al.*, 2015]. In the following analysis, diurnal three-hour running averages are used in the calculation. (Diurnal plot is included in Figure A-7). W_o is calculated using the following equation [*Petters and Kreidenweis*, 2007].

$$W_o = \frac{m_{org}\rho_w}{\rho_{org}} \frac{\kappa_{org}}{\left({}^{1}/_{RH} - 1\right)} \tag{2-5}$$

where m_{org} is the organic mass concentration from AMS [*Xu et al.*, 2015a], ρ_w is water density, and a typical organic density (ρ_{org}) of 1.4 g cm^{-3} is used [*Turpin and Lim*, 2001; *King et al.*, 2007; *Engelhart et al.*, 2008; *Kuwata et al.*, 2012; *Cerully et al.*, 2014].

2.4.3 pH prediction

The thermodynamic model, ISORROPIA-II [*Fountoukis and Nenes*, 2007], calculates the equilibrium particle hydronium ion concentration per volume air (H^+_{air}), which along with the LWC is then used to predict particle pH. To correct for the LWC associated with the organic aerosol (not considered in ISORROPIA-II), we recalculate pH by considering H^+_{air} and total predicted water (W_i and W_o). The modeled concentrations are μg m^{-3} air for H^+_{air} and LWC. The pH is then,

$$pH = -\log_{10} H^+_{aq} = -\log_{10} \frac{1000 H^+_{air}}{W_i + W_o} \tag{2-6}$$

where H^+_{aq} (mol L^{-1}) is hydronium concentration in an aqueous solution.

ISORROPIA-II has been tested in previous field campaigns where a suite of both gas and particle components were measured [*Nowak et al.*, 2006; *Fountoukis et al.*, 2009]. The model was able to predict the equilibrium partitioning of ammonia [*Nowak et al.*, 2006] in Atlanta and nitric acid [*Fountoukis et al.*, 2009] in Mexico City within measurement uncertainty. For instance, NH_3, NH_4^+, HNO_3, and NO_3^- were within 10%, 20%, 80%, and 20% of measurements [*Fountoukis et al.*, 2009]. In this study, ISORROPIA-II was run in the forward mode for metastable aerosol. Forward mode calculates the equilibrium partitioning given the total concentration of various species (gas + particle) together with RH and T as input. Reverse mode involves predicting the thermodynamic composition based only on the aerosol composition. Here we use the forward mode with just aerosol phase data input because it is less sensitive to measurement error than the reverse mode [*Hennigan et al.*, 2015]. The W_i prediction remains the same (reverse vs forward: slope = 0.993, intercept = –0.005, and R^2 = 0.99) no matter which approach is used. Gas phase input does have an important impact on the H^+_{air} calculation. ISORROPIA-II was tested with ammonia partitioning, which is discussed in more detail below. Here it is noted that we found that further constraining ISORROPIA-II with measured NH_3 [*You et al.*, 2014a] resulted in a pH increase of 0.8 at CTR and that the predicted NH_3 matched the measured NH_3 well (slope = 1.07, intercept = –0.12 μg m^{-3}, R^2 = 0.76). This also confirms that ISORROPIA-II predicts the pH in the ambient aerosol with reasonable accuracy, as inputting the total (gas + aerosol) ammonium results in predictions that agree with those observed. This is also in agreement with findings of *Hennigan et al.* [2015] and *Fountoukis*

et al. [2009], both of whom found that ISORROPIA-II reproduced the partitioning of ammonia and inorganic nitrate in Mexico City during the MILARGO campaign.

2.4.4 Assumptions

In the following analysis, we use bulk properties and do not consider variability in parameters with particle size. Particulate organic and inorganic species are assumed to be internally mixed in the liquid phase due to the high RH (73.8 ± 16.1%) typical of this study and because a large fraction of the ambient aerosol organic component is from isoprene SOA [*Xu et al.*, 2015a], which are liquids at RH ≥ 60% [*Song et al.*, 2015]. Particle liquid phase separations are not considered, although they have been measured in bulk extracts of aerosols from the southeast [*You et al.*, 2012]. It is reported that liquid-liquid phase separation can occur when the O:C ratio of the organic material is ≤ 0.5. More experiments showed that it is possible to have phase separation for O:C ≤ 0.7, but not for O:C ≥ 0.8 [*Bertram et al.*, 2011; *Song et al.*, 2012; *You et al.*, 2013]. SOAS average O:C = 0.75 (± 0.12) is in the transition between these two regimes. According to Figure 2 in *Bertram et al.* [2011], at RH typically > 60% and organic:sulfate mass ratio >1, it is not possible to have phase separation, which is the case for our sampling sites. Based on our basic assumption of no liquid-liquid phase separation, pH is homogeneous in a single particle. However, separated phases would likely have different pH if liquid-liquid phase separation occurs. In that case, pH should be calculated based on the amounts of water and H^+_{air} in each phase. Gas-particle partitioning will change according, due to these separated phases. There are models that are set up to calculate these thermodynamics (e.g., AIOMFAC), but none is yet able to address the compositional complexity of ambient SOA [*Zuend et al.*,

2010; *Zuend and Seinfeld*, 2012]. Although it is often true that non-ideal interactions between organic and inorganic species exist, good agreement between measured particle water and ammonia partitioning to predictions using the bulk properties (discussed below) suggests these assumptions are reasonable.

2.5 Results

2.5.1 Summary of meteorology and PM composition at SOAS and SCAPE sites

For the SOAS study period, mean T and RH were 24.7 ± 3.3 ℃ and 73.8 ± 16.1% (mean ± SD), respectively. This resulted in a *f(RH)*_water level of 4.52 ± 3.75 μg m^{-3}, with a maximum value of 28.41 μg m^{-3}. In comparison, SOAS mean dry $PM_{2.5}$ mass was 7.72 ± 4.61 μg m^{-3}, implying that the fine aerosols were roughly composed of 37% water, on average. Mean T and RH for SCAPE sites are listed in Table 2-3. Summer T means were all above 21℃, including CTR. RH means were all high (> 60%) for summer and winter, which is typical for the southeastern US.

Of the sites in the southeastern US discussed in this paper, CTR was the least influenced by anthropogenic emissions having the lowest black carbon (BC) concentrations (measured by a MAAP, Thermo Scientific, model 5012). At CTR, the mean BC = 0.26 ± 0.21 μg m^{-3} (± SD), whereas mean BC concentrations at the other rural site (YRK) was 0.36 μg m^{-3}. The representative Atlanta site (JST) BC was on average 0.71 μg m^{-3}, and higher for sites closer to roadways, 0.96 μg m^{-3} (GIT) and 1.96 μg m^{-3} (RS).

A more comprehensive suite of ions will provide a better prediction of W_i. However, in the southeastern US, inorganic ions are currently dominated by sulfate and ammonium. During SOAS, the PILS-IC provided a more comprehensive and accurate measurement of water-soluble ions than AMS, which measured only non-refractory sulfate, ammonium, nitrate, and chloride. Refractory, but water soluble ions, such as sodium and associated chloride, and crustal elements including calcium, potassium, and magnesium were present in PM_1, but in very low concentrations. Contributions of these ions are more important in $PM_{2.5}$ than for PM_1, which tend to reduce aerosol acidity. For instance, Na^+ has a significantly higher mean in $PM_{2.5}$ at 0.056 µg m^{-3} (the 1st half of SOAS study) than 0.001 µg m^{-3} in PM_1 (the 2nd half of SOAS study). Four, one day-long, dust events (June 12, 13, 16, and 21) in the SOAS data set have been excluded from this analysis as assumptions relating to internal mixing of $PM_{2.5}$ components are less valid in these cases. Excluding these days, the mean Na^+ in $PM_{2.5}$ drops to 0.024 µg m^{-3}.

If the fraction of the refractory ions (e.g., Na^+, K^+, Ca^{2+}, Mg^{2+}) is negligible compared to the SO_4 (Note, SO_4 stands for sulfate in all its possible forms, from free to completely dissociated), NH_4^+, and NO_3^-, the AMS data sufficiently constrains particle composition for thermodynamic calculations; this apparently is the case for most of the time in the southeast (supporting materials A.4). For PM_1 SO_4 and NH_4^+, AMS and PILS-IC were in good agreement (SO_4 slopes within 20 %, $R^2 = 0.90$; NH_4^+ within 1%, $R^2 = 0.81$). Similar agreement was also found for AMS PM_1 SO_4 and NH_4^+ versus PILS-IC $PM_{2.5}$ SO_4 and NH_4^+. (See Figure 2-2 for comparison of complete data set). These data indicate little SO_4 and NH_4^+ between the 1.0 and 2.5 µm size range ($PM_{2.5} - PM_1$). Because of the agreement

between these dominant ions, ISORROPIA-II predicted W_i for all ions measured with the PILS-IC throughout the study (includes both PM_1 and $PM_{2.5}$) agreed with W_i based on AMS inorganic species (i.e., only ammonium and sulfate) having an orthogonal slope of 1.18, Figure 2-2c.

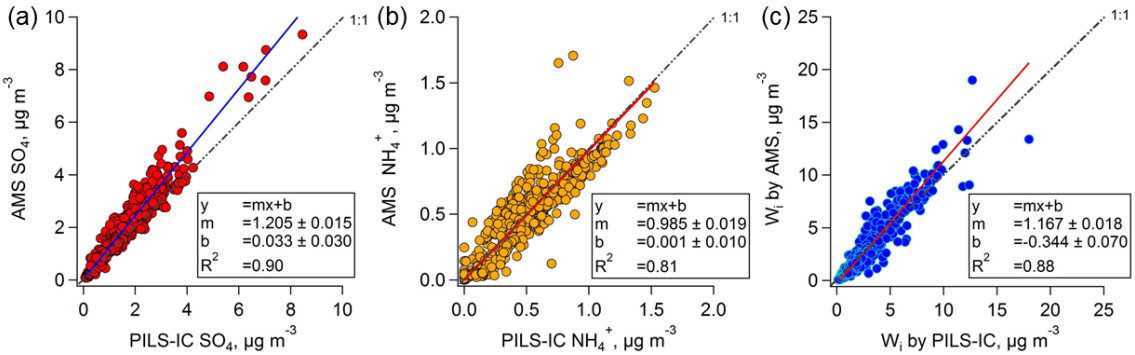

Figure 2-2 Comparisons of PM_1 AMS sulfate, ammonium to PM_1 and $PM_{2.5}$ PILS-IC (i.e. complete SOAS study) and predicted W_i. Orthogonal distance regression (ODR) fits were applied.

2.5.2 Results from the SOAS Centreville site

2.5.2.1 LWC, pH, and ion balances at Centreville

The diurnal variation of LWC contributed by W_i and W_o, along with total measured water, ambient T, RH, and solar radiation at CTR is shown in Figure 2-3. Predicted and measured LWC trends were in good overall agreement, although the largest discrepancy was observed during the daytime when the LWC level was low and more difficult to measure and accurately predict. Nighttime RH median values were between 85% and 90% and resulted in significant water uptake that reached a peak just after sunrise near 7:30 am (local

time). The dramatic peak in LWC starting at roughly 5:00 am, reaching a maximum between 7:30 and 8:00 am is likely due to RH increasing above 90%, at which point uptake of water rapidly increases with increasing RH. The similar rapid hygroscopic growth before sunrise was also observed at GIT, RS, and JST (Nov) (Figure 2-11). After sunrise, rising temperatures led to a rapid drop in RH, resulting in rapid loss of particle water. LWC reached lowest levels in the afternoon ~2 μg m^{-3}, only 20% of the peak value. W_o varied more than W_i diurnally; W_o max/min ratio was 13.1 compared to 4.1 for W_i.

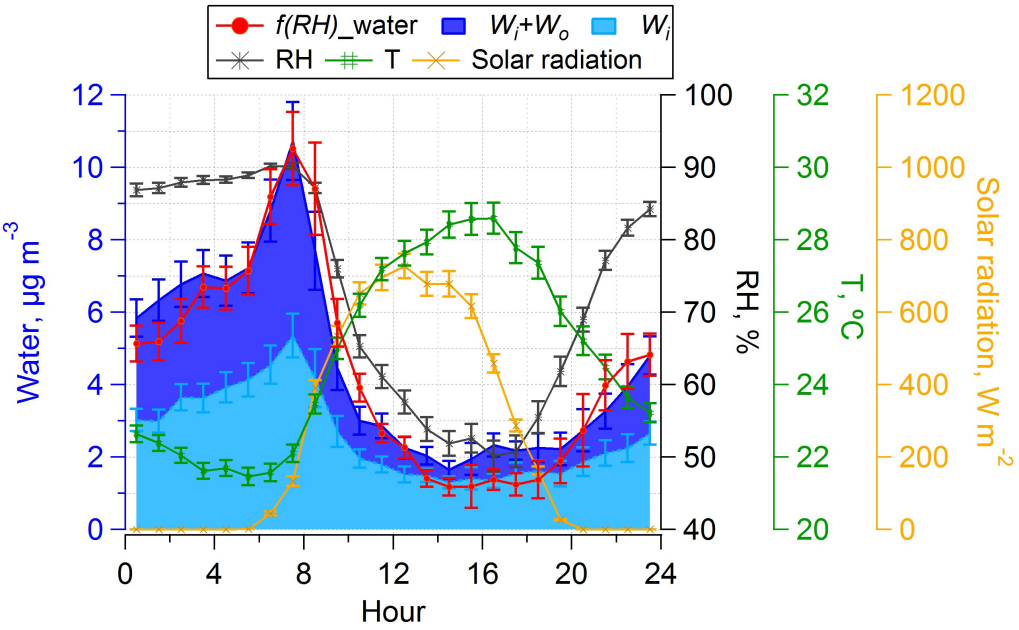

Figure 2-3 CTR (SOAS) diurnal profiles of predicted and measured water, measured RH, T, and solar radiation. Median hourly averages are shown and standard errors are plotted as error bars.

At CTR, the aerosol was highly acidic, with predicted mean pH = 0.94 ± 0.59 (± SD). The minimum and maximum pH were –0.94 and 2.23 respectively, and pH varied by

approximately 1 on average throughout the day (Figure 2-4a). That is, the H^+_{air}/LWC ratio increased by a factor of 10 from night to day. LWC max/min ratio was 5, whereas H^+_{air} diurnal variation was significantly less (Figure 2-4b), indicating that the diurnal pattern in pH was mainly driven by particle water dilution. This is further demonstrated in Figure 2-4d, which shows the diurnal variation in the NH_4^+/SO_4^{2-} molar ratio (the main ions driving pH), with only slightly lower ratios during the day. The study mean (± SD) NH_4^+/SO_4^{2-} molar ratio was 1.4 (± 0.5). As LWC is mainly controlled by RH and temperature, the pH diurnal variation was thus largely driven by meteorological conditions, not aerosol composition.

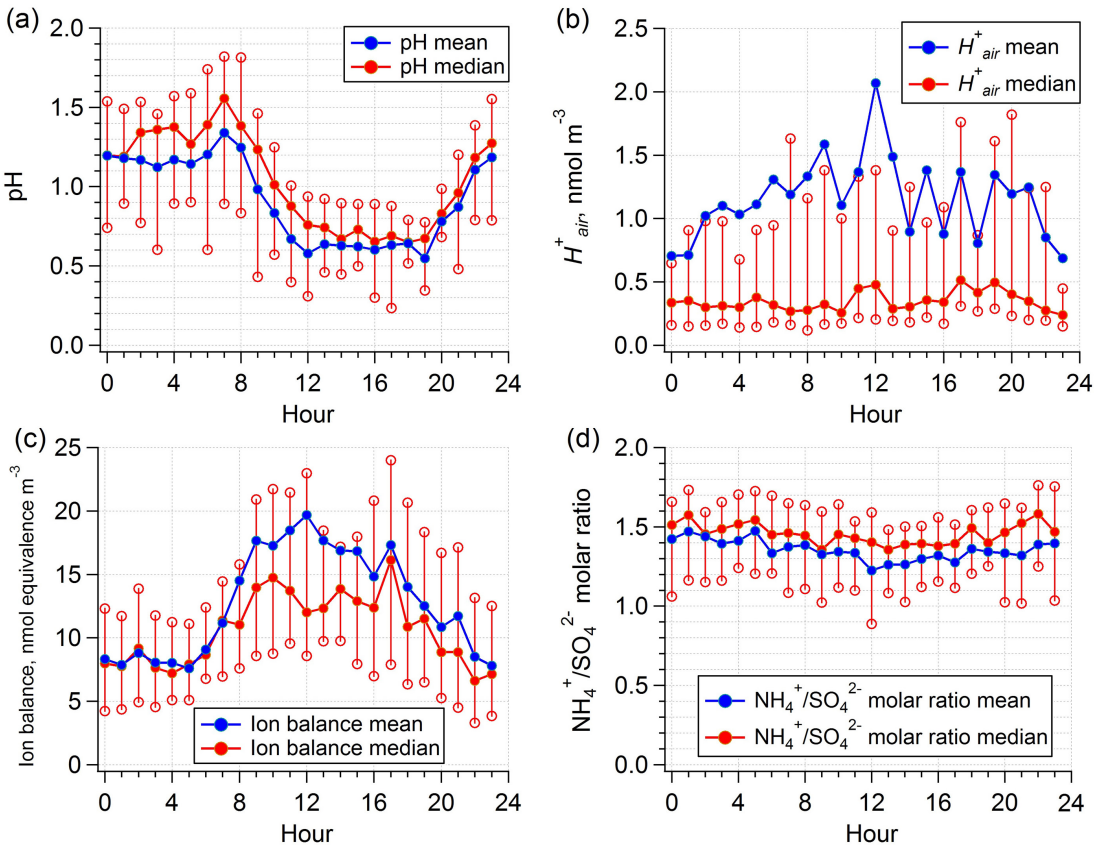

Figure 2-4 CTR (SOAS) diurnal patterns of calculated pH based on total predicted water (W_i + W_o) (a), H^+_{air} predicted by ISORROPIA-II (b), ion balance (c), and NH_4^+/SO_4^{2-} molar ratio (d). Mean and median values are shown, together with 25% and 75% quantiles marked as non-filled circles.

In part, because of the diurnal variation of LWC, a simple ion balance or NH_4^+/SO_4^{2-} molar ratio or per volume air concentration of aerosol hydronium ion (H^+_{air}) alone cannot be used as a proxy for pH in the particle. Figure 2-5a shows a weak inverse correlation ($R^2 = 0.36$) between ion balance and pH. An ion balance of an aerosol is usually calculated as follows (in unit of nmol equivalence m^{-3}), for a NH_4^+-Na^+-SO_4^{2-}-NO_3^--Cl^--water inorganic aerosol.

$$\text{Ion Balance} = \frac{[SO_4^{2-}]}{48} + \frac{[NO_3^-]}{62} + \frac{[Cl^-]}{35.5} - \frac{[NH_4^+]}{18} - \frac{[Na^+]}{23} \quad (2\text{-}7)$$

where $[SO_4^{2-}]$, $[NO_3^-]$, $[Cl^-]$, $[NH_4^+]$, and $[Na^+]$ are concentrations of these ions in units of μg m^{-3} (per volume of air). An ion balance is also a bad indicator of pH because it poorly predicts the aerosol concentration of H^+_{air}. An ion balance assumes all ions are completely dissociated, but multiple forms are possible, depending on pH (e.g., sulfate can be in the form of H_2SO_4, HSO_4^-, or SO_4^{2-}). For example, if aerosol sulfate remains in the free form of H_2SO_4, it doesn't add protons. Thus, an ion balance usually overestimates protons and is only moderately correlated with H^+_{air} (Figure 2-5b).

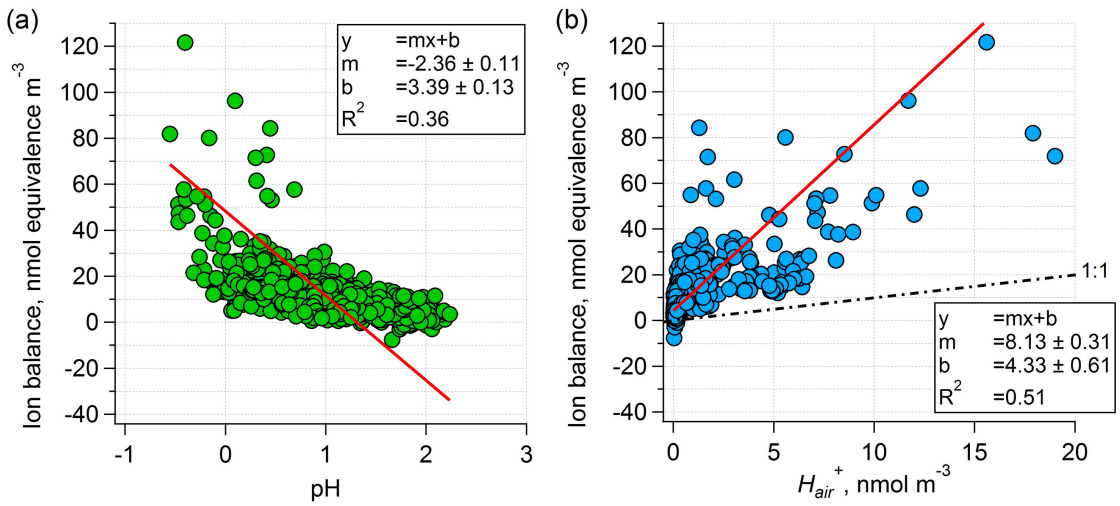

Figure 2-5 Comparison of ion balance to pH (a) and to H^+_{air} (b) at CTR (SOAS). ODR fits were applied.

2.5.2.2 LWC uncertainty:

In estimating the water uncertainty, we consider W_i and W_o separately. The uncertainty of W_i is estimated by propagating the measurement uncertainty of ions and RH through the ISORROPIA-II thermodynamic model by finite perturbations about the model base state. Uncertainties of ions were estimated by difference between IC-ions and AMS-ions, as well as PILS-IC measurement uncertainty (Table 2-2). Na^+ is excluded because it is not measured by the AMS. PILS-IC instrumental uncertainty is estimated to be 15% from the variability in standards (variability is calibration slopes), blanks, sample airflow rate, and liquid flow rate (one SD). The total ion uncertainties are listed in Table 2-2. SO_4 has a higher uncertainty, at 25%, than the rest, which are at 15%. These combined uncertainties lead to an W_i uncertainty of 25% (Figure 2-6), which is the same as the SO_4 uncertainty.

SO_4, one of the most hygroscopic ions [*Petters and Kreidenweis*, 2007], controls W_i uptake.

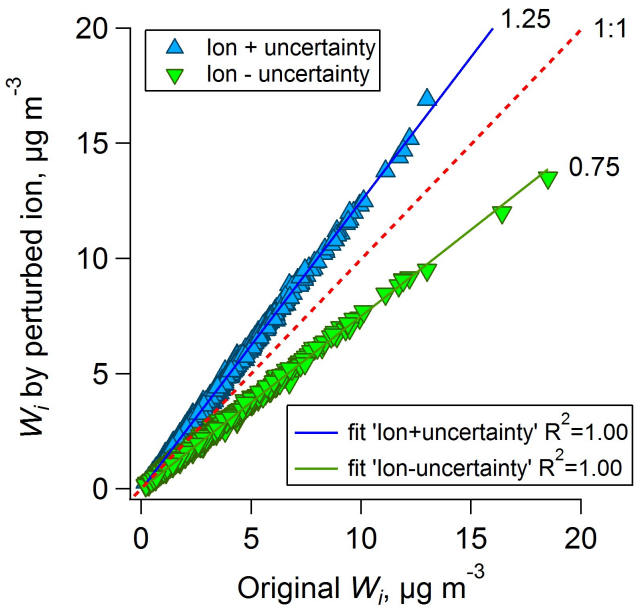

Figure 2-6 W_i based on artificially perturbed ion data at upper and lower uncertainty limits is compared to W_i at base level. The slopes indicate the W_i uncertainty caused by ions.

For the SOAS study, the RH probe in the ambient nephelometer (Humitter 50U, VAISALA Inc.) has a stated maximum uncertainty of 5% at RH = 90%. RH biases with respect to environment conditions can also occur due to placement of the probe. Based on RH comparisons between ARA, Rutgers [*Nguyen et al.*, 2014b], and the Georgia Tech instrumentation, a systematic bias as large as 10% is found. Given this, we consider an RH probe factory uncertainty (5%) as a typical value and inter-comparison difference (10%) as an extreme condition. In this analysis, RH was adjusted by ± 5% and ± 10% and W_i was recalculated (Figure 2-7). A ± 5% perturbation in RH leads to a 91% (slope − 1) error for

5% perturbation above the measured value (1.05RH) and 29% error for a perturbation below the measured value (0.95RH). We take 60% as average uncertainty. Higher uncertainty is introduced with increasing RH, owning to the exponential growth of LWC with RH and results in the asymmetric LWC uncertainty. Combining W_i uncertainty from ions (25%) and RH (60%), the overall uncertainty is calculated as 65%.

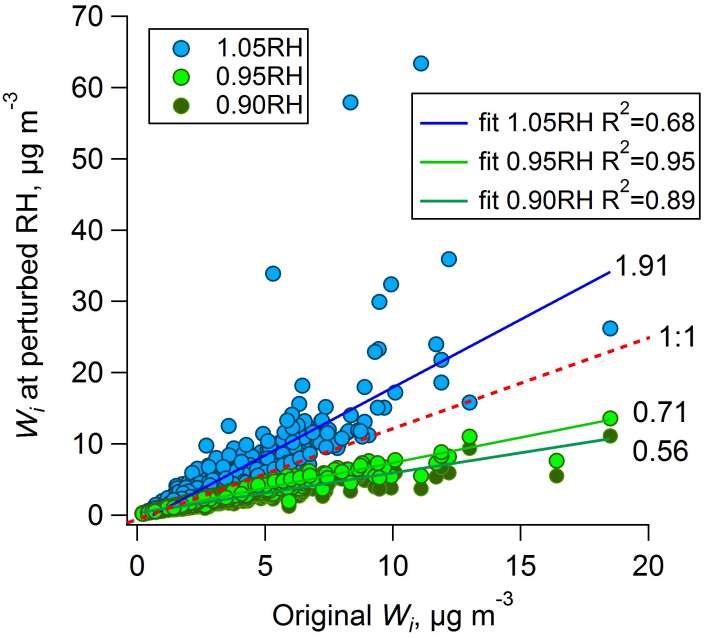

Figure 2-7 W_i based on artificially perturbed RH at upper and lower uncertainty limits compared to W_i at base level. 1.10RH (i.e., RH increased by 10%) is not plotted because it results in much larger W_i than the rest. Slopes and R^2 indicate corresponding W_i uncertainty caused by variability (uncertainty) in RH.

The uncertainty sources for W_o are κ_{org}, ρ_s, m_s, and RH (Equation 2-5). The uncertainties of these parameters are estimated to be 26% (details can be found in supporting materials A.3), 10%, 20%, and 5% (from above), respectively. In summary, the overall uncertainty of W_o is 35%.

The total uncertainty of LWC can be expressed as a sum of W_i and W_o uncertainties, where ε_i is the mass fraction. ε_{W_o} and ε_{W_i} were found to be 36% and 64% of the total LWC.

$$\frac{\delta_{LWC}}{LWC} = \sqrt{\left(\varepsilon_{W_i}\frac{\delta_{W_i}}{W_i}\right)^2 + \left(\varepsilon_{W_o}\frac{\delta_{W_o}}{W_o}\right)^2} \quad (2\text{-}8)$$

Given the above, $\frac{\delta_{LWC}}{LWC}$ is 43%. This method of assessing predicted LWC uncertainty can be applied to SCAPE sites as well. The specific predicted LWC at SCAPE sites were calculated and are listed in Table 2-3. W_i uncertainty associated with ions is the same as noted above, 25%, because it is estimated by PILS-IC and AMS differences. Similar uncertainties in W_i at the SCAPE sites are expected if RH uncertainties are similar at all sites.

2.5.2.3 pH uncertainty:

As pH is based on H^+_{air} and LWC, the uncertainty of pH can be estimated from these two parameters. We applied the adjoint model of ISORROPIA, ANISORROPIA [*Capps et al.*, 2012], to quantify the sensitivity of predicted H^+_{air} to the input aerosol species at the conditions of the thermodynamic calculations. pH uncertainty resulting from aerosol composition is then determined by propagating the input parameter uncertainties, using ANISORROPIA sensitivities, to the corresponding H^+_{air} and pH uncertainty.

We now assess how pH of $PM_{2.5}$ is affected by using an incomplete measurement of ionic species by comparing the pH predicted based on the more complete suite of ions measured by the PILS-IC versus the AMS, during SOAS. Sensitivities of aerosol species to H^+_{air} were calculated by ANISORROPIA with PILS-IC data and presented as partial derivatives

(Table 2-2). Higher sensitivity values imply the inorganic ion is more important for H^+_{air}. In the SOAS study, H^+_{air} is most sensitive to SO_4, and then NH_4^+, as they were the major ions. Uncertainties of ions were estimated by the difference between IC-ions and AMS-ions, as well as PILS-IC measurement uncertainty. Since Na^+ is not measured by AMS, we cannot estimate the difference between PILS-IC and AMS. The loadings and sensitivities of NO_3^- and Cl^- were very low, so they are assumed not to contribute much to $\frac{\delta_{H^+_{air}}}{H^+_{air}}$. Given this, $\frac{\delta_{H^+_{air}}}{H^+_{air}}$ is determined by;

$$\frac{\delta_{H^+_{air}}}{H^+_{air}} = \sqrt{\left(\frac{\partial H^+_{air}}{\partial SO_4}\frac{\delta_{SO_4}}{SO_4}\right)^2 + \left(\frac{\partial H^+_{air}}{\partial NH_4^+}\frac{\delta_{NH_4^+}}{NH_4^+}\right)^2 + \left(\frac{\partial H^+_{air}}{\partial Na^+}\frac{\delta_{Na^+}}{Na^+}\right)^2} \quad (2\text{-}9)$$

Based on the input for Equation 2-9 (Table 2-2), $\frac{\delta_{H^+_{air}}}{H^+_{air}}$ is estimated as 14%. LWC is most sensitive to RH fluctuations, so it is considered the main driver of LWC uncertainty in the pH calculation. As discussed, we artificially adjusted RH by ± 5% and ± 10% (10% is considered an extreme condition). H^+_{air}, W_i, W_o, as well as pH were all recalculated using 90%, 95%, 105%, and 110% of the actual measured RH. RH + 5% and RH − 5% lead to 12% and 6% variation in pH based on orthogonal regression slopes, respectively (Figure 2-8). RH − 10% results in only 10% variation, however, RH + 10% results in a 45% variation, and the coefficient of determination (R^2) between pH calculated based on RH + 10% and original RH drops to only 0.78, while for all other cases $R^2 > 0.96$. The disproportionately large effect of the positive uncertainty is caused by the exponential increase of LWC with RH, as RH reaches high levels (>90%). Assuming the stated

manufacturer uncertainty (5%) for our RH uncertainty, pH uncertainty is estimated to be 6%-12%. We take 12% as $\frac{\partial pH}{\partial LWC}\delta_{LWC}$ for further calculations.

Table 2-2 Sensitivity of H^+_{air} to ions from ANISORROPIA (2nd row) and contribution to uncertainty. Uncertainties of inorganic ions ($\frac{\delta_{Ion}}{Ion}$) are calculated based on a combination of PILS-IC instrumental relative uncertainties (IC uncertainty, referred to as $\frac{\delta_{ion,IC}}{Ion}$, all estimated to be 15%) and the difference between PILS-IC and AMS ($\frac{\delta_{Ion,IC-AMS}}{Ion}$, defined as the (slope − 1) in Figure 2-2a & b) (3rd row), where $\frac{\delta_{Ion}}{Ion} = \sqrt{\left(\frac{\delta_{ion,IC}}{Ion}\right)^2 + \left(\frac{\delta_{Ion,IC-AMS}}{Ion}\right)^2}$ (4th row). Contribution of uncertainty is the ratio of ion uncertainty over H^+_{air} uncertainty ($\frac{\delta_{H^+_{air}}}{H^+_{air}}$, calculated to be 14% by Equation 2-9) (5th row).

PILS-IC ion concentration, μg m^{-3} (mean ± SD)	SO_4	NH_4^+	Na^+	NO_3^-	Cl^-
	1.73 ± 1.21	0.46 ± 0.34	0.03± 0.07	0.08 ± 0.08	0.02 ± 0.03
H^+_{air} Sensitivity (mean ± SD)	$\left\|\frac{\partial H^+_{air}}{\partial SO_4}\right\|$	$\left\|\frac{\partial H^+_{air}}{\partial NH_4^+}\right\|$	$\left\|\frac{\partial H^+_{air}}{\partial Na^+}\right\|$	$\left\|\frac{\partial H^+_{air}}{\partial NO_3^-}\right\|$	$\left\|\frac{\partial H^+_{air}}{\partial Cl^-}\right\|$
	0.51 ± 0.34	0.32 ± 0.31	0.19 ± 0.27	0.002 ± 0.007	0.000 ± 0
$\frac{\delta_{Ion,IC-AMS}}{Ion}$	$\frac{\delta_{SO_4,IC-AMS}}{SO_4}$	$\frac{\delta_{NH_4^+,IC-AMS}}{-NH_4^+}$	$\frac{\delta_{Na^+,IC-AMS}}{Na^+}$	$\frac{\delta_{NO_3^-,IC-AMS}}{NO_3^-}$	$\frac{\delta_{Cl^-,IC-AMS}}{Cl^-}$
	20.5%	1.5%	N/A*	**	**
$\frac{\delta_{Ion}}{Ion}$	$\frac{\delta_{SO_4}}{SO_4}$	$\frac{\delta_{NH_4^+}}{-NH_4^+}$	$\frac{\delta_{Na^+}}{Na^+}$	$\frac{\delta_{NO_3^-}}{NO_3^-}$	$\frac{\delta_{Cl^-}}{Cl^-}$
	25.4%	15.1%	15%	15%	15%
Contribution to H^+_{air} uncertainty	$\frac{\left\|\frac{\partial H^+_{air}}{\partial SO_4}\right\| \cdot \frac{\delta_{SO_4}}{SO_4}}{\frac{\delta_{H^+_{air}}}{H^+_{air}}}$	$\frac{\left\|\frac{\partial H^+_{air}}{\partial NH_4^+}\right\| \cdot \frac{\delta_{NH_4^+}}{NH_4^+}}{\frac{\delta_{H^+_{air}}}{H^+_{air}}}$	$\frac{\left\|\frac{\partial H^+_{air}}{\partial Na^+}\right\| \cdot \frac{\delta_{Na^+}}{Na^+}}{\frac{\delta_{H^+_{air}}}{H^+_{air}}}$	$\frac{\left\|\frac{\partial H^+_{air}}{\partial NO_3^-}\right\| \cdot \frac{\delta_{NO_3^-}}{NO_3^-}}{\frac{\delta_{H^+_{air}}}{H^+_{air}}}$	$\frac{\left\|\frac{\partial H^+_{air}}{\partial Cl^-}\right\| \cdot \frac{\delta_{Cl^-}}{Cl^-}}{\frac{\delta_{H^+_{air}}}{H^+_{air}}}$
	0.93	0.35	0.20	0.002	0.000

* Na^+ is not measured by AMS.

** $\left|\frac{\partial H^+_{air}}{\partial NO_3^-}\right|$ and $\left|\frac{\partial H^+_{air}}{\partial Cl^-}\right|$ are less than 1% of the other H^+_{air} sensitivities, and the loadings of NO_3^- and Cl^- are less than 5% of the total inorganic ion mass. As a result, their contributions to H^+_{air} uncertainty are negligible.

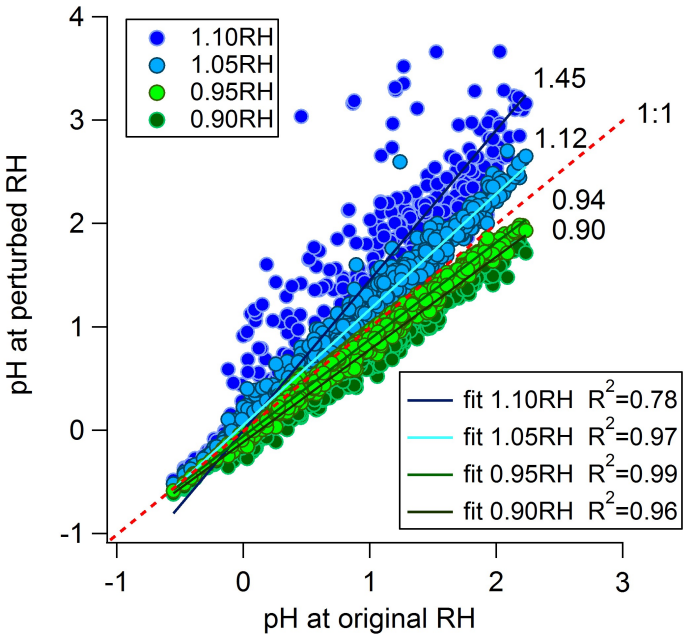

Figure 2-8 pH predictions by perturbing RH compared to pH at base level. W_i, W_o, and H^+_{air} were recalculated based on ± 5% and ± 10% original RH to investigate pH uncertainty. The slopes and R^2 indicate pH uncertainty caused by RH.

SO_4 was found to contribute the most to $\frac{\delta_{H^+_{air}}}{H^+_{air}}$. NH_4^+ and Na^+ followed. SO_4 and NH_4^+ are the two most abundant inorganic components in aerosols and controlling aerosol acidity. Finally, the total pH uncertainty is the combination of LWC and the uncertainty associated with H^+_{air}, which is computed from the definition of pH (Equation 2-6).

$$\frac{\delta_{pH}}{pH} = \sqrt{\left(\frac{\partial pH}{\partial H^+_{air}}\delta_{H^+_{air}}\right)^2 + \left(\frac{\partial pH}{\partial LWC}\delta_{LWC}\right)^2} \quad (2\text{-}10)$$

where $\frac{\partial pH}{\partial H^+_{air}}$ can be derived from Equation 2-6 as

$$\frac{\partial pH}{\partial H^+_{air}} = -\frac{1}{2.303}\frac{1}{\frac{H^+_{air}}{LWC}}\frac{1}{LWC} = -\frac{1}{2.303}\frac{1}{H^+_{air}} \quad (2\text{-}11)$$

From Equation 2-9 and the uncertainties of H^+_{air} and LWC (Equation 2-7 and 2-8), we estimate the pH uncertainty for the SOAS dataset to be 13% (based on the specific uncertainties considering here). pH uncertainties at SCAPE sites were also assessed via this method. As discussed above, $\frac{\delta_{H^+_{air}}}{H^+_{air}}$ was found to be 14% for the SOAS study, due to IC and AMS data set differences and PILS-IC instrumental uncertainty. This same uncertainty is applied to SCAPE, where no PILS-IC data were available. Because aerosol composition at all sites is similar, based on filter IC analysis (Figure A-8, similar sensitivities of H^+_{air} to ions are expected. However, actual uncertainty for each sampling period is possibly higher due to higher loadings of refractory ions at SCAPE sites due to contributions from urban emissions. Refractory ions not measured by the AMS (i.e. Na^+, K^+, Ca^{2+}, Mg^{2+}), have a minor effect on predicting LWC, but may have an important effect on pH (e.g., result in higher pH) in locations where they could substantially contribute to the overall ion balance.

2.5.2.4 Model validation: Prediction of liquid water

Several LWC measurements were made at CTR during SOAS. In addition to $f(RH)$_water (4.52 ± 3.75 μg m^{-3}), particle water was quantified with a Semivolatile Differential Mobility Analyzer (SVDMA). With this method, a SOAS study mean particle water concentration of 4.27 ± 3.69 μg m^{-3} (± SD) was obtained [*Nguyen et al.*, 2014b]. The

orthogonal regression between these two measurements (SVDMA water vs $f(RH)$_water) has slope = 0.91, intercept = –0.03, R^2 = 0.35. Differences could be caused by differences in size-resolved composition (particle composition beyond PM_1 that contributes LWC; SVDMA scans up to 1.1 µm, while $f(RH)$_water is based on $PM_{2.5}$), instrument sample heating (i.e., the degree to which the instrument was close to ambient conditions, especially when ambient RH was high, and most sensitive to slight T differences), and differences in RH probe calibrations.

CTR predicted total LWC, (W_i + W_o), was 5.09 ± 3.76 µg m^{-3} and agreed well with $f(RH)$_water. The total predicted water was highly correlated and on average within 10% of the measured water, with slope = 0.91, intercept = 0.46, R^2 = 0.75 (see Figure 2-9). Since excluding refractory ions and not considering gas phase species in the ISORROPIA-II calculations do not significantly affect the LWC prediction, its comparison across sites is less uncertain than pH.

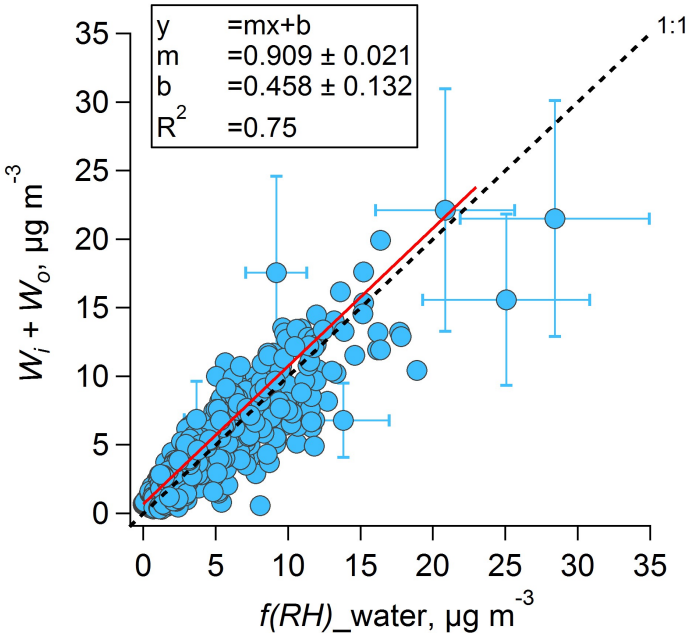

Figure 2-9 Comparison between total predicted and measured water by nephelometers based on hourly averaged data at CTR (SOAS). An ODR fit was applied. Error bars for selected points are shown.

2.5.2.5 Model validation: Prediction of pH

ISORROPIA-II calculations of pH at CTR for the SOAS study were evaluated by comparing measured and predicted NH_3. Although NH_4^+ and NH_3, along with other aerosol components, are input into the model, comparing ambient NH_4^+ and NH_3 to model predictions is not a circular analysis. For each observed data point, the model calculates total ammonia from the NH_4^+ and NH_3 input and then calculates the gas-particle ammonia partitioning assuming equilibrium. There are also other various assumptions/limitations associated with the model. Figure 2-10 shows the SOAS study time series of measured and predicted NH_3 and the fraction of ammonia in the gas phase, $NH_3/(NH_3 + NH_4^+)$. Measured and predicted NH_3 are in good agreement. Periods when almost all ammonia was in the gas

phase (ratio near 1) are related to precipitation events (June 10, 24, 28, July 03, 04) when aerosol concentrations were very low. Not including these events, the study mean (± SD) fraction ammonia in the gas phase was 0.41 (± 0.16) (median value is also 0.41). These results provide confidence in ISORROPIA-II calculations of particle pH and demonstrate the utility of including both measurements of particle and gas phases in these types of studies.

When gas and particle data are not available, pH predictions are not as accurate [*Hennigan et al.*, 2015]. Running ISORROPIA-II in the forward mode, but with only aerosol concentrations as input, may result in a bias in predicted pH due to repartitioning of ammonia in the model. In the southeast, where pH is largely driven by SO_4 and NH_4^+, the aerosol NH_4^+ input will be partitioned in the model between gas and particle phases to establish equilibrium. Sulfate repartitioning does not occur since it is nonvolatile. Thus, NH_4^+ will be lost from the particle and a lower pH predicted. At CTR ammonia partitioning has been included in all model runs, but as no NH_3 was available for SCAPE. Assuming the average NH_3/NH_4^+ ratio from CTR applies to all SCAPE sites to estimate NH_3, along with measured particle composition at each site, we got pH increases ranging from 0.87 to 1.38. In the following, all pH reported for SCAPE are corrected for this bias (i.e., pH increase by 1 to simplify the correction). Note that ammonia partitioning does not significantly affect the LWC prediction (W_i predicted without NH_3 vs W_i predicted with NH_3: slope = 1.00, intercept = –0.01 µg m^{-3}, R^2 = 0.98).

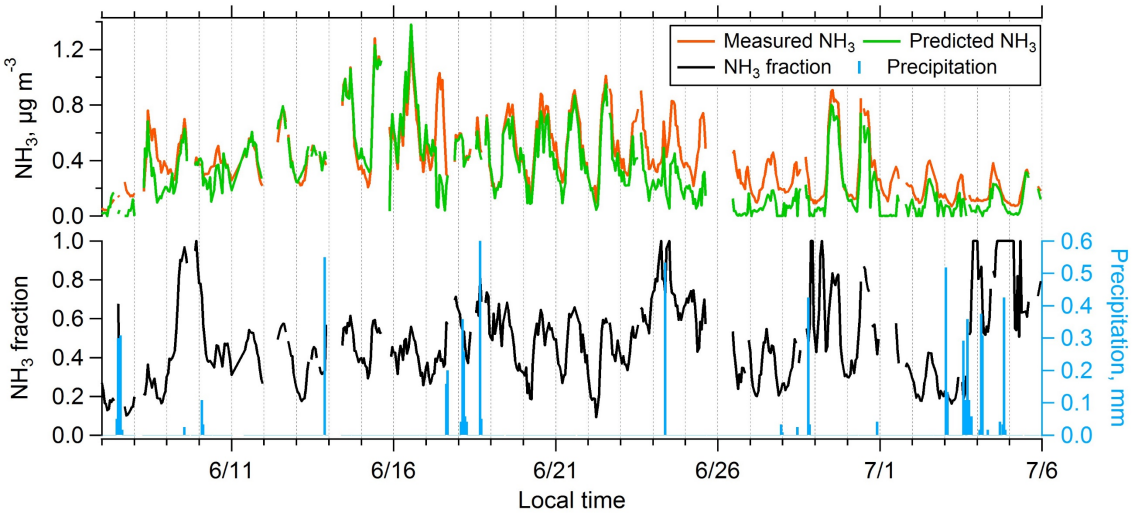

Figure 2-10 CTR (SOAS) time series of hourly averaged measured NH_3, predicted NH_3, NH_3 fraction (i.e., measured $NH_3/(NH_3 + NH_4^+)$) and precipitation.

2.5.3 LWC and pH at other sites in the southeast (SCAPE sites)

<u>Seasonal trends</u>

The methods developed and verified at CTR are now applied to the SCAPE study where fewer species was measured. LWC predictions at all SCAPE sites are shown in Table 2-3, providing insights on seasonal trends of LWC in the southeast. The overall summer LWC mean was 5.02 µg m^{-3} and winter mean 2.22 µg m^{-3}.

At the SCAPE sites, JST, YRK, GIT, and RS, summer mean pH was between 1 and 1.3, similar to CTR (mean of 0.94). In winter the pH (mean between 1.8 and 2.2) was higher by ~ 1 unit. Although LWC was higher in summer, which tends to dilute H_{air}^+ and increase pH, summer pH was lower due to higher ion (i.e., sulfate) concentrations (Table 2-3). Similar diurnal pH patterns were seen at all sites in all seasons and follow the diurnal

variations of particle water (Figure 2-11). Overall the pH in the southeast is very low, between 1 and 2 (mean), in both rural and urban environments. pH values in summer at various sites were similar (1 to 1.3), suggesting a fairly homogeneous distribution of acidity due to spatially uniform sulfate in the southeastern U.S. [*Zhang et al.*, 2012]. In winter the diurnal range in pH was roughly 2 units, while the diurnal range in summer was smaller, with pH varying by roughly 1.

Recall at CTR, 10% RH uncertainty can result in a pH prediction error of up to 45% due to the high RHs observed during the study. We estimated pH uncertainty from W_i and W_o by + 10% RH for each SCAPE site. As Table 2-3 shows, the pH uncertainty associated with RH is much lower in winter (only 1-3%) than summer (20-40%), although RH averages were similar, e.g., JST in May (67 ± 19%) and Nov (63 ± 19%), with even higher RH in winter at YRK. Total pH uncertainty at all SCAPE sites are calculated by the same method as CTR. Table 2-3 shows that higher RH and T result in larger pH uncertainty. In summer, pH uncertainty is mainly caused by RH; while in winter, it can be attributed mostly to uncertainty in ion concentrations.

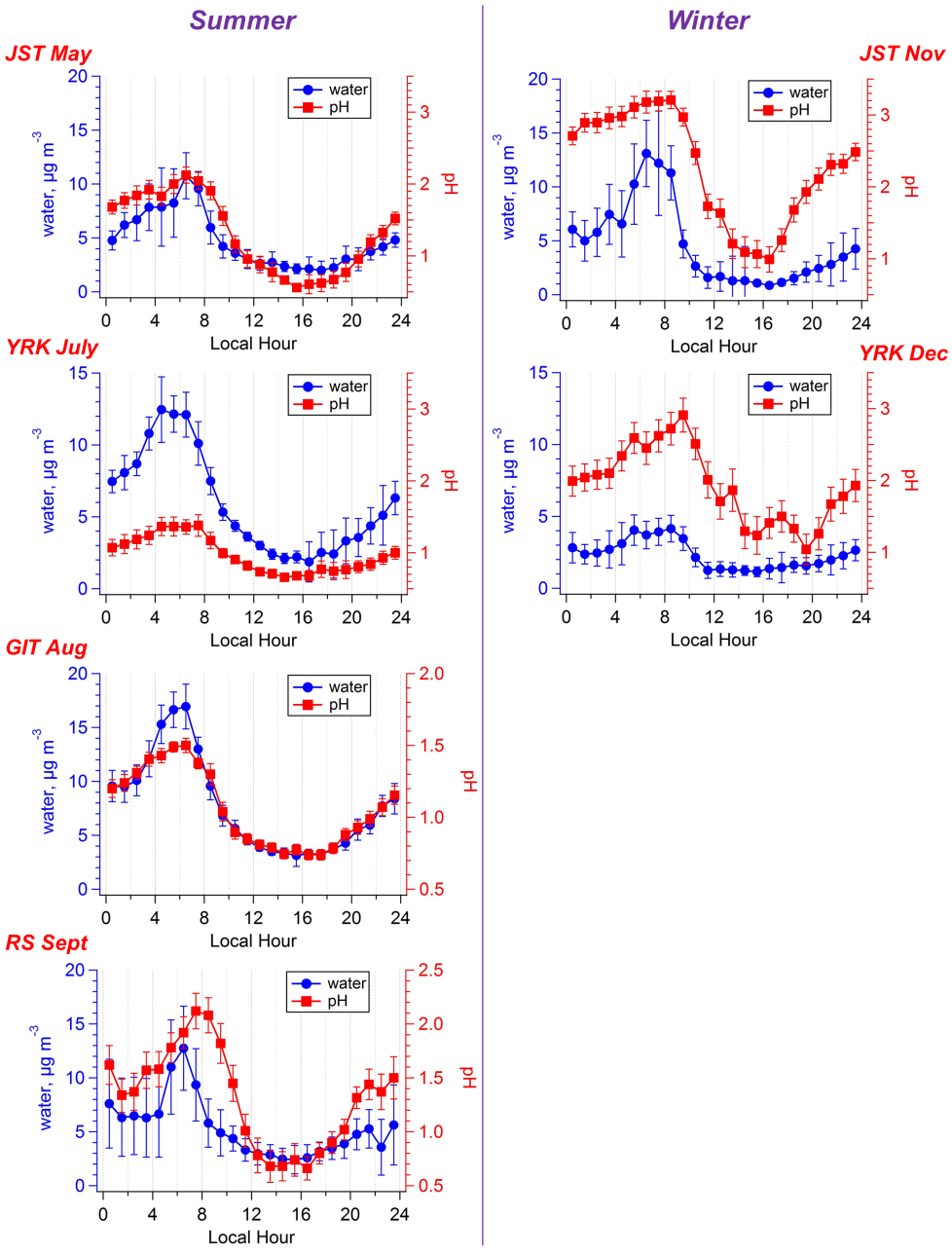

Figure 2-11 LWC and pH diurnal variation at SCAPE sites: comparison between summer and winter. Median hourly averages and standard error bars at local hour are plotted. A bias correction of 1 pH unit is applied due to not considering ammonia partitioning.

The role of W_o

W_o was significant, accounting for on average 29-39% of the total $PM_{2.5}$ particle water for all our sites (Figure 2-12 and Table 2-3). Note that, W_o at SCAPE sites were calculated by in situ AMS measurements at each SCAPE site and the mean κ_{org} (0.126) measured at CTR, due to lack of CCNc. Note that ε_{W_o} could be higher or lower at each site depending on the type of organics presented and the related κ_{org}. Figure 2-12 shows that W_o is related to the organic mass fraction. W_o is comparable to W_i at night. In contrast, it was only 33% of W_i during the daytime (Figure 2-3). The significant fraction, even during daytime, indicates organic aerosol components will have a considerable contribution to aerosol radiative forcing. Although organics are less hygroscopic than ammonium sulfate, a large fraction of the $PM_{2.5}$ (~70%) was organic, making W_o contribution important. Of the organic factors associated with W_o, *Cerully et al.* [2014] showed that MOOOA (more-oxidized oxygenated organic aerosol, also referred to as LVOOA, low-volatile oxygenated organic aerosol) and Isoprene-OA (isoprene derived organic aerosol) were twice as hygroscopic as LOOOA (less-oxidized oxygenated organic aerosol, also referred to as SVOOA, semi-volatile oxygenated organic aerosol). The LWC associated with MOOOA and Isoprene-OA account for ~60% and ~30% of total W_o in the daytime, respectively.

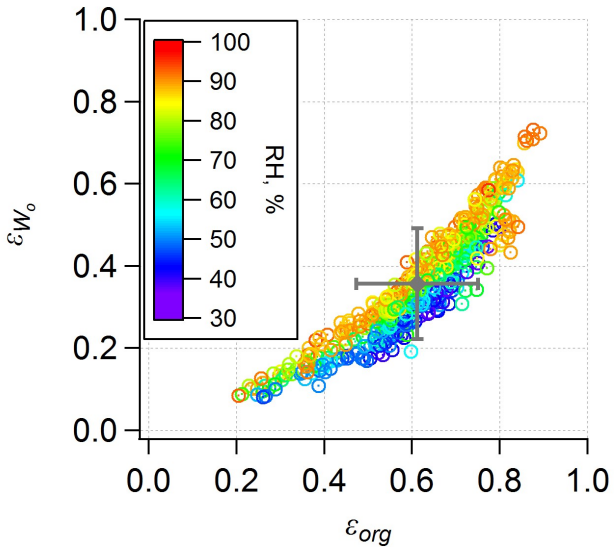

Figure 2-12 W_o mass fraction (ε_{W_o}) plotted versus organic mass fraction at CTR (SOAS). Overall study mean and standard deviation is also shown. ε_{Org} = 61 ± 14% and ε_{W_o} = 36 ± 14%.

The effect of aerosol sources of particle water on pH can also be delineated. pH calculated just by W_i alone will be affected by an underestimation of particle water, resulting in a slightly lower pH (Figure 2-13). W_o is on average 29% to 39% of total water at all sites, as a result pH increases by 0.15 to 0.23 units when W_o is included. Independent of the pH range, a 29% to 39% W_o fraction always increases pH by 0.15 to 0.23 due to the logarithmic nature of pH. The effect of W_o on pH can be simply denoted as $\log_{10}(1-\varepsilon_{W_o})$. For example, when ε_{W_o} is 90%, it shifts pH up by 1 unit. pH based on W_i is highly correlated with pH for total water ($W_i + W_o$) (Slope = 0.94, intercept = –0.14, R^2 = 0.97). This indicates that if organic mass and κ_{org} are not available, ISORROPIA-II run with only ion data will give a reasonable estimate of pH, since both H^+_{air} and W_i are outputs of

ISORROPIA-II, while W_o is predicted based on organic mass and κ_{org}. Accurate temperature and RH are still necessary inputs, especially when RH is high.

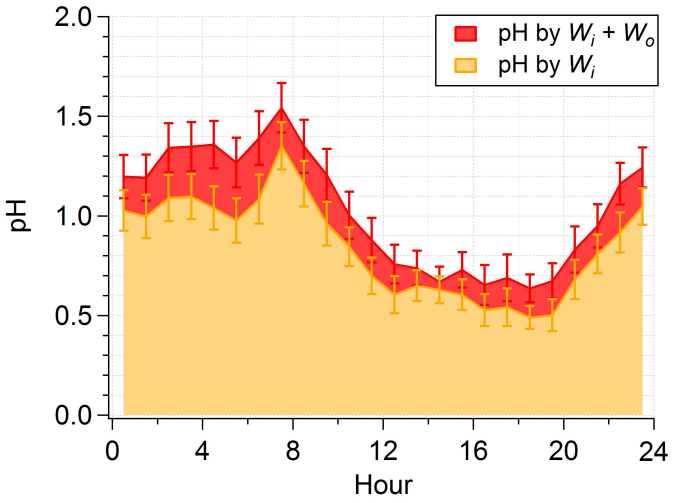

Figure 2-13 CTR (SOAS) pH diurnal profiles based on total predicted water and W_i, respectively. Median hourly averages and standard error bars at local hour are plotted.

Table 2-3 Water and pH prediction for SCAPE sites. Means and SDs are listed, if not specified. Total ion concentration is counted as the sum of AMS inorganics (4th row). ε_{W_o} is the mass fraction of W_o to particle LWC (6th row).

Site month/year	JST 05/2012	YRK 07/2012	GIT 08/2012	RS 09/2012	JST 11/2012	YRK 12/2012
RH, %	67 ± 19	66 ± 21	71 ± 17	72 ± 20	63 ± 19	73 ± 21
T, ℃	23.1 ± 4.3	27.7 ± 4.4	26.3 ± 3.5	21.4 ± 3.8	11.5 ± 4.8	9.8 ± 5.2
Total ion concentration, μg m^{-3}	4.1 ± 2.1	4.5 ± 2.2	5.3 ± 2.6	4.1 ± 2.7	3.6 ± 2.1	2.3 ± 1.8
$\frac{\delta_{pH}}{pH}$ from 1.10RH	22.3%	21.4%	48.3%	22.1%	2.5%	1.4%
Total $\frac{\delta_{pH}}{pH}$	23.9%	23.0%	49.0%	23.7%	8.8%	8.6%
ε_{W_o}, %	34 ± 11	37 ± 8	33 ± 10	38 ± 11	39 ± 16	29 ± 15
LWC, μg m^{-3}	5.98 ± 6.28	8.14 ± 8.47	8.41 ± 7.67	7.81 ± 9.23	5.88 ± 8.69	3.24 ± 3.46
pH*	1.3 ± 0.7	1.1 ± 0.6	1.1 ± 0.4	1.3 ± 0.7	2.2 ± 0.9	1.8 ± 1.0
LWC, μg m^{-3} (median)	3.74 ± 6.28	5.29 ± 8.47	6.06 ± 7.67	4.31 ± 9.23	2.14 ± 8.69	2.02 ± 3.46
pH* (median)	1.2 ± 0.7	1.0 ± 0.6	1.0 ± 0.4	1.2 ± 0.7	2.3 ± 0.9	1.8 ± 1.0

* A bias correction of 1 pH unit is applied due to not considering ammonia partitioning. See Section 2.5.2.5 for details.

2.5.4 Overall implications of low pH

Highly acidic aerosols throughout the southeast during all seasons will affect a variety of processes. For example, aerosol acidity strongly shifts the partitioning of HNO_3 to the gas phase resulting in low nitrate aerosol levels in the southeast during summer (the higher summertime temperature also plays a secondary role). Aerosol acidity also impacts the gas-particle partitioning of semivolatile organic acids. Note, organic acids are not considered in our model, under these acidic conditions (pH = 1) their contributions to the H^+_{air} (hence pH) are expected to be negligible. Because the pK_a (pK_a = – $\log_{10} K_a$, K_a referred as acid

dissociation constant) of trace organic acids are > 2 (e.g., pK_a of formic acid, one of the strongest organic acids, is 3.75, *Bacarella et al.* [1955]), low pH prevents dissociation of the organic acids. Since H^+ is involved in aqueous phase reactions, low pH can affect reaction rates by providing protons. Investigators have found that Isoprene-OA formation is acid-catalyzed and sulfuric acid participates in the reaction as a proton donor in chamber studies [*Surratt et al.*, 2007]. However, aerosol acidity appears not to be a limiting factor for Isoprene-OA formation in the southeastern US, owning to the consistently very low pH [*Karambelas et al.*, 2014; *Xu et al.*, 2015a]. Finally, low pH can affect the solubility of trace transition metals (e.g., mineral dust) such as Fe and Cu, which possibly increases the toxicity of the redox metals [*Ghio et al.*, 2012; *Verma et al.*, 2014] and may also have a long term effect on nutrient distributions in the region [*Meskhidze et al.*, 2003; *Meskhidze et al.*, 2005; *Nenes et al.*, 2011; *Ito and Xu*, 2014].

2.6 Conclusions

Particle pH is important and difficult to measure directly. However, the commonly used pH proxies of ion balances and NH_4^+/SO_4^{2-} molar ratios don't necessarily correlate with pH. Therefore, predicting pH is the best method to analyze particle acidity. By combining several models, we present a comprehensive prediction method to calculate pH and include an uncertainty analysis. ISORROPIA-II is applied to calculate the concentration of H_{air}^+ and W_i from inorganic aerosol measurements, and CCN activity is used to predict W_o. The adjoint model of ISORROPIA, ANISORROPIA, is applied to determine sensitivities, which are used for propagating the measurement uncertainties to pH. We find that W_o should be included when predicting particle LWC when organic loadings are high (such as

in the southeastern U.S.). However, the pH prediction is not highly sensitive to W_o, unless W_o mass fraction to the total particle water is close to 1. Thus, in most cases particle pH can be predicted fairly accurately with just measurements of inorganic species and ISORROPIA-II. However, constraining ISORROPIA-II with gas phase species, such as NH_3, as done in this work (or HNO_3), is highly recommended, along with running ISORROPIA-II in the forward mode. ISORROPIA-II does not consider organic acids, but at the low pHs of this study, they do not contribute protons. However, for pH approaches 7, the dissociation of organic acids cannot be neglected. Finally, the model was validated through comparing predicted to measured liquid water ($W_i + W_o$ to *f(RH)*_water) and predicted to measured NH_3 concentrations.

On average, for the SOAS and SCAPE field studies, particle water associated with the $PM_{2.5}$ organic species (W_o) accounted for a significant fraction of total LWC, with a mean of 35% (± 3% SD) indicating the importance of organic hygroscopic properties to aqueous phase chemistry and radiative forcing in the southeast US. Although organics are less hygroscopic than sulfate and ammonium, the larger mass fraction of organics than inorganics promotes W_o uptake. Predicted LWC was compared to LWC determined from ambient versus dry light scattering coefficients and a TEOM measurement of dry $PM_{2.5}$ mass. In SOAS, the sum of W_i and W_o was highly correlated and in close agreement with the measured LWC (slope = 0.91, R^2 = 0.75). LWC showed a clear diurnal pattern, with a continuous increase at night (median of 10 μg m^{-3} at 7:30 am) reaching a distinct peak when RH reached a maximum near 90% just after sunrise during the period of lowest daily

temperature, followed by a rapid decrease and lower values during the day (median of 2 μg m^{-3} at 2:30 pm).

In the southeastern US, pH normally varied from 0.5 to 2 in the summer and 1 to 3 in the winter, indicating that the aerosol was highly acidic throughout the year. The minimum and maximum pH were –0.94 and 2.2 at CTR, respectively and varied from a nighttime average of 1.5 to daytime average of 0.6, mostly attributable to diurnal variation in RH and temperature. Mean NH_4^+/SO_4^{2-} molar ratios were 1.4 ± 0.5 (SD) and roughly half the ammonia was in the gas phase ($NH_3/(NH_3 + NH_4^+)$ = 41 ± 16 %, mean ± SD). pH at other sites in the southeast (SCAPE study) was estimated based on a limited data set at an estimated uncertainty of 9-49% and a systematic bias of –1 since NH_3 is not included in the thermodynamic model run in the forward mode. pH can still be predicted with only aerosol measurements, but an adjustment of one unit pH increase is recommended for the southeastern US. pH has a diurnal trend that follows LWC, higher (less acidic) at night and lower (more acidic) during the day. pH was also generally higher in the winter (~2) than summer (~1). The low pH has significant implications for gas-aerosol partitioning, acid-catalyzed reactions including Isoprene-OA formation, and trace transition metal mobilization.

CHAPTER 3. FINE PARTICLE PH AND THE PARTITIONING OF NITRIC ACID DURING WINTER IN THE NORTHEASTERN UNITED STATES

3.1 Abstract

Particle pH is a critical but poorly constrained quantity that affects many aerosol processes and properties, including aerosol composition, concentrations, and toxicity. We assess PM_1 pH as a function of geographical location and altitude, focusing on the northeastern US, based on aircraft measurements from the Wintertime Investigation of Transport, Emissions, and Reactivity (WINTER) campaign (Feb 01 to Mar 15 2015). Particle pH and water were predicted with the ISORROPIA-II thermodynamic model and validated by comparing predicted to observed partitioning of inorganic nitrate between the gas and particle phases. Good agreement was found for relative humidity (RH) above 40%; at lower RH observed particle nitrate was higher than predicted, possibly due to organic-inorganic phase separations or nitrate measurement uncertainties associated with low concentrations (nitrate < 1 $\mu g\ m^{-3}$). Including refractory ions in the pH calculations did not improve model predictions, suggesting they were externally mixed with PM_1 sulfate, nitrate, and ammonium. Sample line volatilization artifacts were found to be minimal. Overall, particle pH for altitudes up to 5000 m ranged between –0.51 and 1.9 (10^{th} and 90^{th} percentiles) with a study mean of 0.77 ± 0.96, similar to those reported for the southeastern US and eastern Mediterranean. This expansive aircraft data set is used to investigate causes in variability in pH and pH-dependent aerosol components, such as PM_1 nitrate, over a wide range of temperatures (–21 to 19 ºC), RH (20 to 95%), inorganic gas and particle concentrations and provide further evidence that particles with low pH are ubiquitous.

3.2 Introduction

Fine particles ($PM_{2.5}$) are complex mixtures of organic and inorganic species [*Kanakidou et al.*, 2005; *Zhang et al.*, 2007a] often mixed with significant amounts of liquid water [*Carlton and Turpin*, 2013]. Sulfate, ammonium, and nitrate are typically the most abundant inorganic ions, with lower levels of sodium, chloride, crustal elements, and trace metal cations, depending on location and season [*Cabada et al.*, 2004; *Sardar et al.*, 2005; *Peltier et al.*, 2007a; *Zhang et al.*, 2010; *Fang et al.*, 2015; *Guo et al.*, 2015]. Among the aqueous aerosol species, the hydronium ion (H_3O^+, hereafter denoted simply as H^+, but recognizing that the unhydrated hydrogen ion is rare in aqueous solutions) quantified with a logarithmic scale, pH, drives many processes related to particle composition, gas-particle partitioning, and aerosol toxicity.

H^+ catalyzes heterogeneous reactions such as hydration, polymerization, and carbonyl ring opening [*Jang et al.*, 2002] and may play a key role in secondary organic aerosol (SOA) formation. Laboratory chamber studies have shown the production rate of SOA from some biogenic volatile organic compound (BVOC) precursors, such as isoprene and α-pinene, can be enhanced by strongly acidic particle seeds [*Jang et al.*, 2002; *Gao et al.*, 2004; *Iinuma et al.*, 2004; *Tolocka et al.*, 2004; *Edney et al.*, 2005; *Czoschke and Jang*, 2006; *Kleindienst et al.*, 2006; *Northcross and Jang*, 2007; *Surratt et al.*, 2007; *Eddingsaas et al.*, 2010; *Surratt et al.*, 2010]. Evidence for enhanced acid-catalyzed SOA formation in the ambient atmosphere have been reported in some studies [*Chu*, 2004; *Lewandowski et al.*, 2007; *Zhang et al.*, 2007b; *Tanner et al.*, 2009; *Pathak et al.*, 2011; *Lin et al.*, 2012; *Budisulistiorini et al.*, 2013], while others have observed no SOA enhancement [*Takahama*

et al., 2006; *Peltier et al.*, 2007b; *Karambelas et al.*, 2014]. Possible reasons for a lack of definitive evidence include varying SOA formation precursors and pathways and a range in particle pH, the latter dictating whether acidity is a limiting factor [*Nguyen et al.*, 2014a; *Budisulistiorini et al.*, 2015; *Xu et al.*, 2015a]. The use of pH proxies to infer pH (e.g., ion balances, NH_4^+/SO_4^{2-} molar ratio, etc.) can also obscure the role of H^+ since they are not uniquely related to pH (discussed below) [*Pathak et al.*, 2004; *Guo et al.*, 2015; *Hennigan et al.*, 2015; *Weber et al.*, 2016].

In addition to altering the potential SOA pathways, pH affects particle mass concentrations directly through partitioning of both semivolatile weak (e.g. formic, acetic, and oxalic) and strong acids (e.g., nitric and hydrochloric). Low pH drives these acids to the protonated and volatile states, and hence into the gas phase. In the summer, we reported that $PM_{2.5}$ aerosol pH was consistently low, between 0.5 and 2 in the southeastern US [*Guo et al.*, 2015]. This leads to low concentrations of semivolatile acids in the particle phase. For example, PM_1 inorganic nitrate (NO_3^-) concentrations were on average 0.08 μg m^{-3} in summer in Centerville, Alabama [*Guo et al.*, 2015], with typical summertime partitioning ratios, $\varepsilon(NO_3^-) = NO_3^-/(HNO_3 + NO_3^-)$, of 24 ± 5% (Table 2 in [*Blanchard et al.*, 2013]). By impacting $PM_{2.5}$ mass concentrations, particle pH can affect emission control priorities aimed at meeting air quality standards to protect human health [*Lelieveld et al.*, 2015]. Furthermore, pH-controlled partitioning of these acids and associated ammonium affects deposition patterns of both acids and nitrogen (nitric acid, ammonia) due to large differences in gas and particle deposition rates [*Huebert and Robert*, 1985; *Duyzer*, 1994; *Schrader and Brummer*, 2014] and particle nitrate potentially affects N_2O_5 heterogeneous

reaction rates and NO_x control [*Wahner et al.*, 1998; *Bertram and Thornton*, 2009; *Wagner et al.*, 2013].

pH also affects the solubility of trace metals found in aerosols, such as Fe [*Meskhidze et al.*, 2003; *Oakes et al.*, 2012]. Although mainly present as insoluble oxides, lower pH can dissolve these metals and convert them to soluble forms, such as metal sulfates [*Oakes et al.*, 2012] and thereby significantly change the aerosol environmental impacts. For example, on global scales, metal mobility affects nutrient distributions [*Duce and Tindale*, 1991; *Meskhidze et al.*, 2003; *Meskhidze et al.*, 2005; *Nenes et al.*, 2011; *Ito and Xu*, 2014; *Myriokefalitakis et al.*, 2015; *Myriokefalitakis et al.*, 2016] with important impacts on productivity [*Meskhidze et al.*, 2005], carbon sequestration and oxygen levels in the ocean [*Ito et al.*, 2016], whereas on regional scales soluble transition metals have been linked to aerosol toxicity or aerosol oxidative potential [*Ghio et al.*, 2012; *Verma et al.*, 2014; *Fang et al.*, 2015]. Synergistic adverse health effects have also been observed between ozone and acidic aerosols [*Last*, 1991; *Enami et al.*, 2008] and many epidemiological studies have reported adverse health outcomes associated with strong aerosol acidity [*Koutrakis et al.*, 1988; *Thurston et al.*, 1994; *Dockery et al.*, 1996; *Raizenne et al.*, 1996; *Gwynn et al.*, 2000; *Lelieveld et al.*, 2015].

These broad impacts of particle acidity motivate determining particle pH. Several studies [*Guo et al.*, 2015; *Hennigan et al.*, 2015] evaluated thermodynamic modeling approaches for calculating pH, including ISORROPIA-II [*Nenes et al.*, 1998; *Fountoukis and Nenes*, 2007] and E-AIM (Extended Aerosol Inorganics Model) [*Clegg et al.*, 1998; *Wexler and Clegg*, 2002; *Clegg et al.*, 2003], since an established analytical method that directly

determines aerosol pH does not exist. ISORROPIA-II and E-AIM have been shown to give similar results when both gas and particle phase are input (i.e., models run in the forward mode) [*Hennigan et al.*, 2015]. These thermodynamic models calculate particle hydronium ion concentrations (moles of particle H^+ per volume air, H_{air}^+) and liquid water content that is associated with inorganic components (W_i), based on particle and gas phase inorganic species concentrations and meteorological conditions (relative humidity, RH, and temperature, T). H_{air}^+ and W_i can then be used to calculate particle pH. Accuracy of model pH predictions can be assessed by comparing predicted to measured partitioning of semivolatile species (e.g., NH_3-NH_4^+, HNO_3-NO_3^-), which can be highly sensitive to pH, T, and RH (i.e., W_i) [*Guo et al.*, 2015; *Hennigan et al.*, 2015]. This paper extends our analysis of fine particle pH from the southeastern [*Guo et al.*, 2015] to the northeastern US and presents some of the first data on pH as a function of altitude.

3.3 Methods

The Wintertime Investigation of Transport, Emissions, and Reactivity (WINTER) aircraft study was based out of NASA Langley Research Center (Hampton, Virginia) and focused mainly on the northeastern US. The National Center for Atmospheric Research (NCAR) C-130 aircraft conducted a total of 13 flights from Feb 01 to Mar 15 2015. The payload included a suite of instruments to measure gas and aerosol composition. Here we focus on gas-phase nitric acid and measurements of aerosol inorganic components. Method details are provided below. Ambient T, RH, and aircraft coordinates were provided by the Research Aviation Facility (RAF) as part of the C-130 instrumentation package (http://data.eol.ucar.edu/master_list/?project=WINTER). Aircraft data are typically

reported at a reference temperature and pressure; however, concentration data are reported here at ambient temperature and pressure because thermodynamic partitioning calculations need to be carried out at ambient conditions.

3.3.1 Instrumentation

PILS-IC: PM_1 (particles with aerodynamic diameters < 1.0 μm at ambient conditions) water-soluble ions were measured with a Particle-Into-Liquid Sampler coupled with Ion Chromatographs (PILS-IC; Metrohm 761 Compact ICs) [*Orsini et al.*, 2003; *Hennigan et al.*, 2006; *Sullivan et al.*, 2006; *Peltier et al.*, 2007a; *Liu et al.*, 2012; *Guo et al.*, 2015]. Ambient aerosol was sampled from a submicron aerosol inlet (SMAI) [*Craig et al.*, 2013a; *Craig et al.*, 2013b; *Craig et al.*, 2014; *Moharreri et al.*, 2014] at a flow rate of 15.0 L min^{-1}. Residence time in the inlet and sample lines is estimated at 2 sec. Upstream of the PILS-IC, a non-rotating micro-orifice impactor [*Marple et al.*, 1991] with a 1.0 μm cut size (at 1 atm and 273.15 K) restricted measurements to PM_1 to be comparable with the Aerosol Mass Spectrometer (discussed below). Air temperature was measured just prior to the PILS with a calibrated thermocouple since changes in T (and thus also RH) from ambient can be significant when sampling from aircraft, and especially when ambient temperatures are low. Below we show that the particles did not have sufficient time to adjust to these changing conditions so the impactor cut size can be assumed to be for particles sizes under ambient conditions. (Note that the range in ambient pressures encountered in this study have minor effects on cut size; 10^{th} percentile is 0.99 μm and 90^{th} percentile is 1.00 μm). Therefore, no corrections for PILS-IC measured species are made due to the small deviation from nominal cut size. To eliminate gas interferences, phosphoric acid and

sodium carbonate coated honeycomb denuders were installed before the PILS. The liquid transport flow introduced at the top of the PILS impactor was spiked with lithium fluoride (LiF) and measured with the IC to account for sample liquid dilution. The liquid sample collected from the bottom of the PILS impactor was pumped into two ICs with 150 µL sample loops and operated at a chromatographic separation of 3 min for both the anions (chloride, sulfate, and nitrate) and the cation (lithium, ammonium, etc.). A Metrosep A Supp 15-50/4.0 anion column and a C4-50/4.0 cation column (Metrohm U.S., Riverside, Florida) were operated at an eluent flow rate of 1.05 mL min^{-1} and 1.0 mL min^{-1}, respectively. Eluents used during this campaign were 12 mM Na_2CO_3 (sodium carbonate)/8.0 mM $NaHCO_3$ (sodium bicarbonate) for anion exchange and 2.0 mM dipicolinic acid/3.0 mM HNO_3 for cation exchange. The cation IC (without suppressor) exhibited higher baseline noise during the campaign than the anion IC, so lacked sufficient sensitivity for reliable measurements of NH_4^+. Therefore, NH_4^+ and other ambient cation data from this instrument are not used in the following analysis. For all flights, a valve upstream of the PILS diverted sampled air through a High Efficiency Particulate-Free Air (HEPA) filter (Pall corp.) to provide blank measurements during the first 10 mins after take-off. All data were blank corrected. Limits of detection (LOD) were estimated from the blank measurements (3×SD of blanks) as 0.06 µg m^{-3} (SO_4^{2-}), 0.05 µg m^{-3} (NO_3^-), and 0.12 µg m^{-3} (Cl^-) for a 3 min sampling time. The relative measurement uncertainty for the anions is estimated to be 20% based on uncertainty propagation of sample air flow, liquid flow variations and instrument precision, which is based on variability in calibrations with known liquid standards.

AMS: A high resolution time of flight aerosol mass spectrometer (HR-ToF-AMS, Aerodyne Research Inc., hereafter referred to as "AMS") measured non-refractory components of PM_1 at a rate of 1 sec in total aerosol mass mode. The general operation of the AMS has been described elsewhere [*Jayne et al.*, 2000; *DeCarlo et al.*, 2006; *Canagaratna et al.*, 2007; *Dunlea et al.*, 2009; *Jimenez et al.*, 2009; *Kimmel et al.*, 2011]. Particles were sampled through a NCAR High-Performance Instrumented Airborne Platform for Environmental Research (HIAPER) Modular Inlet (HIMIL) [*Stith et al.*, 2009] at a flow rate of 10 L min^{-1}, into a pressure controlled inlet operated at 325 Torr [*Bahreini et al.*, 2008], then introduced into the high vacuum region of the mass spectrometer through an aerodynamic focusing lens, and transmitted to a detection chamber where particles impacted on a porous tungsten vaporizer (600°C). Non-refractory species are flash vaporized and then ionized with 70 eV electron impact ionization. The generated ions are then extracted and analyzed by time-of-flight mass spectrometry. Residence time from the tip of the HIMIL to the vacuum vaporizer was 0.5 sec. An estimated collection efficiency based on the algorithm proposed by *Middlebrook et al.* [2012] was applied to all data, and relative ionization efficiencies for sulfate, ammonium, and chloride were determined by multiple in-field calibrations. Typical detection limits during the WINTER campaign were 0.02 μg sm^{-3} for sulfate, 0.01 μg sm^{-3} for ammonium, and 0.07 μg sm^{-3} for nitrate and chloride for a 1 sec sampling interval (sm^{-3} refers to standard cubic meters under 1 atm and 273.15 K). Accuracy for AMS detection of inorganic species is estimated at 35% for aircraft operation [*Bahreini et al.*, 2009]. More refractory species, such as $NaNO_3$ (sodium nitrate) and Na_2SO_4 (sodium sulfate) are inefficiently detected by the AMS [*Hayes et al.*,

2013]. AMS data are often used to estimate the fractions of inorganic and organic nitrates using the measured NO_2^+/NO^+ ion ratios in the AMS [*Fry et al.*, 2013]. However, in this study, the presence of particulate nitrite and the likely partial detection of submicron $NaNO_3$ made that method under-determined. For that reason, in addition to total measured nitrate, estimates were made of just inorganic nitrate concentrations based on comparisons of the AMS data to the IC-based instruments.

CIMS: HNO_3 concentrations at a rate of 1 sec were quantified by a high resolution time of flight chemical ionization mass spectrometer (CIMS), which used the I^- reagent ion to selectively detect HNO_3 [*Slusher et al.*, 2004; *Lopez-Hilfiker et al.*, 2012; *Lee et al.*, 2014; *Lopez-Hilfiker et al.*, 2016]. In a heated teflon flow tube at low pressure, iodide ions are produced to selectively cluster with HNO_3 in ambient air. The ions from the flow tube enter a mass spectrometer, where they are detected. The estimated HNO_3 measurement uncertainty is 15%. This includes the accuracy of NO_2 calibration cylinder and in flight variability of continuous calibration source. Detection limit varies from flight to flight and more information regarding the CIMS operation can be found in [*Lee et al.*, 2014; *Lopez-Hilfiker et al.*, 2016].

3.3.2 pH and partitioning calculations

The ISORROPIA-II thermodynamic model [*Fountoukis and Nenes*, 2007] was used to determine the composition and phase state of an NH_4^+-SO_4^{2-}-NO_3^--Cl^--Na^+-Ca^{2+}-K^+-Mg^{2+}-water (or a subset therein) inorganic aerosol in thermodynamic equilibrium with its corresponding gas phase. Using ISORROPIA-II, we have reported on a comprehensive

method for pH prediction, validation, and uncertainty analysis based on the 2013 Southern Oxidant and Aerosol Study (SOAS) [*Guo et al.*, 2015; *Weber et al.*, 2016]. Here, we follow the same approach. pH is defined as,

$$pH = -\log_{10} \gamma_{H^+} H^+_{aq} = -\log_{10} \frac{1000 \gamma_{H^+} H^+_{air}}{W_i + W_o} \cong -\log_{10} \frac{1000 \gamma_{H^+} H^+_{air}}{W_i} \quad (3\text{-}1)$$

where γ_{H^+} is the hydronium ion activity coefficient (assumed = 1), H^+_{aq} (mole L^{-1}) the hydronium ion concentration in particle liquid water, H^+_{air} (μg m^{-3}) the hydronium ion concentration per volume of air, and W_i, W_o (μg m^{-3}) are particle water concentrations associated with inorganic and organic species, respectively. *Guo et al.* [2015] found that pH predicted solely with W_i is fairly accurate; pH was 0.15-0.23 units systematically lower than pH predicted with total particle water (W_i + W_o) (R^2 = 0.97). This is likely an upper bound on the error since organic aerosol mass fractions in that study were high (~60%, [*Xu et al.*, 2015b]). A lower contribution from W_o is expected in WINTER due to lower organic aerosol mass fractions (~40%); ΔpH was estimated to be +0.07 units including W_o with assumed organic hygroscopic parameter κ_{org} as 0.13 [*Cerully et al.*, 2015]. Given this, and that organic aerosol hygroscopicity was not measured, we determine pH only considering W_i since neglecting W_o appears to cause only a minor effect on the pH characterization.

The behavior of pure inorganic salts, under variable RH, including deliquescence and efflorescence, are well established both experimentally and theoretically [*Tang*, 1976; *Wexler and Seinfeld*, 1991; *Tang and Munkelwitz*, 1994]. The behavior of mixed inorganic and organic particles is more complex due to possible liquid-liquid or solid-liquid phase separation between organics and inorganics at lower RH and O:C ratio (organic aerosol

atomic O:C ratio) conditions [*Bertram et al.*, 2011; *Song et al.*, 2012; *You et al.*, 2013; *You et al.*, 2014b; *You and Bertram*, 2015]. Therefore, liquid or solid phases of atmospheric aerosols (deliquescence or efflorescence) depend on the RH and T history, and composition. To simplify the simulations, ISORROPIA-II was run assuming particles are "metastable", with no solid precipitates (H^+ is not stable in effloresced aerosol), although we did a sensitivity study assuming solid phases were present. Therefore, we excluded data with RH < 20%, a condition where aerosols are less likely to be in a completely liquid state [*Ansari and Pandis*, 2000; *Malm and Day*, 2001; *Fountoukis and Nenes*, 2007; *Bertram et al.*, 2011]. Furthermore, at such a low RH range, uncertainties in the pH prediction are expected to be high due to highly uncertain activity coefficients associated with highly concentrated solutions [*Fountoukis et al.*, 2009]. Data for RH > 95% was also excluded due to the exponential growth in particle liquid water with RH, which leads to high W_i and subsequently large pH uncertainty due to propagation of RH uncertainties [*Malm and Day*, 2001; *Guo et al.*, 2015] and potential issues with inlet transmission losses. Between these extremes, thermodynamic predictions are also assessed for differing RH ranges.

In running ISORROPIA-II to predict pH and semivolatile acid partitioning, it is also assumed that the particles are internally mixed, and that pH does not vary with particle size (so that bulk properties represent the overall aerosol pH) and that the ambient aerosols and gases are in thermodynamic equilibrium. For submicron aerosol (PM_1), equilibrium states are typically achieved within 30 minutes under ambient conditions [*Dassios and Pandis*, 1999; *Cruz et al.*, 2000; *Fountoukis et al.*, 2009]. The ISORROPIA-II input RH and T during the WINTER campaign were as low as 20% and –21°C. Therefore, the timescale of

equilibration could be much longer than 30 mins [*Zobrist et al.*, 2008; *Tong et al.*, 2011; *Shiraiwa and Seinfeld*, 2012], so thermodynamic calculations may deviate from observed partitioning of inorganic semivolatiles. Also, organic-containing aerosol may become semi-solid or glassy at low RH and T, which can further increase the equilibration timescale considerably. This potential impact is evaluated below. For conditions during the SOAS study in the southeastern US in summer (T = 25 ± 3 °C and RH = 74 ± 16%), *Guo et al.* [2015] found that thermodynamic calculations accurately predicted bulk particle water and ammonia partitioning over the complete T (18 to 33 °C) and RH (36 to 96%) ranges.

3.4 Results

3.4.1 Comparison between methods for measuring particle ionic composition

Several instruments measured aerosol inorganic chemical composition during this study. For PM_1, along with the PILS-IC and AMS, a second PILS was coupled to a fraction collector and the vials analyzed off-line by IC for water-soluble ions and carbohydrates (e.g., levoglucosan). A filter sampling system was used to collect nominally PM_4 [*McNaughton et al.*, 2007], which were subsequently analyzed for water-soluble ions by IC. (Methods for PILS with fraction collector and the filter sampling system are described in the supporting materials B.1 [*Dibb et al.*, 1999; *Dibb et al.*, 2000; *Sorooshian et al.*, 2006]). A summary comparing sulfate and nitrate from these various instruments can be found in the Figure B-1. Good correlations were found between the various instruments for sulfate, with R^2 between 0.72 and 0.83. However, systematic differences were observed, with orthogonal regression slopes between 1.05 and 1.52. On average, PILS-IC sulfate

(PM_1) was the lowest and filter sulfate (PM_4) the highest. Somewhat similar results were also found for nitrate, with R^2 between 0.65 and 0.87 and slopes between 0.86 and 1.43. The two PILS measurements were most similar. The lowest correlation was observed between filter and both PILS (also for AMS) nitrate, which is likely due to nitrate associated with particles larger than PM_1. The better agreement with sulfate between these instruments suggests the coarse fraction is mostly devoid of sulfate (with the exception of periods during Flight 13, which was conducted far offshore). We note that although the size cut is nominally the same (PM_1) between PILS and AMS, there are differences between the actual cuts as they are imposed by very different physical devices and under different pressure conditions (see e.g. [*DeCarlo et al.,* 2004]). During periods in which larger particles are present, this effect could lead to some measurement differences.

Ammonium data are not compared since PILS-IC cation data were not available. In the subsequent analyses, we estimated an NH_4^+ concentration that would be consistent with the PILS-IC by multiplying the AMS NH_4^+, merged to PILS time-resolution, by a constant factor of 0.7 (the average of PILS-IC/AMS nitrate and sulfate slope, Figure B-1).

In the following analyses of fine particle pH, we use both the PILS and AMS data to calculate pH, since each method has distinct advantages, and also to test the sensitivity of predicted pH using different methods for measuring ion concentrations. The PILS-IC (or any other IC analysis method) directly measures aerosol inorganic aqueous ion concentrations making the data directly applicable to pH calculations. (Note, in these methods the extractions result in highly dilute solutions so that ions are completely dissociated and measured by the IC). The AMS does not specifically measure ionic

concentrations, which can potentially raise a number of issues under certain circumstances. First, refractory species that are at least to some degree soluble (e.g., NaCl, $NaNO_3$, $Ca(NO_3)_2$, $Mg(NO_3)_2$, $MgSO_4$, KCl, KNO_3, K_2SO_4, etc.) can have a large impact on pH, even at low concentrations, but are not efficiently detected by AMS. However, often these species are mostly found in the supermicron size fraction and have little influence on PM_1 pH (discussed in more detail in the section 3.4.8).

The AMS also cannot readily distinguish between inorganic and organic forms of nitrate and sulfate. For example, evidence from AMS and PILS data (not shown) indicates that nitrites and organic nitrates are variably present during WINTER, and could explain some of the differences in nitrate observed between these instruments, especially when inorganic concentrations are low (Figure B-2). Similar interferences could occur for sulfate. Unlike the PILS-IC, the AMS provides higher time resolution and a more precise measurement of the suite of ions, as the same detector is used for anions and cations. These issues are pertinent to this study. Here, we analyze the data to utilize the PILS accuracy and AMS precision. We will show, that for this study, the AMS precision is more beneficial for assessing factors that influence pH, while the PILS accuracy is important for constraining the absolute value of pH, especially when there are nonvolatile cations present.

3.4.2 Predicting pH

For the WINTER data set and the full range of RH sampled (20-95%) we first predict pH with ISORROPIA-II using ambient T, RH, HNO_3 and either *i*) PILS NO_3^-, SO_4^{2-}, and scaled AMS NH_4^+, or *ii*) AMS NO_3^-, SO_4^{2-}, and NH_4^+. Figure 3-1 shows that pH from these

two data sets are, on average, in agreement, slope = 1.08, but there is substantial scatter R^2 = 0.44. Also, although AMS sulfate and nitrate are systematically 52% and 43% higher than PILS-IC measurement (Figure B-1), these differences do not systematically influence the calculated pH since the difference likely applies to all species. We conclude that pH is not highly sensitive to systematic aerosol input differences, even up to 50%, as long as the ion ratios are scaled accordingly.

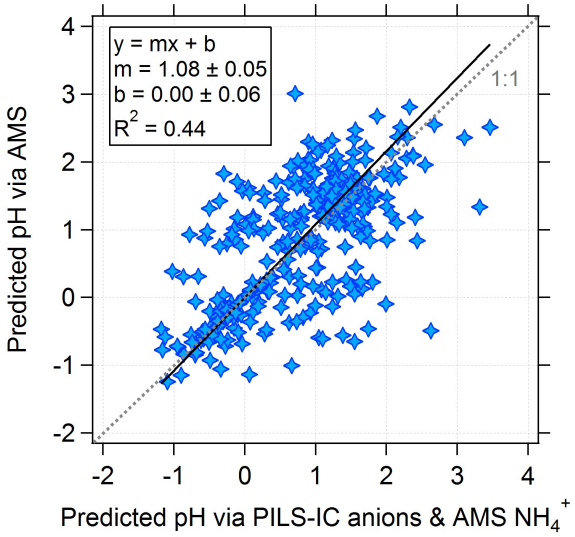

Figure 3-1 Comparisons of PM_1 pH predicted with aerosol phase input (NH_4^+, NO_3^-, SO_4^{2-}) from the AMS vs. PILS-IC anions and scaled AMS NH_4^+. Gas phase HNO_3 and ambient RH, T input are the same for the two predictions. Orthogonal distance regression (ODR) fit is shown.

A potential limitation with the pH prediction with this data is lack of reliable gas phase ammonia (NH_3). Not including NH_3 is expected to result in an overestimation of particle acidity because the partitioning of NH_3-NH_4^+ is derived based on only the NH_4^+ mass loadings; this means a fraction of the measured NH_4^+ is partitioned as NH_3 to the gas-phase

and releasing more particulate H^+ in the process. NH_3 was measured as part of the WINTER campaign, however, there were known uncertainties with detection limits and artifacts associated with the inlets/sampling system. When included in the thermodynamic model, it resulted in NO_3^- overpredicted by 65% compared to the measurement and the R^2 of predicted vs. measured $\varepsilon(NO_3^-)$ decreased from 0.70 to 0.40 (the modeling of HNO_3-NO_3^- partitioning will be discussed in the next section). Instead, to assess the effect of lack of NH_3 data, we iterated ISORROPIA-II using the predicted NH_3 data to calculate total ammonia ($NH_3 + NH_4^+$) as input for the next iteration, until NH_3 predictions converge. A more straightforward method, predicting gas phase NH_3 based on aerosol composition in ISORROPIA-II reverse mode, is not chosen because the prediction is highly sensitive to NH_4^+ input (i.e., 35% instrument uncertainty can cause large errors [*Hennigan et al.*, 2015]). Based on the iteration method, predicted WINTER mean NH_3 concentrations were 0.10 μg m^{-3} (10^{th} percentile = 0.0 μg m^{-3}, 90^{th} percentile = 0.25 μg m^{-3}) and most of the ammonia partitions to the particle phase ($\varepsilon(NH_4^+)$ = 91 ± 22 %). Particle pH changed by only approximately 3% (slope = 0.97, R^2 = 0.81), with a pH systematically ~0.2 pH units (regression intercept) higher for the iterated solution compared to not including NH_3 data. Therefore, not including gas phase NH_3 in the thermodynamic calculations for this study has a minor effect and reported pH is not corrected by the iterated NH_3.

3.4.3 Verification of the Thermodynamic Model: Comparison of nitric acid-nitrate partitioning

Validity of thermodynamic model predictions may be assessed by comparing predicted and measured gas partitioning fractions of the semivolatile species. Comparing completely

nonvolatile or volatilized components is not a viable or useful test. The best semivolatile species for evaluation, however, depends on the pH levels of a given study. For example, in SOAS (summer in the southeastern US) the conditions were such that HNO_3 was almost entirely in the gas phase, whereas NH_3 was evenly distributed between phases, $\varepsilon(NH_4^+) = NH_4^+/(NH_3 + NH_4^+) = 59 \pm 16\%$, making it the better species to test the model [*Guo et al.*, 2015]. In this study (winter in the northeastern US), NH_3 was estimated to be mainly in the particle-phase, as discussed above, and HNO_3 was more evenly distributed between particle and gas, $\varepsilon(NO_3^-) = NO_3^-/(HNO_3 + NO_3^-) = 31\%$ PILS data and 39% AMS data, making it the better parameter to compare. Using predicted gas-particle partitioning concentrations is a valid test since when operating in forward mode, ISORROPIA-II calculates the gas-particle equilibrium partitioning concentrations based on the input of total concentration of a species (gas + particle).

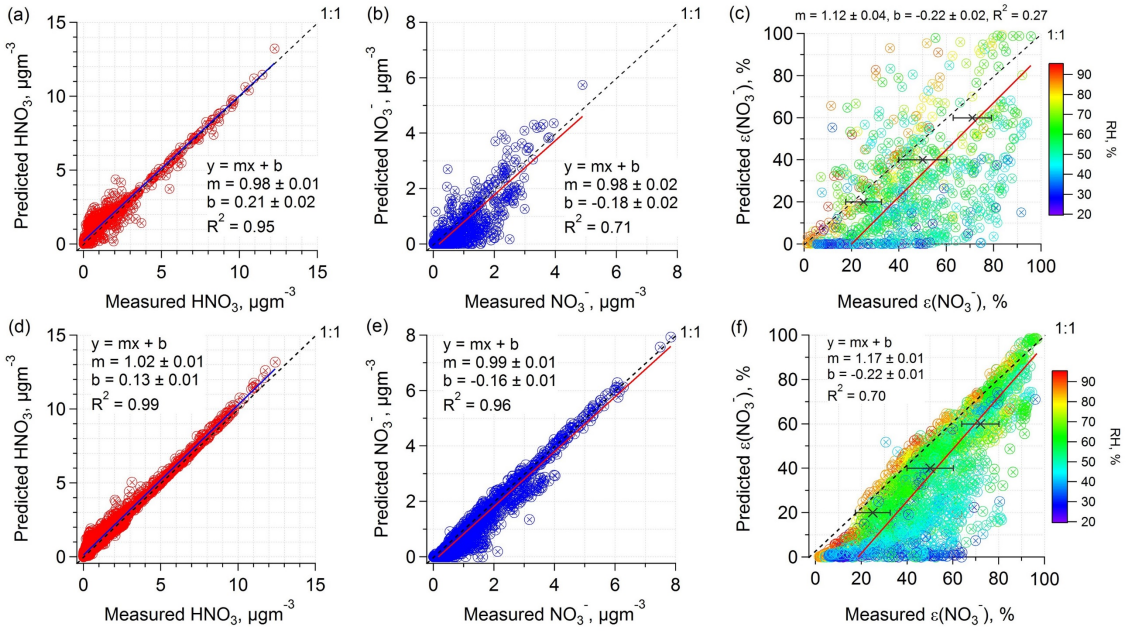

Figure 3-2 Comparisons of predicted and measured HNO_3 (nitric acid), (NO_3^-) (nitrate), and $\varepsilon(NO_3^-)$ (particle nitrate fraction of total nitrate) for data from the complete WINTER study: (a-c) PILS-IC anion input with scaled AMS ammonium (NH_4^+); (d-f) AMS input. Example error bars at three selected data points illustrate the uncertainty in measured $\varepsilon(NO_3^-)$ from combined HNO_3 (15%) and NO_3^- (35%) uncertainties. ODR fits are shown. Average conditions for each RH range are given in Table 3-1.

A comparison of predicted HNO_3 and NO_3^- to measured values is shown in Figure 3-2. Overall, for the 20-95% RH data set, the model captures the observed HNO_3 and NO_3^-. Less scatter is seen when ISORROPIA-II is run with the AMS aerosol data, consistent with expectation that it is more precise than the combined PILS anions and AMS NH_4^+ data set (Note that including predicted NH_3 results in a better comparison between predicted and PILS-IC measured NO_3^-, with the R^2 increasing from 0.71 to 0.77, not shown). From Figure 3-2, ISORROPIA-II predicted HNO_3 and NO_3^- are on average within 10% of the measurements and highly correlated. However, there is much more scatter for the $\varepsilon(NO_3^-)$ comparison, partly due to propagation of the uncertainties from both HNO_3 and NO_3^- measurements needed for the calculation. (Note, individual data below 2×LOD concentrations were excluded for $\varepsilon(NO_3^-)$, due to larger relative uncertainties). Not all the spread in $\varepsilon(NO_3^-)$, however, can be attributed to the impact of measurement errors or noise, as higher discrepancies tend to be associated with lower RH.

Focusing on narrower RH ranges permits a more detailed exploration of the systematic biases. Figure 3-3 shows the predicted and measured HNO_3 and NO_3^- concentrations, and $\varepsilon(NO_3^-)$ for three RH ranges, 20-40%, 40-60%, and 60-95%. The least discrepancy is found for the 60-95% RH range, and the largest bias is found for 20-40% RH, which also has the

lowest total nitrate concentrations (Table 3-1). The larger discrepancy at lower RH may be due to a number of factors, including ignoring possible phase separations and measurement limitations. Each factor is considered below.

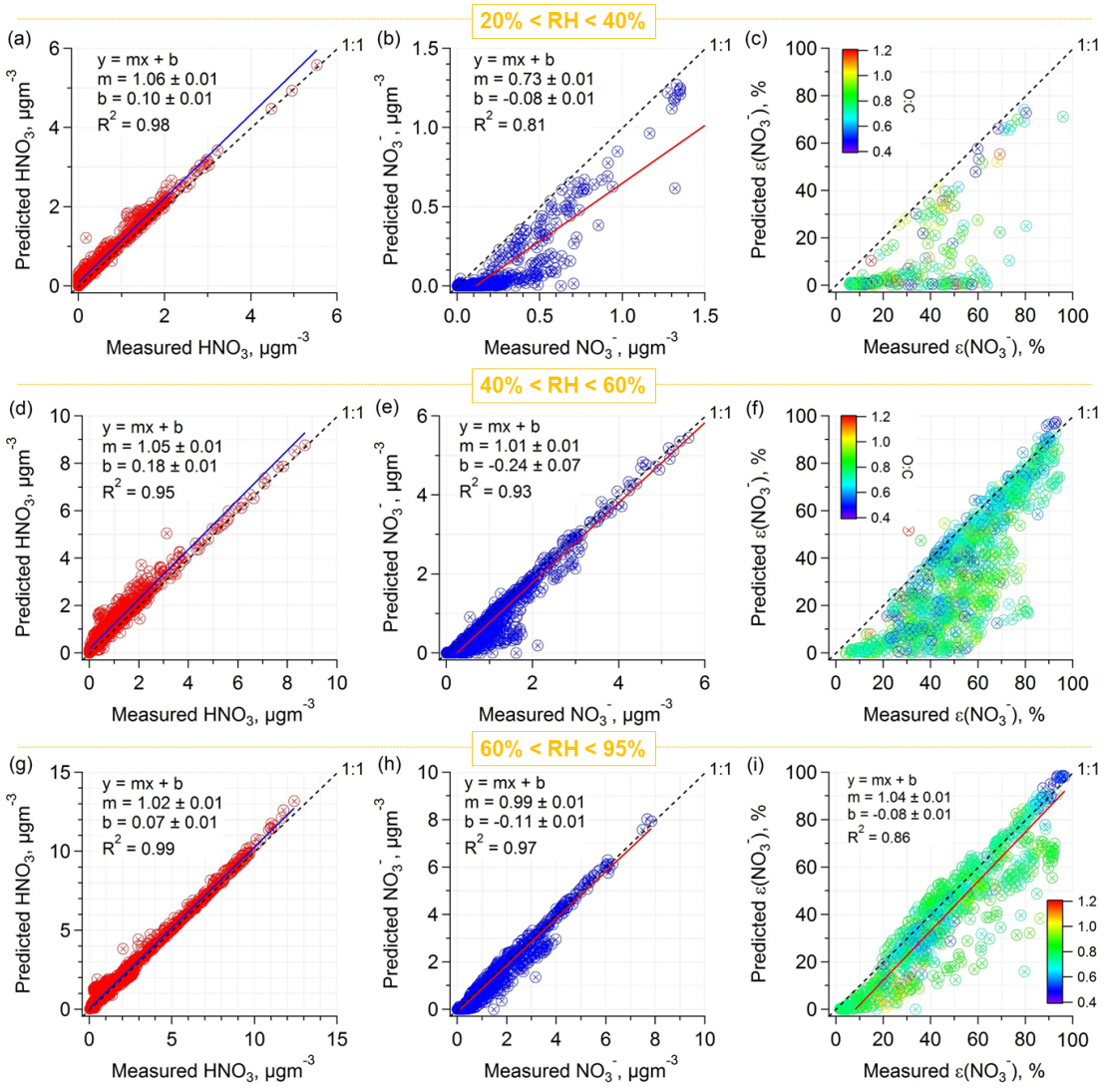

Figure 3-3 Comparisons between predicted and measured HNO_3, NO_3^-, and $\varepsilon(NO_3^-)$ with data from the complete WINTER study (AMS aerosol data only) for different ambient RH ranges: (a-c) 20-40%; (d-f) 40-60%; (g-i) 60-95%. ODR fits are included in most plots. Note that for the concentrations, the axis ranges get smaller with decreasing RH.

Phase Separation: Two types of phase separations are possible, solid-liquid and liquid-liquid. Considering just the inorganic phase first, assuming solid salts precipitate from a supersaturated aqueous phase (i.e., ISORROPIA-II runs in stable mode instead of metastable) does not improve the predictions, but rather worsens them; NO_3^- is much more substantially underpredicted by the model as RH decreases (Figure B-3), compared to metastable aerosol calculations. At high RH, there is little difference between the metastable and semi-solid assumptions because the inorganic salts (e.g., NH_4NO_3 and $(NH_4)_2SO_4$) deliquesce. Overall, we find that running ISORROPIA-II in metastable mode over the 20-95% RH range agrees better with observations (although there are still discrepancies at lower RHs), thus solid-liquid phase separations of the inorganic species does not appear to explain the $\varepsilon(NO_3^-)$ discrepancies at low RH.

Table 3-1 Summary of ambient temperature and PM_1 organic aerosol (OA) atomic O:C ratio, OA to sulfate mass ratio, nitrate concentrations (all from AMS data), and gas-phase nitric acid concentrations for data binned by ambient RH.

RH	T, °C	O:C	$OA:SO_4^{2-}$	NO_3^-, μg m^{-3}	HNO_3, μg m^{-3}	Total NO_3^-, μg m^{-3}	Points #
20 - 40%	0.0 ± 7.6	0.79 ± 0.20	1.36 ± 0.72	0.37 ± 0.36	1.04 ± 0.71	1.41 ± 0.75	272
40 - 60%	-1.6 ± 6.9	0.76 ± 0.16	1.54 ± 0.91	0.66 ± 0.79	0.99 ± 1.04	1.65 ± 1.65	1192
60 - 95%	-0.7 ± 5.3	0.78 ± 0.11	1.75 ± 0.79	1.40 ± 1.28	2.37 ± 2.40	3.77 ± 2.77	902

Organic-inorganic liquid phase separations are also possible. Lab studies show that liquid-liquid phase separation is always observed at aerosol O:C (organic aerosol atomic O:C

ratio) ≤ 0.5, whereas no phase separations occur for O:C ≥ 0.8 [*Bertram et al.*, 2011; *Song et al.*, 2012; *You et al.*, 2013; *You et al.*, 2014b]. Although these experiments were performed at temperatures between 17 and 27 ºC, the results should still be applicable to the WINTER study (minimum T of –21 ºC), since liquid-liquid phase separation is not a strong function of temperature for temperatures between –29 and 17 ºC [*Schill and Tolbert*, 2013; *You and Bertram*, 2015]. To assess if conditions are conducive to liquid-liquid phase separation, T, O:C, OA:SO_4^{2-} (organic-to-sulfate aerosol mass ratio), and nitrate mass loadings are contrasted for the three RH ranges (Table 3-1). Temperatures are similar with only 2 ºC difference in the means, and so likely not a cause for the ε(NO_3^-) bias at low RH (also shown in Figure B-4). The O:C ratios are generally at the upper end of the range where phase separation can occur. Furthermore, for O:C in the "transition regime" (0.5<O:C<0.8), the case here, if OA:SO_4^{2-} is larger than unity, phase separations are less likely [*Bertram et al.*, 2011]. All OA:SO_4^{2-} are on average above unity, suggesting no phase separations, but there is a trend with the smallest ratio (1.36 ± 0.72) coinciding with the 20-40% RH bin, which is where the largest ε(NO_3^-) bias is seen. Furthermore, in the O:C transition regime, the possibility of liquid-liquid phase separation increases as RH decreases. Thus, the trends are consistent with increasing likelihood of organic-inorganic phase separations at the lower RH range, but the conditions are not such that phase separation is definitively expected at the lowest RH range, as no clear dependence on O:C is observed in Figure 3-3c, f, and i.

Organic-inorganic phase separations may lead to measured ε(NO_3^-) (or NO_3^- concentrations) larger than thermodynamic predictions. For example, during a drying

event, an organic semi-solid liquid coating formed over the inorganic aqueous phase (or possibly an inorganic solid core) containing the ions might inhibit gas-particle equilibrium, lowering the evaporation of semivolatile NO_3^-. pH of the separate phases would also differ. The thermodynamic model predicts pH assuming all ions are only in the inorganic aqueous phase. However, if NO_3^- is miscible in the organic-rich aqueous phase, and the pH higher than the inorganic aqueous phase, measured bulk aerosol NO_3^- would be higher than the thermodynamic prediction. Whereas the inorganic phase pH was between –1 and 0 (25^{th} and 75^{th} percentiles), we estimate that an organic-rich phase pH of ~ 3 would increase NO_3^- concentrations sufficiently to bring predicted $\varepsilon(NO_3^-)$ into closer agreement with observed. Higher organic-rich phase pH is possible because of the weaker organic acids compared to sulfuric acid. One of the strongest organic acid, formic acid, has a pK_a of 3.75 [*Bacarella et al.*, 1955]. *Bougiatioti et al.* [2016] also found that organic-rich aged biomass burning aerosols sampled in the eastern Mediterranean had pH levels ~ 3, consistent with strong nitrate partitioning onto the aerosol.

Uncertainties in measured inorganic nitrate at low concentrations: Another factor associated with increasing discrepancies between predicted and measured $\varepsilon(NO_3^-)$ with lower RH is that total nitrate concentrations were also lowest in this RH range (Table 3-1 and Figure B-5). This can lead to discrepancies in two ways. First, at lower concentrations, the measurements have larger relative uncertainties. Secondly, we have used the AMS data for this analysis since it is more precise than the PILS-IC data, but AMS nitrate may also include some contributions from organonitrates. The relative contribution of organonitrates is likely to be higher when inorganic nitrate concentrations are lower, consistent with

higher observed nitrate compared to the model at lower RH. Because the PILS-IC only measures inorganic nitrate, we compared the PILS-AMS nitrate measurements for the three RH ranges. No evidence was found for AMS nitrate being systematically higher at lower RH (Figure B-2). An attempt was also made to account for the possibility of interferences in AMS-reported nitrate due to other forms of nitrate or to nitrite. On a flight-by-flight basis, AMS inorganic nitrate (inorgNO_3^-) was estimated by scaling AMS NO_3^- to PILS-IC NO_3^- (see Figure B-6 comparing AMS inorgNO_3^- to AMS NO_3^-). This type of variable scaling factor resulted in thermodynamic-predicted nitrate for all data on average 24% higher than observed (Figure B-7), whereas for AMS total nitrate the slope was 0.99 (Figure 3-2e). Comparison between predicted and measured NO_3^- was also more scattered (R^2 = 0.88 for estimated AMS inorgNO_3^- versus R^2 = 0.96 for AMS total nitrate). Therefore, in the following analysis, we simply use AMS total NO_3^- instead of estimated AMS inorgNO_3^-.

Role of fine mode nonvolatile cations: If the particles are internally mixed and with uniform composition versus particle size, nonvolatile cations (NVCs) such as Na^+, K^+, Ca^{2+}, Mg^{2+} can affect pH. These refractory cations have so far not been considered in the thermodynamic calculations. Including them in ISORROPIA-II does not significantly affect pH, until the concentrations become significant relative to the anions. For example, when NaCl is less than 50% of the aerosol ionic molar mass (Na^+-NH_4^+-SO_4^{2-}-NO_3^--Cl^-), including PILS-fraction collector PM_1 Na^+ and Cl^- data with AMS NH_4^+, NO_3^-, SO_4^{2-} in the ISORROPIA-II analysis does not significantly change the particle pH; the mean change in pH is +0.4 units. Although small, this change in pH can be important for the fraction of

total nitrate that partitions to the aerosol if in the pH-sensitive region (discussed below in section 3.4.6). The general small impact from the nonvolatile Na^+ is because the aerosols were acidic enough so that H^+ is a major ion in the system. However, when the NaCl becomes a significant fraction relative to the total ions (mole fraction > 50%), the pH can dramatically increase (Figure B-8). This is observed in the ambient data when there was a dramatic drop in PM_1 sulfate and increase in PM_1 Na^+, resulting in an aerosol of mainly Na^+-containing salts, where pH can change from near zero to above 3. For typical WINTER conditions, a sensitivity analysis shows that this transition occurs at Na^+ greater than 0.5 μg m^{-3}, pH exceeds 2-3 and drives nitric acid partitioning to the aerosol (Figure B-9). However, including NaCl causes greater deviation between predicted and measured HNO_3-NO_3^- partitioning (Figure B-10) suggesting that these other cations are likely not internally mixed with the PM_1 NH_4^+, NO_3^-, and SO_4^{2-}. Therefore, in the remaining analysis, the reported particle pH is calculated without any refractory ions present. The role of coarse mode salts is discussed below (Section 3.4.8).

In summary, the overall good agreement between the model and measurements of nitric acid partitioning (HNO_3 and NO_3^- regression slopes deviate < 5%, and $R^2 > 0.9$) suggests that when RH is greater than 40%, the assumption of a metastable aerosols (i.e., complete aqueous solution) with no phase separation appears reasonable for the conditions of this study. At lower RH, phase separation may occur and could account for the larger observed discrepancies (e.g., enriched nitrate in the organic phase with higher pH compared to the inorganic phase), although measurement uncertainty, size-cut differences, and/or interferences (e.g., organonitrates and nitrites that are part of AMS nitrate) may also

explain some of the differences. PM_1 refractory water-soluble ions (e.g. Na^+, K^+, Ca^{2+}, Mg^{2+}) were generally either at too low concentrations or not internally mixed with NH_4^+, NO_3^-, SO_4^{2-} such that they had little influence on bulk PM_1 pH. Overall, the analysis based on the complete WINTER data shows that the predicted pH is accurate at RH > 40%; similar to what we found in the southeastern US (minimum RH was 36%) [*Guo et al.*, 2015].

3.4.4 Sample line heating effect

During flight, aircraft cabin temperature was maintained at approximately 20 ºC. Combined with ram air heating, the temperature of sample air was substantially above ambient before it reached the measurement instrumentation. As a result, sampled air RH decreased, resulting in loss of particle water. Heating and loss of particle water leads to potential evaporation of semivolatile components, such as nitrate and ammonium, which would lead to an incorrect calculation of pH. For WINTER, the ambient T was on average –3.0 ± 8.6 ºC and the measured PILS sample line T was typically ~ 24 ºC higher. Sample line RH was calculated assuming conservation of water vapor under isobaric heating, a good assumption given the short residence time in the tubing (0.5 s for AMS, 2 sec for PILS-IC). Heating of air in the sample line lowered the RH to 23% from an ambient average of 75%.

ISORROPIA-II was run with aerosol and gas-phase species at the sample line T and RH and compared to predictions from ambient T and RH. Figure 3-2 shows that using sample line T and RH at the PILS-IC inlet, the nitric acid partitioning is inconsistent with

observations. For example, predicted sample line $\varepsilon(NO_3^-)$ was 0.2 ± 0.3%, indicating that all nitrate was in the gas-phase, whereas measured $\varepsilon(NO_3^-)$ was 31 ± 23%, and nitrate concentrations were non-zero (1.16 ± 0.88 μg m^{-3}). As noted above, using ambient T and RH resulted in good agreement between predicted and measured nitric acid partitioning, therefore we conclude that repartitioning of volatile inorganics did not substantially affect the measurements and attribute this to the limited residence time within the sample lines. Several studies on mass transfer rates indicate that it takes roughly 15 to 30 minutes for semivolatile components to reach partitioning equilibrium for particles up to 1μm [*Dassios and Pandis*, 1999; *Cruz et al.*, 2000; *Fountoukis et al.*, 2009], which is over two orders of magnitude longer than the estimated sampling line residence times of the aerosol instrumentation of this study (0.5-2 sec). Note, for a 2 sec residence time an upper limit volatilization loss of ~35% NH_4NO_3 was estimated with a thermo-kinetic model for diluted aircraft ambient sample [*Shingler et al.*, 2016]. Since a sheath flow lacking gas-phase HNO_3 causes more NO_3^- evaporation, these results are not directly applicable to the non-diluted AMS and PILS-IC measurement techniques used in this study. In the following analysis, we ignore any possible artifacts due to changes in aerosol during sampling and use ambient conditions in the thermodynamic calculations.

Table 3-2 Comparisons between measurements of PM_1 nitrate concentrations to thermodynamic simulations assuming ambient conditions (T, RH) and conditions in the sample line. Only periods when both ambient and sample line data were available and RH was in the 20-95% range are shown (i.e., data are a subset of the WINTER campaign, not a study average). Aerosol data shown in the table are from AMS measurements, and sample line T was measured just upstream of PILS-IC. Saturation water vapor pressures were calculated by Equation 21 in Alduchov and Eskridge [1996] to estimate sample line RH.

	Ambient		Sample line	
	Measured	Simulated	Measured	Simulated
Points #	323	323	323	323
T	4 ± 2 ºC	N/A	21 ± 1 ºC	N/A
RH	75 ± 11%*	N/A	23 ± 3%*	N/A
$\varepsilon(NO_3^-)$	31 ± 23%**	23 ± 22%	31 ± 23%**	0.2 ± 0.3%
NO_3^-, μg m^{-3}	1.16 ± 0.88**	0.87 ± 0.88	1.16 ± 0.88**	0.01 ± 0.02

* RH < 20% was excluded.
** Measured by instruments inside the C-130 aircraft.

3.4.5 pH geographical and vertical distribution

Research flights were conducted mainly in the northeastern US, with some flights extending into the southeast (Figure 3-4). Bulk PM_1 pH was low, with a campaign average of 0.77 ± 0.96 (median of 0.91; 10^{th} percentile of -0.51; 90^{th} percentile of 1.9). Figure 3-4 shows the geographical distribution of particle pH, particle nitrate, and $\varepsilon(NO_3^-)$. No clear systematic spatial distribution is observed in any of these parameters. Higher nitrate plumes, however, were usually observed simultaneously with higher $\varepsilon(NO_3^-)$, which were recorded in regions of higher particle pH, as expected.

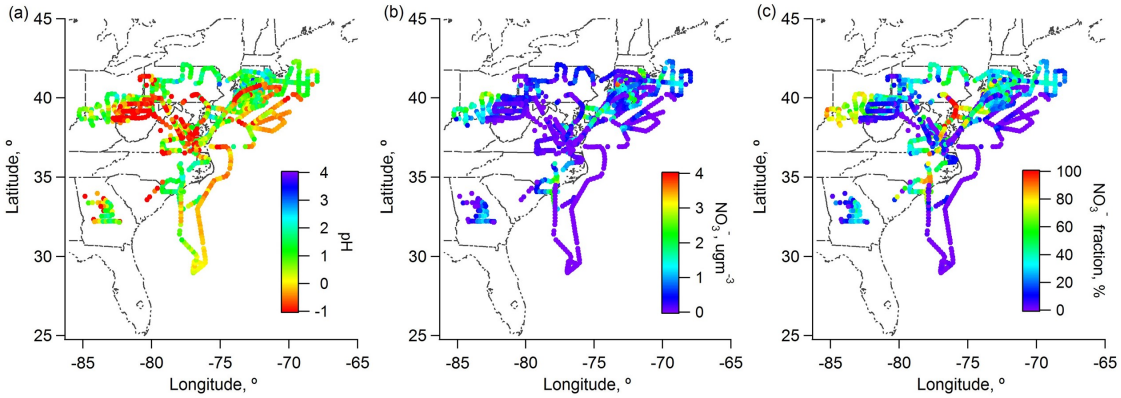

Figure 3-4 WINTER all flight geographical distributions of PM_1 particle (a) pH, (b) PILS-IC NO_3^- and (c) ε(NO_3^-). The particle pH plotted is calculated based on aerosol phase inputs of PILS-IC anions and scaled AMS NH_4^+.

The pH vertical distribution is shown in Figure 3-5. Most measurements were below 2 km since WINTER focused on the lower atmosphere. The data points above 2 km are more scattered and uncertain due to low aerosol mass loading. Despite this, as with the geographical distribution, there is no obvious gradient in pH from about 1 to 5 km altitude, but the pH exhibited a broad variation and ranged between –1 and 2 (Figure 3-5a). 500m altitude-binned statistics show a uniform pH range of –0.5 to 2 below 3 km and a slightly lower pH range of –1 to 0.5 above 3km (Figure 3-5b). Very little PM_1 nitrate aerosol was observed aloft. Below 1 km altitude, there was a somewhat similar range in pH as aloft, but a wide range in PM_1 nitrate (0-8 μg m^{-3}), with notably higher nitrate measured at higher predicted pH. To understand this observed nitrate variability, interactions between nitrate and pH are explored.

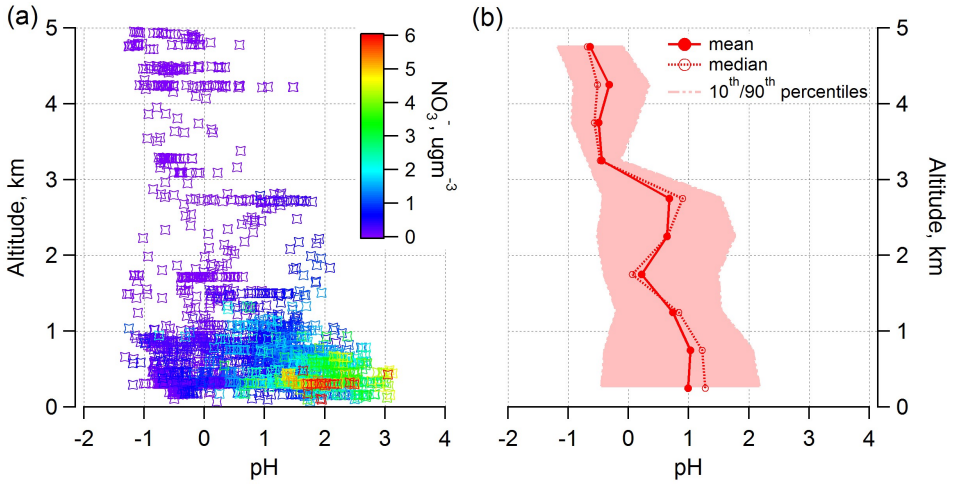

Figure 3-5 pH as a function of altitude above ground: (a) colored by the nitrate concentration for all WINTER data; (b) 500m-binned mean and median, and 10th, 90th percentiles. The particle pH plotted is calculated based on aerosol phase inputs of AMS.

3.4.6 Nitrate dependency on pH, W_i, and T

To study factors affecting nitric acid partitioning, and to test the validity of the thermodynamic model, we first investigate a simpler analytical prediction of $\varepsilon(NO_3^-)$ and compare to measurements and ISORROPIA-II predictions. Equilibrium between HNO_3 and NO_3^- can be simplified as:

$$HNO_{3(g)} \leftrightarrow {NO_3}^- + H^+, \quad H^*_{HNO_3} \tag{3-2}$$

where $H^*_{HNO_3}$ (mole^2 kg^{-2} atm^{-1}) is the equilibrium constant and is equal to the "conventional" Henry's law constant multiplied by the dissociation constant of nitric acid (K_{n1}) [*Clegg and Brimblecombe*, 1990]. $\varepsilon(NO_3^-)$ can be directly calculated by the following equation:

$$\varepsilon(NO_3^-) = \frac{H^*_{HNO_3} RTW_i \times 0.987 \times 10^{-14}}{\gamma_{H^+}\gamma_{NO_3^-} H^+_{aq} + H^*_{HNO_3} RTW_i \times 0.987 \times 10^{-14}} \tag{3-3}$$

Note, this is similar to the Equation 6 in *Meskhidze et al.* [2003], but includes activity coefficients to account for solution non-ideality, and assuming that $\left(\frac{\gamma_{H^+}\gamma_{NO_3^-}}{\gamma_{HNO_3}}\left[H^+_{aq}\right] + K_{n1}\right) \approx K_{n1}$ where γ_{HNO_3} is the activity coefficient of protonated HNO_3 in the aqueous phase. This equation, plotted in Figure 3-6 (activity coefficients are assumed equal to one) for varying temperatures and particle water concentrations, illustrates the relationship between nitric acid partitioning and pH. From Figure 3-6 it can be seen that for a given W_i and T, it takes about four pH units to go from complete gas-phase to particle-phase partitioning. Dropping T by 20 °C shifts the partitioning fraction curve roughly one pH unit lower, which can result in a considerable shift in nitric acid to the particle phase, if pH and W_i are constant. Likewise, more nitrate aerosol formation also occurs with increased W_i; a factor of 10 increase in W_i also shifts $\varepsilon(NO_3^-)$ to lower pH by approximately one unit. The dependence of nitric acid partitioning on T is directly related to the equilibrium constant, $H^*_{HNO_3}$, which increases by 700% from 20 °C to 0 °C; the increase is mainly due to changes in the Henry's law constant, thus the vapor pressure of HNO_3.

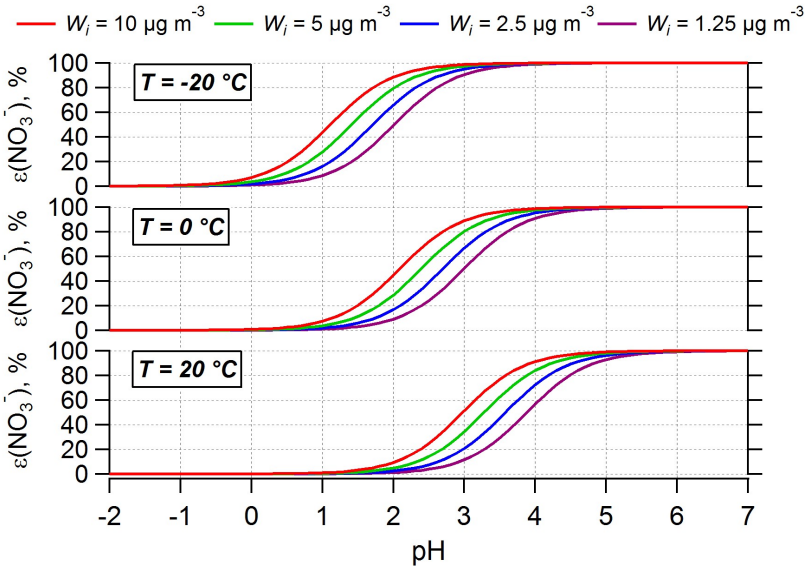

Figure 3-6 Simulated ε(NO_3^-) at –20 °C, 0 °C, 20 °C and various particle liquid water levels (1.25, 2.5, 5, 10 µg m^{-3}) assuming ideal solutions. The WINTER average W_i was 2.6 µg m^{-3}; 1.25 and 10 µg m^{-3} are approximately 50% and 400% of the average W_i levels, respectively. WINTER average temperature was –0.4 °C.

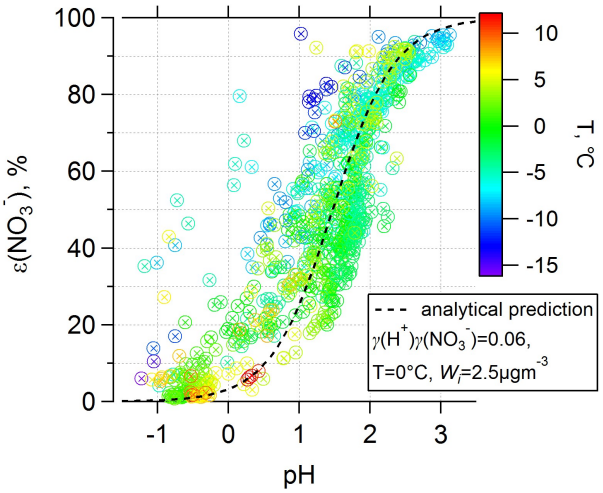

Figure 3-7 The measured ε(NO_3^-) versus predicted pH colored by ambient T for all WINTER data (AMS PM_1 data). Data are restricted to particle liquid water content (W_i), predicted by ISORROPIA-II from inorganic aerosol levels, in the range of 1.5 to 5 µg m^{-3}. The S curve fits the selected data well and is calcualted based on T = 0 °C, W_i = 2.5 µg m^{-3}, and the average activity coefficients in WINTER ($\gamma_{H^+}\gamma_{NO_3^-}$ = 0.06), using Equation 3-3.

WINTER data shows evidence for a similar temperature effect on nitric acid partitioning. In Figure 3-7 measured $\varepsilon(NO_3^-)$ is plotted versus particle pH, for data over a relatively narrow W_i range ($1.5 < W_i < 5$ μg m^{-3}). For a given pH between 0 and 2, higher $\varepsilon(NO_3^-)$ was observed at a lower ambient T. There are differences between the measured $\varepsilon(NO_3^-)$ of Figure 3-7 and the analytical prediction of Figure 3-6. The S-curve in Figure 3-6 tends to shift one pH unit higher compared to the observed data (Figure 3-7) and is due to the ideal solution assumption (unity activity coefficients), whereas ISORROPIA-II calculates multicomponent activity coefficients [*Fountoukis and Nenes*, 2007]. Given that the WINTER mean particle ionic strength was as high as 38 mole L^{-1} (based on PILS-IC anions and scaled AMS NH_4^+), the ideal solution assumption was invalid. ISORROPIA-II predicts that the mean activity coefficient of the H^+-NO_3^- ion pair, $\gamma_{H^+-NO_3^-} = 0.23$. Given that, $\gamma_{H^+-NO_3^-} = \sqrt{\gamma_{H^+}\gamma_{NO_3^-}}$, we have $\gamma_{H^+}\gamma_{NO_3^-} = 0.06$ [*Meissner and Tester*, 1972; *Pitzer and Mayorga*, 1973; *Meier*, 1982; *Nenes et al.*, 1998]. Introducing this information in Equation 3-3 shifts the $\varepsilon(NO_3^-)$ curves to lower pH by 1.2 units, much closer to ISORROPIA-II predicted $\varepsilon(NO_3^-)$, shown as the S curve in Figure 3-7. Although Figure 3-6 is somewhat inaccurate at identifying the exact pH at which nitric acids shifts between gas and particle phases, it provides the ideal conceptual framework for understanding how semivolatile partitioning is affected by pH, T, and RH.

The influence of particle water on nitric acid partitioning is also evident. Figure 3-8 shows measured AMS NO_3^- (PILS NO_3^- shows a similar result, but with more scatter) versus particle pH for all WINTER flight data, segregated by predicted W_i. The figure shows that

NO_3^- concentrations are affected by pH and W_i, the latter controls much of the pH variability. These results are consistent with expectations. For example, in Figure 3-8, at a constant pH, more NO_3^- is measured at higher W_i; whereas at a constant W_i, more NO_3^- is measured at higher pH. W_i depends primarily on RH and the hygroscopic aerosol mass, which in this case mainly consists of $(NH_4)_2SO_4$, NH_4HSO_4, and NH_4NO_3 (i.e., not considering organic aerosol contributions). Nonlinear relationships are observed between NO_3^- and pH because NO_3^- constitutes part of the aerosol mass and is highly hygroscopic [*Fountoukis and Nenes*, 2007]. SO_4^{2-} is the other major anion with high hygroscopicity in WINTER PM_1. Since W_i is predicted by ISORROPIA-II from the inorganic species mass concentrations, one would expect it to be proportional to particle inorganic anion mass (NO_3^- + SO_4^{2-}) and RH (mass loadings of the other AMS-measured anion, 0.02 µg m^{-3} Cl^-, were too small to affect W_i). Figure 3-9a shows that at a given RH, W_i is nearly linearly related to the sum of nitrate and sulfate mass. (A similar graph plotted with the AMS-measured total ions is shown in Figure B-11)

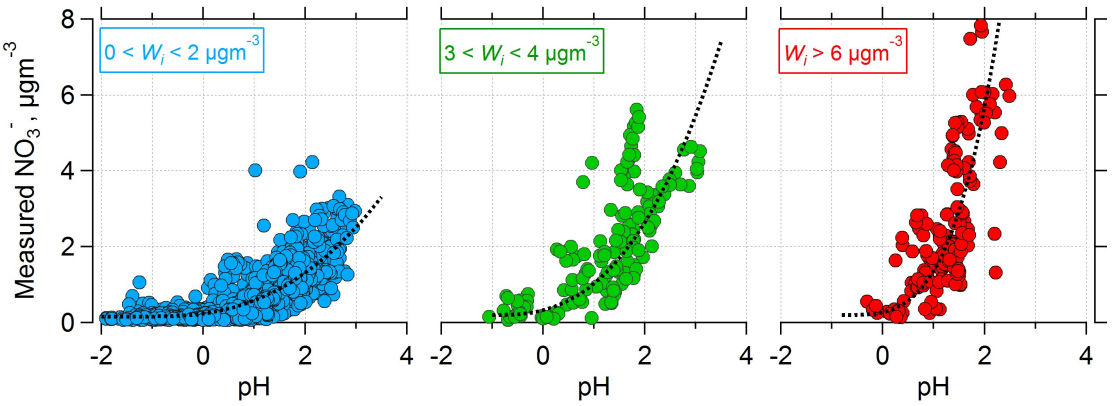

Figure 3-8 Measured nitrate versus predicted pH for all WINTER data segregated by predicted inorganic liquid water content (W_i) in the ranges of 0-2, 3-4, and >6 µg m^{-3}.

ISORROPIA-II using AMS data is shown, excluding NO_3^-, SO_4^{2-}, and HNO_3 concentrations that were within 2×LOD.

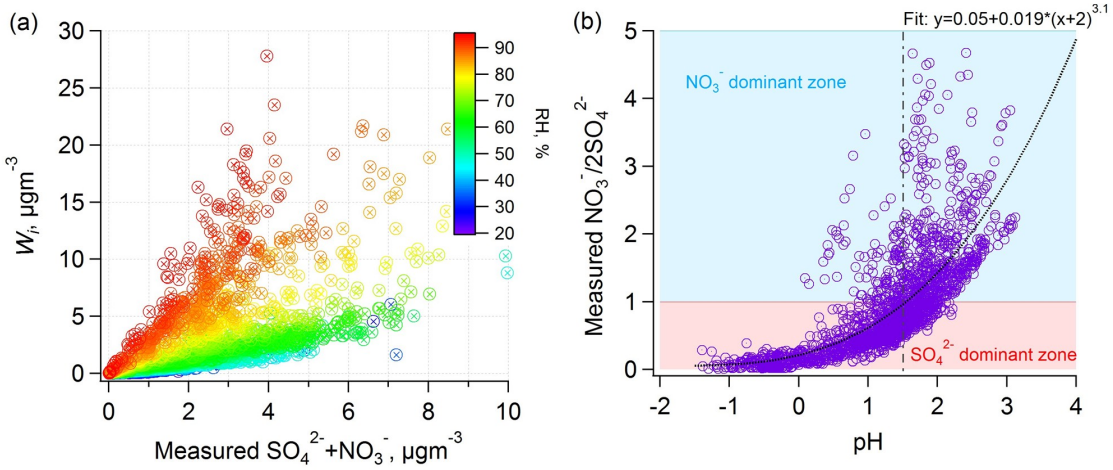

Figure 3-9 (a) Predicted W_i versus AMS sulfate plus nitrate concentrations. Color scale shows RH dependence. (b) Measured $NO_3^-/2SO_4^{2-}$ ratio (mole mole^{-1}) versus predicted pH based on AMS data. NO_3^- or SO_4^{2-} dominant zone denotes $NO_3^-/2SO_4^{2-} > 1$ or < 1. For both plots the complete WINTER data is shown.

To simplify the relationship between NO_3^- and pH, which is affected by W_i (Figure 3-8), the $NO_3^-/2SO_4^{2-}$ ratio (mole mole^{-1}) is plotted against pH (Figure 3-9b). From this figure it can be seen that when aerosol anionic composition was dominated by nitrate ($NO_3^-/2SO_4^{2-} > 1$), particle pH was generally above 1, whereas when dominated by sulfate ($NO_3^-/2SO_4^{2-} < 1$), particle pH was below 2 and could reach as low as –1.5. The relationship between $NO_3^-/2SO_4^{2-}$ versus pH can be explained by the analytical prediction of $\varepsilon(NO_3^-)$ given in Equation 3-4. Neglecting non-ideality, $NO_3^-/2SO_4^{2-}$:

$$NO_3^-/2SO_4^{2-} = \frac{NO_{3,total}}{2SO_4^{2-}}\varepsilon(NO_3^-) = \frac{NO_{3,total}}{2SO_4^{2-}}\frac{1}{kH_{aq}^+ + 1} \quad (3\text{-}4)$$

where $NO_{3,total}$ is the sum of NO_3^- and HNO_3 (mole m^{-3}) and k represents $1/\left(H^*_{HNO_3}RTW_i \times 0.987 \times 10^{-14}\right)$. At low pH ($H^+_{aq}$ high), $\varepsilon(NO_3^-)$ is close to zero and $NO_3^-/2SO_4^{2-}$ is very small (i.e., very little nitrate aerosol). At sufficiently high pH (H^+_{aq} low), $\varepsilon(NO_3^-)$ approaches unity, thus $NO_3^-/2SO_4^{2-}$ is no longer a function of $\varepsilon(NO_3^-)$ and is simply equal to $\frac{NO_{3,total}}{2SO_4^{2-}}$ (in this case, $NO_{3,total} \cong NO_3^-$). This explains why the $NO_3^-/2SO_4^{2-}$ increases dramatically at higher pH levels and is expected to asymptotically increase with increasing pH. When $\varepsilon(NO_3^-)$ is 1 (i.e., no HNO_3) it lacks any dependence on pH (Equation 3-4). At intermediate pH, the $NO_3^-/2SO_4^{2-}$ is driven by both $\varepsilon(NO_3^-)$ and $\frac{NO_{3,total}}{2SO_4^{2-}}$. Since $NO_3^-/2SO_4^{2-}$ is not only driven by pH but also the total amount of nitrate (related to the sources and sinks of HNO_3 and NO_3^-), it is not a very accurate pH proxy (another pH proxy, ion equivalence ratio, will be discussed in Section 3.4.9).

3.4.7 Low vs. high nitrate case studies

Flights 6 and 8 were selected to contrast cases of low nitrate (Flight 6 mean: 0.15 ± 0.32 μg m^{-3}) vs. high nitrate loadings (Flight 8 mean: 0.88 ± 0.82 μg m^{-3}), illustrating the relationships between NO_3^-, HNO_3, SO_4^{2-}, W_i, T, and pH. Flights 6 and 8 covered similar geographical regions of coastal New York, New Jersey and Delaware (Figure 3-10). Hybrid Single Particle Lagrangian Integrated Trajectory Model (HYSPLIT) back trajectories suggest that Flight 8 measured outflow from the greater New York City metropolitan area, at some distance off-shore, and Flight 6 encountered outflow from a wider eastern coastal area. Back trajectory plots are shown in the supplementary material (Figure B-12).

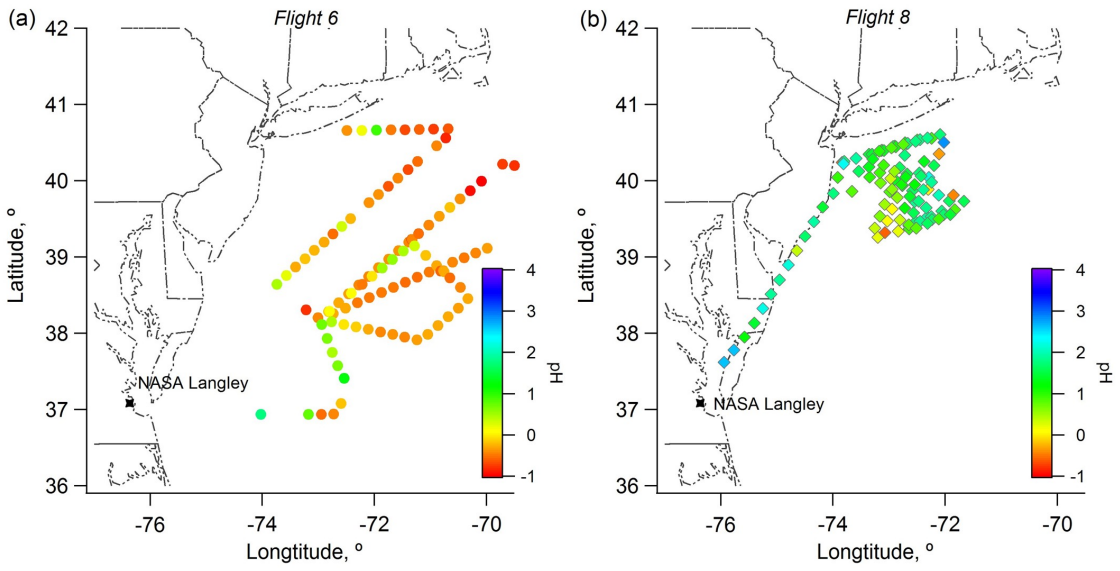

Figure 3-10 pH geographical distributions for Flights 6 (a) and 8 (b).

The time series of measured inorganic species, predicted pH, W_i, and T are shown in Figure 3-11. Although plumes of high total nitrate (HNO_3 + NO_3^-) were intercepted on Flight 6 (flight mean: 7.1 ± 3.2 μg m^{-3}), observed NO_3^- concentrations were low, but HNO_3 concentrations were high (flight mean: 6.9 ± 3.0 μg m^{-3}), with measured ε(NO_3^-) only 2 ± 3%. In contrast, for Flight 8, plumes of high total nitrate were again observed (yellow shaded regions in Figure 3-11b), but in this case significant concentrations of NO_3^- were also measured and ε(NO_3^-) varied between 20%-60%. These differences can be attributed to pH and temperature. In Flight 6, pH was nearly two units on average lower (–0.2 ± 0.5) than within-plumes of Flight 8 (1.5 ± 0.4). Temperature also played a role. Flight 8 was on average 9 °C colder than Flight 6. Thus, the combination of higher pH and lower T resulted in substantially more HNO_3 partitioning into the particle phase during Flight 8.

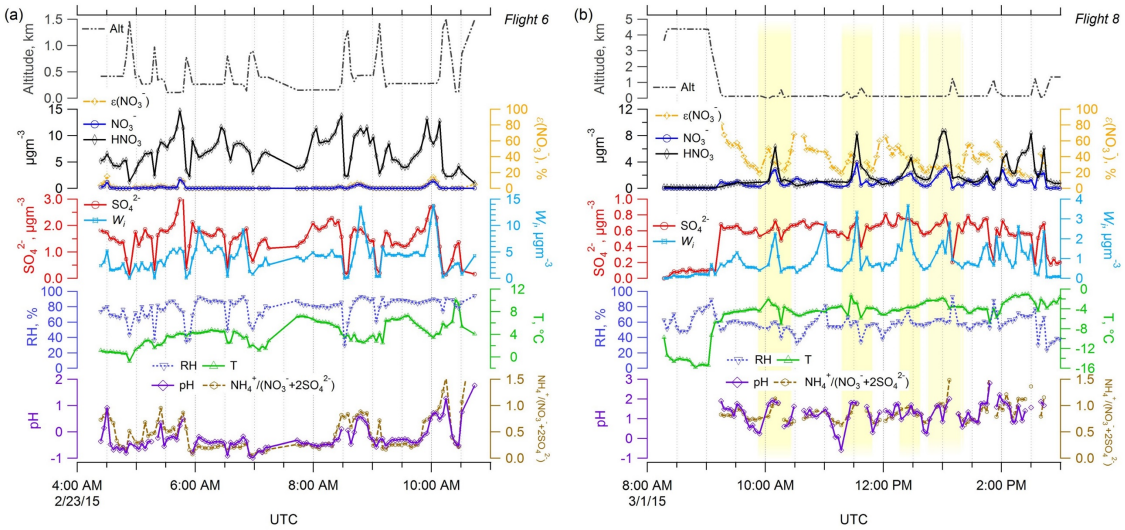

Figure 3-11 WINTER Flights (a) 6 and (b) 8 time series of altitude, measured NO_3^-, HNO_3, $\varepsilon(NO_3^-)$, SO_4^{2-}, RH, T, $NH_4^+/(NO_3^- + 2SO_4^{2-})$ ratio (mole mole^{-1}) and predicted W_i, pH. For both plots PILS-IC anions and scaled AMS NH_4^+ were used for the pH calculations. The yellow shaded area in (b) illustrates four high nitrate plumes.

Note in Figure 3-11b that the NO_3^-, W_i and pH all peaked in the plumes of Flight 8. The cause for these peaks demonstrates the inter-relationships between these parameters. Nitrate is highly hygroscopic, so when more HNO_3 partitions to the particle-phase due to high pH, the particle can take up more water (note, RH did not significantly change), this dilutes H^+, raises the pH and further enhances HNO_3 to NO_3^- partitioning. The interactions between NO_3^-, W_i, and pH are complex and nonlinear. In the case of Flight 6, the high sulfate concentrations led to higher predicted W_i (Flight 6 W_i = 4.1 ± 2.6 μg m^{-3}; Flight 8: W_i = 0.8 ± 0.7 μg m^{-3}), which could potentially raise pH and allow more HNO_3 dissolution, however, this effect did not compensate for the higher H^+ contributed by sulfate, which prevented nitrate aerosol formation.

3.4.8 Nitric acid and coarse mode cations

Overall, good agreement has been found between ISORROPIA-II predictions and observations, indicating that PM_1 nitrate was in thermodynamic equilibrium. However, during the study, there were at times significant amounts of coarse mode ions (Na^+, Cl^-, etc.), as well as NO_3^-. Here, coarse mode refers to particles with aerodynamic diameters between 1 and nominally 4 μm, the difference between the filter (PM_4) and PILS or AMS (PM_1) measurements. For the entire WINTER campaign, the PM_1/PM_4 ratios were on average ± SD: (AMS) NO_3^- 82 ± 83%, SO_4^{2-} 79 ± 26%, Cl^- 13 ± 36%, NH_4^+ 71 ± 52%. Other PM_4 ions were also non-negligible; Na^+ = 0.50 ± 0.88 μg m^{-3}, Cl^- = 0.69 ± 1.60 μg m^{-3}, K^+ = 0.03 ± 0.05 μg m^{-3}, Ca^{2+} = 0.12 ± 0.12 μg m^{-3}, Mg^{2+} = 0.07 ± 0.11 μg m^{-3}. Not surprisingly, sodium and chlorine were the highest since many flights were made over or near coastal regions. The PM_4 Cl^-/Na^+ molar ratio was 0.7 ± 0.6, indicating that some fraction of the Na^+ had likely combined with acidic species (i.e. SO_4^{2-}, NO_3^-) resulting in depleted Cl^- [*Gard et al.,* 1998]. Flight 6 provides an example for comparing equilibrium predictions for fine and coarse modes. During flight 6, the coarse mode NO_3^- fraction, ($PM_4 - PM_1$)/PM_4, was 76 ± 18%, more than four times that of the campaign average (18 ± 17%) and higher than the coarse mode SO_4^{2-} and NH_4^+ fractions, 14 ± 19% and 48 ± 21% respectively. A time series of PM_1, filter PM_4, and coarse mode NO_3^- fraction is shown in Figure B-13. To contrast a thermodynamic analysis on the fine versus coarse mode ions of Flight 6, we assume internal mixtures within each of the modes, and that all the following ions were exclusively in the coarse mode: Na^+, Cl^-, Ca^{2+}, Mg^{2+}, K^+. For the coarse mode there is largely disagreement between measured and predicted $\varepsilon(NO_3^-)$; more than half predicted $\varepsilon(NO_3^-)$ is nearly 100%, whereas observed $\varepsilon(NO_3^-)$ was between 0 and 20%

(Figure B-14). In contrast, ISORROPIA-predicted $\varepsilon(NO_3^-)$ agreed fairly well with predictions for equilibrium with the fine mode (predicted vs measured $\varepsilon(NO_3^-)$ regression, $y = 0.64x - 0.01$, $R^2 = 0.90$), considering the low $\varepsilon(NO_3^-)$ range (all below 20%). In such cases, a small overestimation in HNO_3 leads to amplified underestimation of NO_3^- and it is more difficult for the model to accurately predict the smaller mass species (predicted vs measured HNO_3 regression, $y = 1.04x - 0.12$, $R^2 = 1.00$ vs. NO_3^- regression, $y = 0.63x - 0.06$, $R^2 = 0.92$). The above fine vs. coarse mode results can be explained by the fine mode reaching equilibrium, but not the coarse mode as the latter process is kinetically limited [*Dassios and Pandis*, 1999; *Cruz et al.*, 2000; *Fountoukis et al.*, 2009]. Both modes compete for nitric acid. In this type of situation, over an extended period of time, the semivolatile fine mode ammonium nitrate and gas phase nitric acid will be depleted, impacting fine mode pH, and accumulate in the coarse mode in a nonvolatile form, such as sodium nitrate or calcium nitrate. However, because this process is slow, fine mode nitrate can persist and be accurately predicted by assuming thermodynamic equilibrium.

3.4.9 Ion Equivalence Ratios and Particle pH

Since running a thermodynamic model to predict pH is not necessarily straightforward, other proxies for particle acidity, based directly on measurement data, are often used instead. This includes ion balances, ammonium-sulfate molar ratios or cation-anion equivalence ratios. We have noted that this can lead to incorrect conclusions about particle pH and its effects, such as formation of nitrate [*Guo et al.*, 2015; *Hennigan et al.*, 2015; *Weber et al.*, 2016]. Given that the thermodynamic calculations for PM_1 were based solely on NH_4^+, NO_3^- and SO_4^{2-} and accurately predicted the partitioning concentrations of HNO_3

and NO_3^-, we compare the $NH_4^+/(NO_3^- + 2SO_4^{2-})$ equivalence ratio (mole $mole^{-1}$) with the model-predicted pH to assess the utility of this commonly used pH proxy. In Figure 3-11, time-series of the equivalence ratio and pH are plotted for the two case studies, and a direct comparison of the data are shown in Figure 3-12a. These plots illustrate that although they may appear to track at times in Figure 3-11, there is not a simple unique relationship between the ratios and pH (Figure 3-12a). This is also true for the complete WINTER data set, Figure 3-12b, which shows the equivalence ratio vs pH for all WINTER data (40-95% RH). An equivalence ratio of unity is interpreted as a fully neutralized aerosol, while smaller ratios reflect a higher particle acidity. For this data set, although the ratio shows a general increasing trend with pH, it provides little overall insight on pH. Considering data for pH greater than approximately 1 (the flatter anvil region of the data points); pH can range from approximately 1 to 3, whereas $NH_4^+/(NO_3^- + 2SO_4^{2-})$ always remained near 1, which would be interpreted as a neutral aerosol. For the other cluster of points, the opposite occurs, equivalence ratios span a range from approximately 0.8 to near 0, while pH remains between -1 and 1 indicating the aerosol is highly acidic at all times. There is a moderate correlation between the equivalence ratio and pH in this range, $R^2 = 0.32$, but with near vertical slope, there is little predictive capability. Furthermore, it is often assumed that nitric acid partitions to the particle to form NO_3^- only after the molar ratios reach 1. Figure 3-12b shows an increasing trend with NO_3^- mass concentration, but significant NO_3^- is found at ratios less than one and a lack of sensitivity inhibits accurate NO_3^- prediction in the flatter anvil region (equivalence ratio > 0.8). These results demonstrate that these forms

of particle acidity proxies should be employed with great care when used to infer particle pH and its impacts.

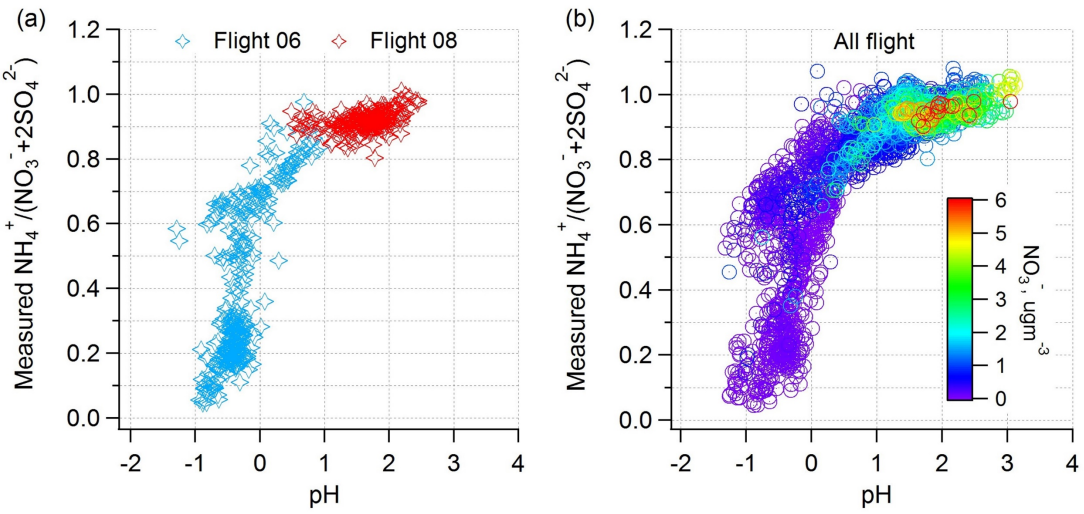

Figure 3-12 Measured $NH_4^+/(NO_3^- + 2SO_4^{2-})$ ratio (mole $mole^{-1}$) vs. pH for (a) Flight 6 (entire flight) and Flight 8 plumes (NO_3^- > 0.5 µg m^{-3}) and (b) for the entire WINTER data set. AMS data are used in the two plots.

3.5 Conclusions

Fine particle pH and the partitioning of HNO_3 is characterized over a large geographical region and for altitudes up to 5 km based on an aircraft campaign conducted from Feb 01 to March 15 2015 mainly in the northeastern US. PM_1 pH was predicted from the thermodynamic model ISORROPIA-II based on a data set spanning a wide range of ambient conditions. The following results were found:

1. Although there were differences of up to 50% between instruments measuring inorganic aerosol concentrations, this had a minor effect on overall predicted PM_1

average pH. Generally, systematic errors for all measured ionic species do not have a large effect on predicted pH, although corrections that affect single components do adversely affect predicted pH. This means that thermodynamic calculations can provide an additional constraint for evaluating the consistency of datasets.

2. Considering only the PM_1 NH_4^+, NO_3^- and SO_4^{2-}, ISORROPIA-II accurately predicted the partitioning of HNO_3-NO_3^- (HNO_3 and NO_3^- regression slopes deviate < 5%, and $R^2 > 0.9$) over a broad range of RH (40 to 95%), T (–21 to 19 ºC), and component concentrations (1-min average: HNO_3, 0.05 to 12 μgm^{-3}; SO_4^{2-}, 0.02 to 11 μgm^{-3}; NO_3^-, 0.07 to 7.8 μgm^{-3}; NH_4^+, 0.01 to 3.3 μgm^{-3}). Best agreement was observed at higher RH (60 to 95%), reasonable agreement was found in the 40 to 60% RH range, and significant discrepancies were observed for RH under 40%. The lowest RH range was also associated with the lowest HNO_3, NO_3^- and liquid water content. Discrepancies between observed and measured $\varepsilon(NO_3^-)$ could be due to: uncertainty in measured species at low concentrations, such as inclusion of organic acids in AMS-measured nitrate, division by small numbers when calculating $\varepsilon(NO_3^-)$, and organic-inorganic phase separations. No clear evidence that any effect single affect dominated the discrepancy was found.
3. Substantial sample heating in the aircraft aerosol sample line did not appear to produce artifacts because the residence times (0.5-2 sec) in sample lines were insufficient to allow alteration of semivolatile aerosol components. This finding is applicable to other aircraft or ground measurements.

4. PM_1 aerosol is highly acidic; for altitudes up to 5000 m pH ranged between –0.51 and 1.9 (10^{th} and 90^{th} percentiles) with a study mean of 0.77 ± 0.96. The pH range is similar to those reported for the southeastern US (0.5 to 2 in summer, 1 to 3 in winter) [*Guo et al.*, 2015] and the northern Colorado US (2 to 3 in winter) [*Young et al.*, 2013]. These pHs are also similar to those reported in the Mediterranean, which ranged between 0.5 to 2.8 (highest pH was found in biomass burning plumes, which were not investigated here) [*Bougiatioti et al.*, 2016].
5. Factors that affect $\varepsilon(NO_3^-)$ were investigated with ideal solution analytical calculations. A major factor was pH; $\varepsilon(NO_3^-)$ was sensitive to pH in the range of approximately –1 (all residing in the gas-phase) to 3 (all residing in the particle-phase). As expected, increases in partitioning to the particle phase were observed at lower temperatures and higher particle liquid water concentrations. Lower temperatures shift the pH at which the transition occurs to lower values allowing NO_3^- at lower pH. High liquid water contents dilute H^+ and raise the pH. These factors are inter-related in complex ways and can only be captured and resolved with a thermodynamic model.
6. PM_1 ions other than NH_4^+, NO_3^-, SO_4^{2-}, such as Na^+, Cl^-, did not change the predicted pH if included in the thermodynamic calculations (assumed to be internally mixed), for NaCl mole fractions (relative to all input aerosol ions) below 50%. Note that, the subtle pH variation (< 0.4 units) can be important for HNO_3-NO_3^- partitioning when $\varepsilon(NO_3^-)$ is close to 50%. At higher NaCl mole fractions (which were rare), pH was substantially increased. However, Na^+ and

Cl^- appear not to be completely internally mixed with NH_4^+, NO_3^-, SO_4^{2-}, since larger deviation between predicted and measured HNO_3-NO_3^- partitioning is introduced.

7. Occasionally, coarse mode ($PM_4 - PM_1$) cations and nitrate were found to be abundant. Large discrepancies between observed and predicted HNO_3 and coarse mode NO_3^- indicate a lack of thermodynamic equilibrium due to kinetic limitations. However, HNO_3 and PM_1 NO_3^- partitioning were accurately predicted, indicating equilibrium.
8. Traditional pH proxies, such as $NH_4^+/(NO_3^- + 2SO_4^{2-})$ equivalence ratios were not uniquely related to pH and NO_3^-, implying that their utility for predicting impacts of particle acidity on aerosol processes or properties is suspect. The $NO_3^-/2SO_4^{2-}$ ratio was more closely related to particle pH in this study but lost sensitivity to pH when relatively low $NO_3^-/2SO_4^{2-}$ ratios were present (e.g. 0.3). The same ratio is also sensitive to emissions of HNO_3, so a universally-applicable correlation may not be possible.
9. Particle pH should be explicitly determined to accurately assess its effects on aerosol mass, atmospheric processes, and other health and environmental impacts, including the partitioning of nitric acid between the gas and particle phases and sensitivities thereof to errors.

CHAPTER 4. FINE PARTICLE PH AND GAS-PARTICLE PHASE PARTITIONING OF INORGANIC SPECIES IN PASADENA, CALIFORNIA, DURING THE 2010 CALNEX CAMPAIGN

4.1 Abstract

pH is a fundamental aerosol property that affects ambient particle concentration and composition, linking pH to all aerosol environmental impacts. Here, PM_1 and $PM_{2.5}$ pH are calculated based on data from measurements during the California Research at the Nexus of Air Quality and Climate Change (CalNex) study from May 15 to June 15 2010 in Pasadena CA. Particle pH and water were predicted with the ISORROPIA-II thermodynamic model and validated by comparing predicted to measured gas-particle partitioning of inorganic nitrate, ammonium, and chloride. The study mean ± standard deviation PM_1 pH was 1.9 ± 0.5 for the SO_4^{2-}-NO_3^--NH_4^+-HNO_3-NH_3 system. For $PM_{2.5}$, internal mixing of sea-salt components (SO_4^{2-}-NO_3^--NH_4^+-Na^+-Cl^--K^+-HNO_3-NH_3-HCl system) raised the bulk pH to 2.7 ± 0.3 and improved predicted nitric acid partitioning with $PM_{2.5}$ components. The results show little effect of sea-salt on PM_1 pH, but significant effects on $PM_{2.5}$ pH. A mean PM_1 pH of 1.9 at Pasadena was approximately one unit higher than what we have reported in the southeastern U.S., despite similar temperature, relative humidity and sulfate ranges and is due to higher total nitrate concentrations (nitric acid plus nitrate) relative to sulfate, a situation where particle water is affected by semivolatile nitrate concentrations. Under these conditions nitric acid partitioning can further promote nitrate formation by increasing aerosol water, which raises pH by dilution, further increasing nitric acid partitioning and resulting in a significant increase in fine particle nitrate and pH. This

study provides insights on the complex interactions between particle pH and nitrate in a summertime coastal environment and a contrast to recently reported pH in the eastern U.S. in summer and winter and the eastern Mediterranean. All studies have consistently found highly acidic PM_1 with pH generally below 3.

4.2 Introduction

Ambient aerosol particles affect human health and climate [*Lim et al.*, 2012; *IPCC*, 2013], and have many other environmental effects. Particle pH is linked to all of these by altering the fundamental aerosol properties of particle mass and chemical composition. For example, some important pathways leading to secondary organic aerosol (SOA) formation from biogenic volatile organic compounds (VOCs), such as isoprene and α-pinene, are catalyzed by H^+ [*Jang et al.*, 2002; *Gao et al.*, 2004; *Edney et al.*, 2005; *Surratt et al.*, 2007; *Eddingsaas et al.*, 2010; *Surratt et al.*, 2010; *Han et al.*, 2016a]. pH directly affects particle mass and composition through altering the partitioning of both semivolatile inorganic and organic acids between particle and gas phases [*Guo et al.*, 2016]. pH affects the nitrogen cycle through gas-particle partitioning of nitric acid, ammonia and nitrate, ammonium, impacting deposition patterns due to large differences in gas versus particle dry deposition rates [*Huebert and Robert*, 1985; *Duyzer*, 1994; *Schrader and Brummer*, 2014].

Particle pH is linked to adverse health impacts, both directly and indirectly. Synergistic adverse health effects have been observed between ozone and acidic aerosols [*Last*, 1991; *Enami et al.*, 2008] and epidemiological studies have reported adverse health outcomes associated with strong aerosol acidity [*Koutrakis et al.*, 1988; *Thurston et al.*, 1994; *Dockery et al.*, 1996; *Raizenne et al.*, 1996; *Gwynn et al.*, 2000; *Lelieveld et al.*, 2015].

Low pH increases the solubility of transition metals, such as iron and copper [*Meskhidze et al.*, 2003; *Oakes et al.*, 2012; *Longo et al.*, 2016; *Fang et al.*, 2017], which have been linked to aerosol toxicity through aerosol oxidative effects [*Ghio et al.*, 2012; *Verma et al.*, 2014; *Fang et al.*, 2015; *Fang et al.*, 2017]. Metal mobility also affects nutrient distributions with important impacts on photosynthesis productivity [*Duce and Tindale*, 1991; *Meskhidze et al.*, 2003; *Nenes et al.*, 2011; *Ito and Xu*, 2014; *Myriokefalitakis et al.*, 2015; *Li et al.*, 2017], carbon sequestration and ocean oxygen levels [*Ito et al.*, 2016].

Due to limitations with direct particle pH measurement techniques, fine particle pH has often been indirectly inferred from aerosol composition based on ion balances or cation-anion molar balances, e.g., ammonium to sulfate (NH_4^+/SO_4^{2-}) molar ratios. However, these are largely inaccurate pH proxies [*Guo et al.*, 2015; *Hennigan et al.*, 2015; *Guo et al.*, 2016; *Weber et al.*, 2016], which if used can provide misleading indications on the level of acidity present in the aerosol and pH-related properties. Alternatively, particle pH is more accurately calculated with a thermodynamic model, such as ISORROPIA-II [*Nenes et al.*, 1998; *Fountoukis and Nenes*, 2007] or E-AIM [*Clegg et al.*, 1998; *Wexler and Clegg*, 2002; *Clegg et al.*, 2003], which consider particle water, solution non-ideality, and variable dissociation of inorganic species in solution and equilibrium of semivolatiles between gas and aerosol (aqueous and solid) phases. In forward mode, which utilizes both gas and particle phase inputs, the accuracy of pH predictions can be assessed by comparing predicted to measured partitioning of semivolatile species, such as NH_3-NH_4^+, HNO_3-NO_3^- and HCl-Cl^- pairs. The semivolatile species with the most information content about pH

depend on the conditions at a specific location (e.g., when the specific component is not completely in the gas or particle phase).

This work adds to our investigation of particle pH in differing locations and under different emission characteristics. We have reported that ground level pH in the southeastern US is 0.9 ± 0.6 (mean ± SD) in summer and 2.0 ± 1.0 in winter [*Guo et al.*, 2015], and 0.8 ± 1.0 in the boundary layer and lower free troposphere (< 5 km altitude) over broad regions of the eastern US in winter, based on aircraft data [*Guo et al.*, 2016]. A pH of 1.3 ± 1.1 has also been reported in various air masses advected to Crete in the eastern Mediterranean [*Bougiatioti et al.*, 2016]. This study focuses on particle pH in an urban coastal site, Pasadena, California, and investigates the reasons for significantly higher nitrate mass loadings compared to those of the southeastern US [*Zhang et al.*, 2007a; *Hand et al.*, 2012b].

4.3 Methods

4.3.1 Sampling site

Aerosol and gas measurements were conducted on the California Institute of Technology campus in Pasadena, California (34.140582 N, 118.122455 W, altitude above sea level: 235 m), as part of the 2010 California Research at the Nexus of Air Quality and Climate Change (CalNex) campaign from May 15 to June 15 2010 [*Ryerson et al.*, 2013]. The CalNex ground site was located within the Los Angeles Basin and approximately 16 km northeast of the central Los Angeles city (hereafter referred to as LA), and 5 km south of the San Gabriel Mountains. With the dominant wind from the southwest, the site was

regularly impacted by emissions transported from the coast and central LA area [*Washenfelder et al.*, 2011; *Hayes et al.*, 2013]. Meteorological data used in the following analysis is from the National Oceanic and Atmospheric Administrations (NOAA) CalNex researchers meteorological station.

4.3.2 Instrumentation

PILS-IC: $PM_{2.5}$ (particles with aerodynamic diameters < 2.5 μm at ambient conditions) water-soluble ions were measured with a Particle-Into-Liquid Sampler coupled with Ion Chromatographs (PILS-IC), similar to that described elsewhere [*Orsini et al.*, 2003; *Hennigan et al.*, 2006; *Sullivan et al.*, 2006; *Peltier et al.*, 2007a]. The operation details of PILS-IC during CalNex has been discussed by *Liu et al.* [2012] in detail. Ambient air was sampled through a URG (Chapel Hill, NC, U.S.) $PM_{2.5}$ cyclone and mixed with near 100°C water vapor generated from deionized water. After growth, droplets were collected by impaction, producing a continuous liquid sample for online IC analysis. All ambient data were blank-corrected by periodically measuring filtered ambient air. $PM_{2.5}$ anion data were available throughout the CalNex study, whereas cation data were only available for the last week (June 08-14). Since particle acidity predictions require both anion and cation data, discussions on $PM_{2.5}$ pH will include only the last week of data. The measurement uncertainties of anions and cations, based on calibration variability, sample air flow rates, liquid flow rates, and field blanks, were estimated to be 13% for anions and 8% for cations. Detection limits were 0.015 μg m^{-3} SO_4^{2-}, 0.03 μg m^{-3} NO_3^-, 0.01 μg m^{-3} Cl^- for anions, and 0.02 μg m^{-3} NH_4^+, 0.02 μg m^{-3} Na^+, 0.04 μg m^{-3} K^+ for cations (Ca^{2+} and Mg^{2+} were not measured).

AMS: PM_1 non-refractory inorganic and organic components were measured by a high resolution time of flight aerosol mass spectrometer (HR-ToF-AMS, Aerodyne Research Inc., hereafter referred to as AMS; *DeCarlo et al.* [2006]). The operation procedure of the AMS during this study has been described in *Hayes et al.* [2013] and measurement uncertainty estimated at 30% [*Middlebrook et al.*, 2012]. The AMS detects non-refractory species in dried aerosols through an aerodynamic focusing lens, a detection chamber where aerosols are flash vaporized and ionized, followed by time-of-flight mass spectrometry. The comparison of AMS PM_1 and PILS-IC $PM_{2.5}$ measurements was summarized in *Hayes et al.* [2013] and is discussed further below. In the following analysis PM_1 species are AMS data and $PM_{2.5}$ species are PILS-IC data.

PALMS: Single aerosol composition and size for diameters 0.15-3 μm were measured by an online Particle Analysis by Laser Mass Spectrometry (PALMS) [*Murphy et al.*, 2006; *Froyd et al.*, 2010]. In this method, individual aerosols scatter light from a continuous laser beam and trigger an excimer laser that ionize the single particle. The resulting ions are analyzed by a time of light mass spectrometer to generate a complete positive or negative mass spectrum per particle. In this study, PALMS data provides insights into the aerosol mixing state.

QC-TILDAS: gas-phase NH_3 was quantified using a Quantum Cascade Tunable Infrared Laser Differential Absorption Spectrometer (QC-TILDAS), developed by Aerodyne Research Inc. and described in details in *Ellis et al.* [2010]. QC-TILDAS uses a thermoelectrically cooled pulsed Quantum Cascade (QC) laser, which measures NH_3 at 967 cm^{-1} in the infrared regime. The laser beam is directed into an astigmatic Herriot

absorption cell, where it passes between two highly reflective mirrors before leaving the cell and arriving at a thermoelectrically cooled Mercury Cadmium Telluride (HgCdTe) infrared detector. A 12 m heated (40 ± 2°C) and insulated 0.95 cm PFA line (Clayborn Lab, Truckee, California, U.S.) connects a short (10 cm; 8 m above ground) custom-designed quartz inlet to the QC-TILDAS. The inlet includes two ports for the introduction of calibration and background gas designed so that the flows follow the same path through the inlet as the ambient sample. Zero air measurements and ammonia calibrations were performed periodically during the CalNex campaign. The detection limit was 1.5 ppbv for 1 sec data and decreased to 0.42 ppbv for 1 min averaging data. The overall NH_3 measurement uncertainty was 10%.

NI-PT-CIMS: gas phase HNO_3 and HCl measurements were made using a negative-ion proton-transfer chemical ionization mass spectrometer (NI-PT-CIMS; hereafter referred to as "CIMS"). Details of the NI-PT-CIMS design and operation during CalNex have been reported in *Veres et al.* [2008]. Acidic molecules are ionized by proton transfer with acetate ions and detected as conjugate anions with a quadrupole mass spectrometer. The CIMS was placed on top of an instrument trailer at 3 m height with a heated (75°C) 0.32 cm Teflon inlet, 1.3 m in length, sampling at 5 m relative to ground level. (Possible biases in measured HNO_3 and HCl due to aerosol volatilization in the heated inlet is discussed in Section 4.5.1). In the field, instrument backgrounds were quantified every 190 min for a duration of 30 min. The detection limits were 0.080 ppbv for HNO_3 and 0.055 ppbv for HCl. Overall measurement uncertainty was 35%. All gas-phase concentrations reported in ppbv were converted to μg m^{-3} at ambient conditions to be consistent with particle-phase

measurements and for thermodynamic calculations. In all cases, gas and particle concentrations are reported and utilized in the model using ambient conditions (i.e., all volumetric concentrations are at ambient temperature and pressure).

4.3.3 pH and gas-particle partitioning modeling

pH is defined as the logarithm of the hydronium ion (H_3O^+) activity in an aqueous solution. Hereafter we denote H_3O^+ as H^+ for simplicity, while recognizing that the unhydrated hydrogen ion is rare in aqueous solutions. pH is given by,

$$pH = -\log_{10} \gamma_{H^+} H^+_{aq} = -\log_{10} \frac{1000 \gamma_{H^+} H^+_{air}}{W_i + W_o} \cong -\log_{10} \frac{1000 \gamma_{H^+} H^+_{air}}{W_i} \quad (4\text{-}1)$$

where γ_{H^+} is the hydronium ion activity coefficient (in this case assumed = 1), H^+_{aq} (mole L^{-1}) the hydronium ion concentration in particle liquid water, H^+_{air} (μg m^{-3}) the hydronium ion concentration per volume of air, and W_i and W_o (μg m^{-3}) the bulk particle water concentrations associated with inorganic and organic species, respectively. W_o can be calculated by Equation 5 in *Guo et al.* [2015]. Both H^+_{air} and W_i are outputs of the thermodynamic model, ISORROPIA-II, which was used to determine the composition and phase state of an NH_4^+-SO_4^{2-}-NO_3^--water inorganic aerosol in thermodynamic equilibrium with its corresponding gases. (In some cases, Cl^--Na^+-K^+ were also included). A similar approach has been used in several studies for contrasting summer and winter conditions in the eastern U.S. [*Guo et al.*, 2015; *Guo et al.*, 2016; *Weber et al.*, 2016] and eastern Mediterranean [*Bougiatioti et al.*, 2016; *Bougiatioti et al.*, 2017].

In previous studies, the effect of W_o on pH has been investigated and found to be minor [*Guo et al.*, 2015]. pH in that study based solely on W_i was 0.15-0.23 units systematically lower than pH predicted with total particle water (W_i + W_o) and highly correlated (R^2 = 0.97). In this study, ΔpH of +0.12 and +0.19 units were estimated when including W_o based on average and maximum organic hygroscopic parameter κ_{org} of 0.13 and 0.23, respectively [*Mei et al.*, 2013]. Sensitivity of pH to effects of W_o are smaller in CalNex due to smaller fractions of W_o to total particle water (21%) compared to that found in SOAS (35%) (Southern Oxidant and Aerosol Study). Given this relatively small deviation (on average 0.12 unit), we report pH only considering W_i.

ISORROPIA-II was run assuming particles were "metastable" with no solid precipitates (H^+ is not stable in an effloresced aerosol); a reasonable assumption considering the high RH range observed during this study (mean ± SD of RH = 79 ± 17%). In our previous pH studies, we only considered data for RH between 20-95%. At low RH (e.g., < 20%), aerosols are less likely to be in a completely liquid state [*Ansari and Pandis*, 2000; *Malm and Day*, 2001; *Fountoukis and Nenes*, 2007; *Bertram et al.*, 2011], and the "glassy" SOA may impede the partitioning of semivolatile species due to decreased diffusion in the particles [*Ye et al.*, 2016], and uncertainties in predicted pH are expected to be large due to uncertain activity coefficients associated with highly concentrated solutions [*Fountoukis et al.*, 2009]. At RH > 95%, large pH uncertainty is introduced due to the exponential growth in particle liquid water with RH and propagation of RH sensor uncertainties [*Malm and Day*, 2001; *Guo et al.*, 2015]. The CalNex RH ranged from 22% to 100%, therefore periods for RH above 95% were excluded.

The model was also run in forward mode, which calculates the gas-particle equilibrium partitioning concentrations based on the input of total concentration of a species (i.e., gas + particle). Use of total species as ISORROPIA-II inputs produces substantially better predictions compared with only particle phase concentration inputs in either forward or reverse mode since in the former cases (forward mode with only particle phase input), particle phase semivolatile species concentration is under-predicted due to some fraction repartitioned into the gas phase in the model, and in the latter cases (reverse mode), measurement errors often result in large model biases in pH [*Hennigan et al.*, 2015].

The predicted gas or particle phase semivolatile compounds can be compared to measurements for validating the thermodynamic calculations. Possible partitioning pairs for ISORROPIA-II are HNO_3-NO_3^-, NH_3-NH_4^+, and HCl-Cl^- (discussed in Section 4.4.2&4.4.3). This method is effective when gas and particle phase components have substantial fractions in both the gas and particle phases. For example, in the southeastern US in summer, ammonia partitioning (gas/(gas + particle)) varied between 10 to 80%, whereas nitric acid partitioning was mostly near 80% and PM_1 nitrate level close to the detection limit (larger uncertainty), making ammonia partitioning much more useful than nitric acid for evaluating thermodynamic models [*Guo et al.*, 2015]. In contrast, nitric acid partitioning, ranged from 0% to 100% (average ~ 50%) and so was used to evaluate pH predicted in the northeastern US in the cold season [*Guo et al.*, 2016].

Using gas-particle partitioning to constrain particle pH can be complicated by the presence of multiple phases within the particle, which may distribute inorganic species amongst multiple phases, each with their own water activity and hence inorganic concentration. Lab

studies show that liquid-liquid phase separations are always observed at O:C (organic aerosol atomic O to C ratio) $\leq$ 0.5, whereas no phase separations occur for O:C $\geq$ 0.8 [*Bertram et al.*, 2011; *Song et al.*, 2012; *You et al.*, 2013; *You et al.*, 2014b]. The likelihood for phase separation decreases at higher RH and only has a weak dependence on T [*Schill and Tolbert*, 2013; *You and Bertram*, 2015]. For conditions during SOAS (O:C = 0.75 ± 0.12, RH = 74 ± 16%, T = 25 ± 3°C), we found that thermodynamic calculations accurately predicted bulk particle water and ammonia partitioning over the complete T (18 to 33 °C) and RH (36 to 96%) ranges [*Guo et al.*, 2015]. During the Wintertime Investigation of Transport, Emissions, and Reactivity (WINTER) aircraft study (O:C = 0.78 ± 0.11, T = 0 ± 8°C), we found that HNO_3-NO_3^- partitioning was accurately predicted for RH > 60% [*Guo et al.*, 2016]. Compared to SOAS and WINTER (both in the eastern US), in this study the smaller O:C (0.52 ± 0.10) [*Hayes et al.*, 2015] mean we cannot outright exclude the possibility of phase separation, but very high RH (79 ± 17%) makes it less likely.

In running ISORROPIA-II to predict pH and semivolatile species partitioning, it is also assumed that the particles are internally mixed, that pH does not vary with particle size (i.e., bulk properties represent the overall aerosol pH), and that the ambient aerosols and gases are in thermodynamic equilibrium. For the WINTER study, which included measurements over coastal and marine areas, we found that PM_1 pH was accurately predicted with only particle phase SO_4^{2-}, NO_3^-, NH_4^+ (and gas phase HNO_3); whereas sea-salt components had some, but generally small, effects on the prediction of particle pH (except on rare occasions when the mole fraction of NaCl to total soluble inorganic ions

was greater than 50%) [*Guo et al.*, 2016]. The mixing state of sea-salts with SO_4^{2-}, NO_3^-, NH_4^+ is a critical issue in predicting particle pH in LA and is discussed below.

4.4 Results

4.4.1 PM_1 and $PM_{2.5}$ inorganic composition and gas-particle partitioning

Time series for various measured parameters during CalNex are shown in Figure 4-1. CalNex T and RH were 18 ± 4°C and 79 ± 17% (mean ± SD). During the first half of the campaign, May 15 to May 29, daily maximum T was below 26°C and PM_1 (AMS) and $PM_{2.5}$ (PILS-IC) SO_4^{2-}, NO_3^-, NH_4^+ showed a general decreasing trend ($PM_{2.5}$ NH_4^+ data was not available in this period). The second half of the campaign started with a warmer period (May 30 to June 7), with the highest T reaching 29°C. During this period, SO_4^{2-}, NO_3^-, NH_4^+, and HNO_3 were significantly higher than the first half and reached campaign maximums of 9.7 μg m^{-3} PM_1 SO_4^{2-}, 20.1 μg m^{-3} PM_1 NO_3^-, 9.6 μg m^{-3} PM_1 NH_4^+, and 33.1 μg m^{-3} HNO_3. The peak concentrations of combined PM_1 inorganics alone exceeded The National Ambient Air Quality Standard (NAAQS) $PM_{2.5}$ 24-hour limit of 35 μg m^{-3} (https://www.epa.gov/criteria-air-pollutants/naaqs-table), with the largest contribution from NO_3^-. Gaseous components other than HNO_3, such as NH_3 and HCl, showed different patterns than the above species, indicating different sources and sinks.

PM_1 (AMS) SO_4^{2-}, NO_3^-, NH_4^+ were highly correlated with $PM_{2.5}$ (PILS-IC) measurements, with R^2 between 0.8 and 0.9 (Figure C-1). $PM_1/PM_{2.5}$ mass ratios were 97.5 ± 5.4% for SO_4^{2-}, 63.5 ± 22.1% for NO_3^-, and 92.3 ± 9.9% for NH_4^+. Note that, the mass fractions for SO_4^{2-} and NO_3^- are campaign averages, but NH_4^+ mass fraction is only for the

last week when $PM_{2.5}$ NH_4^+ was available. Nearly 40% of the NO_3^- was found between 1 and 2.5 μm, whereas most SO_4^{2-} and NH_4^+ were associated with PM_1. (Ratios based on regression slopes are shown in Figure C-1). Hence, the NO_3^- for the 1 to 2.5 μm size range was likely associated with some nonvolatile cations, such as Na^+ and K^+ instead of NH_4^+. The $PM_{2.5}$ Cl^-/Na^+ molar ratio was 0.5 ± 0.2. Given that these species are mainly transported from the coastal regions in the form of sea-salts (NaCl), this indicates that roughly half of the Na^+ had reacted with HNO_3 resulting in depleted Cl^- [*Robbins et al.*, 1959; *Langer et al.*, 1997]. These results are consistent with the analysis of *Hayes et al.* [2013].

Measurements of semivolatile particle (NO_3^-, NH_4^+, Cl^-) and corresponding inorganic gases (HNO_3, NH_3, HCl) are used to investigate partitioning. The gas-particle partitioning is described as the particle phase mass concentration divided by the total mass concentration (gas + particle), e.g., $\varepsilon(NO_3^-) = NO_3^-/(HNO_3 + NO_3^-)$. The campaign average partitioning ratios were as follows; for PM_1 $\varepsilon(NO_3^-) = 39 \pm 16\%$, PM_1 $\varepsilon(NH_4^+) = 56 \pm 26\%$, $PM_{2.5}$ $\varepsilon(NO_3^-) = 54 \pm 10\%$, and $PM_{2.5}$ $\varepsilon(Cl^-) = 39 \pm 26\%$. All partitioning ratios are near 50%, making them useful for assessing pH predictions by comparing measured versus ISORROPIA-predicted ratios.

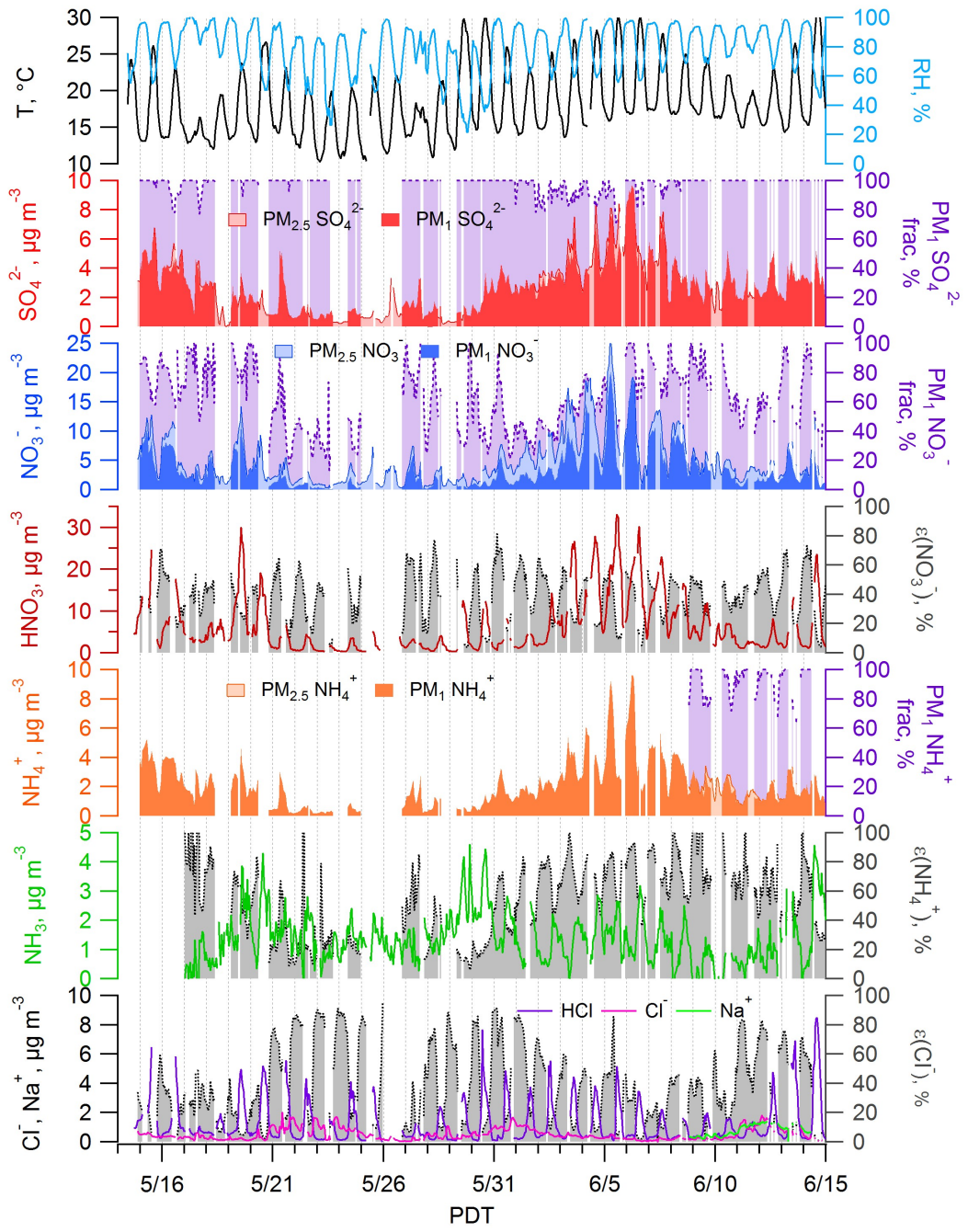

Figure 4-1 CalNex campaign time series of meteorological conditions (T, RH), particle and gas phase inorganic compound mass loadings (SO_4^{2-}, NO_3^-, Cl^-, NH_4^+, Na^+; HNO_3, NH_3, HCl), particle phase mass fractions of total (gas plus particle; $\varepsilon(NO_3^-)$, $\varepsilon(NH_4^+)$ based on PM_1 and $\varepsilon(Cl^-)$ based on $PM_{2.5}$, all denoted by grey color), and PM_1 to $PM_{2.5}$ mass fractions of SO_4^{2-}, NO_3^-, NH_4^+ (all denoted by purple color).

4.4.2 PM_1 pH prediction and verification

PM_1 pH was determined to be on average (± SD) 1.9 ± 0.5 for the complete study, for model inputs of PM_1 inorganic AMS-measured components SO_4^{2-}, NO_3^-, NH_4^+, and gases HNO_3 and NH_3. Although the CalNex ground site was influenced by sea-salt components, Na^+ and Cl^- were not included in the PM_1 pH since NaCl is typically found mainly at sizes above 1 μm and the mixing states of PM_1 NaCl with SO_4^{2-}, NO_3^-, NH_4^+ remains to be investigated. PALMS single particle data indicated that for the particle size range with D_{ve} (dry volume-equivalent diameter) between 0.15 and 780 nm (~1 μm), by number 27% of PM_1 sea-salt particles (Na^+-rich particles without crustal materials) had observable NO_3^- signals and by mass only 12% of PM_1 are sea-salt types (Table 4-1), suggesting external mixing of NaCl with NO_3^- is the main form. For the 1 to 2.5 μm size range the number and mass fractions were 85% and 63%, respectively.

Table 4-1 Number fraction of sea-salt particles with observable nitrate signals and mass fraction of sea-salt particles to total mass in two size ranges, 0.15-1 and 1-2.5 μm. Sea-salt particles are identified as Na^+-rich particles without crustal elements. The number fraction was determined directly from the PALMS data and the mass fraction was calculated based on the number fractions and size distributions, assuming dry particle densities.

Particle size, μm	Number fraction of sea-salt particles with observable nitrate signal	Sea-salt particles mass fraction to total
0.15-1	27%	12%
1-2.5	85%	63%

We assess predicted pH from the thermodynamic model by comparing predicted and measured gas-particle partitioning of NH_3-NH_4^+, HNO_3-NO_3^-. Comparison of HNO_3-NO_3^- and NH_3-NH_4^+ predictions to their measured values is shown as Figure 4-2. Gas phase HNO_3, NH_3 and particle phase NH_4^+ are on average within 10% and highly correlated, $R^2 > 0.8$. Despite a high correlation ($R^2 = 0.76$), ISORROPIA-II predicted particle phase NO_3^- is systematically higher than observed, with a regression slope of 1.28. Two bands are observed that are related to RH or time of day (Figure 4-2b); for mid-range RH (50-70%) daytime data, ISORROPIA-II slightly underpredicts NO_3^- and for high RH (~90%) nighttime data, NO_3^- is overpredicted. This leads to a regression slope of 2 comparing predicted to measured $\varepsilon(NO_3^-)$ and a large intercept (Figure 4-2c, also see Figure C-5). In contrast, predicted versus measured $\varepsilon(NH_4^+)$ is close to 1:1 and highly correlated ($R^2 = 0.8$, Figure 4-2f), and there is a much weaker systematic variability related to RH or time of day.

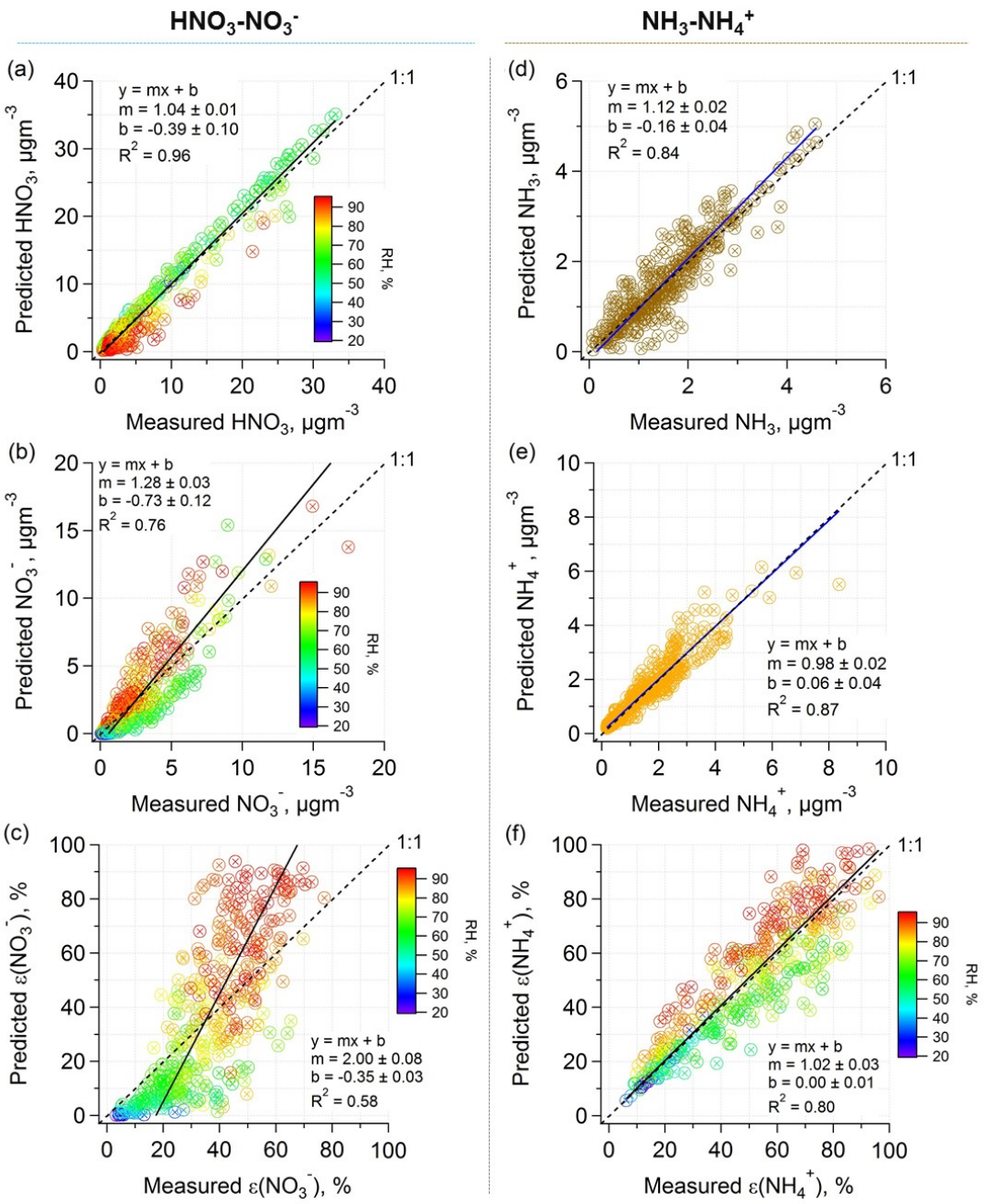

Figure 4-2 Comparisons of predicted and measured HNO_3, NO_3^-, and $\varepsilon(NO_3^-)$ (a, b, c) and NH_3, NH_4^+, and $\varepsilon(NH_4^+)$ (d, e, f) for data from the complete CalNex study. Particle phase data are all AMS PM_1. Orthogonal distance regression (ODR) fits are shown and uncertainties in the fits are one standard deviation.

4.4.3 $PM_{2.5}$ pH prediction and verification

Predicting the bulk pH of $PM_{2.5}$ is more complicated since the particles larger than 1 μm in the $PM_{2.5}$ fraction are not necessarily in equilibrium due to increased timescale for equilibration (> 20-30 mins) [*Fountoukis et al.*, 2009], especially in an environment with rapidly changing concentrations of key species (e.g. HNO_3). This leads to greater uncertainty when predicting partitioning of semivolatile species. Furthermore, the pH analysis now needs to consider sea-salt components (SO_4^{2-}-NO_3^--NH_4^+-Na^+-Cl^--K^+-HNO_3-NH_3-HCl system). Whereas single particle PALMS data suggested that only a small fraction (27%) of the sea-salt particles less than 1 μm were internally mixed with nitrate, for sizes between 1 and 2.5 μm, the majority (85%) were. Overall, we find bulk $PM_{2.5}$ pH considering sea-salt components higher than PM_1 by 0.8 units on average. For data from the last week of the study (i.e., period of PILS data that includes measurements of sea-salt components), PM_1 pH was 1.9 ± 0.4, similar to that of the complete study (1.9 ± 0.5), and in contrast to an average $PM_{2.5}$ pH of 2.7 ± 0.3. A comparison of the pH is shown in Figure 4-3. Addition of nonvolatile Na^+ and K^+ increases pH. Na^+ is the more important cation in this case, as the Na^+ levels were several times larger than K^+ (0.77 ± 0.39 vs. 0.20 ± 0.09 μg m^{-3}, or 0.33 vs. 0.05 mol m^{-3}).

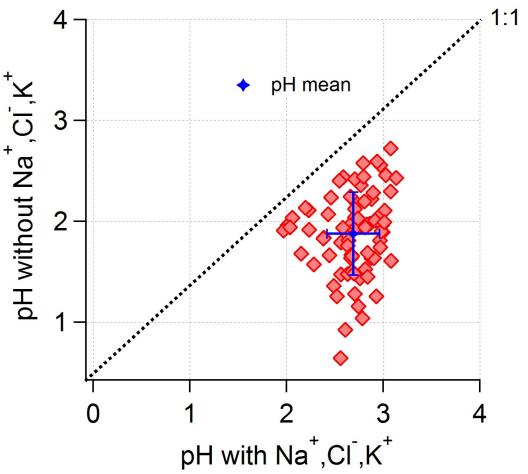

Figure 4-3 Comparison of predicted $PM_{2.5}$ particle pH assuming external versus internal mixing of Na^+, Cl^-, K^+ with SO_4^{2-}, NO_3^-, NH_4^+ for data from the last week of the CalNex study (i.e., SO_4^{2-}-NO_3^--NH_4^+-HNO_3-NH_3 system vs. SO_4^{2-}-NO_3^--NH_4^+-Na^+-Cl^--K^+-HNO_3-NH_3-HCl system). For these two cases, pH increased from 1.9 ± 0.4 to 2.7 ± 0.3 with the input of Na^+, Cl^-, K^+. Figure 4-4 and Figure 4-5 show that for $PM_{2.5}$, inclusion of Na^+, Cl^-, K^+ provides better predicted portioning of nitric acid.

To examine the effects of sea-salt components on the thermodynamic predictions, we compared the observed to measured partitioning of $PM_{2.5}$ semivolatile species in Figure 4-4. ISORROPIA-II was run with two differing inputs, one with Na^+, Cl^-, K^+ and the other run without these ions. In both cases, only PILS-IC $PM_{2.5}$ data are used. All other input parameters, including NH_4^+, SO_4^{2-}, NO_3^-, RH, and T, were the same. Figure 4-4 shows that inclusion of Na^+, Cl^-, K^+ improves the prediction of HNO_3-NO_3^- partitioning. For HNO_3, NO_3^-, and $\varepsilon(NO_3^-)$, predicted levels are somewhat closer to the measurements and the scatter in the data is reduced. However, like the PM_1 analysis above, the slope between predicted and measured $\varepsilon(NO_3^-)$, 2.4, is significantly larger than 1. The deviation is again related to RH, resulting from a diurnal dependence. Unlike the HNO_3-NO_3^- partitioning, NH_3-NH_4^+ partitioning is not as sensitive to inclusion of Na^+, Cl^-, K^+. Overall, $\varepsilon(NH_4^+)$ is

on average underestimated by 17% compared to measured (average ratio). HCl-Cl^- partitioning is well captured by ISORROPIA-II with regression slopes of 1.05, 0.95, 1.14 and R^2 of 0.98, 0.84, 0.81 for HCl, Cl^-, $\varepsilon(Cl^-)$, respectively.

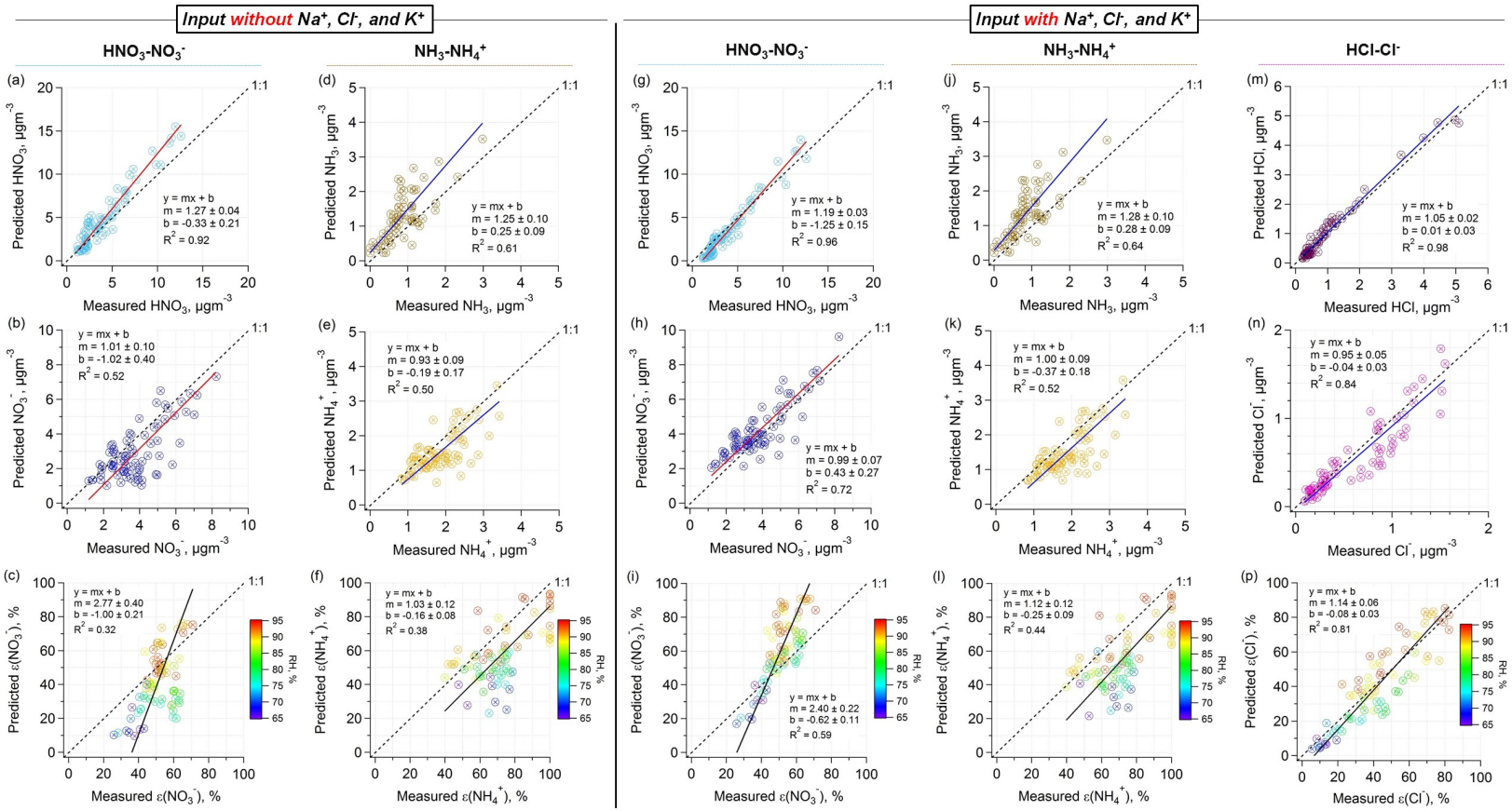

Figure 4-4 Inter-comparisons of predicted and measured gas-particle phase partitioning for $PM_{2.5}$ particles for two scenarios: ISORROPIA-II input without (left) and with (right) Na^+, Cl^- (and HCl), K^+. The other input SO_4^{2-}, NO_3^-, NH_4^+, NH_3, HNO_3, RH, and T are the same in the two cases. The $PM_{2.5}$ data for the last week during CalNex study are shown above. ODR fits are applied.

An analytical calculation of HNO_3-NO_3^- partitioning can also be used to assess if one pH unit shift caused by Na^+, Cl^-, K^+ is consistent with observed nitric acid partitioning for $PM_{2.5}$. The analytical calculation is based on Equation 3 in *Guo et al.* [2016] and a detailed equation derivation can be found in the supporting materials C.2. To minimize the effects of T and W_i variability on partitioning, and focus on the role of pH, data for a relatively small T (17-23°C) and W_i (5-15 μg m^{-3}) range were selected. Predicted activity coefficients, γ_{H^+} and $\gamma_{NO_3^-}$, extracted from ISORROPIA-II, were input in the analytical calculation to account for solution non-ideality. The product of the activity coefficients, $\gamma_{H^+}\gamma_{NO_3^-}$, was on average 0.28 with Na^+, Cl^-, K^+ in the model and 0.19 without Na^+, Cl^-, K^+ ($\gamma_{H^+}\gamma_{NO_3^-}$ is smaller without Na^+, Cl^-, K^+ due to less predicted W_i, thus overall larger ionic strength). The analytical calculated S curves are plotted with the measurements and ISORROPIA-II predictions in Figure 4-5. As noted, including these components changes the activity coefficient $\gamma_{H^+}\gamma_{NO_3^-}$ (as can be seen by the difference in the two curves in Figure 4-5) and also slightly increases the liquid water. But the most important effect is reducing H^+, resulting in a shift to higher pH. This analysis also shows that the measured $\varepsilon(NO_3^-)$ comes into better agreement with its theoretical S curve for the SO_4^{2-}-NO_3^--NH_4^+-Na^+-Cl^--K^+-HNO_3-NH_3-HCl system (red points closer to red curve compared to blue points and blue curve). Similar to $\varepsilon(NO_3^-)$, measured $\varepsilon(Cl^-)$ is also found to be in good agreement with S curve (Figure C-2).

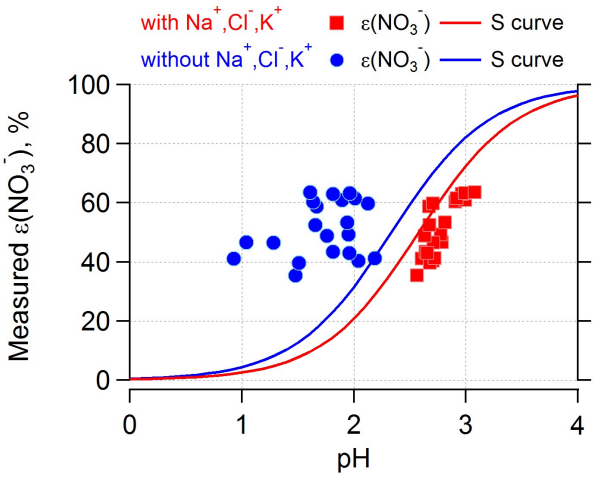

Figure 4-5 Comparison of measured $\varepsilon(NO_3^-)$ for $PM_{2.5}$ (data points) to S curves, which are predicted from theory and include activity coefficients from ISORROPIA-II. The product of the activity coefficients, $\gamma_{H^+}\gamma_{NO_3^-}$, was on average 0.28 with Na^+, Cl^-, K^+ and 0.19 without Na^+, Cl^-, K^+. In both cases pH (data points) is predicted by ISORROPIA-II.

4.4.4 Average diurnal trends

PM₁: The diurnal variations of T, RH, pH, LWC, HNO_3-NO_3^- and NH_3-NH_4^+ partitioning are shown together in Figure 4-6. Due to the inverse variation between T and RH diurnal patterns, predicted particle water (W_i) reached a daily maximum before dawn and decreased rapidly with RH after sunrise. To be consistent with pH, particle water data is not plotted for RH above 95%. (For RH above 95%, particle water increased continuously at night until reaching the daily highest RH at 5:30). Between 13:00 and 20:00 local time, W_i stayed consistently low (~ 5 μgm^{-3}). PM_1 pH generally tracked liquid water. pH was lower in the daytime due to less liquid water, reaching a minimum value of 1.6 at approximately 16:00. After that, pH continued to increase to its daily maximum of 2.4 at midnight, tracking the liquid water concentrations. This pH diurnal pattern is similar to that

observed in the southeastern U.S. [*Guo et al.*, 2015]. A very large peak in gaseous HNO_3 was observed during the day produced from rapid photochemical reactions of NO_x with the hydroxyl radical in the LA outflows [*Veres et al.*, 2011]. In contrast, NO_3^- peaked at dawn under conditions of low T and high RH, which favored nitrate condensation (S curves shifted to lower pH, see Figure C-3 and Figure C-4), consistent with a previous study in Mexico City [*Hennigan et al.*, 2008b]. There was also a small peak in NO_3^- near midday when HNO_3 peaked, simply due to the large amount of fresh HNO_3, despite the trend of a continuous $\varepsilon(NO_3^-)$ decrease. The diurnal variation of $\varepsilon(NO_3^-)$ was similar to liquid water and pH. The PM_1 NH_4^+ trend followed NO_3^- and all inorganic species (NH_4^+, SO_4^{2-}, NO_3^-), and exhibited a minor peak during the day. $\varepsilon(NH_4^+)$ had a similar diurnal pattern as $\varepsilon(NO_3^-)$.

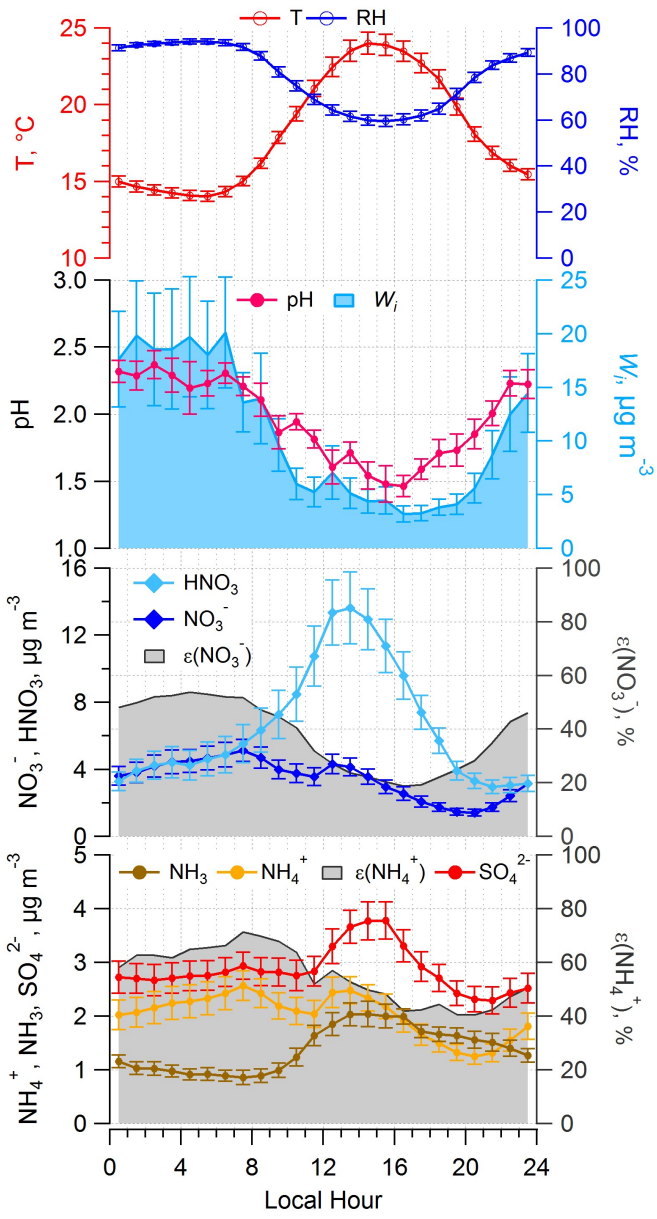

Figure 4-6 Diurnal profiles of predicted pH, LWC and measured T, RH, particle and gas phase inorganic compound mass loadings (SO_4^{2-}, NO_3^-, NH_4^+, HNO_3, NH_3), and particle phase fractions ($\varepsilon(NO_3^-)$, $\varepsilon(NH_4^+)$). Data shown above are for the complete CalNex campaign, and particle phase data are AMS PM_1. Mean hourly averages are shown and standard errors are plotted as error bars.

$PM_{2.5}$: Figure 4-7 compares the diurnal trends of PM_1 pH (AMS data, SO_4^{2-}, NO_3^-, NH_4^+) and $PM_{2.5}$ pH (PILS-IC SO_4^{2-}, NO_3^-, NH_4^+, Na^+, Cl^-, K^+) for the last week of the study. PM_1 pH had a similar profile to that for the complete study; lower in the afternoon and followed the W_i trend, whereas the $PM_{2.5}$ diurnal pH trend was nearly flat. The difference was caused by more nonvolatile Na^+ than volatile Cl^- ($PM_{2.5}$ Cl^-/Na^+ molar ratio was 0.5 ± 0.2), which is related to the HNO_3 and HCl trends. Sea-salt components in the 1 to 2.5 μm size range react with the daytime high HNO_3 forming NO_3^- and gas phase HCl (simplified as $Cl^- + HNO_3 \rightarrow NO_3^- + HCl$) [*Robbins et al.*, 1959; *Langer et al.*, 1997]. This "chloride depletion" is a result of the higher volatility of HCl versus HNO_3 in the deliquesced sea-salt aerosol [*Nenes et al.*, 1998; *Fountoukis and Nenes*, 2007]. The process can partly account for the large HCl peak and stronger Cl^- depletion (wider gap between Na^+ and Cl^-) during the day, coinciding with high HNO_3 and low W_i (evaporation of HCl occurs during evaporation of droplets). The slightly higher Na^+ generally increased pH due to the added nonvolatile cations. These data are consistent with the discussion above indicating that bulk $PM_{2.5}$ pH is higher due to the contributions of sea-salt aerosol components solely in the 1 to 2.5 μm range. For smaller particles (PM_1), these components don't significantly affect the SO_4^{2-}-NO_3^--NH_4^+-HNO_3-NH_3 system resulting in a lower bulk PM_1 pH. Size resolved particle pH and solubility of metals, reported in another study, are consistent with these findings [*Fang et al.*, 2017]. (Note, an attempt to calculate pH in the PM_1 to $PM_{2.5}$ size range was not successful due to highly scatter data resulting from particle concentrations determined by difference from two separate measurements).

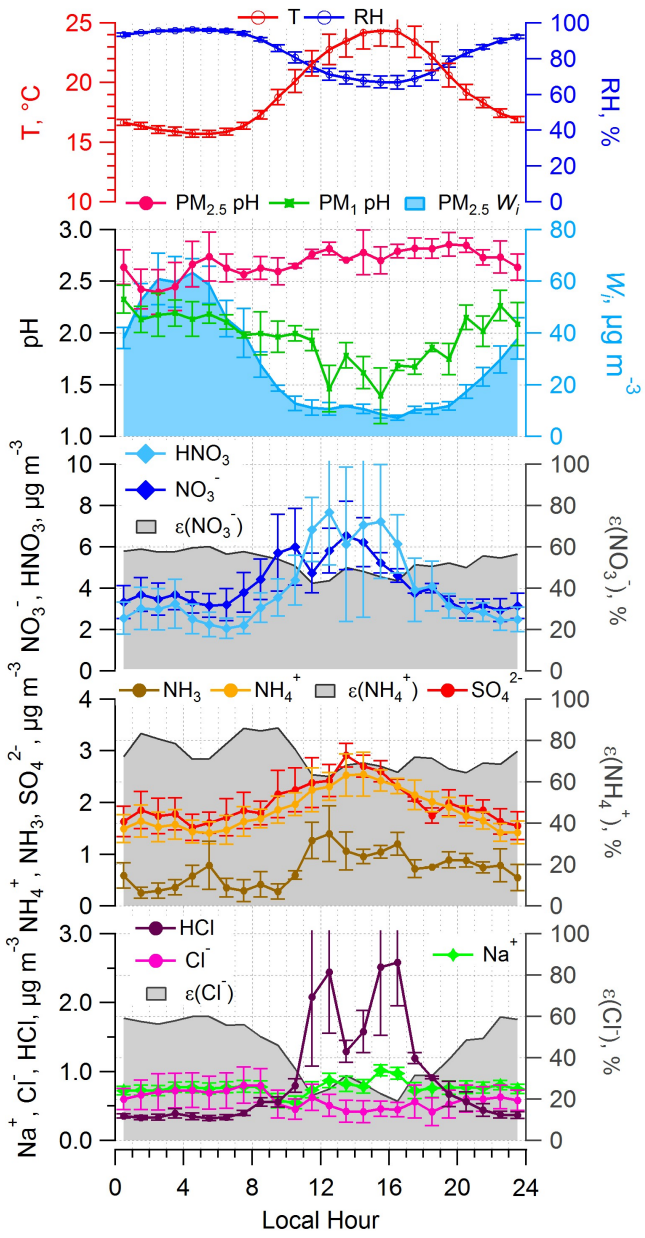

Figure 4-7 Diurnal profiles for the last week of CalNex of predicted pH and LWC, and measured T, RH, particle and gas phase inorganic compound mass loadings (SO_4^{2-}, NO_3^-, Cl^-, NH_4^+; HNO_3, NH_3, HCl), particle phase fractions ($\varepsilon(NO_3^-)$, $\varepsilon(NH_4^+)$, $\varepsilon(Cl^-)$). Particle phase data are all PILS-IC $PM_{2.5}$. Median hourly averages are shown, and standard errors are plotted as error bars.

4.5 Discussion

4.5.1 Cause for bias in $\varepsilon(NO_3^-)$

The bias between ISORROPIA-predicted and observed nitrate partitioning may be a result of several causes. Since the $\varepsilon(NO_3^-)$ bias is seen for both PM_1 (AMS-data) and $PM_{2.5}$ (PILS-IC data), the cause is apparently not associated with a specific aerosol measurement method. For the aerosol measurements, sampling artifacts associated with differences in indoor-outdoor temperatures that varied with time of day could be one cause for the biases. Sample heating is most likely to occur at night (indoor T > ambient T) and can cause semivolatile NO_3^- loss, whereas sample cooling during the day (indoor T < ambient T) can lead to vapor condensation and higher NO_3^-. Differences in observed versus predicted NO_3^- are consistent with these trends (Figure C-5); measured NO_3^- is lower than predicted at night (negative artifact) and higher than predicted during the day (positive artifact). The same will apply to NH_3-NH_4^+ partitioning, but to a lesser degree due to the addition of nonvolatile sulfate. Indoor temperatures were recorded to be fairly constant at ~25°C for the AMS trailer (Figure C-6, PILS trailer indoor temperatures are expected to be similar). Aerosol samples were heated by ~10°C at night and negligibly during the middle of the day (Table C-1). Possible biases due to effects of the altered RH and T on aerosol measurements were examined by comparing measurements to model results for partitioning of HNO_3-NO_3^-, NH_3-NH_4^+ using sample line versus ambient conditions (Figure C-7 and Figure C-8), with all other model inputs the same. We find that ambient RH and T result in better agreement for NO_3^-, $\varepsilon(NO_3^-)$, NH_4^+, $\varepsilon(NH_4^+)$, although some minor effect may be possible. We note that more extreme ambient to sample line temperature differences were experienced during the WINTER aircraft campaign (ΔT on

average +24°C). In that case, a similar analysis also found no evidence for nitrate loss due to sample line heating [*Guo et al.*, 2016]. (Sample line residence times of 0.5 to 2 seconds are in a same range for both studies).

The sampling systems for HNO_3 and NH_3 involved heated sample inlets, which could also lead to bias due to evaporation of aerosol components. Here we only focus on the CIMS sampling line heating (75°C) since it was more extreme than the NH_3 (40°C). For the CIMS system, a 75°C inlet may cause particle nitrate and chloride evaporation, resulting in over-measurement of HNO_3 and HCl (the species measured by this instrument). To examine whether this is the cause for the differences in predicted and observed $\varepsilon(NO_3^-)$, we compared the partitioning of HNO_3-NO_3^-, NH_3-NH_4^+ based on "corrected" HNO_3 assuming 10%, 20% and 30% of the measured NO_3^- evaporated in the CIMS inlet (the "corrected" HNO_3 is lower by subtracting the various fractions of PM_1 NO_3^- from measured HNO_3). Comparing the orthogonal regression fitting lines in the Fig. S8, only slight improvements in predicted to measured $\varepsilon(NO_3^-)$ are found for increased NO_3^- loss (Fig. S8c), but all lines converge at the same intercept. At 30% evaporation, the comparison becomes worse for both $\varepsilon(NO_3^-)$ and $\varepsilon(NH_4^+)$. We conclude that potential inlet artifacts associated with the aerosol or gas phase sampling systems cannot explain the predicted versus measured $\varepsilon(NO_3^-)$ bias.

Another possible cause of the $\varepsilon(NO_3^-)$ bias is the effect of a large sea-salt coarse mode on fine mode semivolatile species. For example, during nighttime when HNO_3 concentrations are much lower relative to daytime, ISORROPIA-II may have overestimated NO_3^- due to ignoring the presence of a larger more neutral coarse mode when calculating fine mode

aerosol concentrations assuming equilibrium. Various studies show the typical time for the fine mode to reach thermodynamic equilibrium is on the order of 20 minutes [*Dassios and Pandis*, 1999; *Fountoukis et al.*, 2009], whereas time scales for the coarse mode to equilibrate are much larger. The mixing of fine particles with high concentrations of coarse mode, mainly sea-salt, particles could disrupt fine mode equilibrium by the mass transfer of volatile fine mode NO_3^-, via HNO_3, to the coarse mode, forming nonvolatile salts, such as $NaNO_3$. This mechanism is consistent with the presence of high levels of sea-salt in the LA region and the anti-correlation of a NO_3^- prediction bias with HNO_3 concentration (Figure C-5). During the daytime, when HNO_3 concentrations are high, this bias would be minimal, but at night when HNO_3 concentrations are low, the model, which ignores the presence of the coarse mode, would overpredict NO_3^- concentrations, by not considering fine mode nitrate loss to the coarse mode. Again, partitioning of NH_3-NH_4^+ would not be affected as much by this process since some fraction of the NH_4^+ would be associated with SO_4^{2-}. Of the various locations where we have investigated pH, this study has the highest coarse mode inorganic aerosol concentrations and is the only one where we have observed this bias [*Guo et al.*, 2016].

4.5.2 Why is nitrate much higher in LA compared to other regions investigated?

A comparison of pH and related statistics in five field studies is summarized in Table 4-2. The campaigns are CalNex, SOAS, SENEX, and WINTER, all conducted in the continental US. Also included are results from a study in the eastern Mediterranean (the campaign acronyms are given in Table 4-2). The SOAS (ground-based) and SENEX (aircraft-based) studies provide an interesting contrast with CalNex; that is between the

southeastern versus southwestern U.S. in summertime. WINTER aircraft data adds the dimension of seasonal variation (summer versus winter). The eastern Mediterranean data provides a remote European (Crete) and urban (Athens) perspective, and a case where air masses were known to be impacted by biomass burning (BB). All pH in Table 4-2 were calculated by ISORROPIA-II in forward metastable mode, but only the US data (SOAS, WINTER, CalNex) used gas-particle phase partitioning to constrain and verify the pH prediction for all the data analyzed. Lack of NH_3 or HNO_3 data for the eastern Mediterranean means that pH was likely underestimated by ~0.5 units [*Bougiatioti et al.*, 2016]. This was verified with a limited set of data when both aerosol and gas-phase data was available. It is noteworthy that in all studies, pH was low and on average below 3. The eastern U.S. regions are characterized with the lowest pH (~1) throughout the year, from ground level up to 5 km aloft [*Guo et al.*, 2015; *Guo et al.*, 2016; *Xu et al.*, 2016]. The highest pH of 2.8 ± 0.6 was consistently observed in biomass burning impacted air masses, regardless of season in both the remote and urban eastern Mediterranean and attributed to an abundance of NH_3 and fine particle K^+ in biomass burning emissions, which raised pH and NO_3^- concentrations significantly [*Bougiatioti et al.*, 2017]. Biomass burning also accounted for the high pH, which approaches 3, in Athens during winter.

Comparing LA (CalNex) to the other summertime measurements in the eastern US (SOAS, SENEX), Table 4-2 shows that the LA ground site had uniquely higher NO_3^- and HNO_3 mass concentrations and NO_3^- was the most abundant (by mass) inorganic ion for PM_1 or $PM_{2.5}$. In contrast, in the southeastern US in summertime, SO_4^{2-} was the dominant ion, NO_3^- was only 5-14% of the SO_4^{2-} mass. The higher total NO_3^- (HNO_3 + NO_3^-) in LA

indicates high local NO_x relative to SO_2 sources. LA also had roughly 1 unit higher PM_1 pH, and much higher NO_3^- concentrations relative to SO_4^{2-}. Total ammonia ($NH_3 + NH_4^+$) was also higher (Table 4-2). The ratio of total NO_3^- and SO_4^{2-} (sulfate is nonvolatile so total sulfate is equivalent to sulfate) was ~ 4 for CalNex, compared to 0.3 for SOAS and 0.8 for SENEX. The higher ratio of total NO_3^- to SO_4^{2-} can explain the higher LA pH through coupling of particle composition, hygroscopicity, and acidity. Consider the situation where there is initially a high HNO_3 concentration. Some HNO_3 will condense onto very acidic particles (e.g., even at low $\varepsilon(NO_3^-)$, with very high HNO_3, some NO_3^- can form). If this this NO_3^- is significant relative to SO_4^{2-}, it substantially increases the particle W_i, which dilutes the H^+ and raises the pH, since NO_3^- has a similarly high hygroscopicity as SO_4^{2-} [*Nenes et al.*, 1998]. Higher pH leads to more NO_3^- formed. This positive feedback, which reaches equilibrium at some point, and along with the condition of higher abundance of NH_3 compared to the southeast (Table 4-2), may explain the higher NO_3^- and one unit higher pH in LA. This feedback process only happens for semivolatile highly hygroscopic species. Sulfate will not have this effect since it is nonvolatile. It also can only happen when the semivolatile species contributes a large fraction to the particle W_i, hence high total NO_3^- to SO_4^{2-} ratios, which is why the effect is not seen in the eastern US in summertime.

Table 4-2 Comparisons between different studies for particle pH, major inorganic ions and gases and meteorological conditions. All pH values are from ISORROPIA-II run in forward mode. The campaign acronyms other than CalNex stand for Southern Oxidant and Aerosol Study (SOAS), Southeastern Nexus of Air Quality and Climate (SENEX), Wintertime Investigation of Transport, Emissions, and Reactivity (WINTER).

Campaign	CalNex		SOAS	SENEX[c]	WINTER	Studies in the eastern Mediterranean		
Type	Ground	Ground	Ground	Aircraft	Aircraft	Ground	Ground	(BB plumes)[f]
PM cut size	PM_1	$PM_{2.5}$[a]	PM_1&$PM_{2.5}$[b]	PM_1	PM_1	PM_1	PM_1	PM_1
Year	2010		2013	2013	2015	2012	2013-2014	2012-2014
Season	(Early) Summer		Summer	Summer	Winter	Summer-Autumn	Winter	Summer-Winter
Region/Location	SW US		SE US	SE US	NE US	Crete, Greece	Athens, Greece	Crete&Athens
SO_4^{2-}, μg m^{-3}	2.86 ± 1.70	1.88 ± 0.69	1.73 ± 1.21	2.05 ± 0.80	1.02 ± 0.77	2.31 ± 1.61	2.31 ± 1.32	1.66 ± 1.49
NO_3^-, μg m^{-3}	3.58 ± 3.65	3.74 ± 1.53	0.08 ± 0.08	0.28 ± 0.09	0.80 ± 1.03	0.12 ± 0.07	2.21 ± 2.02	1.79 ± 1.49
HNO_3, μg m^{-3}	6.65 ± 7.03	4.45 ± 3.59	0.36 ± 0.14	1.35 ± 0.66	1.41 ± 1.83	\	\	0.91 ± 0.39
ε(NO_3^-)	39 ± 16%	51 ± 18%	22 ± 16%	18 ± 6%	37 ± 28%	< 20%[e]	\	65 ± 14%
Total NO_3^-, μg m^{-3}	10.22 ± 9.74	8.19 ± 3.89	0.45 ± 0.26	1.63 ± 0.70	2.21 ± 2.21	\	\	3.36 ± 2.08
NH_4^+, μg m^{-3}	2.06 ± 1.67	1.79 ± 0.65	0.46 ± 0.34	1.06 ± 0.25	0.50 ± 0.43	0.81 ± 0.58	1.96 ± 1.30	1.02 ± 0.93
NH_3, μg m^{-3}	1.37 ± 0.90	0.75 ± 0.61	0.39 ± 0.25	0.12 ± 0.19	\	\	\	\
ε(NH_4^+)	55 ± 25%	71 ± 19%	50 ± 25%	92 ± 11%	\	\	\	\
Total NH_4^+, μg m^{-3}	3.44 ± 1.81	2.54 ± 0.89	0.78 ± 0.50	1.17 ± 0.81	\	\	\	\
Na^+, μg m^{-3}	\	0.77 ± 0.39	0.03 ± 0.07	\	0.23 ± 0.46[d]	0.19 ± 0.43	0.13 ± 0.11	0.08 ± 0.05
Cl^-, μg m^{-3}	\	0.64 ± 0.48	0.02 ± 0.03	\	0.34 ± 0.38[d]	0.22 ± 0.53	0.14 ± 0.19	0.20 ± 0.19
RH, %	79 ± 17	87 ± 9	74 ± 16	72 ± 9	58 ± 19	57 ± 11	80 ± 9	68 ± 16
T, °C	18 ± 4	18 ± 3	25 ± 3	22 ± 3	0 ± 8	27 ± 3	12 ± 3	20 ± 9
pH	**1.9 ± 0.5**	**2.7 ± 0.3**	**0.9 ± 0.6**	**1.1 ± 0.4**	**0.8 ± 1.0**	**1.3 ± 1.1**	**2.4 ± 0.8**	**2.8 ± 0.6**
Reference	This study		[*Guo et al.*, 2015]	[*Xu et al.*, 2016]	[*Guo et al.*, 2016]	[*Bougiatioti et al.*, 2016]	[*Bougiatioti et al.*, 2017]	[*Bougiatioti et al.*, 2016, 2017]

[a] Only the last week of CalNex; [b] $PM_{2.5}$ was sampled in the 1st half and PM_1 sampled in the 2nd half of the study; various parameters were similar in both cases, crustal components were higher, but overall generally low so differences had minor effects, e.g., $PM_{2.5}$ Na^+ was 0.06 ± 0.09 and PM_1 Na^+ was 0.01 ± 0.01 μg m^{-3}; [c] Only one flight (June 16 2013) statistic from the reference is shown; [d] Externally mixed, thus not included in pH calculation; [e] Estimated from offline measurement; [f] Averaged from identified biomass burning (BB) plumes from Crete and Athens studies due to the similar pH; K^+ was 0.36 ± 0.38 μg m^{-3};

To better understand the relationship between NO_3^-, pH and T across different campaigns, S curves calculated from solubility and dissociation of a species in water, with activity coefficients included, provide a useful conceptual means for comparing pH predictions from the thermodynamic model to measurements of semivolatile species partitioning between gas-particle phases (see Figure 4-5). The inter-comparison between the various campaigns is shown in Figure 4-8. For each campaign, data are selected within a narrow range (see Figure 4-8 caption) to limit the effects of W_i and T variations on gas-particle partitioning. (CalNex $PM_{2.5}$ pH is not included in Figure 4-8 due to very limited points since CalNex $PM_{2.5}$ W_i was much higher due to high inorganic mass loadings and an average RH of 87%). S curves are calculated based on a W_i of 2.5 μgm^{-3} and T of 0 and 20 °C for wintertime or summertime conditions, respectively. ISORROPIA-II predicted activity coefficients, $\gamma_{H^+}\gamma_{NO_3^-}$, is included to account for aqueous solution non-ideality.

Consider the nitrate partitioning case, $\varepsilon(NO_3^-)$, comparing SOAS to WINTER (Figure 4-8a versus b). Although the data pH ranges are similar in these studies (on average ~ 1), there is higher $\varepsilon(NO_3^-)$ in winter (T = 0 °C) due to the S curve shifting to lower pH (~1 unit) relative to summer (T = 20 °C), illustrating the effect of T (which is mainly through HNO_3 Henry's law constant sensitivity to T). Considering only Figure 4-8b; as noted above, the temperature ranges were more similar for the SOAS, SENEX and Calnex studies, yet CalNex had higher particle pH (PM_1) and more nitrate compared to SOAS and SENEX due to higher total NO_3 relative to SO_4^{2-}, which leads to more nitrate formation through

feed backs involving particle water and pH, as discussed above. This can also be seen in Figure 4-8b.

$\varepsilon(NH_4^+)$ S curves and data from the field studies are shown in Figure 4-8c and d. Note that the $\varepsilon(NO_3^-)$ and $\varepsilon(NH_4^+)$ face opposite directions since acid versus base. NH_3 data was not available during WINTER so no measured $\varepsilon(NH_4^+)$ points were plotted at 0°C and no comparisons as a function of T can be made. At 20°C, the $\varepsilon(NH_4^+)$ of CalNex, SOAS, and SENEX all converge around one S curve, which was calculated assuming $\gamma_{H^+}\gamma_{NH_4^+} = 1$. The lower pH of SOAS and SENEX relative to CalNex resulted in generally higher $\varepsilon(NH_4^+)$, more ammonia partitioned to the particle phase. The data and predicted $\varepsilon(NH_4^+)$ are in fairly good agreement.

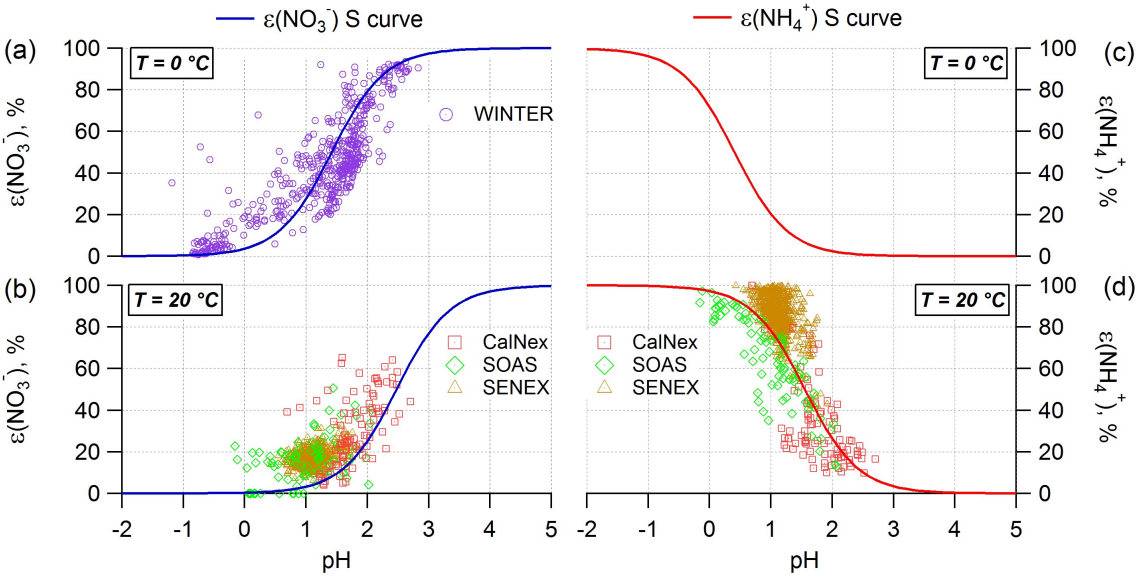

Figure 4-8 Analytically calculated S-curves of $\varepsilon(NO_3^-)$ and $\varepsilon(NH_4^+)$ and ambient data, plotted with ISORROPIA-predicted pH for CalNex, SOAS, SENEX, and WINTER studies. $\varepsilon(NO_3^-)$ and $\varepsilon(NH_4^+)$ are the fraction of the total (gas+particle) in the particle phase. For the data, a narrow range in W_i (1-4 μg m^{-3}) and T (-5 < T < 5 °C for T = 0 °C, 15 < T < 25 °C for T = 20 °C) data were selected to be close to the analytical calculation input

(i.e., W_i = 2.5 μg m^{-3} and various T). For analytical calculations (S curves), $\gamma_{H^+}\gamma_{NH_4^+}$ = 1 was applied; ISORROPIA-II predicted $\gamma_{H^+}\gamma_{NO_3^-}$ 0.06 (WINTER) and 0.084 (CalNex 0.084, SOAS 0.078, SENEX 0.068) were used.

S curves have significant utility for understanding how T, RH, and pH affect partitioning (e.g., see Figure C-3 & Figure C-4), but we also note that they can be used to estimate activity coefficients based on partitioning data, which may be particularly useful in situations where the data is not available from literature (e.g., organic acids above a mixture of inorganic and organics).

4.6 Conclusions

pH of PM_1 and $PM_{2.5}$, and the semivolatile gas-particle partitioning of HNO_3-NO_3^-, NH_3-NH_4^+ and HCl-Cl^- in the Los Angeles basin during the 2010 CalNex study were investigated. As a coastal urban site impacted by high sea-salt aerosol components, and high total nitrate (HNO_3 + NO_3^-), and ammonia levels, this study provided a contrast to pH we have reported in the eastern US and eastern Mediterranean.

PM_1 single particle analysis showed that 73% (by number) of PM_1 sea-salt particles did not contain nitrate and sea-salt type particles only contributed to 12% to PM_1 mass. Therefore, PM_1 pH was predicted solely on the SO_4^{2-}-NO_3^--NH_4^+-HNO_3-NH_3 system (ISORROPIA-II inputs). This approach provided good agreement between observed and model-predicted partitioning of NH_3-NH_4^+ and HNO_3-NO_3^-, although a bias in ε(NO_3^-) was observed that depended on RH (day vs. night). Altering gas and particle temperatures from ambient due to the sampling configurations did not explain the bias. A likely cause is the

loss of fine mode NO_3^- to coarse mode sea-salt, mainly at night when HNO_3 concentrations are low, which is not considered by the thermodynamic model used to predict fine mode concentrations.

The study mean (± SD) PM_1 pH in the LA basin was 1.9 ± 0.5, roughly one unit higher than the average pH observed in summer in the southeastern US (0.9 ± 0.6 and 1.1 ± 0.4), despite similar RH and T ranges and both calculated for the SO_4^{2-}-NO_3^--NH_4^+-HNO_3-NH_3 system. The cause may be much higher total nitrate concentrations (high NOx and proximity to locations of HNO_3 formation) relative to sulfate in LA. For example, high levels of HNO_3 can lead to at least some particulate NO_3^-, even if conditions are such that NO_3^- partitioning is low (e.g., $\varepsilon(NO_3^-)$ is small). NO_3^- increase the particle water, which raises pH by dilution of H^+, allowing more partitioning (i.e., increases $\varepsilon(NO_3^-)$). When nonvolatile sulfate dominates over total nitrate, sulfate controls liquid water and this effect is not observed. The complex interactions between pH, LWC, T, and NO_3^- are clearly illustrated by analytical (S curve) analyses.

Single particle analysis showed that 85% by number of sea-salt particles in the 1 to 2.5 µm nominal range contained nitrate and that the model predicted partitioning of HNO_3-NO_3^- for $PM_{2.5}$ agreed better with the observed partitioning when sea-salt components were included (SO_4^{2-}-NO_3^--NH_4^+-Na^+-Cl^--K^+-HNO_3-NH_3-HCl system). Bulk $PM_{2.5}$ pH was 2.7 ± 0.3, whereas for the same time period PM_1 pH was 1.9 ± 0.4 and the diurnal pH profiles of PM_1 and $PM_{2.5}$ also differed, all apparently due to the influence of sea-salt aerosols.

The CalNex data provides unique contrast to pH reported in other regions and demonstrates the complex interactions between pH and emissions. It also supports the general application of SO_4^{2-}-NO_3^--NH_4^+-HNO_3-NH_3 system for predictions of PM_1 pH and gas-particle phase partitioning without considering sea-salts or crustal elements, useful for regional or global modeling. It further illustrates that fine particles have surprisingly low pH in many locations, which has significant effects on the many environmental impacts of fine particles.

CHAPTER 5. HIGH AEROSOL ACIDITY DESPITE DECLINING ATMOSPHERIC SULFATE CONCENTRATIONS OVER THE PAST 15 YEARS

5.1 Abstract

Particle acidity affects aerosol concentrations, chemical composition and toxicity. Sulfate is often the main acid component of aerosols, and largely determines the acidity of fine particles under 2.5 μm in diameter, $PM_{2.5}$. Over the last 15 years, atmospheric sulfate concentrations in the southeastern United States have decreased by 70%, whereas ammonia concentrations have been steady. Similar trends are occurring in many regions globally. Aerosols have been assumed to have increasing concentrations of ammonium nitrate compensating for decreasing sulfate, a result of anticipated increasing neutrality. Here we use a comprehensive set of observations collected at a rural southeastern U.S. site in June and July, 2013 and a thermodynamic model that predicts pH and the gas-particle equilibrium concentrations of inorganic species from observed gas and aerosol composition, humidity and temperature, to show that $PM_{2.5}$ at the site is acidic. Moreover, pH buffering by partitioning of ammonia between the gas and particle phases has resulted in a relatively constant particle pH of 0-2 throughout the 15 years of decreasing atmospheric sulfate concentrations, and little change in particle ammonium nitrate concentrations. We conclude that the reductions in aerosol acidity widely anticipated from sulfur reductions, and potential benefits for human health and climate, are unlikely to occur until atmospheric sulfate concentrations drop to near pre-anthropogenic levels.

5.2 Introduction

Trends of decreasing sulfur dioxide (SO_2) and sulfate aerosol have been observed throughout the U.S. [*Hand et al.*, 2012a] and are largely attributable to emission reductions from coal-fired electrical generating units through scrubbing and fuel switching. These trends are expected to endure as additional controls on SO_2 are put in place to continue the decline of $PM_{2.5}$ mass. In contrast, the source of the main fine particle acid-neutralizing agent, gas phase ammonia (NH_3), is largely linked to agricultural activities, which have been relatively steady and are expected to remain so. These trends have led to a long-standing and continuing belief that the aerosol will become increasingly neutral, shifting inorganic aerosol composition from ammonium sulfate to ammonium nitrate and minimizing the effectiveness of SO_2 reductions on $PM_{2.5}$ mass control [*West et al.*, 1999; *Pinder et al.*, 2007; *Tsimpidi et al.*, 2007; *Pinder et al.*, 2008; *Heald et al.*, 2012]. This postulation has wide-ranging ramifications, from changing the emphases on what emission sources to control (e.g., agricultural) to protect human health [*Lelieveld et al.*, 2015] to effects on aerosol radiative forcing [*Bellouin et al.*, 2011]. Other environmental impacts linked to particle pH are also expected to change. For example, lower pH more effectively converts ubiquitous isoprene emissions by forested regions to $PM_{2.5}$ through heterogeneous acid-catalyzed reactions [*Xu et al.*, 2015a]. Low pH increases solubility of metals associated with mineral dust and anthropogenic sources, which can be either ecosystem nutrients [*Meskhidze et al.*, 2003], or have detrimental health impacts through *in vivo* generation of reactive oxygen species [*Ghio et al.*, 2012; *Fang et al.*, 2017]. Particle strong

acidity has also been directly linked to adverse respiratory effects [*Thurston et al.*, 1994; *Raizenne et al.*, 1996].

Despite large investments in sulfur emission reductions, we show that the acidic/alkaline gas-particle system in the southeastern U.S. is buffered by the partitioning of semivolatile NH_3, making it insensitive to changing SO_2 levels. Counter to expectations, acidic pH effects on air quality will therefore remain largely unchanged. Although our analysis focuses on the southeastern U.S., it serves as a model, demonstrating the need for detailed thermodynamic analyses at locations globally to accurately evaluate the effects of sulfate reductions on particle acidity and aerosol composition.

To assess if decreasing sulfate leads to substantial changes in aerosol pH, we investigate the sensitivity of pH in the southeastern U.S. to changes in sulfate (SO_4^{2-}) and gas phase ammonia (NH_3) levels, focusing on summertime data from a rural Southeastern background site, Centreville (CTR). The historical breadth of data collected at CTR, and the detailed observations of key aerosol and gas phase species measured during a recent intensive study at the site (SOAS), make it ideal for a thermodynamic analysis to predict and evaluate pH at high temporal resolution and for comparisons to historical trends.

A detailed pH calculation that involves both gas and aerosol composition data was performed using average conditions from a subset of the CTR SOAS experiment (June 11 to June 23 2013). This time period was selected because it excludes periodic precipitation and dust events, providing representative conditions consistent with the mean summertime aerosol state in the region. ISORROPIA-II predicted NH_3 agreed with independently

measured concentrations (Figure 5-1), demonstrating that the thermodynamic analysis accurately represents the aerosol state, as deviations in predicted pH would lead to large biases in predicted NH_3.

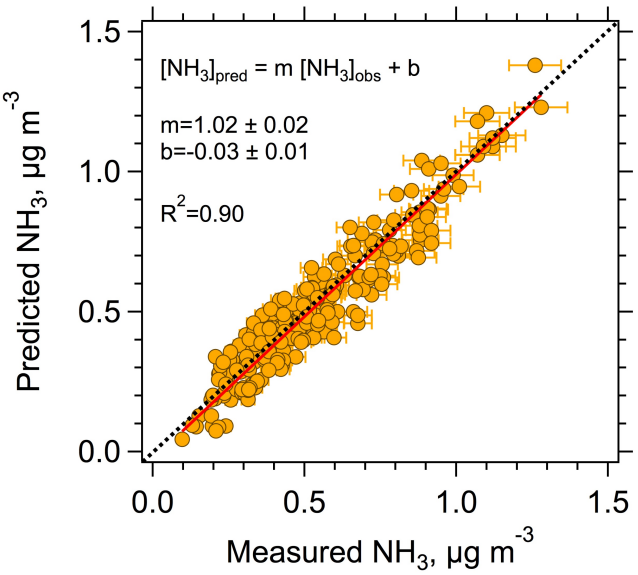

Figure 5-1 Evaluation of the thermodyamic model. Comparison of measured NH_3 to ISORROPIA-II predicted concentrations. Data are from SOAS (i.e., SEARCH CTR site) for measurements between June 11 and June 23 2013. NH_3 was measured via a Chemical Ionization Mass Spectrometer (CIMS) [*You et al.*, 2014a]. Orthogonal regression and the uncertainty in the measured NH_3 1hr-avg data (10%) are shown. Fit parameter uncertainties are for 95% confidence intervals. The good agreement validates the model predictions of pH.

Measurements at various SEARCH air quality monitoring network sites throughout the Southeast show that annual mean SO_4^{2-} concentrations have dropped substantially from 1999 to 2014, with concentrations going from roughly 6 to 2 µg m^{-3} [*Hidy et al.*, 2014]. Historical NH_3 concentrations are not as well known, however, data from SEARCH sites [*Saylor et al.*, 2015] and the Ammonia Monitoring Network (AMoN)

(http://nadp.sws.uiuc.edu/amon/) show steady overall concentrations going back to 2004. Between 2008 and 2014, CTR mean summer concentration was 0.23 μg m^{-3}, similar to measurements at CTR during SOAS (mean: 0.36 μg m^{-3}) [*You et al.*, 2014a]. Ammonia at other sites in the Southeast generally ranged between 0.1 and 2 μg m^{-3}, with highest levels observed at sites more influenced by agricultural activities (e.g., at Yorkville, a rural SEARCH site, mean NH_3 is 1.74 μg m^{-3}). A mass balance analysis indicates that NH_3 concentrations are directly driven by NH_3 emission rates (see Methods). Given this, and that emissions are relatively steady [*Xing et al.*, 2013], NH_3 concentrations have likely been at similar levels even further into the past.

5.3 Methods

The Site: Centerville is part of the SEARCH (Southeastern Aerosol Research and Characterization) air-quality monitoring network [*Saylor et al.*, 2015]) and is located in rural Alabama (CTR; 32.90289 N, 87.24968 W; altitude: 126 m, Brent, Alabama). It was also the location of the intensive multi-investigator Southern Oxidant Aerosol Study (SOAS, June 1 to July 15, 2013). We have reported on a detailed analysis of pH as part of SOAS and have shown that pH throughout the southeast is fairly uniform [*Guo et al.*, 2015], similar to levels at CTR. More information on the site, instrumentation, thermodynamic calculations, including an uncertainty analysis, can be found in [*Guo et al.*, 2015].

Thermodynamic Model: Direct and accurate measurement of particle pH of the atmospheric aerosol is not currently possible. Measurements of semivolatile partitioning

of key inorganic species (such as NH_3/NH_4^+, HNO_3/NO_3^-) coupled with thermodynamic models are the best approaches for predicting particle pH with a high degree of accuracy [*Hennigan et al.*, 2015]. For this study we use ISORROPIA-II [*Nenes et al.*, 1998; *Fountoukis and Nenes*, 2007], which computes the equilibrium composition of an NH_4^+-SO_4^{2-}-NO_3^--Cl^--Na^+-Ca^{2+}-K^+-Mg^{2+}-water inorganic aerosol. Proxies for pH, such as ammonium-sulfate molar ratios, NH_4^+/SO_4^{2-} (referred to *R* hereafter), have been used in the past. Although the molar ratio is commonly used as a measure of aerosol acidity, it is not uniquely related to pH, which is the parameter that truly describes acidity and its impacts [*Hennigan et al.*, 2015]. Here we more narrowly define the ammonium-sulfate molar ratios as ammonium minus nitrate to sulfate molar ratio; $(NH_4^+ - NO_3^-)/SO_4^{2-}$ and refer to this ratio as R_{SO4}. This is preferred to the simpler R (NH_4^+/SO_4^{2-}) as R_{SO4} excludes NH_4^+ associated with NO_3^- when calculating ratios based on bulk composition data (e.g., $PM_{2.5}$), since ammonium sulfate and ammonium nitrate are typically associated with different sized particles.

pH is defined as the hydrogen ion activity in an aqueous solution [*Stumm and Morgan*, 1996].

$$pH = -\log_{10} \gamma_{H^+} H_{aq}^+ \tag{5-1}$$

where γ_{H^+} is the hydronium ion activity coefficient (in this case assumed = 1), H_{aq}^+ (mole L^{-1}) the hydronium ion concentration in particle liquid water. ISORROPIA-II computes the particle liquid water content due to water uptake by inorganic species, phase partitioning and chemical speciation, and makes the simplifying assumption that the hydrogen ion

activity is one (γ_{H^+} = 1). Details on how the model was run (e.g., forward mode), an extensive uncertainty analyses, and predictions of pH at various sites in the southeast, are discussed in [*Guo et al.*, 2015]. In applying ISORROPIA-II, we assumed no compositional dependence on particle size, treating the measured chemical constituents as bulk $PM_{2.5}$ properties, and that the aerosol was internally mixed and always a single aqueous phase that contained the inorganic species, without phase separations that could affect pH (along with partitioning of semivolatile inorganic species). The validity of these assumptions has been evaluated. We have shown that the fine particles contain significant levels of liquid water (water mass typically ranged from 1 to 5 μg m^{-3}) [*Guo et al.*, 2015]. Existence of one organic-inorganic phase is reasonable given that the measured organic aerosol oxidation state (average O/C ratio of ~ 0.7) [*Cerully et al.*, 2015] and RH (mean ± SD of 74 ± 16%) [*Guo et al.*, 2015] for this study are typically at levels for which separate phases are not observed [*You et al.*, 2014a]. pH calculated under these assumptions (bulk properties, no phase separations, dissolved components in equilibrium with the gas phase) is supported by the ability of ISORROPIA-II to reproduce independently measured gas phase NH_3 concentrations (Figure 5-1). Furthermore, multiple studies in the past have shown the ability of ISORROPIA-II (under similar assumptions to what are used here) to reproduce the observed behavior of semivolatile inorganic aerosol in the southeast [*Zhang et al.*, 2002] and at other locations [*Fountoukis et al.*, 2009].

The approach for generating the contour plots of Figure 5-2 is as follows. Average SOAS data collected between June 11 and June 23 2013 (T = 297.9 K, RH = 73.8%, Na^+ = 0.03 μg m^{-3}, NO_3^- = 0.08 μg m^{-3}, Cl^- = 0.02 μg m^{-3}), along with a selected sulfate concentration,

are input to ISORROPIA-II. Total ammonia (gas + particle) is left as the free variable. The equilibrium concentrations of various components (e.g., gas phase NH_3, and particle phase NH_4^+, SO_4^{2-}, and NO_3^-) and particle pH (along with other variables) are predicted by ISORROPIA-II. Data for the contour plots are generated by varying sulfate from 0.1 to 10 μg m^{-3}.

Ammonia Mass Balance: Ammonia emissions can be linked to ambient concentrations through a mass balance analyses. Boundary layer ammonia levels can be estimated from emissions and losses by:

$$\frac{d[NH_3]}{dt} = E_{NH_3} - \frac{v_d^{NH_3}}{h}[NH_3] - \frac{v_d^{NH_4^+}}{h}[NH_4^+] \quad (5\text{-}2)$$

where $[NH_3]$ and $[NH_4^+]$ are the concentrations of gas ammonia and fine particle ammonium, E_{NH_3} is the gas phase NH_3 emission rate, $v_d^{NH_3}$ the gas phase deposition velocity, $v_d^{NH_4^+}$ the particle phase deposition velocity, and *h* the boundary layer mixed depth. Since average values are being considered here, we assume steady state, in which case emissions are balanced by deposition losses. It follows then that for sulfate concentrations dropping below current levels (~2 μg m^{-3}), loss of ammonia by deposition is largely controlled by gas phase losses, since $v_d^{NH_3}$ is roughly an order of magnitude larger then $v_d^{NH_4^+}$, and ambient concentrations of NH_4^+ and NH_3 comparable [*Guo et al.*, 2015]. For example, the dry deposition velocity of NH_3 is about 1-2 cm s^{-1} over forests, agricultural, or mixed-use land, and 10 times that of ammonium [*Duyzer*, 1994; *Schrader and Brummer*, 2014]. For sulfate levels below ~2 μg m^{-3} (NH_4^+ ~ 0.5 μg m^{-3}, Figure 5-1)

and NH_3 concentration of 0.1 to 1, the last term is relatively small and so ambient levels of NH_3 are largely controlled by emissions, such that: $[NH_3] \cong \frac{hE_{NH_3}}{v_d^{NH3}}$. This shows that for the past, and into the future, gas phase NH_3 concentrations are directly related to gas phase NH_3 emissions rates.

5.4 Discussion

5.4.1 Conceptual model

To test if these trends imply that the aerosol is becoming less acidic we first consider a simplified scenario of an isolated ammonium sulfate aqueous particle. At the average SOAS meteorological conditions, for this particle the equilibrium NH_3 vapor concentration is approximately 160 µg m^{-3} (220 ppbv) and pH is near 3. However, for ammonium bisulfate the equilibrium NH_3 concentration drops dramatically to approximately 0.06 µg m^{-3} (0.08 ppbv), and pH is near 0. Since typical observed NH_3 concentrations range between 0.1 to 2 µg m^{-3}, ambient NH_3 concentrations will rarely ever reach the 160 µg m^{-3} needed for equilibrium with pure ammonium sulfate, meaning that it will almost never exist. However, NH_3 will always be present in the gas phase, even at very low pH. Furthermore, the dramatic drop in equilibrium NH_3 when going from $(NH_4)_2SO_4$ to $(NH_4)HSO_4$ (160 to 0.06 µg m^{-3}) with a pH change of only 3 to 0, independent of sulfate concentrations, also demonstrates the low sensitivity of pH to NH_3 concentrations.

Now consider an ammonium sulfate solution that is aerosolized into pure air. The aerosol would reach equilibrium by some of the ammonia volatilizing, leaving an aerosol of mixed

$(NH_4)_2SO_4$-NH_4HSO_4 with a pH between 0 and 3, and some ammonia in the gas phase. If the volume of air were very large compared to the amount of ammonium sulfate originally present, the resulting aerosol would be predominantly ammonium bisulfate. (Ammonium sulfate molar ratios observed in the southeastern U.S. are in the range of 1.5 to 1.8, which is discussed more below). Although conceptually insightful, the full thermodynamic model must be run since pure aerosol species in isolation do not exist and a quantified pH is needed to assess the impacts of acidity.

5.4.2 Sensitivity analyses with a full thermodynamic model

We expand on the historical ranges of both NH_3 and SO_4^{2-} for a more comprehensive sensitivity analyses. Sulfate and total ammonia (gas + particle) were independently varied over 2 orders of magnitude and used as input to ISORROPIA-II. The resulting predicted equilibrium pH is shown in Figure 5-2. As seen above, these results indicate a very weak sensitivity of pH to a wide range of SO_4^{2-} and NH_3, suggesting that the observed decrease in SO_4^{2-} should have little influence on pH. Our predictions are consistent with the historical summertime observations at CTR. Trends in fine particle SO_4^{2-} and NH_4^+ and gas phase NH_3 are shown in Figure 5-3 and are similar to the general trends of the southeast [*Hidy et al.*, 2014; *Saylor et al.*, 2015], and likely much of the eastern US [*Hand et al.*, 2012a]. pH estimated from the CTR historical aerosol ionic composition dataset also demonstrates that summertime pH has remained remarkably constant and low (between 0 and 1) throughout the last 15 years, similar to the range of roughly 0 and 2 predicted in the sensitivity analyses.

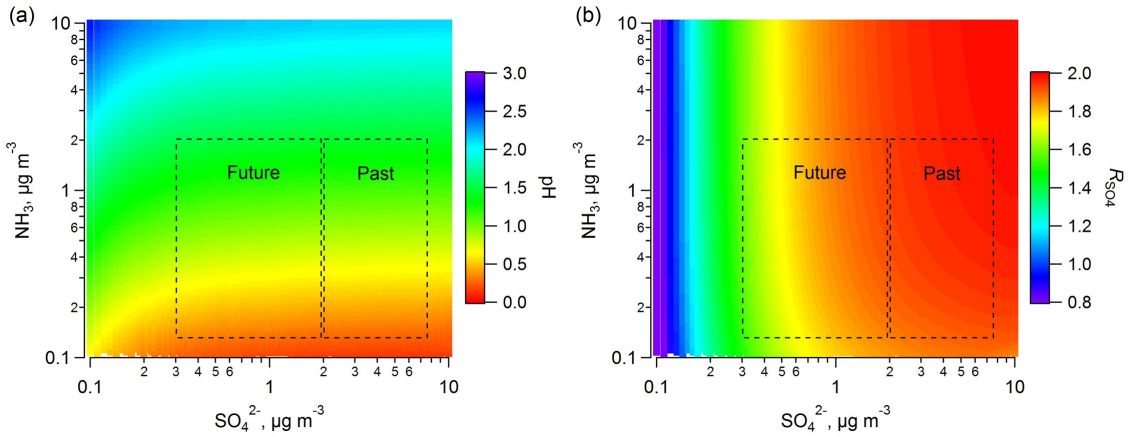

Figure 5-2 Sensitivity of $PM_{2.5}$ pH and R_{SO4} to gas phase ammonia (NH_3) and $PM_{2.5}$ sulfate (SO_4^{2-}) concentrations. R_{SO4} is $(NH_4^+ - NO_3^-)/SO_4^{2-}$ in unit of mol mol^{-1}. The results are predictions from a thermodynamic analysis assuming equilibrium between the gas and particle phases for typical summer conditions in the southeastern US. Boxes define estimated concentration ranges over the previous 15 years and ranges expected in the future.

A further assessment of the thermodynamics can be gained from ammonium-sulfate molar ratios, R_{SO4}. [*Hidy et al.*, 2014] reports R_{SO4} has ranged roughly between 1.5 and 1.8 at sites in the southeast, corresponding to a mixture of ammonium sulfate and ammonium bisulfate as the dominant salts. Surprisingly, R_{SO4} decreased by 0.01 to 0.03 units per year over the last 15 years. This is counterintuitive since it shows that as sulfate is reduced and the NH_3 to neutralize it remains constant, the aerosol is increasingly enriched in acidic ammonium bisulfate, whereas the expectation is that the aerosol should become more neutral over time (i.e., R_{SO4} increasing and approaching 2). CTR R_{SO4} follows a similar decreasing trend (Figure 5-3) and the thermodynamic sensitivity analysis (Figure 5-2b) is consistent with these observations.

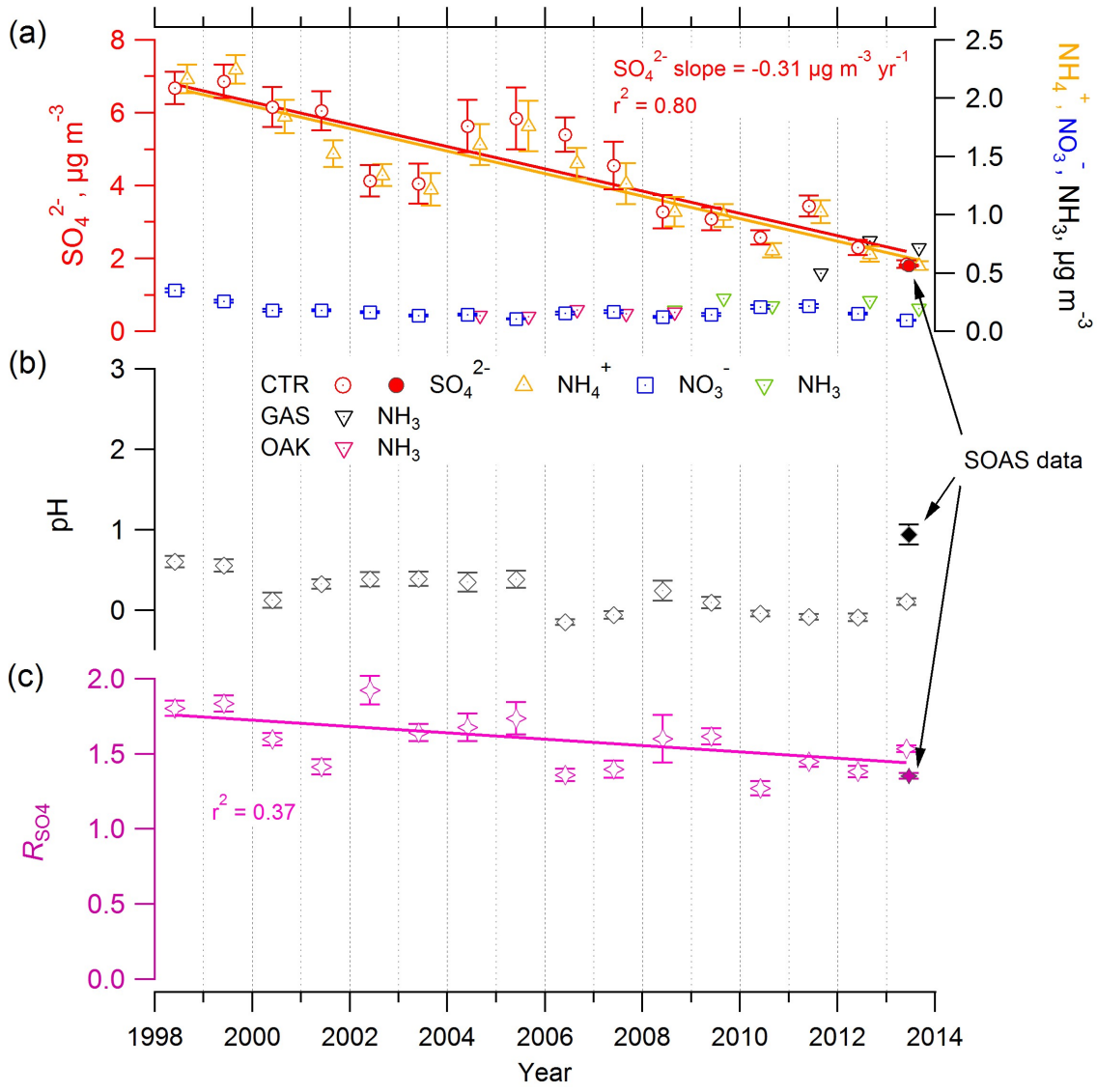

Figure 5-3 Mean summer (June-Aug) trends in $PM_{2.5}$ composition, NH_3, R_{SO4}, and predicted $PM_{2.5}$ pH at the SEARCH-CTR site. NH_3 data are from the SEARCH rural sites Centreville (CTR, Alabama) and Oak Grove (OAK, Mississippi) and AMoN Georgia Station (GAS, Georgia) site. SOAS mean data (June 1 to July 15 2013) are also plotted. Error bars represent data ranges (standard errors). pH was estimated with ISORROPIA-II run in the forward mode without gas phase species input, resulting in pH systematically low by approximately one unit [*Guo et al.*, 2015]. Uncertainties: ions ± 15%, molar ratios ± 26%, NH_3 ± 15 to 40%.

All these results can be explained by the nonvolatility of sulfate and semivolatility of ammonia, meaning that only NH_3 moves to establish equilibrium between the condensed aqueous and gas phase. For example, decreasing R_{SO4} occurs because particle phase ammonium roughly tracks SO_4^{2-} (Figure 5-3), so at lower SO_4^{2-} there is less ammonium available when establishing equilibrium with gas phase NH_3. During equilibration, ammonium (NH_4^+) is lost to the gas phase (NH_3) releasing H^+ in the aerosol and decreasing R_{SO4}. Since a larger relative loss in ammonium occurs at lower SO_4^{2-}, R_{SO4} is lower. The semivolatility of ammonium is also responsible for the remarkably weak sensitivity of pH to SO_4^{2-}. Further evidence is that pH begins to rise in the sensitivity analyses (Figure 5-2a) for SO_4^{2-} below roughly 0.3 μg m^{-3}; the thermodynamic analysis suggests this is due to association of SO_4^{2-} with other nonvolatile cations that starts to mitigate the buffering effect of NH_3 partitioning, significantly increasing pH (see Figure 5-4).

The sensitivity analysis (Figure 5-2a) does show a pH increase with increasing NH_3, but it is relatively weak, a consequence of the buffering effect of semivolatile NH_3 partitioning. For SO_4^{2-} between 0.1 and 10 μg m^{-3}, it is not until NH_3 is over 10 μg m^{-3} (14 ppbv at STP) before pH approaches 3; the minimum pH roughly at which ammonium nitrate begins to form for conditions of this study (see Figure 5-5). In summary, for typical summer conditions the observed trends in pH and R_{SO4} are expected and due to gas-particle thermodynamic equilibrium, along with relatively constant NH_3 levels that have been below a few μg m^{-3} over the past 15 years.

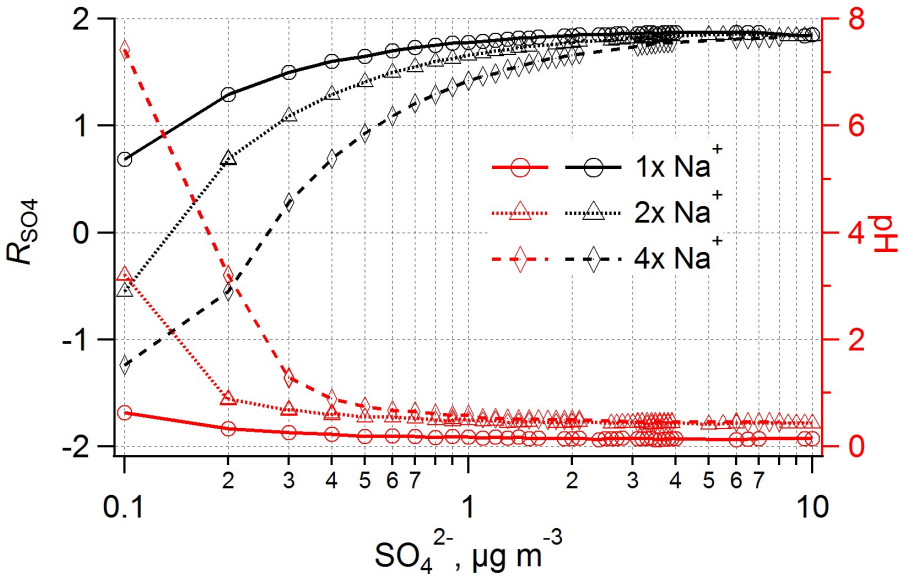

Figure 5-4 Predicted pH versus sulfate as a function of changes in concentrations of cations other than ammonium. In this sensitivity analyses, NO_3^- and Cl^- are unchanged at 0.08 and 0.02 µg m^{-3}, respectively. Na^+, originally at 0.03 µg m^{-3} is increased by factors of 2 and 4. The plot shows that the decrease in molar ratio (R_{SO4} = (NH_4^+ − NO_3^-)/SO_4^{2-}) at lower sulfate is related to the other nonvolatile cations associating with sulfate. Note that even at significantly higher nonvolatile cation levels internally mixed with fine particles, pH remains below 1 until sulfate drops below roughly 0.3 µg m^{-3}.

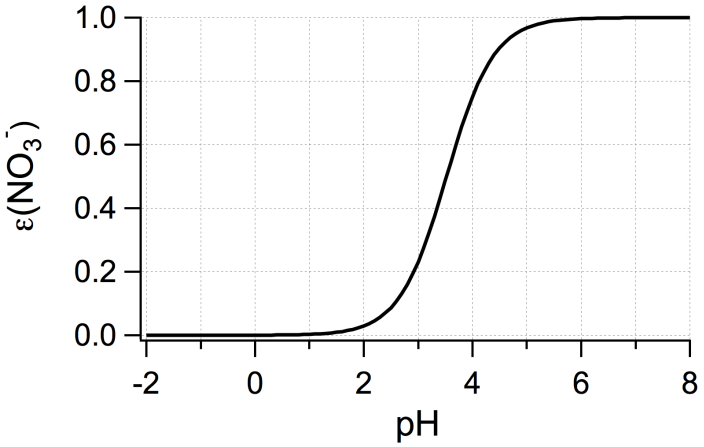

Figure 5-5 Fraction of total nitric acid in the particle phase. The partitioning of nitric acid between the condensed (NO_3^-) and gas phase (HNO_3), ε(NO_3^-) = NO_3^-/(NO_3^- + HNO_3), as a function of pH, assuming ideal solutions (activity coefficients of 1) for the average summer conditions during SOAS. The figure shows little nitrate aerosol when pH is below approximately 3, the pH observed in the southeastern US in the past and expected in the

future. Lower temperatures shift the curve to the left, accounting for possibly higher $\varepsilon(NO_3^-)$ in colder seasons.

5.4.3 Future pH

The thermodynamic sensitivity analyses was continued for SO_4^{2-} down to 0.1 μg m^{-3}, levels characteristic of remote regions [*Heintzenberg*, 1989]. As emissions of NH_3 are decoupled from SO_4^{2-}, linked mainly to agricultural and biogenic activities, in the foreseeable future one may expect this source to remain largely flat, or modestly increase as agricultural production follows population increases. This indicates that future gas phase NH_3 concentrations will not deviate considerably from current levels [*Saylor et al.*, 2015]. The area of expected future conditions in Figure 5-2 shows that summertime pH will remain in the 0 to 2 range, similar to current levels and those of the past 15 years. The system insensitivity to NH_3 implies that it is a poor indicator of fine aerosol pH. Furthermore, if the aerosol is in an aqueous phase the presence of NH_3 does not necessarily imply a neutral aerosol, as often assumed [*Kim et al.*, 2015], as some NH_4^+ always needs to volatilize to achieve equilibrium.

The sensitivity analysis also predicts changes in gas/particle portioning ratios with changing SO_4^{2-} and NH_3. Over the broad SO_4^{2-} range of 0.1 to 10 μg m^{-3}, the fraction of NH_3 in the gas phase relative to total (gas + particle) varies from about 90 to 10%, indicting coupling of gas-particle ammonia concentrations across this SO_4^{2-} range. In contrast, nitric acid is predicted to remain largely in the gas phase unaffected by SO_2 controls due to the predicted low pH. Nitrate aerosol is only expected once pH is over 2 to 3, and so minimal

particle phase inorganic nitrate is expected for typical summer conditions; neither in the past as SO_4^{2-} has decreased, and verified by the historical data (Figure 5-3), nor for some time into the future, given expected pH ranges (Figure 5-2). If there are no significant changes in future nonvolatile cation levels in the fine aerosol mode (e.g., increases in mineral dust due to land use changes or desertification, see next paragraph), summertime $PM_{2.5}$ in the Southeastern U.S. will remain highly acidic until average sulfate levels approach those of very clean remote continental sites (~ 0.3 μg m^{-3}) [*Heintzenberg*, 1989; *Hand et al.*, 2012a] and particulate nitrate will not become an increasing air quality issue for a long time into the future, counter to expectations.

The future aerosol pH scenario presented, although highly likely, can be affected by increases in suspended dust from land use changes, drought or other meteorological changes. High concentrations of alkaline mineral dust or transported sea-salt components, (carbonates and soluble salts of Ca^{2+}, Mg^{2+}, K^+, Na^+) would force the system to respond differently to sulfate reductions. The dust alkalinity can not only neutralize a larger fraction of acidic sulfate formed in the atmosphere, but also precipitate it out from the aqueous aerosol phase, primarily in the form of gypsum (calcium sulfate). Dust and sea-salt alkalinity raises pH at lower sulfate levels (see Figure 5-4) and favors the formation of nitrate, in the forms of Ca^{2+}, Mg^{2+}, K^+ salts and NH_4NO_3. It is also noted that there are instances where the NH_3 mass balance can be more complex, which we have not considered since our interest is on average summer conditions and long-term trends. For example, during cool (winter) or periods of very high relative humidity, significant levels of particle ammonium nitrate could be formed as pH increases due to uptake of substantial quantities

of water (e.g., resulting in H^+ dilution). The NH_3 balance would then need to include gas phase nitric acid production and ammonium nitrate deposition. Comprehensive simulations with chemical transport models (CTMs) that include emissions and losses of the major components involved, along with detailed size-resolved particle-gas interactions and aerosol chemistry, would provide greater details. More complex simulations will not change the findings of this work.

Although our analysis focuses on the southeastern U.S., it applies to all locations that are impacted by SO_2 emissions and which lack major sources of nonvolatile cations (e.g., sea-salt or mineral dust); conditions commonly found in many regions globally. Although reductions in sulfur dioxide (SO_2) and nitrogen oxides (NO_x) will reduce sulfate, nitrate and ammonium aerosol concentrations, leading to improved air quality, we show that fine particles are highly acidic and will likely remain so despite substantial sulfate reductions. Furthermore, particle pH must be explicitly considered to accurately gauge its impacts on heterogeneous chemical processes, particle composition, mass concentrations and toxicity.

CHAPTER 6. THE UNDERAPPRECIATED ROLE OF NONVOLATILE CATIONS ON AEROSOL AMMONIUM-SULFATE MOLAR RATIOS

6.1 Abstract

Overprediction of fine-particle ammonium-sulfate molar ratios (*R*) by thermodynamic models is suggested as evidence for an organic film that only inhibits the equilibration of gas-phase ammonia (but not water or nitric acid) with aerosol sulfate and questions the equilibrium assumption long thought to apply for submicron aerosol. The ubiquity of such organic films implies significant impacts on aerosol chemistry. We test the organic film hypothesis by analyzing ambient observations with a thermodynamic model and find that *R* and ammonia partitioning can be accurately reproduced when small amounts of nonvolatile cations (NVC), consistent with observations, are considered in the thermodynamic analysis. Exclusion of NVCs results in predicted *R* consistently near 2. The error in *R* is positively correlated with NVC and not organic aerosol mass fraction or concentration. These results strongly challenge the postulated ability of organic films to perturb aerosol acidity or prevent ammonia from achieving gas-particle equilibrium for the conditions considered.

6.2 Introduction

pH is a fundamental aerosol property that affects aerosol formation and composition through pH-sensitive reactions [*Jang et al.*, 2002; *Eddingsaas et al.*, 2010; *Surratt et al.*,

2010] and gas-particle partitioning of semivolatile species [*Guo et al.*, 2016; *Guo et al.*, 2017a]. Acidity also modulates aerosol toxicity and atmospheric nutrient supply to the oceans through changing solubility of transition metals [*Meskhidze et al.*, 2003; *Nenes et al.*, 2011; *Longo et al.*, 2016; *Fang et al.*, 2017]. Despite its importance, the inability to directly measure fine mode particle pH (e.g. *Rindelaub et al.* [2016] presents an indirect method that detects particle pH for sizes above 10 μm) has led to the use of measurable aerosol properties as acidity proxies, such as aerosol ammonium-sulfate ratio or ion balances (e.g. [*Paulot and Jacob*, 2014; *Wang et al.*, 2016; *Silvern et al.*, 2017]). Recent work has shown that acidity proxies are not uniquely related to pH, which in turn strongly questions any conclusions derived from its use. There are numerous reasons why acidity proxies do not represent pH well; they do not capture the variability in particle water content, ion activity coefficients, or partial dissociation of species in the aerosol phase [*Guo et al.*, 2015; *Hennigan et al.*, 2015; *Guo et al.*, 2016]. The method that best constrains aerosol pH is comparison between a thermodynamic analysis and observations of gas-particle partitioning of semivolatile species that are sensitive to pH at the given environmental conditions (i.e., gas-particle concentration ratios near 1:1) [*Guo et al.*, 2015; *Guo et al.*, 2016; *Weber et al.*, 2016; *Guo et al.*, 2017a]. NH_3-NH_4^+, HNO_3-NO_3^-, and HCl-Cl^- pairs often meet this condition. The method has been utilized for a range of meteorological conditions (RH, T) and gas/aerosol concentrations demonstrating that model predictions are often in agreement with observations.

It has been noted that thermodynamic models fail to accurately predict ammonium-sulfate molar ratios when just considering the NH_4^+-SO_4^{2-}-NO_3^- aerosol system in equilibrium with

the corresponding gas species [*Kim et al.*, 2015; *Silvern et al.*, 2017]. In the southeastern US, where total ammonium ($NH_x = NH_3 + NH_4^+$) is observed to be in large excess of particle sulfate and observed NH_4^+/SO_4^{2-} molar ratios are in the range of 1-2 [*Hidy et al.*, 2014; *Guo et al.*, 2015; *Kim et al.*, 2015], thermodynamic models often predict very low pH (0.5 to 2) [*Guo et al.*, 2015] and molar ratios close to 2 [*Kim et al.*, 2015; *Weber et al.*, 2016; *Silvern et al.*, 2017]. The molar ratio discrepancy has led to the hypothesis that thermodynamic predictions are incorrect, and particles are coated by organic films that inhibit the condensation of NH_3 from the gas phase and give rise to the molar ratio discrepancy [*Silvern et al.*, 2017]. Such kinetic limitations, if prevalent, opposes the validity of aerosol thermodynamic equilibrium and could significantly impact aerosol chemistry and acidity-mediated processes, given the large organic aerosol mass fractions worldwide [*Zhang et al.*, 2007a] and expected increasing organic mass fractions in the future due to changing emission, such as SO_2 emission reduction in the eastern US [*Hand et al.*, 2012a; *Attwood et al.*, 2014; *Hidy et al.*, 2014]. The hypothesis of organic films, however, is in stark contrast to established literature showing that NH_3, water vapor, and HNO_3 equilibrate with organic-rich aerosols [*Fountoukis et al.*, 2009; *Guo et al.*, 2015; *Guo et al.*, 2016; *Guo et al.*, 2017a]. Such a film, as proposed by *Silvern et al.* [2017], selectively limits NH_3, but not H_2O and HNO_3, molecules that are both larger than NH_3 hence more difficult to diffuse through media. At low temperature or low relative humidity, aerosols may be in semi-liquid or glassy state and have very low diffusivity of molecules throughout its volume [*Tong et al.*, 2011; *Bones et al.*, 2012]. This may severely limit gas-particle mass transfer of all components and require much longer time scales to equilibrate.

However, we have not observed such an effect for the conditions in the eastern US, as there is good agreement between observed and predicted particle water, and partitioning of NH_3-NH_4^+ and HNO_3-NO_3^- (the bias in NO_3^- prediction becomes progressively worse when RH drops below 40%, likely owning to glassy states during the wintertime) [*Guo et al.*, 2015; *Guo et al.*, 2016].

Other reasons that are unrelated to organic films may drive the molar ratio discrepancy. One is related to the variation of aerosol composition with size, which may translate to a large range of acidity, hence equilibrium composition [*Keene et al.*, 1998; *Nenes et al.*, 2011; *Bougiatioti et al.*, 2016; *Fang et al.*, 2017]. Another related issue is the presence of soluble nonvolatile cations (NVC, such as Na^+, K^+, Ca^{2+}, Mg^{2+}), which are often neglected in thermodynamic calculations because of their relatively minor contribution to aerosol mass or are not routinely included in aerosol composition measurements (e.g., those made with an aerosol mass spectrometer). Here we show that ignoring even small amounts of NVC as inputs to the thermodynamic model results in predicted NH_4^+/SO_4^{2-} molar ratios close to 2 due to the model criteria of electrical neutrality, but has a smaller effect on predicted pH, whereas including small levels of NVC brings model-predicted molar ratios into agreement with observed levels.

6.3 Methods

Molar ratios definition: Two ammonium-sulfate aerosol molar ratios are used in the following analysis,

$$R = \frac{\mathrm{NH_4^+}}{\mathrm{SO_4^{2-}}} \quad (6\text{-}1)$$

$$R_{\mathrm{SO_4}} = \frac{\mathrm{NH_4^+} - \mathrm{NO_3^-}}{\mathrm{SO_4^{2-}}} \quad (6\text{-}2)$$

both are based on inorganic mole concentrations in units of μmol m^{-3}. R_{SO4} is a more narrowly defined molar ratio that excludes NH_4^+ associated with NO_3^- because ammonium sulfate and ammonium nitrate are typically associated with different sized particles (externally mixed) [*Zhuang et al.*, 1999] and molar ratios are calculated based on bulk composition data ($PM_{2.5}$ or PM_1). The upper limit for R and R_{SO4} is 2 for a particle composition of pure $(NH_4)_2SO_4$, the lower limit is 0 for R when SO_4^{2-} is associated with other cations instead of NH_4^+ (e.g. Na_2SO_4) or if there is free H_2SO_4 in the aerosol. A negative R_{SO4} can occur for conditions of high NO_3^- and low NH_4^+, SO_4^{2-} concentrations (e.g., $NaNO_3$), but rare for ambient fine particles. R or R_{SO4} is typically observed in the range of 1 and 2 in the southeastern US (i.e., between NH_4HSO_4 and $(NH_4)_2SO_4$) [*Hidy et al.*, 2014; *Guo et al.*, 2015; *Weber et al.*, 2016]. In cases where NO_3^- levels are low relative to SO_4^{2-}, the two ratios, R_{SO4} and R, are equivalent, as is observed in the summertime southeastern US, where NO_3^- is typically ~0.2 μg m^{-3}, NH_4^+ ~1 μg m^{-3}, and SO_4^{2-} ~3 μg m^{-3} [*Blanchard et al.*, 2013].

Observations: Two datasets are used for analysis, the Southern Oxidant and Aerosol Study (SOAS) and the Wintertime Investigation of Transport, Emissions, and Reactivity (WINTER). The SOAS study was conducted from June 1 to July 15 in the summer of 2013 at a rural ground site in Centreville (CTR), Alabama, representative of the southeastern US background atmosphere in summer. The WINTER data was produced from 13 research

aircraft flights from Feb 1 to Mar 15 in 2015 mainly sampling over the northeastern US. Details of the campaigns and instruments, and calculations and verification of pH based on the observation datasets, have been described in *Guo et al.* [2015] and *Guo et al.* [2016], respectively. In the following analysis, we use R for summertime datasets with low NO_3^- and R_{SO4} for wintertime datasets with high NO_3^- concentration. Both datasets report highly acidic aerosols with average pH~1 [*Guo et al.*, 2015; *Guo et al.*, 2016]. At these pH levels, aerosol sulfate can be in the partially deprotonated form of HSO_4^- instead of SO_4^{2-}. For example, 14% sulfate is predicted to be HSO_4^- and the rest as SO_4^{2-} in the winter dataset [*Guo et al.*, 2016]. Free form H_2SO_4, which requires even lower pH, is rare in the ambient aerosol. The SO_4^{2-} in this study refers to the sum of total aqueous aerosol sulfate (SO_4^{2-}, HSO_4^-, and H_2SO_4), the same definition (i.e., S(VI)) used in *Silvern et al.* [2017], since aerosol instruments normally report total aqueous sulfate as just SO_4^{2-}. The same applies to NH_4^+ and NO_3^-. The observation data are from two widely deployed aerosol instruments; a Particle-Into-Liquid-Sampler coupled with an Ion Chromatograph (PILS-IC) and a High-Resolution Time-of-Flight Aerosol Mass Spectrometer (hereafter referred to as AMS). The PILS-IC detects aerosol water-soluble anions and cations collected and diluted by deionized water to the extent of complete deprotonation of H_2SO_4 in the aqueous sample [*Orsini et al.*, 2003]. The AMS vaporizes aerosols and ionizes non-refractory species with a 70 eV electron impact ionization and cannot distinguish the dissociation states of inorganic ions [*DeCarlo et al.*, 2006].

Thermodynamic analysis of observations: The thermodynamic model ISORROPIA-II [*Fountoukis and Nenes*, 2007] was used to determine the composition and phase state of

an NH_4^+-SO_4^{2-}-NO_3^--Cl^--Na^+-Ca^{2+}-K^+-Mg^{2+}-water inorganic aerosol (or a subset therein) and its partitioning with corresponding gases. Using this model, we have developed a method for pH prediction that includes appropriate validation and uncertainty assessment [*Guo et al.*, 2015] and applied the methods to several other locations [*Bougiatioti et al.*, 2016; *Guo et al.*, 2016; *Weber et al.*, 2016; *Guo et al.*, 2017a; *Guo et al.*, 2017b]. Here pH is defined following the same approach,

$$\mathrm{pH} = -\log_{10}\gamma_{H^+}H^+_{aq} = -\log_{10}\frac{1000\gamma_{H^+}H^+_{air}}{W_i + W_o} \cong -\log_{10}\frac{1000\gamma_{H^+}H^+_{air}}{W_i} \quad (6\text{-}3)$$

where γ_{H^+} is the hydronium ion activity coefficient (assumed = 1), H^+_{aq} (mol L^{-1}) the hydronium ion concentration in particle liquid water, H^+_{air} (μg m^{-3}) the hydronium ion concentration per volume of air, and W_i, W_o (μg m^{-3}) are particle water concentrations associated with inorganic and organic species, respectively. pH predicted solely with W_i is fairly accurate; pH was 0.15-0.23 units systematically lower than and highly correlated to (r^2 = 0.97) pH predicted with total particle water (W_i + W_o) in the southeastern U.S., where W_o accounted for 35% of total particle water [*Guo et al.*, 2015]. For simplicity, we therefore use W_i for the following pH calculations.

ISORROPIA-II was run in forward mode to calculate gas-particle equilibrium concentrations based on the input of total concentration of various inorganic species (e.g., NH_3 + NH_4^+). The best agreement between model and observations were achieved assuming "metastable" particles with no solid precipitates (H^+ is not stable in an effloresced aerosol). We also assumed that the particles were internally mixed, and that pH did not vary with size (so that bulk properties represent the aerosols, including pH) and gas-particle

partitioning was in thermodynamic equilibrium. For submicron aerosol (PM_1), equilibrium states are typically achieved within 30 minutes under ambient conditions [*Dassios and Pandis*, 1999; *Cruz et al.*, 2000; *Fountoukis et al.*, 2009]. The prediction of gas-particle partitioning has been found to be in good agreement with observations when using particle bulk concentrations as model input [*Guo et al.*, 2015; *Guo et al.*, 2016; *Guo et al.*, 2017a], although particle pH is size dependent. pH increases for particles above 1 μm as a result of NVC [*Fang et al.*, 2017] resulting in particle mixing state becoming more important with increasing particle size [*Guo et al.*, 2017a].

6.4 Discussion

6.4.1 The cause for discrepancy between modeled and measured molar ratios (R)

We first investigate the issue of *R* discrepancy using PILS-IC $PM_{2.5}$ data from a 12-day period (June 11-23) of the SOAS campaign. The same period has been used to study pH sensitivity to sulfate and ammonia and shown to accurately predict NH_3-NH_4^+ partitioning compared to observations [*Weber et al.*, 2016]. To test the sensitivity of ISORROPIA-II predictions we ran the model with the same input as *Weber et al.* [2016], (inputs include Na^+, (NH_4^++NH_3), SO_4^{2-}, NO_3^-, Cl^-, Ca^{2+}, Mg^{2+}, K^+, RH, T, where Ca^{2+}, Mg^{2+}, K^+ inputs were zero, NH_4^+, SO_4^{2-}, NO_3^-, Cl^- concentrations were from PILS-IC $PM_{2.5}$ observational data, NH_3 was from chemical ionization mass spectrometer measurements [*You et al.*, 2014a]) and tested three different Na^+ levels: (1) Na^+ determined from an ion charge balance by $Na^+ = 2SO_4^{2-} + NO_3^- + Cl^- - NH_4^+$ (unit: μmol m^{-3}); (2) measured $PM_{2.5}$ Na^+ from PILS-IC; (3) $Na^+ = 0$.

Different Na^+ concentrations were used to investigate the impact of Na^+ on model output. The inferred Na^+ was on average 0.28 ± 0.18 μg m^{-3}, higher than the measured level of 0.06 ± 0.09 μg m^{-3}. Note that, the limit of detection (LOD) of PILS-IC Na^+ in this study was 0.07 μg m^{-3}, close to the reported average level. Unlike the standard procedure of reporting below LOD values as ½ LOD, we use the Na^+ concentrations directly from the instrument, including those below the LOD because, as will be shown, R is highly sensitive to trace levels of NVC. Also, we note that all other NVC, such as Ca^{2+} and Mg^{2+}, were generally below the PILS-IC LOD (therefore set to zero in the model input). The charge balance predicted Na^+ should then be viewed, for this data set, as the concentration of generic NVC concentrations with a valence of 1. The charge balance predicted Na^+ must be above zero; for calculated values below zero (8 out of 229 points, 3% of the data), due to combined measurement uncertainty, a small positive value of 0.005 μg m^{-3} is assigned.

The concentration of H^+ is also ignored in the ion charge balance calculation as it is 2-3 orders of magnitude smaller than the major inorganic ions, even at these low pH (between 0 and 2). For example, the average $PM_{2.5}$ mole concentrations per volume of air for the ions measured by the PILS-IC were NH_4^+ = 0.0354, SO_4^{2-} = 0.0211, NO_3^- = 0.0037, Na^+ = 0.0029, and Cl^- = 0.00082 μmol m^{-3}, compared to ISORROPIA-predicted H^+ = 0.00031 μmol m^{-3} for this period. The observed Na^+ appeared to be mainly associated with NO_3^-, and to a lesser degree with Cl^-, based on high linear correlations, r^2 = 0.82 and 0.64, respectively. A typical level of "chloride depletion" was observed as a Cl^-/Na^+ ratio of 0.24 ± 0.16 (mol mol^{-1}), due to higher volatility of HCl versus HNO_3 [*Fountoukis and Nenes*, 2007]. In this case, Cl^- input to ISORROPIA is negligible as it does not affect the

predictions of pH or molar ratios due to the measured Cl^- concentration being small, 0.03 ± 0.04 μg m^{-3} (LOD = 0.01 μg m^{-3}).

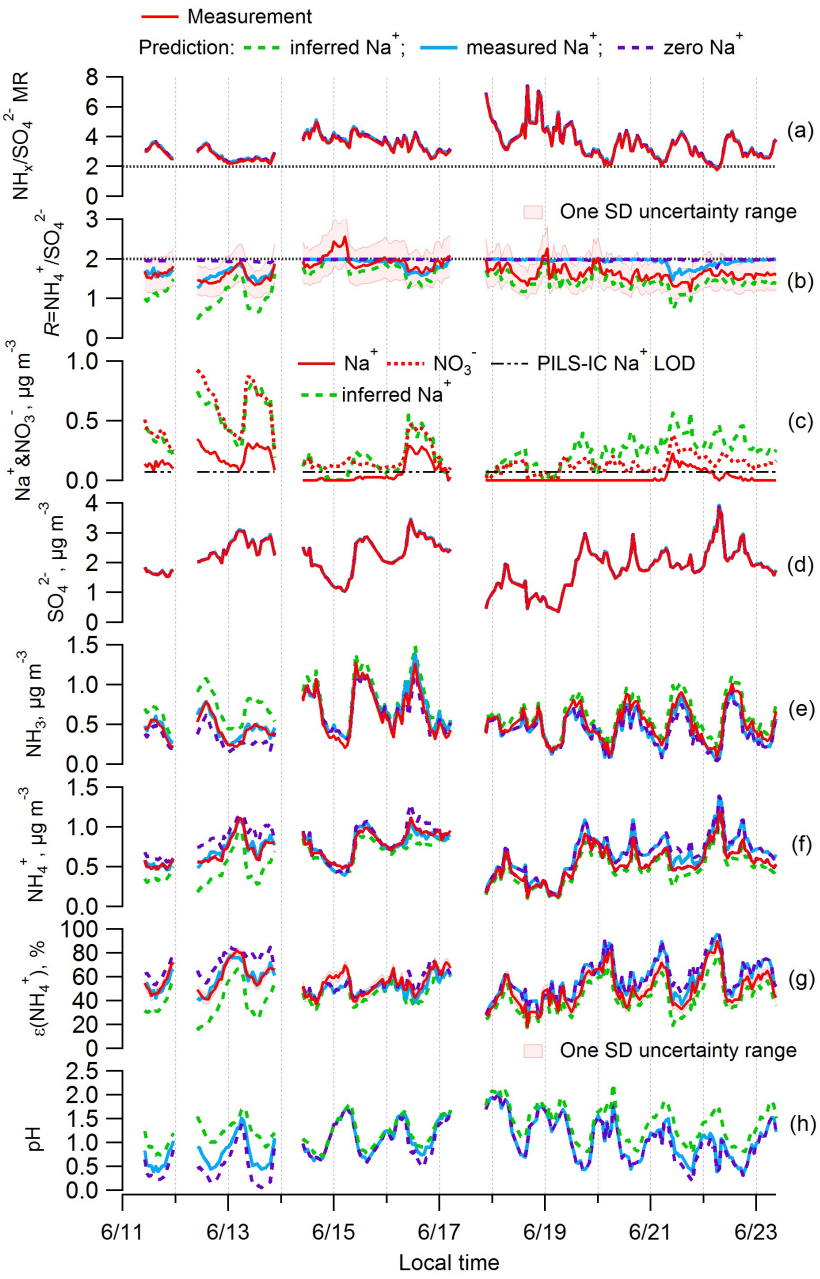

Figure 6-1 Time series of various measured and ISORROPIA-predicted parameters and $PM_{2.5}$ component concentrations for a select period of the SOAS study, with periods of rainfall removed. Thn charge balance ($Na^+ = 2SO_4^{2-} + NO_3^- + Cl^- - NH_4^+$, μmol m^{-3}; mean value of 0.28 ± 0.18 μg m^{-3}) in green, measured Na^+ blue, and zero Na^+ in purple. All other inputs were the same. Na^+ represents generic nonvolatile cations (NVC). Specific plots are as follows: (a) total ammonium ($NH_x = NH_4^+ + NH_3$) to sulfate molar ratio (NH_x/SO_4^{2-}), (b) aerosol ammonium-sulfate ratios ($R = NH_4^+/SO_4^{2-}$), (c) Na^+ and NO_3^-, (d) SO_4^{2-}, (e) NH_3, (f) NH_4^+, (g) particle-phase fractions of total ammonium, $\varepsilon(NH_4^+)$, and (h) particle pH.

Figure 6-1 shows the time series of various parameters for the SOAS 12-day period investigated. From these data, the effect of Na^+ (i.e., NVC) on ISORROPIA-predicted SO_4^{2-}, NH_4^+, NH_3, *R*, and pH is investigated. Figure 6-1a and d show the overall behavior of total ammonium ($NH_x = NH_3 + NH_4^+$) and sulfate. SO_4^{2-} is nonvolatile so remains unchanged by the model, as does total ammonium and hence the NH_x/SO_4^2 molar ratio. Therefore, the discrepancy between modeled and measured *R* must result from the NH_4^+ prediction. It is noteworthy that NH_x/SO_4^{2-} is generally above 2, indicating excess NH_x compared to SO_4^{2-}. Under such conditions, it is often interpreted that NH_3 must completely neutralize SO_4^{2-} [*Kim et al.*, 2015; *Silvern et al.*, 2017]. The thermodynamic model predicts otherwise; despite the excess NH_x, $PM_{2.5}$ is predicted to be highly acidic, with a pH range between 0 and 2 (Figure 6-1h), resulting from NH_4^+ semivolatility and SO_4^{2-} being virtually nonvolatile at any atmospherically-relevant concentration and acidity [*Weber et al.*, 2016].

The predicted time series of NH_3-NH_4^+ partitioning agrees most with observations when measured Na^+ is included in the model compared to model results with identical inputs, except with zero Na^+ or inferred Na^+ from ion charge balance (Figure 6-1e, f, g, and Figure 6-2). For ISOROPPIA simulations with measured Na^+ as input, the orthogonal linear regression of ISORROPIA-predicted versus measured particle-phase fractions of total ammonium, where $\varepsilon(NH_4^+) = NH_4^+/NH_x$, is: $\varepsilon(NH_4^+)_{predicted} = (1.00 \pm 0.03)\ \varepsilon(NH_4^+)_{observed} + (0.03 \pm 0.02)$, with $r^2 = 0.76$ and "±" is one standard deviation (SD). Mean $\varepsilon(NH_4^+)_{observed}$ was 54 ± 13%, making the partitioning sensitive to pH [*Guo et al.*, 2017a]. As the nonvolatile Na^+ competes with semivolatile NH_4^+, predicted NH_4^+ decreases when higher levels of Na^+ are input to the model, whereas predicted gas phase NH_3 increases, for

conservation of input NH_x. Thus, since the ion charge balance inferred Na^+ is often higher than measured Na^+ (Figure 6-1c), the lowest NH_4^+ and $\varepsilon(NH_4^+)$ are predicted with the input of inferred Na^+. In contrast, the highest NH_4^+ and $\varepsilon(NH_4^+)$ are predicted with zero Na^+ input, whereas the predicted values with measured Na^+ as model input are between these two. For the period in Figure 6-1, measured Na^+ was 0.06 μg m^{-3} and the inferred value was 0.28 μg m^{-3}.

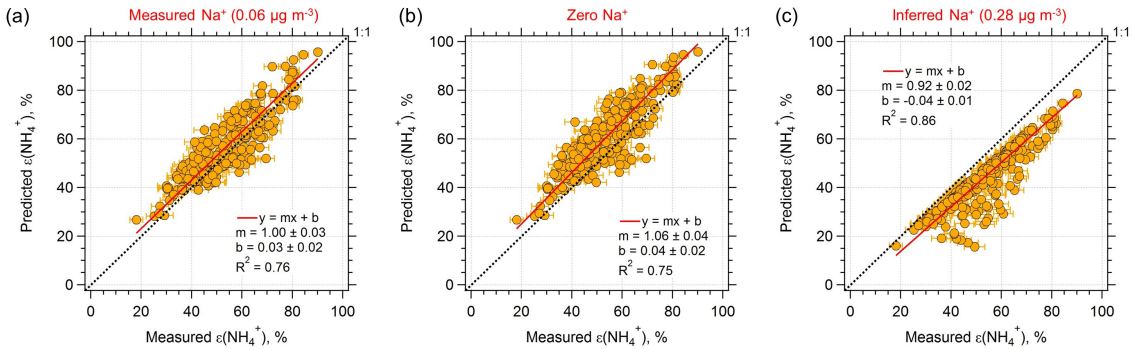

Figure 6-2 Comparisons of predicted and measured particle phase fractions of total ammonium, $\varepsilon(NH_4^+) = NH_4^+/(NH_3 + NH_4^+)$, for data from the 12-days of the SOAS study. NH_4^+ was measured with a PILS-IC ($PM_{2.5}$ cut size) and NH_3 from a CIMS. (a) Prediction is based on an ISORROPIA input of measured Na^+, (NH_4^+ + NH_3), SO_4^{2-}, NO_3^-, Cl^-; (b) Model input identical to (a), except that Na^+ is set to zero; (c) Same model input, but Na^+ inferred from an ion charge balance. Orthogonal distance regression (ODR) fits are shown and uncertainties in the fits are one standard deviation (SD). The uncertainty of measured $\varepsilon(NH_4^+)$ is derived from error propagation of NH_4^+ (15%) and NH_3 (6.8%) measurements. The best prediction of NH_3-NH_4^+ partitioning is achieved by using measured Na^+ as input for the least deviation from a 1:1 line.

R also depends on the input Na^+ concentration. For the Figure 6-1 period, predicted *R* was on average 1.43 ± 0.32 for an ISORROPIA input with inferred Na^+, 1.85 ± 0.17 for measured Na^+ input, and the highest *R* at 1.97 ± 0.02 when zero Na^+ was used as model input. The average measured *R* was 1.70 ± 0.23 by PILS-IC and 1.75 ± 0.20 by another $PM_{2.5}$ water-soluble ion measurement [*Allen et al.*, 2015]. Thus, model *R* with measure Na^+ input was closest to the measured *R*. Under the meteorological conditions of the southeast in summertime (T = 25 ± 5 °C, RH = 68 ± 18 %), the thermodynamic model predicts *R* always near or equal to 2, when input NVCs are set to zero and the only other particle composition inputs are SO_4^{2-}, NH_4^+), and NO_3^-, with paired gases NH_3 or HNO_3, indicating a particle composition of mainly $(NH_4)_2SO_4$; expected for electroneutrality of the aerosol aqueous phase. These are the model inputs when particle composition are from an AMS (e.g. [*Kim et al.*, 2015; *Silvern et al.*, 2017]) and explains why ISORROPIA-predicted *R* disagreed with measured values, which is a basis for the organic film hypothesis [*Silvern et al.*, 2017].

Contrasts between measured and predicted *R* for periods of differing model input Na^+ levels can be seen in Figure 6-1. First, if the ambient Na^+ mass concentration was higher than the PILS-IC LOD, such as the period of June 11-13 & 16, the predicted and measured *R* agree when measured Na^+ is input. Inferred Na^+ from the ion charge balance appears to be overestimated at these times, and this causes a noticeable bias in the prediction of *R*, NH_3, NH_4^+, and $\varepsilon(NH_4^+)$. The pH calculated based on the inferred Na^+ also differs compared to the pH calculated from the measured Na^+ for this period. During periods when ambient Na^+ mass concentration was below the measurement LOD, but close to zero, no

discrepancy in *R* is found since both values are near 2 (e.g., around the time of June 16 midnight). This results from negligible effects of NVC since concentrations are very low. When ambient Na^+ concentrations were below LOD, but not zero, there is a discrepancy between predicted and observed *R* for ISORROPIA with input of measured Na^+ or zero Na^+, however, inferred Na^+ results in better agreement. For instance, during the period of June 18-20 & 22-23, the predicted *R* with the inferred Na^+ input follows (but is slightly lower than) observations; this is consistent with an overestimation of Na^+ from the ion charge balance calculation. Overall, the time series analysis demonstrates how model-predicted molar ratios are affected by measurement accuracy and LODs of NVC and the sensitivity of ISORROPIA-predicted *R* to NVCs input concentrations. Note that a few measured *R* points were above 2 (e.g. midnight of June 15), a result of measurement uncertainty and error propagation at low SO_4^{2-} concentrations.

6.4.2 Quantification of NVC effects on R and pH

We have shown that the discrepancy in *R* can be resolved for this data set by adding small amounts of Na^+, either measured (when near or above LOD) or inferred from an ion charge balance analysis when not measured or significantly below the measurement method LOD. However, due to propagation of SO_4^{2-}, NH_4^+, and NO_3^- measurement errors, the uncertainty in inferred Na^+ data may cause a noticeable bias in the prediction of *R* or pH, such as observed on June 11-13 (Figure 6-1b). Because of this, quantifying the sensitivities of *R* and pH to Na^+, or any other NVC, is of interest. Here we use Na^+ as an example since it was the highest NVC concentration measured in this study; K^+ and Mg^{2+} have similar

effects. Ca^{2+} behaves differently due to $CaSO_4$ solids precipitating out, shown as Figure 6-3.

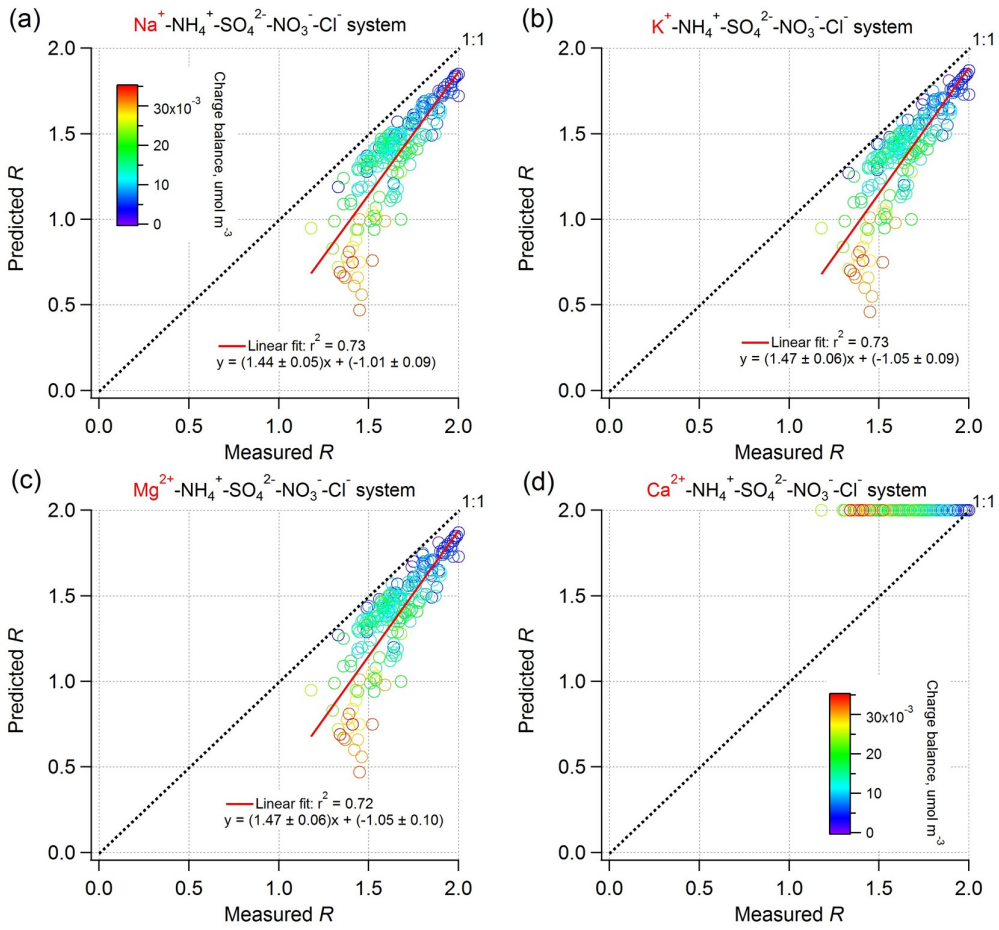

Figure 6-3 Comparison between ISORROPIA-predicted and PILS-IC-measured $PM_{2.5}$ R (R_{SO4} = NH_4^+/SO_4^{2-}, mol mol^{-1}), where the model predictions are based on NVC-NH_4^+-SO_4^{2-}-NO_3^--Cl^- system for the SOAS study. NVC (nonvolatile cation) was determined by an ion charge balance (color wave), that is, ($2SO_4^{2-} + NO_3^- + Cl^- - NH_4^+$) in units of μmol m^{-3}. This results in 200% mole-equivalent concentrations of Na^+ and K^+ compared to Ca^{2+} and Mg^{2+} due to +1 versus +2 charges. NH_4^+, SO_4^{2-}, NO_3^-, Cl^- are observed PILS-IC mass concentrations. For each graph, NVC is set to be a single ion, shown as (a) Na^+, (b) K^+, (c) Ca^{2+}, (d) Mg^{2+}. Adding Na^+ or K^+ or Mg^{2+} results in predicted R (generally underpredicted) agreeing better with measured R, compared to predicted R equal or close to 2 with zero NVC input. Ca^{2+} doesn't work at all as it precipitates out from the aqueous phase as $CaSO_4$. The solubility of $CaSO_4$ is only 0.2 g per 100 mL water at 20 °C. The average predicted particle liquid water W_i (3.0 μg m^{-3}) could only dissolve 0.006 μg m^{-3} Ca^{2+}, a tenfold lower

amount than the inferred Ca^{2+} of 0.23 μg m^{-3} from an ion charge calculation. ODR fits are shown and uncertainties in the fits are one SD.

Differences in predicted *R* with and without measured Na^+ are plotted against Na^+ mass and organic aerosol mass fractions in Figure 6-4a; Δ*R* is defined as ISORROPIA predicted *R* with Na^+ minus ISORROPIA predicted *R* without Na^+. Figure 6-4a shows that Δ*R* is highly correlated with Na^+ (r^2 = 0.93). Based on an orthogonal linear regression Δ*R* = (–1.74 ± 0.03) Na^+ + (0.001 ± 0.003). From the regression slope, the average measured Na^+ level of 0.06 μg m^{-3}, a background level of $PM_{2.5}$ Na^+ in the southeast, causes a response of –0.10 in *R*. At a Na^+ level of only 0.3 μg m^{-3}, Δ*R* reaches –0.5, indicating a rapid decrease from *R* = 2 (no NVC) to *R* = 1.5 (with NVC) for these conditions. Thus, not only is Δ*R* highly correlated with Na^+, it is also highly sensitive to Na^+. This is not seen for the organic aerosol mass fraction, here used as a proxy for the film thickness because it constrains the organic volume per particle. A similar plot based on organic aerosol mass concentration is shown in Figure 6-5. In stark contrast to Na^+, Figure 6-4a shows no correlation between Δ*R* and organic aerosol mass fraction. There is also no correlation when Δ*R* is plotted against OA mass concentration for data points Δ*R* = measured *R* − 2, and an inverse correlation is observed for some points between Δ*R* and organic aerosol mass concentration for Δ*R* = predicted *R* (with Na^+) − predicted *R* (no Na^+), see Figure 6-5. These results are inconsistent with the bias in *R* being linked to increases in mass fraction of organic species, as proposed by *Silvern et al.* [2017].

In comparison to *R*, pH is less sensitive to inclusion of Na^+, or other NVCs in general. ΔpH is only 0.07 for the average Na^+ level of 0.06 μg m^{-3}, and increases to 0.38 at 0.3 μg m^{-3} Na^+ (Figure 6-4). The magnitude of ΔpH is relatively small and consistent with our previous studies where we investigated the effects of sea-salt on pH [*Guo et al.*, 2016; *Weber et al.*, 2016]. ΔpH would be higher in regions with more abundant NVC. For instance, a ΔpH of 0.8 unit was found in Pasadena, California, where the average $PM_{2.5}$ Na^+ mass was 0.77 μg m^{-3} [*Guo et al.*, 2017a]. Differences in sensitivity of *R* and pH to Na^+ can be seen based on linear regressions. The magnitude of the Δ*R*-Na^+ slope is –1.74 compared to ΔpH-Na^+ slope of 1.27. Sensitivities of pH and *R* (or R_{SO4}) to Na^+ are discussed further below, next we investigate NVC effects on *R* and pH for a different data set.

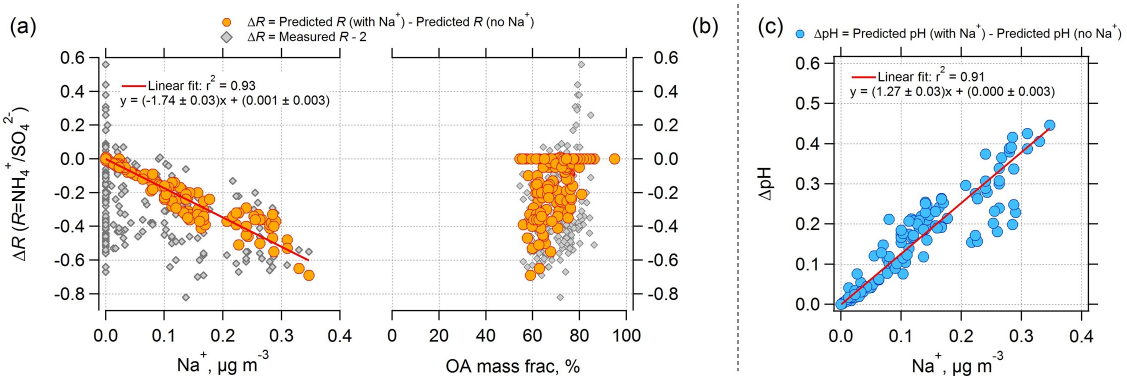

Figure 6-4 Effect of nonvolatile cations (NVC) on the $PM_{2.5}$ ammonium-sulfate molar ratio (*R*) and pH as a function of measured Na^+ and organic aerosol (OA) concentrations. The orange circular points in plots (a) and (b) are for Δ*R* equal to ISORROPIA predicted *R* with measured Na^+ included in the model input minus ISORROPIA predicted *R* without Na^+ in the model input. ΔpH in plot (c) is determined in a similar way. The grey diamonds in plots (a) and (b) are for Δ*R* equal to the actual measured *R* minus 2. Note that Δ*R* should be negative since including Na^+ in the thermodynamic model results in *R* lower than 2, whereas not including Na^+ results in an *R* close to 2 (on average *R* predicted without Na^+ is 1.97±0.02), a measured *R* is generally less than 2. Plot (a) is Δ*R* versus measured Na^+, (b) Δ*R* versus measured OA mass fraction, and (c) ΔpH versus measured Na^+. Orthogonal distance regression (ODR) fits are shown and uncertainties in the fits are one standard

deviation. A plot similar to (b), but versus OA mass concentration can be found as Figure 6-5

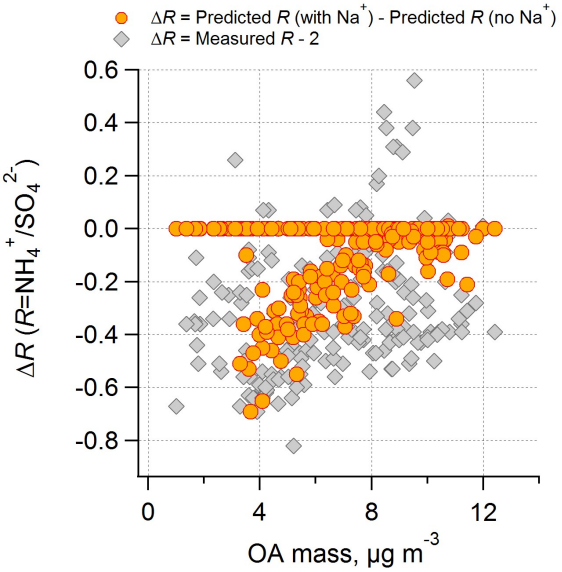

Figure 6-5 Effect of nonvolatile cations (NVC) on the $PM_{2.5}$ ammonium-sulfate molar ratio (*R*) as a function of measured organic aerosol (OA) concentrations based on AMS data (SOAS). The orange circular points denote Δ*R* calculated from ISORROPIA predicted *R* with measured Na^+ included in the model input minus ISORROPIA predicted *R* without Na^+ in the model input. Grey diamonds are for Δ*R* equal to measured *R* minus 2. Note that Δ*R* should be negative since including Na^+ in the thermodynamic model results in *R* lower than 2, whereas not including Na^+ results in an *R* close to 2 (on average *R* predicted without Na^+ is 1.97 ± 0.02).

6.4.3 NVC effects on molar ratios and pH based on winter data

The above discussion is based on data collected at a ground site in summertime (SOAS), we expand the investigation of the *R* discrepancy to a larger geographical scale and for a different season by performing a similar analysis with the WINTER study dataset collected in wintertime. In this study, NVCs were generally higher, especially when the aircraft sampled near coastlines (e.g. PM_1 Na^+ = 0.23 µg m^{-3}). Also, PM_1 nitrate was comparable

to sulfate, largely owing to lower temperatures (NO_3^- 0.013 μmol m^{-3} vs. SO_4^{2-} 0.011 μmol m^{-3}) [*Guo et al.*, 2016]. Therefore, R_{SO4} was calculated instead of *R*. In this case the aerosol inorganic composition data input for ISORROPIA-II is from an AMS. Since the AMS does not efficiently detect ions associated with refractory species, such as Na^+ and associated Cl^- from NaCl, in our past analysis of the WINTER aerosol pH, we only included NH_4^+, SO_4^{2-}, and total nitrate (NO_3^- + HNO_3) as input for ISORROPIA-II. (NH_3 should be included, but was not measured, although in this case it was found to have a small effect on predicted pH: ~0.2 higher pH when including an NH_3 concentration of 0.10 μg m^{-3} determined from an iteration method). With these assumptions, we found good agreement between predicted and measured HNO_3-NO_3^- partitioning (average $\varepsilon(NO_3^-)$ = 39%), especially when RH was above 60% [*Guo et al.*, 2016]. However, again Fig. 3a shows that the model overpredicted R_{SO4}. Also, when concentrations of NVC were low, predicted and measured R_{SO4} was generally 2. (Note that the predicted R_{SO4} should be biased low since NH_4^+ was underpredicted due to lack of NH_3 data, resulting in some fraction of input particle phase NH_4^+ repartitioned in the model to the gas phase). On average, predicted R_{SO4} was 1.68 ± 0.51 versus the measured value of 1.47 ± 0.43. In Figure 6-6a, the gray error bars show the propagated uncertainties for R_{SO4} based on a 35% AMS measurement uncertainty for NH_4^+, SO_4^{2-}, and NO_3^- [*Bahreini et al.*, 2009].

As in the SOAS data set, including NVCs also brings predicted and measured ammonium-sulfate molar ratios into agreement (Figure 6-6). Here, the amounts of NVC needed for an ion charge balance involving NVC-NH_4^+-SO_4^{2-}-NO_3^- aerosols were calculated based solely on NVC assumed to be Na^+. The thermodynamic results based on other NVCs are shown

in Figure 6-7. K^+ and Mg^{2+} work similarly to Na^+, while Ca^{2+} can precipitate sulfate in the form of $CaSO_4$. Overall, Na^+ is chosen as a proxy NVC in our dataset because it constitutes most of the NVC mass and does not precipitate out of solution. The choice of Na^+ as a NVC proxy, although appropriate here, is not generally applicable; in regions with considerable dust contributions, treating NVC as "equivalent Na^+" in the thermodynamic calculations can result in large prediction errors (e.g., [*Fountoukis et al.*, 2009]). As done before, in this analysis, when the ion charge balance predicts negative Na^+ concentrations (137 data points out of 3226, 4%), a small positive value of 0.005 μg m^{-3} is assigned. It is clear in Figure 6-6b that with the added NVC, the predicted R_{SO4} is in good agreement with the observation, with regression result $R_{SO4,predicted} = (1.05 \pm 0.01)\ R_{SO4,observed} + (-0.12 \pm 0.01)$, $r^2 = 0.99$. Again, the molar ratio bias from the thermodynamic model is simply a matter of not including small amounts of NVC (e.g. 0.15 μg m^{-3} Na^+ or 0.26 μg m^{-3} K^+). The average amount of inferred Na^+ from the ion charge balance in this case is smaller than what was measured offline during the study; PM_1 Na^+ of 0.23 μg m^{-3} [*Guo et al.*, 2016]. The analysis using measured PM_1 Na^+ results in highly scattered data due to the high sensitivities of R_{SO4} to NVC and the significant Na^+ measurement uncertainty at these low levels and the analytical method used in this study.

Because molar ratios are sensitive to NVCs and NVC concentrations are often very low, use of molar ratios to test the thermodynamic model should be done with caution, but actually not recommended. Since NVC associated with sea-salt and crustal materials are normally very small fractions of the PM_1 inorganic mass, it is typically reasonable to ignore these species when determining PM_1 NH_4^+ and NO_3^- partitioning, or pH, using

ISORROPIA-II, as we have shown [*Guo et al.*, 2016; *Guo et al.*, 2017a]. Since the molar ratio is a pH proxy that is highly sensitive to small mass concentrations of NVCs, as well as measurement errors, and only provides limited insights on pH and its effects (see discussion in the Introduction), we view this as a minor issue since pH should be used instead [*Guo et al.*, 2017a]. Alternatively, if accurate NVC data is not available, NVC can be estimated through an ion charge balance calculation with the measured NH_4^+-SO_4^{2-}-NO_3^- data and include the resulting inferred NVC in the ISORROPIA input, which will produce a better estimate of *R* than setting NVC to zero in the model input.

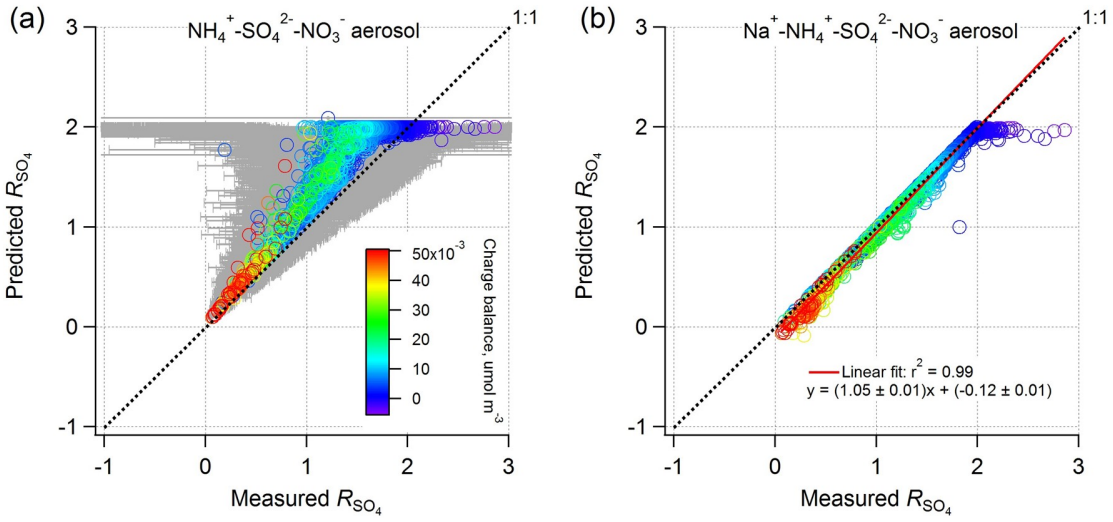

Figure 6-6 Comparison between PM_1 ISORROPIA-predicted R_{SO4} and AMS-measured R_{SO4} ($R_{SO4} = (NH_4^+ - NO_3^-)/SO_4^{2-}$) (mol mol^{-1}), where the ISORROPIA-prediction is based on (a) NH_4^+-SO_4^{2-}-NO_3^- aerosol and (b) Na^+-NH_4^+-SO_4^{2-}-NO_3^- aerosol constrained by HNO_3. All measurement data are from the WINTER study. NVC was determined by an ion charge balance with the molar concentration shown as the color wave. For this data, the average predicted Na^+ concentration is 0.15 μg m^{-3}, comparable to the offline PILS fraction collector IC-measured PM_1 Na^+ of 0.23 μg m^{-3}. The one SD uncertainty range for the measured R_{SO4} is shown as gray error bars. The data points with low SO_4^{2-} levels (<0.2 μg m^{-3}; 9% of the total points) were excluded for high uncertainties. In both plots, the molar ratios are zero when concentrations of NH_4^+ are near zero and NVC concentrations highest. In plot (a), as molar ratios approach 2, predicted NVC levels drop, but the effect of not including them in the thermodynamic model results in larger deviations in predicted versus

measured R_{SO4}. Error bars also increase due to subtraction of higher concentrations of nitrate and thus more subject to measurement error. As with the SOAS data, including NVC in the model results in agreement between predicted and measured ammonium-sulfate molar ratios.

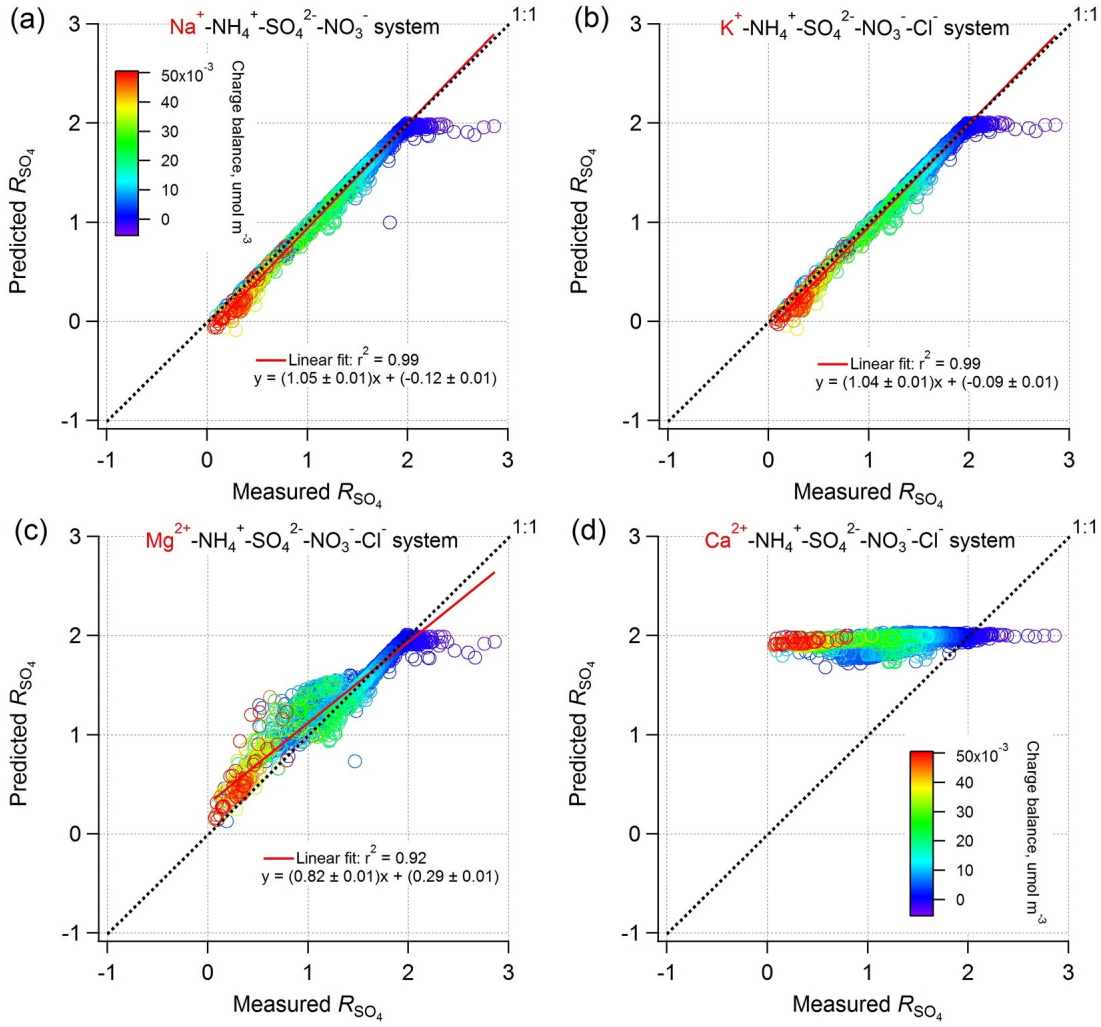

Figure 6-7 Comparison between ISORROPIA-predicted and AMS-measured PM_1 R_{SO4}, where the model predictions are based on NVC-NH_4^+-SO_4^{2-}-NO_3^-(-Cl^-) system for the WINTER study. NVC (nonvolatile cation) was determined by an ion charge balance (color wave), that is, ($2SO_4^{2-} + NO_3^- - NH_4^+$) in units of μmol m^{-3}. This results in 200% mole-equivalent concentrations of Na^+ and K^+ compared to Ca^{2+} and Mg^{2+} due to +1 versus +2 charges. NH_4^+, SO_4^{2-}, NO_3^- are observed AMS mass concentrations. For each graph, NVC is set to be a single species, including (a) Na^+, (b) K^+, (c) Ca^{2+}, (d) Mg^{2+}. For K^+, Ca^{2+}, and Mg^{2+}, the assumed trace amount of total chloride (0.01 μg m^{-3}) doesn't perturb normal calculations of pH or HNO_3-NO_3^- partitioning at all for only 0.0012 μg m^{-3} Cl^- (12% of total chloride) predicted in the aerosol, but eliminates potential model errors. (Note that,

Cl^- is only assumed for ISORROPIA input but not included in the charge balance calculation. The predicted 0.0012 μg m^{-3} Cl^- is negligible compared to NH_4^+, SO_4^{2-}, and NO_3^-.) Adding Na^+ and K^+ results in predicted R_{SO4} agreeing with measured R_{SO4}. Mg^{2+} also results in closer agreement, although some points deviate. Ca^{2+} doesn't work at all as it precipitates out from the aqueous phase as $CaSO_4$. The solubility of $CaSO_4$ is only 0.2 g per 100 mL water at 20 °C. An approximate calculation on $CaSO_4$ solubility shows that the average predicted particle liquid water W_i (2.0 μg m^{-3}) could only dissolve 0.004 μg m^{-3} Ca^{2+}, a tenfold lower amount than the inferred Ca^{2+} of 0.13 μg m^{-3} from an ion charge calculation. ODR fits are shown and uncertainties in the fits are one SD.

6.4.4 Effects of not fully considering NVC of pH

The molar ratios and pH reported for SOAS [*Guo et al.*, 2015] and WINTER [*Guo et al.*, 2016] may exhibit biases since NVCs were not fully considered. This was because the NVC (Na^+, K^+, Ca^{2+}, Mg^{2+}) concentrations were low, often close to or below the PILS-IC LOD during the SOAS study (the 1st half period measuring $PM_{2.5}$ and the 2nd half period measuring PM_1 with even lower NVC) and not measured by an AMS during the WINTER study. We have discussed the effect of NVC on R and R_{SO4} above, here we focus on the effect on pH and the implications.

Here we use the inferred Na^+ calculated from the ion charge balance as representative of generic NVCs (valence of one), to investigate the impacts on pH and molar ratios from NVCs if not fully considered. A varying Na^+ input from 0 to 1 μg m^{-3} was applied to the average conditions of the SOAS and WINTER studies; all other model inputs, including composition and meteorological conditions (RH & T), were unchanged in the simulation. An upper limit of 1 μg m^{-3} Na^+ was based on the maximum inferred levels in SOAS and WINTER studies, much higher than the measured levels of 0.1-0.2 μg m^{-3}. Figure 6-8

shows that pH responds linearly to the added Na^+ for a 0-0.6 μg m^{-3} Na^+ range for SOAS and a wider range of 0-1 μg m^{-3} for WINTER. The sensitivities of pH and molar ratios to NVC and the linear ranges of pH are different between the two studies because of differences in aerosol mass concentration and composition. For instance, SOAS aerosol was mainly composed of $(NH_4)_2SO_4$ and the WINTER aerosol was a mixture of $(NH_4)_2SO_4$ and NH_4NO_3, so adding Na^+ only perturbs NH_3-NH_4^+ partitioning in SOAS, but also affects HNO_3-NO_3^- partitioning in WINTER. Note that, 0.6 μg m^{-3} Na^+ accounts for 34% mole fraction of the average SOAS aerosol composition, a large number that can alter H_{air}^+ and W_i in the aerosol system. As a result, particle pH is changed accordingly. The R_{SO4} for WINTER decreases even below zero due to decreasing NH_4^+ (due to competition with Na^+) and increasing NO_3^- (due to higher pH) trends when adding Na^+ to the model input. Note that, R_{SO4} was typically observed above zero in the southeastern U.S. [*Hidy et al.*, 2014], which in turn sets an upper limit of the Na^+ as 0.48 μg m^{-3} that could be in the PM_1.

In our datasets, ion charge balance inferred Na^+ (or K^+, Mg^{2+}) is an upper limit (for assuming complete dissociation; e.g., all sulfate is in the form of SO_4^{2-}) on soluble NVC based on the observed NH_4^+-SO_4^{2-}-NO_3^- data, and satisfies the criterion of aerosol electrical neutrality. As shown above, H^+ is negligible in ion charge balance calculation even at such low pH of 1. Using an inferred Na^+ as a reference value, a worst case of zero NVC in the input results in an underestimation of pH by 0.32 for SOAS and 0.49 for WINTER, and overestimation of molar ratios by 0.58 for SOAS (R) and 0.62 for WINTER (R_{SO4}), respectively. Using measured Na^+ as input instead of zero NVC results in a difference in pH of –0.26 and 0.22, and in molar ratio of 0.46 (R) and –0.33 (R_{SO4}), for SOAS and

WINTER, respectively. NVCs are seen to have a larger effect on molar ratios than pH based on the regression slopes (see Figure 6-4), and the effect is even more pronounced considering observed ranges in molar ratios (R or R_{SO4} from 0 to 2) are less than pH (from –1 to 3) (see Figure 6-8) [*Guo et al.*, 2015; *Guo et al.*, 2016].

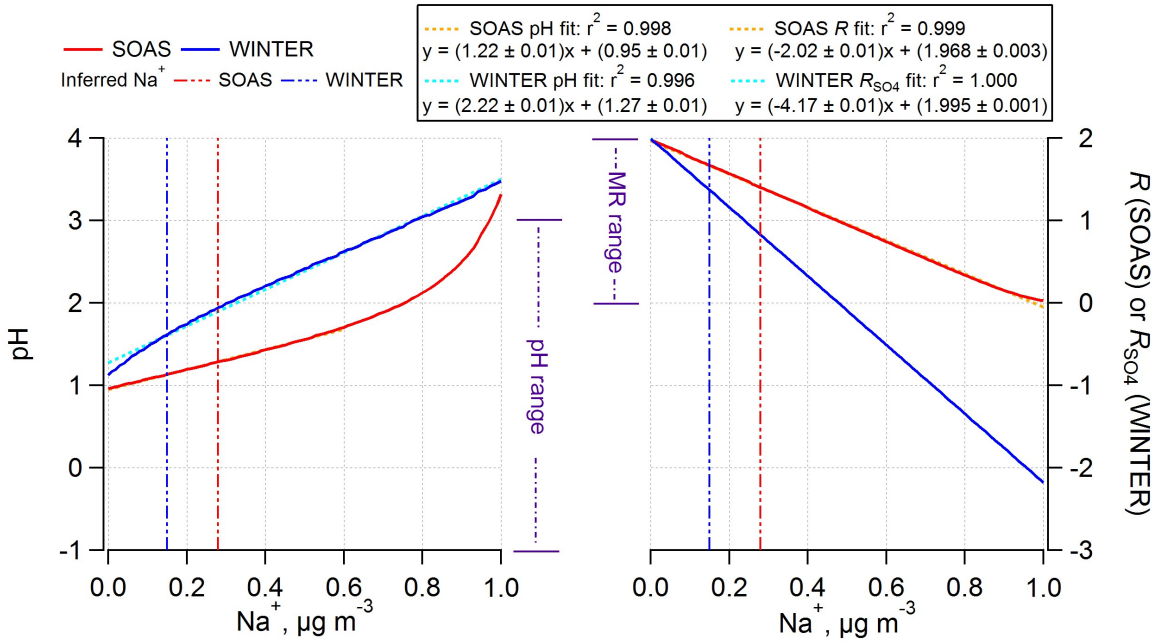

Figure 6-8 Predicted particle pH and molar ratios as a function of Na^+, $R = NH_4^+/SO_4^{2-}$ for SOAS and $R_{SO4} = (NH_4^+ - NO_3^-)/SO_4^{2-}$ for WINTER. In this sensitivity analyses, all model inputs are kept constant as the average SOAS or WINTER conditions and only Na^+ concentration varies. For the SOAS 12-day period (June 11-23) ISORROPIA-II inputs are: 2.03 μg m^{-3} SO_4^{2-}, 1.14 μg m^{-3} (NH_3 + NH_4^+), 0.23 μg m^{-3} NO_3^-, 0.03 μg m^{-3} Cl^-, zero K^+, Ca^{2+}, Mg^{2+}, and 68% RH, 298.2 K T. For the WINTER study, the inputs are: 1.02 μg m^{-3} SO_4^{2-}, 0.50 μg m^{-3} NH_4^+, 2.21 μg m^{-3} (HNO_3 + NO_3^-), zero Cl^-, K^+, Ca^{2+}, Mg^{2+}, and 58% RH, 272.1 K T. Average inferred Na^+ concentrations from the ion charge balance were 0.28 μg m^{-3} for SOAS and 0.15 μg m^{-3} for WINTER, shown as the vertical dashed lines. In comparison, average measured Na^+ was 0.06 μg m^{-3} in SOAS and 0.23 μg m^{-3} in WINTER. ODR fits are shown and uncertainties in the fits are one SD. Since the pH response to Na^+ in the SOAS study becomes nonlinear above 0.6 μg m^{-3} Na^+, the fit is only applied to the range below. Ranges in pH and molar ratios (R and R_{SO4}) in the eastern U.S. are shown as the purple marks.

As noted, NVC concentrations may be uncertain due to low concentrations, measurement uncertainties or not measured at all. Comparing observed and predicted partitioning of NH_3-NH_4^+ or HNO_3-NO_3^- provides insights on the accuracies of NVC concentrations used in the thermodynamic analysis. For example, as discussed above for the June 11-13 period in Figure 6-1, the model fairly accurately predicts NH_3-NH_4^+ partitioning with input of measured Na^+, whereas inclusion of inferred Na^+ does not produce as good a result. Overall, our previously reported pH for SOAS and WINTER studies appears sufficiently accurate for the majority of the data since the pH and predicted partitioning was in reasonable agreement with observed partitioning of NH_3-NH_4^+ or HNO_3-NO_3^- without ion charge balance inferred NVC as input. (For example, see the 12-day SOAS data (Figure 6-2) and the WINTER data for periods of 60-95% RH [*Guo et al.*, 2016]). However, during periods when a bias is observed between measured and predicted partitioning, including or slightly adjusting NVC concentrations can be tested as a possible cause (note that increasing NVCs always increases the pH).

Even though the effect of NVC on pH may appear relatively small (e.g., difference of 0.2 to 0.5 pH units) the impact on predicted partitioning of a semivolatile species can be significant due to the highly non-linear response of NH_3-NH_4^+ or HNO_3-NO_3^- partitioning to pH (i.e., S curve) [*Guo et al.*, 2016; *Guo et al.*, 2017a]. For example, for SOAS average conditions, a 0.3 unit pH bias (i.e., as noted above) results in ~ 20% bias in prediction of $\varepsilon(NH_4^+)$ or $\varepsilon(NO_3^-)$ when $\varepsilon(NH_4^+)$ or $\varepsilon(NO_3^-)$ = 50%, or no bias at all when the species are completely in one phase, $\varepsilon(NH_4^+)$ or $\varepsilon(NO_3^-)$ = 0% or 100%. For the WINTER data set, a 0.5 (see above) unit pH bias causes up to 30% bias in $\varepsilon(NH_4^+)$ or $\varepsilon(NO_3^-)$ (illustrated in

Figure 6-9). These partitioning biases may constitute a significant source of bias for aerosol nitrate formation, especially if the total nitrate present in the gas-aerosol system is significant. In fact, the bias from the NVC may completely change the predicted response of nitrate to aerosol emissions and lead to errors in the predicted vs. observed trends in pH, such as was seen in the southeastern U.S. [*Vasilakos et al.*, 2017].

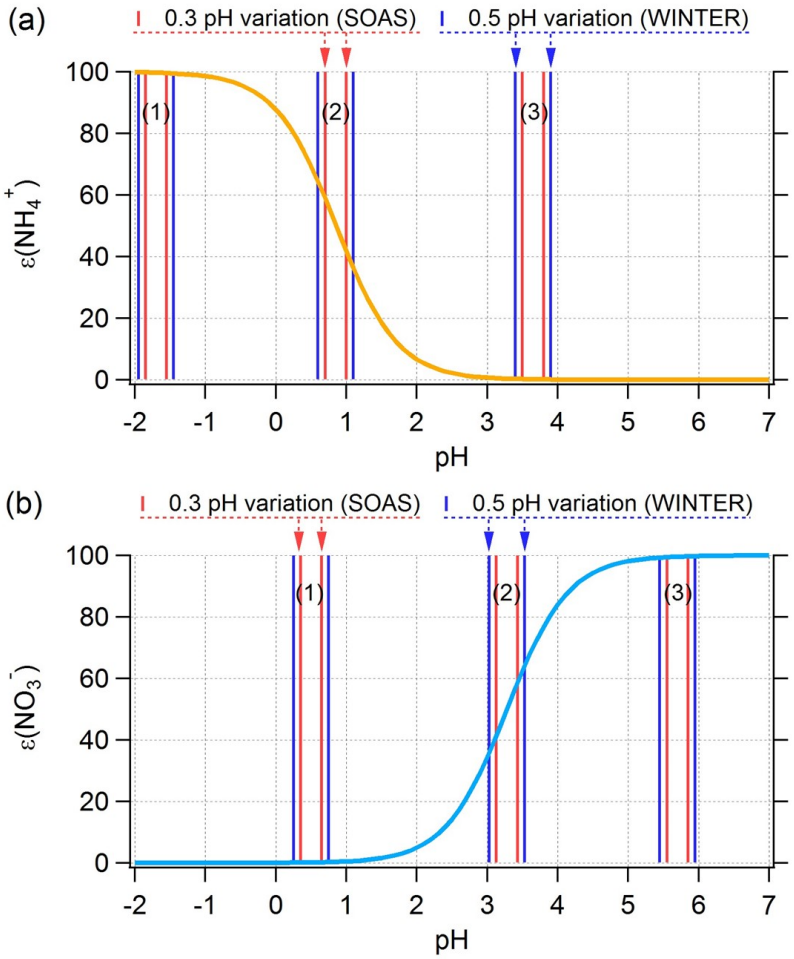

Figure 6-9 S curves illustrate the nonlinear response in particle phase fraction, $\varepsilon(NH_4^+)$ or $\varepsilon(NO_3^-)$, to variation in pH: (a) $\varepsilon(NH_4^+)$ and (b) $\varepsilon(NO_3^-)$ plotted vs. pH. The two S curves are calculated based on T = 20 °C, particle liquid water level = 5 μg m^{-3}, and ideal solution (i.e. γ = 1). The S curve equations can be found at *Guo et al.* [2017a]. Non-ideality only shifts the S curves but does not change the shapes. The 0.3 unit pH (SOAS) and 0.5 unit pH (WINTER) variations (biases) are the upper limit values based on the difference

between zero and inferred Na^+ inputs (Figure 6-8) and indicated by paired red and blue sticks, respectively. The response of $\varepsilon(NH_4^+)$ or $\varepsilon(NO_3^-)$ to pH reaches maximum at 50% $\varepsilon(NH_4^+)$ or $\varepsilon(NO_3^-)$ (i.e., position (2), 0.3 unit pH change causes ~20% or 0.5 unit pH change causes ~30% shift in the particle phase fraction), but down to nearly zero when 100% or 0% $\varepsilon(NH_4^+)$ or $\varepsilon(NO_3^-)$ (e.g. position (1) or (3)).

In our past studies, we also investigated trends in pH and molar ratios over time periods of changing emissions. Our interest was on the lack of change in pH over the past 15 years of despite a 70% reduction in sulfate aerosol (Figure 6-10) [*Weber et al.*, 2016] (CHAPTER 5 in the thesis). For example, *Weber et al.* [2016] reported thermodynamic calculations based on an average $PM_{2.5}$ and PM_1 PILS-IC Na^+ concentration of 0.03 μg m^{-3} from the SOAS study applied to all historical data (Fig. 2 in that paper). The Na^+ concentration was uncertain due to being significantly below the Na^+ measurement LOD (0.07 μg m^{-3}) and substantially lower than period average Na^+ of 0.28 μg m^{-3} calculated from a charge balance. This simplification did not consider historical Na^+ trends (although there was no trend in Na^+ mole fraction, see Figure 6-10). With a constant ISORROPIA Na^+ input of 0.03 μg m^{-3}, predicted R_{SO4} does not follow the widespread observed trend of R_{SO4} decreasing from 1998 to end of 2013 in the southeastern US, but instead was nearly constant at ~1.9. Repeating the calculations using Na^+ inferred from the ion charge balance of Na^+-NH_4^+-SO_4^{2-}-NO_3^-, determined for each daily data point, results in good agreement between observed and predicted R_{SO4}; ISORROPIA-predicted R_{SO4} now reproduces the observed decrease R_{SO4} trend (Figure 6-10 & Figure 6-11). In contrast, using these different Na^+ input concentrations did not change the trends in ISORROPIA-predicted pH, in both

cases it remained relatively constant (Figure 6-10), but as expected the pH was slightly higher with higher input Na^+ concentrations (i.e., from ion charge balance).

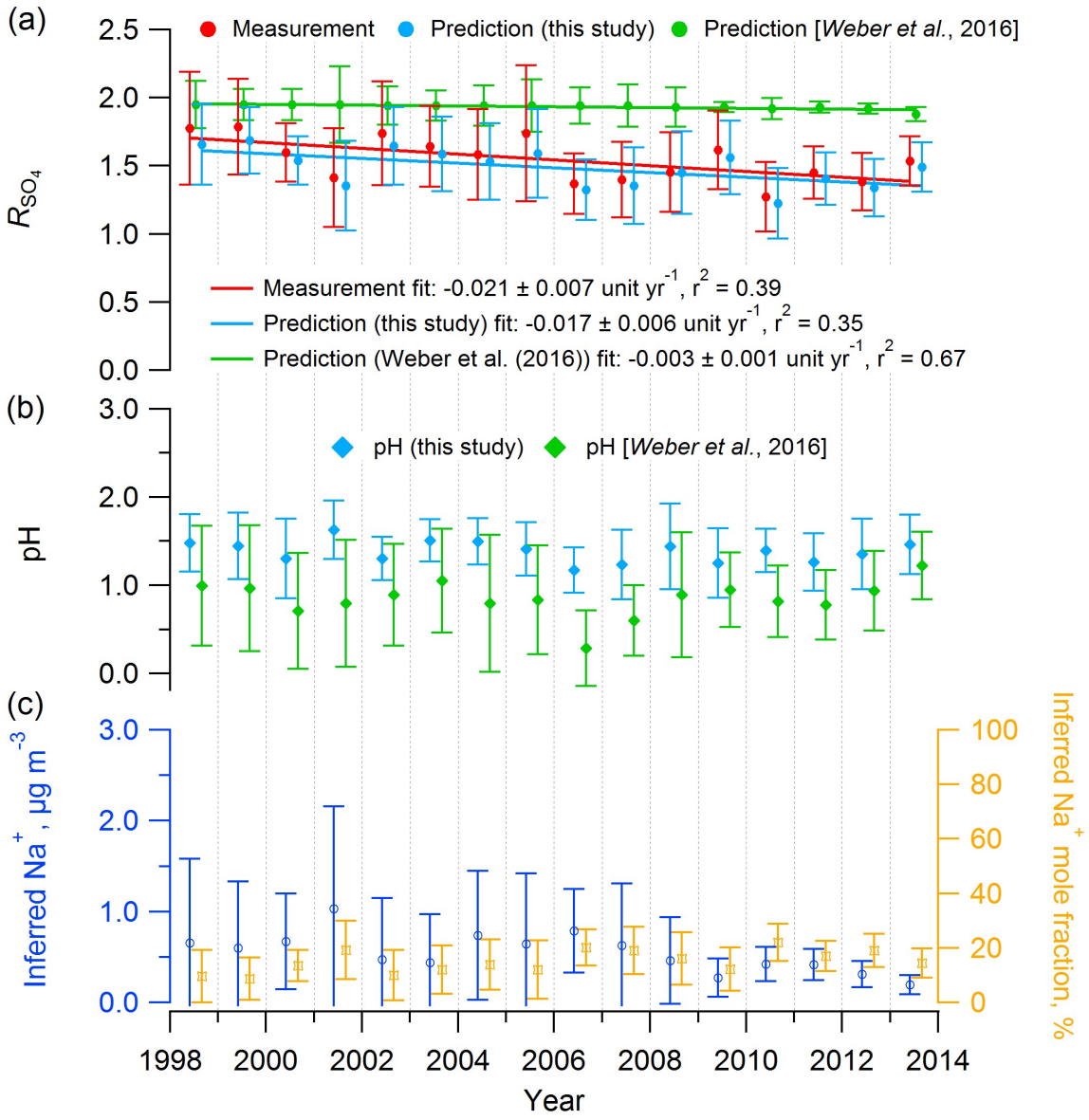

Figure 6-10 Mean summer (June–August) trends in (a) measured and predicted R_{SO4}, (b) predicted $PM_{2.5}$ pH, and (c) inferred Na^+ (from ion charge balance of Na^+-NH_4^+-SO_4^{2-}-NO_3^- aerosols) concentration and mole fraction at the SEARCH-CTR site. Model input includes the observational $PM_{2.5}$ composition data (NH_4^+, SO_4^{2-}, NO_3^-) and meteorological data (RH, T) at CTR. R_{SO4} and pH were estimated with ISORROPIA-II run in forward mode with an assumed NH_3 level of 0.36 µg m^{-3}, the mean concentration from the SOAS

study (CTR site, summer 2013), due to limited NH_3 data before 2008. Historical NH_3 mean summer concentration at CTR were 0.2 μg m^{-3} (2004-2007) [*Blanchard et al.*, 2013] and 0.23 ± 0.14 μg m^{-3} (2008-2013) [*Weber et al.*, 2016]. 41 out of the total 609 (7%) daily mean R_{SO4} were observed above 3 due to measurement error, above the upper limit of R_{SO4} = 2, therefore, excluded in the model input. Error bars represent daily data ranges (SD). Linear regression fits are shown and uncertainties in the fits are one SD. In (a), based on regression slope, the observed R_{SO4} trend was –0.021 ± 0.007 at CTR versus a predicted value of –0.017 ± 0.006 unit yr^{-1} for ISORROPIA run with Na^+ from the charge balance, and –0.003 ± 0.001 unit yr^{-1} for a constant Na^+ of 0.03 μg m^{-3}, used by *Weber et al.* [2016]. These results are consistent with the reported R_{SO4} trend of –0.01 to –0.03 yr^{-1} reported by *Hidy et al.* [2014] for SEARCH data set. In (b), the pH predictions with inferred Na^+ or with limited Na^+ of 0.03 μg m^{-3} shows a fairly stable $PM_{2.5}$ pH in the last 15 years. In (c), the inferred Na^+ shows a general decreasing trend while the inferred Na^+ mole fraction stays relatively stable around 15% (± 4%).

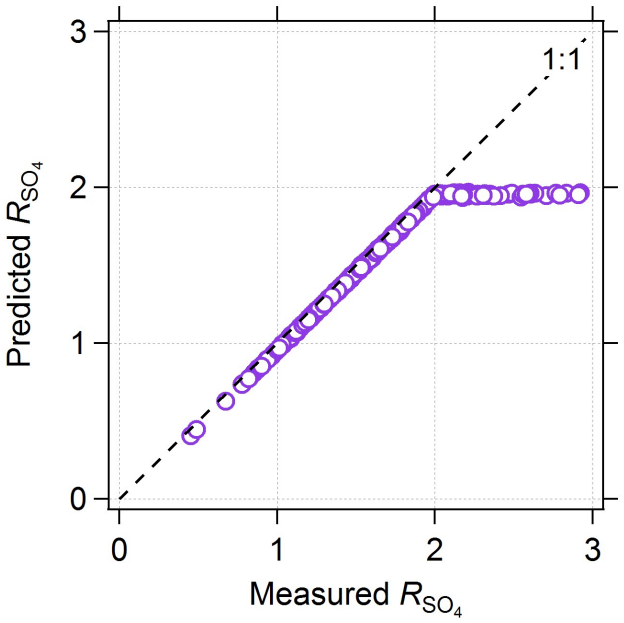

Figure 6-11 Comparison of the measured and predicted R_{SO4} (with inferred Na^+ as input), summer means at CTR, as shown in the Figure 6-10. The upper limit of R_{SO4} is 2 for a composition of $(NH_4)_2SO_4$ in ambient aerosols. A few observed points above 2 are results of measurement uncertainties.

6.5 Conclusion

Excluding minor amounts of submicron NVC in thermodynamic calculations results in predicted ammonium-sulfate molar ratios (*R*) near 2, which is generally higher than observed values. This results from the model criteria for aerosol electrical. Less absolute discrepancy is associated with predicted particle pH with or without NVC because pH is on a logarithmic scale of H_{aq}^{+} and the range of pH is larger than that of *R* (or R_{SO4}) in the eastern US. However, neglecting NVC can induce pH biases that imply important partitioning errors for semivolatile species like ammonium, nitrate, chloride, and even organic acids. An important finding is that including small amounts of NVCs in the thermodynamic model brings predicted and measured *R* into agreement. Because NVCs are often minor constituents of fine particles, especially PM_1, implying low ambient concentrations and high measurement uncertainties, assessing thermodynamic model predictions through molar ratios is problematic. Good agreement between predicted (with measured NVC in SOAS model input and no NVC in WINTER input) and measured partitioning of NH_3-NH_4^+ [*Guo et al.*, 2015; *Weber et al.*, 2016] (and this work), HNO_3-NO_3^- [*Guo et al.*, 2016] and water vapor-aerosol liquid water [*Guo et al.*, 2015] ideally with measured NVC as input, together with a lack of correlation of the bias with organic fraction discounts any influence of organic films and validates the thermodynamic equilibrium assumption for submicron aerosol. If organic films were limiting mass transfer, the discrepancy in *R* should worsen as the films become thicker. We find the opposite, the discrepancy in *R* is positively correlated with NVC and not correlated with the organic mass fraction or mass concentration. If NVCs were not measured, or significantly below

the measurement LOD, for the data sets investigated here, an ion charge balance could be used to inferred NVCs. Comparing measured and thermodynamic model predicted partitioning of semivolatile species provides insights on the importance of NVCs in the model predictions. Fully considering NVC doesn't change the finding of nearly constant fine particle pH in the southeastern U.S. (summertime) despite a large sulfate reduction, the result supported by predicting a R_{SO4} decreasing trend agreeable to the 15 years' observations. Overall, we find that the unique and non-intuitive behavior of pH reported in our past studies can be simply and consistently explained by thermodynamics without the need for organic films with selective ion transport properties.

CHAPTER 7. THE SENSITIVITY OF PARTICLE PH TO AMMONIA: CAN HIGH AMMONIA CAUSE LONDON FOG CONDITIONS?

7.1 Abstract

High levels of ammonia (NH_3) have been suggested to elevate ambient particle pH levels to near neutral acidity (pH = 7), a condition that promotes rapid SO_2 oxidation by NO_2 to form aerosol sulfate concentration consistent with "London fog" levels. This postulation is tested using aerosol data from representative sites around the world to conduct a thorough thermodynamic analysis of aerosol pH and its sensitivity to NH_3 levels. We find that particle pH, regardless of ammonia levels, is always acidic even for the unusually high NH_3 levels found in Beijing (pH = 4.5) and Xi'an (pH = 5), locations where sulfate production from NO_x is proposed. Therefore, major sulfate oxidation through a NO_2-mediated pathway is not likely in China, or any other region of the world (e.g., U.S., Mediterranean) where the aerosol is consistently more acidic. The limited alkalinity from the carbonate buffer in dust and sea-salt can provide the only likely set of conditions where NO_2-mediated oxidation of SO_2 outcompetes with other well-established pathways. The mildly acidic levels associated with excessive amounts of ammonia can promote high rates of SO_2 oxidation through transition metal chemistry, this may be an alternative important aerosol chemical contributor to the extreme pollution events.

7.2 Introduction

pH is a fundamental particle property that affects aerosol formation, composition, toxicity and nutrient delivery [*Gwynn et al.*, 2000; *Jang et al.*, 2002; *Meskhidze et al.*, 2003; *Guo et al.*, 2016; *Longo et al.*, 2016; *Fang et al.*, 2017]. Sulfate is a ubiquitous inorganic aerosol species that strongly regulates aerosol acidity and is produced by aqueous and gas phase oxidation of SO_2 along well-established pathways. Aqueous pathways dominate depending on the pH level (O_3 under alkaline and H_2O_2 under acidic conditions [*Seinfeld and Pandis*, 2006]). Aqueous oxidation of bisulfite (HSO_3^-) has recently been proposed as the major mechanism of haze formation in China but requires fine particle pH levels that are close to neutral (pH 6-7) or higher [*Cheng et al.*, 2016; *Wang et al.*, 2016]. It is well-known that upon emission, fresh dust or sea-salt particles can have a pH level that exceeds 6 [*Katoshevski et al.*, 1999; *Stockdale et al.*, 2016], hence provide aerosol where NO_2-mediated oxidation of sulfate is possible; however, the acidic sulfate that forms upon these particles rapidly depletes their alkaline carbonate buffer and limits any substantial NO_2-mediated production of sulfate. Acidification is fast for submicron particles, since acidic gases (e.g., HNO_3 and H_2SO_4) are rapidly scavenged by alkaline aerosols [*Hanisch and Crowley*, 2001; *Meskhidze et al.*, 2005], dust and sea-salt are only minor ionic fractions compared to sulfate and nitrate [*Fang et al.*, 2017], and equilibrium states with gases are typically achieved within 30 minutes under ambient conditions [*Dassios and Pandis*, 1999; *Cruz et al.*, 2000; *Fountoukis et al.*, 2009]. The good agreements between model and observation for the semivolatile species partitioning of NH_3-NH_4^+ and HNO_3-NO_3^- species, using aerosol bulk properties as model input, suggest the thermodynamic equilibrium states in many circumstances and that the ambient fine mode aerosol is consistently (and often

strongly) acidic [*Fountoukis and Nenes*, 2007; *Guo et al.*, 2015; *Guo et al.*, 2016; *Guo et al.*, 2017a]. Unlike fine haze particles, fogs and cloud drops can have pH closer to neutral owing to dilution of H^+ by the orders of magnitude more liquid water.

Wang et al. [2016] and *Cheng et al.* [2016] argue that very high levels of NH_3 from intense agriculture (e.g., up to 50-60 ppbv in Beijing and Xi'an, China) can sufficiently elevate pH in fine mode aerosol (PM_1 and $PM_{2.5}$) to promote rapid sulfate formation from NO_2 oxidation of SO_2. We explore this by carrying out a thorough thermodynamic analysis with the ISORROPIA-II model [*Guo et al.*, 2015] for conditions of aerosol and gas phase constituents that characterize a broad range of aerosol acidities and drivers thereof. We limit our analysis to fine mode ($PM_{2.5}$) aerosol, as the majority of the sulfate mass resides in that fraction [*Tian et al.*, 2014; *Fang et al.*, 2017] (hence its pH being the most relevant for sulfate formation), and which is also the size range where thermodynamic analysis for acidity inference works best [*Guo et al.*, 2015; *Guo et al.*, 2016; *Weber et al.*, 2016; *Guo et al.*, 2017a].

7.3 Methods

pH affects the equilibrated partitioning of semivolatile compounds, such as NO_3^- and NH_4^+, between gas and particle phases. Based on this sensitivity, the current most reliable method for fine particle pH is via prediction through a thermodynamic model, such as ISORROPIA-II, with gas and particle phase concentrations, and meteorological conditions (RH&T) as model input. ISORROPIA-II computes the equilibrium composition of an

NH_4^+-SO_4^{2-}-NO_3^--Cl^--Na^+-Ca^{2+}-K^+-Mg^{2+}-water inorganic aerosol (available online at http://isorropia.eas.gatech.edu) [*Nenes et al.*, 1998; *Fountoukis and Nenes*, 2007].

$$pH = -\log_{10}\gamma_{H^+}H^+_{aq} = -\log_{10}\frac{1000\gamma_{H^+}H^+_{air}}{W_i + W_o} \cong -\log_{10}\frac{1000\gamma_{H^+}H^+_{air}}{W_i} \quad (7\text{-}1)$$

pH is defined as the hydrogen ion activity in an aqueous solution [*Stumm and Morgan*, 1996], where γ_{H^+} is the hydronium ion activity coefficient (assumed as one; discussed further below), H^+_{aq} (mole L^{-1}) is the hydronium ion mole fraction in particle liquid water, H^+_{air} (μg m^{-3}) is the hydronium ion concentration per volume of air, and W_i and W_o (μg m^{-3}) are the bulk particle water concentrations associated with inorganic and organic species, respectively. W_o needs to be calculated independently by Equation 5 in *Guo et al.* [2015], while both H^+_{air} and W_i are the outputs of ISORROPIA-II. Particle liquid water (W_i + W_o), which is essential for pH calculation, is well predicted compared to the measurement [*Guo et al.*, 2015]. Due to a small bias between 0 and −0.2 pH often found without considering W_o in the pH calculation (the logarithmic nature of pH) [*Guo et al.*, 2015; *Guo et al.*, 2016; *Guo et al.*, 2017a], in this study we only calculate pH based on W_i, a reasonable assumption given the lower organic mass fraction reported in Beijing (on average 20-60%) [*Cheng et al.*, 2016; *Wang et al.*, 2016] compared to the southeastern U.S. (on average 60%) [*Xu et al.*, 2015a] resulting in an even smaller effect of organic particle water on pH.

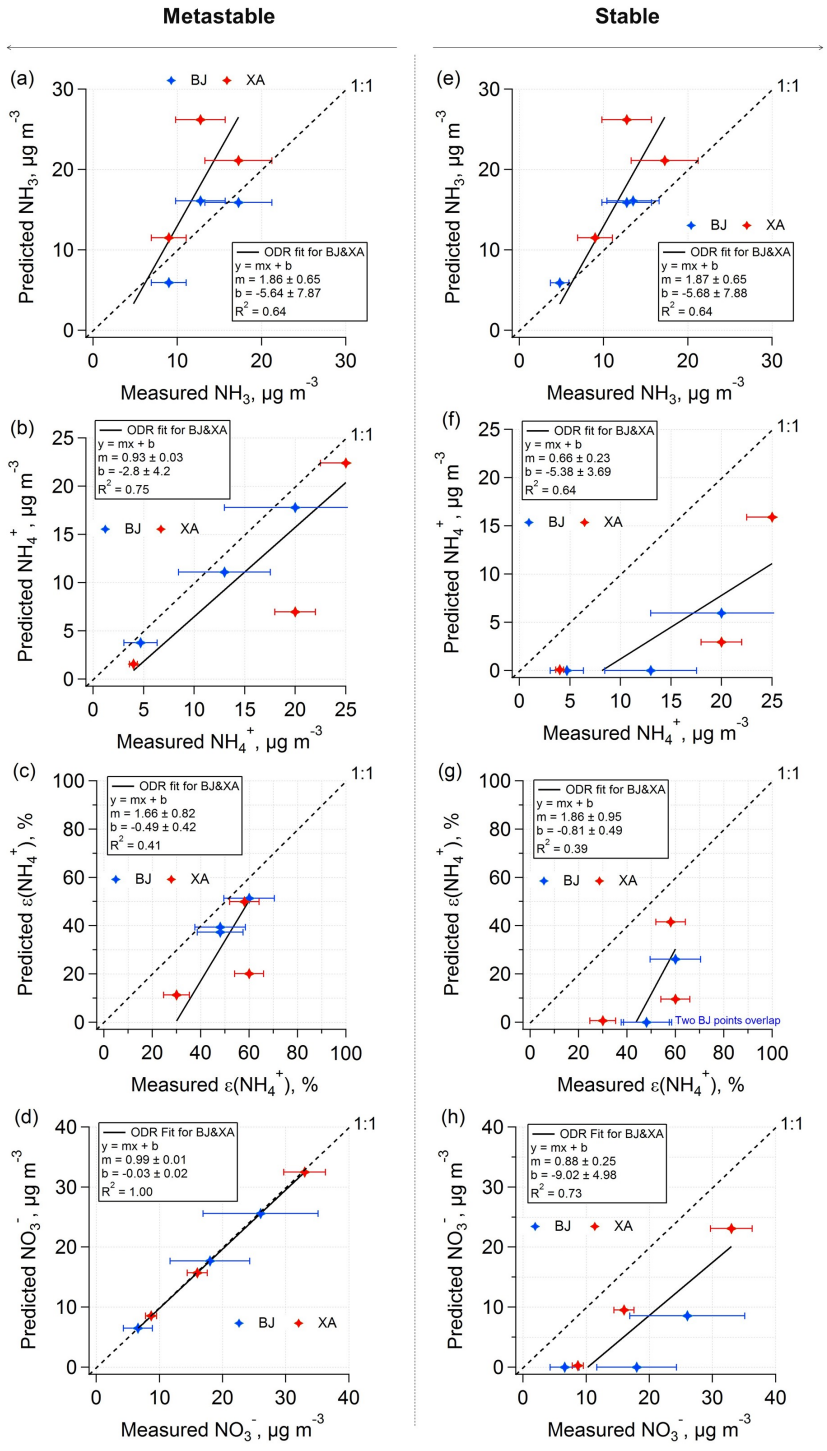

Figure 7-1 Comparisons of predicted and measured NH_3, NH_4^+, $\varepsilon(NH_4^+)$ (ammonium particle phase fraction, $NH_4^+/(NH_4^+ + NH_3)$), NO_3^- for metastable mode (left: a-d) and stable mode (right: e-h) runs in ISORROPIA-II. Data input are the average aerosol&gas concentrations and RH&T reported in *Wang et al.* [2016] (Table S1&S2) for Beijing (BJ)

and Xi'an (XA) for clean, transition, and polluted periods. For HNO_3-NO_3^- partitioning, only NO_3^- is plotted for lack of HNO_3 data, which is predicted to be < 1% of NO_3^- on condition of high pH in BJ and XA. Orthogonal distance regression (ODR) fits are shown and uncertainties in the fits are one standard deviation. Measurement uncertainties are shown as error bars. Since the *Wang et al.* [2016] and related papers didn't specify the measurement uncertainties, a typical 35% AMS measurement uncertainty was used for Beijing PM_1 data [*Bahreini et al.*, 2009], and a 10% measurement uncertainty assumed for Xi'an $PM_{2.5}$ data based on the MARGA methodology [*Makkonen et al.*, 2012; *Rumsey et al.*, 2014]. NH_3 was measured by MARGA in Beijing and Xi'an. According to *Rumsey et al.* [2014], an 23% measurement uncertainty is assumed for NH_3. The uncertainties in $\varepsilon(NH_4)^+$ are calculated based on error propagation of the NH_3 and NH_4^+ measurements.

ISORROPIA-II assumes γ_{H^+} as unity, however, the activity coefficients of the other water-soluble ions are calculated as ionic pairs (including H^+, e.g. H^+-NO_3^-). The pH calculated from this method is proven to be similar to models that specifically calculate γ_{H^+}, such as E-AIM [*Hennigan et al.*, 2015], and observed and predicted gas-particle partitioning of semivolatile species are in good agreement [*Guo et al.*, 2016; *Guo et al.*, 2017a]. We note that it is difficult to retrieve activity coefficients in concentrated aqueous solutions. The ISORROPIA-II has been tested by several ambient particle datasets with strong ionic strength, for example, the mean ionic strength 38 mole L^{-1} in the eastern U.S. [*Guo et al.*, 2016]. The ionic strength in Beijing haze polluted period (36 mole L^{-1}) is on the same magnitude despite the much higher particle mass loadings (i.e. more particle water).

Details on how the model was run (e.g., forward mode, metastable aerosols), an extensive uncertainty analyses, and predictions of pH at various sites in the southeastern US are discussed in *Guo et al.* [2015]. The pH predictions are accurate to a high degree based on the consistency between the predicted and measured partitioning of NH_3-NH_4^+ or HNO_3-NO_3^- examined in a number of studies in various locations from summer to winter

conditions [*Guo et al.*, 2015; *Hennigan et al.*, 2015; *Bougiatioti et al.*, 2016; *Guo et al.*, 2016; *Weber et al.*, 2016; *Bougiatioti et al.*, 2017; *Guo et al.*, 2017a]. The thermodynamic model results are further supported by a single pair of semivolatile partitioning calculation, which appears as "S curves" and are thoroughly discussed in the section 3.6 of *Guo et al.* [2016] and in the section 4.2 of *Guo et al.* [2017a], respectively. In applying ISORROPIA-II, we assumed no compositional dependence on particle size, treating the measured chemical constituents as bulk PM_1 or $PM_{2.5}$ properties, and that the aerosol (NH_4^+, SO_4^{2-}, NO_3^-) was internally mixed and composed of a single aqueous phase that contained the inorganic species, without phase separations that could affect pH (along with partitioning of semivolatile inorganic species). In Beijing and Xi'an, the large amounts of nitrates present in the aerosol (which exhibit very low efflorescence relative humidity) and other dissolved electrolytes and organics that further depress crystallization [*Seinfeld and Pandis*, 2006] strongly favor the presence of a single aqueous phase. pH calculated under these assumptions (bulk properties, no phase separations, dissolved components in equilibrium with the gas phase) is supported by the ability of ISORROPIA-II to reproduce independently measured gas and particle phase semivolatiles concentrations (e.g. NH_3, HNO_3, HCl). It should be noted that *Wang et al.* [2016] heavily relied on the usage of aerosol molar ratios as a proxy of acidity, which have been shown to not represent pH well [*Guo et al.*, 2015; *Hennigan et al.*, 2015; *Guo et al.*, 2016; *Weber et al.*, 2016]. pH levels reported in that study were carried out with ISORROPIA-II but in stable mode and were evaluated only by predicted equilibrium NH_3 levels by the model. Evaluation of model pH based on predicted NH_3 (or HNO_3) alone is insufficient because gas phase predictions are

insensitive to pH errors (Figure 7-1; also shown as Figure B-3 for HNO_3). Particle phase concentrations, such as NH_4^+, NO_3^-, Cl^-, are however sensitive to the assumption of phase state assumed by ISORROPIA-II and should be used for evaluation purposes (Figure 7-1), which were not carried out by *Wang et al.* [2016]. When carrying out such an evaluation (Figure 7-1), the metastable option reproduces aerosol NH_4^+, NO_3^-, Cl^- considerably better than assuming a stable aerosol, hence pH calculations from the metastable option of the model are more consistent with observed thermodynamic partitioning, hence used here. Comparing measured and predicted particle-phase fractions (e.g. $\varepsilon(NH_4^+) = NH_4^+/(NH_4^+ + NH_3)$) provides a means for evaluation of the predicted pH. *Cheng et al.* [2016] also carried out estimates of aerosol pH using ISORROPIA-II with the assumption of metastable aerosol, but a combination of forward and reverse-mode calculations were used; the strong dependence of pH with size [*Fang et al.*, 2017] and the extreme sensitivity of ammonia equilibrium vapor pressure to small errors in aerosol NH_4^+ when pH approaches neutral conditions [*Hennigan et al.*, 2015] also makes pH assessments subject to considerable uncertainty.

The approach for generating the contour plots of Figure 7-2 is as follows. Average RH, T, and total NO_3^- ($HNO_3 + NO_3^-$) for the eastern US or Beijing in wintertime, along with a selected sulfate concentration, are input to ISORROPIA-II. Total NH_4^+ ($NH_3 + NH_4^+$) is left as the free variable. The equilibrium concentrations of various components (e.g., gas phase NH_3, and particle phase NH_4^+, SO_4^{2-}, and NO_3^-) and particle pH (along with other variables) are predicted by ISORROPIA-II. Data for the contour plots are generated by varying sulfate from 0.1 to 100 μg m^{-3} while equilibrated NH_3 covers from a wide range

between 0.1 and 1000 μg m^{-3} (0.13 - 1333 ppbv at STP). The calculation of the sensitivity lines in Figure 7-2 utilizes a simpler approach than the above due to fixed sulfate concentration at the reported campaign averages, which can be found in Table 7-1.

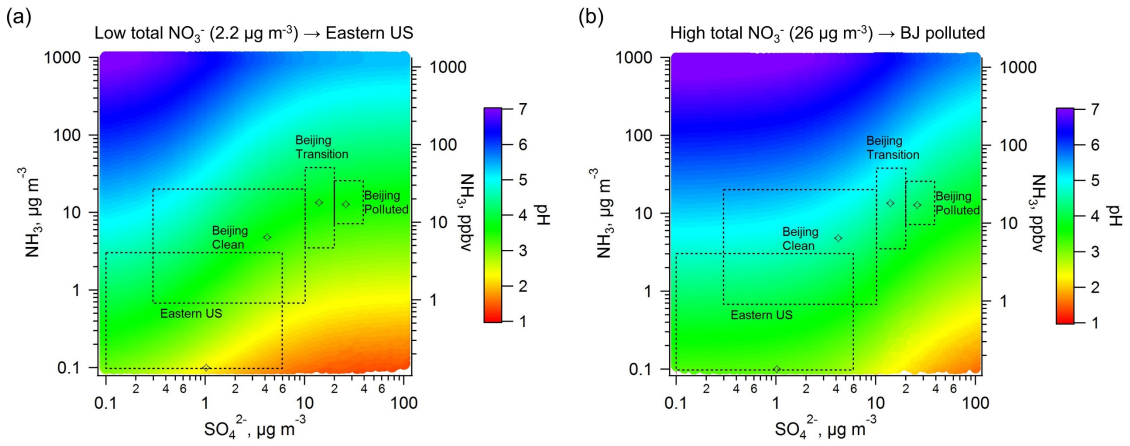

Figure 7-2 Sensitivity of PM_1 pH to gas-phase ammonia (NH_3) and PM_1 sulfate (SO_4^{2-}) concentrations. The results are predictions from a thermodynamic analysis assuming equilibrium between the gas and particle phases for typical winter conditions (RH = 58%, T = 273.1K) in (a) the eastern U.S. with low total NO_3^- (HNO_3 + NO_3^-) concentrations, 2.2 μg m^{-3}, and (b) Beijing haze pollution periods with high total NO_3^-, 26 μg m^{-3}. Boxes define observed concentration ranges for the eastern U.S. and Beijing and open symbols represent mean NH_3 and SO_4^{2-} conditions. Average total NO_3^- for eastern U.S., Beijing (BJ) clean, BJ transition, BJ polluted were 2.2, 6.6, 18, 26 μg m^{-3}, respectively. Since total NO_3^- during Beijing clean and transition periods were 6.6 μg m^{-3} and 18 μg m^{-3}, respectively, graph (a) better represents the Beijing clean period and graph (b) better for the Beijing transition period.

Table 7-1 The study average aerosol composition and meteorological conditions for Figure 2 ISORROPIA-II input. The reported concentrations and RH, T are based on field measurements unless noted specifically. Total NH_4^+ (NH_3 + NH_4^+) is left as the free variable for ISORROPIA-II calculations. The high pH predicted at Beijing and Xi'an indicate > 99% total NO_3^- (HNO_3 + NO_3^-) is NO_3^-, so no report of HNO_3 data causes negligible bias.

Region/Location	SE US	NE US	SW US		Greece	Beijing, China		Xi'an, China	
Campaign	SOAS	WINTER	CalNex		(Biomass burning)[d]	(Clean)	(Polluted)	(Clean)	(Polluted)
Sampling type	Ground	Aircraft	Ground	Ground	Ground	Ground		Ground	
PM cut size	PM_1&$PM_{2.5}$[a]	PM_1	PM_1	$PM_{2.5}$[c]	PM_1	PM_1		$PM_{2.5}$	
Year	2013	2015	2010		2012&2014	2013		2013	
Season	Summer	Winter	(Early) Summer		Summer&Winter	Winter		Winter	
Na^+, μg m^{-3}	0.03	0	0	0.77	0.08	0	0	3.6	4.2
SO_4^{2-}, μg m^{-3}	1.73	1.02	2.86	1.88	1.66	4.2	14	5.9	38
Total NH_4^+, μg m^{-3}	0.78	0.50	3.44	2.54	1.02	9.5	33.5	13	44.3
Total NO_3^-, μg m^{-3}	0.45	2.21	10.22	8.19	3.36	6.6	18	8.7	33
Cl^-, μg m^{-3}	0.02	0	0	0.64	0.20	0.8	1.6	4.0	14
Ca^{2+}, μg m^{-3}	0	0	0	0	0	0	0	1.6	2.3
K^+, μg m^{-3}	0	0	0	0	0.36	0	0	1.3	4.6
Mg^{2+}, μg m^{-3}	0	0	0	0	0	0	0	0.2	0.3
RH, %	74	58	79	87	68	40[e]	56	46	68
T, °C	25	0	18	18	20	0.4	0.9	5.7	4.1
NH_4^+, μg m^{-3}	0.46	0.50	2.06	1.79	1.02	4.7	20	4.0	25
NH_3, μg m^{-3}	0.39	0.10[b]	1.37	0.75	\	4.8	13.5	9.0	17.3
NO_3^-, μg m^{-3}	0.08	0.80	3.58	3.74	1.79	6.6	18	8.7	33
HNO_3, μg m^{-3}	0.36	1.41	6.65	4.45	0.91	\	\	\	\
Reported pH	0.9 ± 0.6	0.8 ± 1.0	1.9 ± 0.5	2.7 ± 0.3	2.8 ± 0.6	\	\	\	\
Reference	[*Guo et al.*, 2015]	[*Guo et al.*, 2016]	[*Guo et al.*, 2017a]		[Bougiatioti et al., 2016, 2017]	[*Wang et al.*, 2016]			

ISORROPIA-II input

[a] $PM_{2.5}$ was sampled in the 1st half and PM_1 sampled in the 2nd half of the study; various parameters were similar in both cases, crustal components were higher in $PM_{2.5}$, but generally low so differences had minor effects, e.g., $PM_{2.5}$ Na^+ was 0.06 ± 0.09 μg m^{-3} and PM_1 Na^+ was 0.01 ± 0.01 μg m^{-3}; [b] Prediction based on iteration; [c] Only the last week of CalNex; [d] Averaged from the identified biomass burning plumes from Crete and Athens studies due to the similar pH; [e] The reported 21% RH was too low for a completely aqueous aerosol, therefore, not suitable for discussion on pH and pH affected aqueous reactions in this study. An assumed 40% RH is applied, as the efflorescence RH of ammonium sulfate is right below 40% [*Tang and Munkelwitz*, 1994].

7.4 Results

To understand the major drivers of aerosol acidity, we explore pH levels for aerosol of increasing chemical complexity, and its sensitivity to NH_3 levels found throughout the world; we focus on two well-characterized "extremes" of anthropogenic influence: the relatively clean southeastern US and the heavily polluted regions of Beijing and Xi'an, China. In our analysis, we first focus on the simplest possible composition that is atmospherically relevant: aerosol dominated by NH_4^+, HSO_4^-/SO_4^{2-}, i.e., where the effects of NO_3^-, Cl^- or nonvolatile cations (Na^+, K^+, Ca^{2+}, Mg^{2+}) is negligible. The summertime southeastern US meets this criteria, and was thoroughly studied by *Weber et al.* [2016]; the same study predicted that large amounts of NH_3, ~ 160 μg m^{-3} (220 ppbv), is required for equilibrium with a deliquesced ammonium sulfate aerosol. Under such conditions, aerosol pH is equal to 3.2. The pH drops to about 0.1 for aerosol composed of deliquesced ammonium bisulfate, requiring a low gas-phase NH_3 level of 0.06 μg m^{-3} (0.08 ppbv) to be in equilibrium. The transition from NH_4HSO_4 to $(NH_4)_2SO_4$ aerosol increases equilibrium NH_3 by 2700 times and aerosol acidity by roughly 3 pH units, regardless of SO_4^{2-} level in the range of 0.1-10 μg m^{-3}. Expanding the thermodynamic analysis to include the effects of other minor inorganic constituents and organic water found in the southeastern US aerosol do not change this finding; hence a 10-fold increase in NH_3 increases aerosol pH by about one unit over a wide range of ambient NH_3 and SO_4^{2-} concentration (0.1-10 μg m^{-3}) [*Weber et al.*, 2016].

For a more chemically-complex aerosol, where pH is controlled by the NH_4^+, HSO_4^-/SO_4^{2-} and NO_3^- system (wintertime Beijing and Xi'an meet this criteria; [*Cheng et al.*, 2016;

Wang et al., 2016]), co-condensation of gas phase NH_3 occurs with HNO_3 to form NH_4NO_3 aerosol if the ambient temperature is low enough and sufficient liquid water content is present [*Guo et al.*, 2015]. This co-condensation also reduces the concentration of hydronium ions in the aerosol aqueous phase (i.e., increases pH) because the salts formed are less acidic than sulfate, and the additional condensed aerosol water further dilutes the aqueous phase [*Guo et al.*, 2016; *Guo et al.*, 2017a]. The response of pH to NH_3 in this more complex aerosol may differ from the simpler NH_4^+, HSO_4^-/SO_4^2 system discussed above. To study this, we carry out pH calculations for T and RH conditions representative of the eastern US and Beijing during wintertime (~0°C and 58% RH; [*Guo et al.*, 2016; *Wang et al.*, 2016]) under conditions of "low" ($HNO_3 + NO_3^-$ = 2.2 μg m^{-3}, characteristic of eastern US), and "high" ($HNO_3 + NO_3^-$ = 26 μg m^{-3}; characteristic of Beijing haze) total inorganic nitrate levels. The results of the simulations are shown in Figure 7-2a and b, respectively. Regardless of total NO_3^- concentration, at any SO_4^{2-} concentration from 0.1 to 100 μg m^{-3}, a 10-fold increase in NH_3 raises pH by one unit over a wide range of NH_3 concentrations (0.1 to 1000 μg m^{-3}). In Figure 7-2a, a weak sensitivity of pH to SO_4^{2-} is predicted for SO_4^{2-} above 10 μg m^{-3}, similar to the situation found in the southeastern US in summer [*Weber et al.*, 2016]. For this SO_4^{2-} range, SO_4^{2-} mass is high enough to dominate over any effect of NO_3^- on water uptake and pH, and maintains aerosol pH at 2.5 or below; for lower SO_4^{2-} concentrations, NO_3^- becomes increasingly important (for constant NH_3) and pH increases accordingly to levels that may range between 3 and 4.5 for atmospherically-relevant levels of NH_3. At higher levels of total nitrate (Figure 7-2b), the transition from SO_4^{2-}-controlled acidity (pH < 2.5) and NO_3^--dominant acidity (pH > 3)

occurs at levels above 100 μg m^{-3} SO_4^{2-}. Therefore, for conditions of modest sulfate and high ammonia and total nitrate levels, acidity in Beijing tends to be reduced compared to the southeastern US and is largely controlled by a "nitrate-dominated" pH level.

Based on the above, the important question on what controls aerosol pH can be seen to be the relative amounts of $HNO_3 + NO_3^-$, SO_4, and $NH_3 + NH_4^+$ of the system considered. The boxes indicated in Figure 7-2 define characteristic areas corresponding to eastern US and Beijing aerosol (similar RH and T in winter); the pH levels inside these boxes then characterize the inherent particle acidity level of each location. The NH_3 in the eastern US normally ranges between 0.1 and 2 μg m^{-3} with some extremes as high as 3-4 μg m^{-3} according to field measurements [*You et al.*, 2014a], and the Ammonia Monitoring Network (AMoN, http://nadp.sws.uiuc.edu/amon) [*Puchalski et al.*, 2015]. NH_3 levels in Beijing were observed to be much higher, up to 38 μg m^{-3} (51 ppbv), during a heavy haze event in 2015 (Table S2 in *Wang et al.* [2016]). SO_4^{2-} concentration in the same event reached a maximum of 38 μg m^{-3}. The lowest pH is predicted for the eastern US due to the lower NH_3 and SO_4^{2-} compared to Beijing in Figure 7-2. However, for a wide range in NH_3 and SO_4^{2-}, particle pH for Beijing during clean, transition, and polluted periods are all around 4, and do not exceed 5. Although an extreme maximum of 300 μg m^{-3} SO_4^{2-} was reported in another wintertime in Beijing in 2013 [*Cheng et al.*, 2016], the weak dependency of pH on SO_4^{2-} (> 10 μg m^{-3}) results in a somewhat lower pH but still within the sub-100 μg m^{-3} SO_4^{2-} ranges discussed above.

The main conclusions derived from Figure 7-2 do not change when the thermodynamic analysis is expanded to include a broader temperature range or the small amount of fine

mode nonvolatile cations found in each region. This is shown in Figure 7-3, which presents the equilibrium particle pH versus ammonia for summertime (T ~20 °C) and wintertime (T ~0 °C) conditions at different locations. Partitioning of NH_3 and HNO_3 towards particle-phase NH_4^+ and NO_3^- is enhanced in lower temperatures, which as expected tends to increase particle pH. All lines become parallel for > 20 μg m^{-3} NH_3, exhibiting a sensitivity of roughly one unit pH unit increase per 10-fold increase in NH_3. The slope of the eastern US summertime line (green) is constant throughout the entire NH_3 range due to negligible effects of NO_3^- or other nonvolatile cations on pH. The lowest range of NH_3 and pH (0.9) is also found in the eastern US in summer. Due to the impact of high HNO_3 and NO_3^- observed in the southwestern US, the lines shift to higher pH levels, despite a T, RH, and NH_3 range similar to the eastern U.S. In that case the study mean $PM_{2.5}$ pH (2.7) is nearly one unit higher than PM_1 pH (1.9) owing to nonvolatile cations from sea-salt being internally mixed with $PM_{2.5}$, confirmed by particle mixing states measurements and thermodynamic simulations [*Guo et al.,* 2017a]. The difference between the southwestern US PM_1 (red line) and $PM_{2.5}$ (orange line) decreases with NH_3, as the influence of seasalt on particle pH decreases as more and more ammonium nitrate forms. Biomass burning plumes observed in Greece reached the highest PM_1 pH (2.8) from the effects of K^+ and NH_3 co-condensation with HNO_3 [*Bougiatioti et al.,* 2016; *Bougiatioti et al.,* 2017] and the corresponding sensitivity line (yellow) converges with the southwestern US Some extreme concentrations of NH_3 (e.g. 10 μg m^{-3}) in the US would increase pH to 3.5 in summer conditions. In winter conditions, although the eastern U.S. line (purple) is very close to the Beijing lines (blue) and Xi'an polluted (black) line, the actual pH is much lower in the

eastern US due to a tenfold or more lower NH_3 concentration (on the level of 0.10 μg m^{-3}); by comparison, Beijing observed on average NH_3 4.8 μg m^{-3} and 12.8 μg m^{-3} during clean and polluted periods respectively, and Xi'an observed even higher NH_3 levels at 9.0 μg m^{-3} and 17.3 μg m^{-3} for clean and polluted periods. Owing to the high levels of NH_3, the PM_1 pH of Beijing is predicted to be 4.2 regardless of the air quality condition (clean or polluted), and the $PM_{2.5}$ pH of Xi'an are predicted to be 4.6 and 5.4. The highest pH in Xi'an is caused by a large fraction of nonvolatile cations (Na^+, Ca^{2+}, K^+, Mg^{2+}; 31% to total aerosol ions by moles); given however that Xi'an data corresponds to $PM_{2.5}$, and that the mixing state between the PM_1 and $PM_{2.5}$ can cause pH to vary up to 3 units [*Fang et al.*, 2017], it is likely that the aerosol pH in Xi'an exhibits a strong size-dependence that is not reflected in a simple bulk measurement and thermodynamic analysis used here. The maximum NH_3 in Beijing and Xi'an increase pH up to 4.5 and 5.0, respectively, while the maximum NH_3 in the southwestern US increases pH up to 3.3 in the summertime.

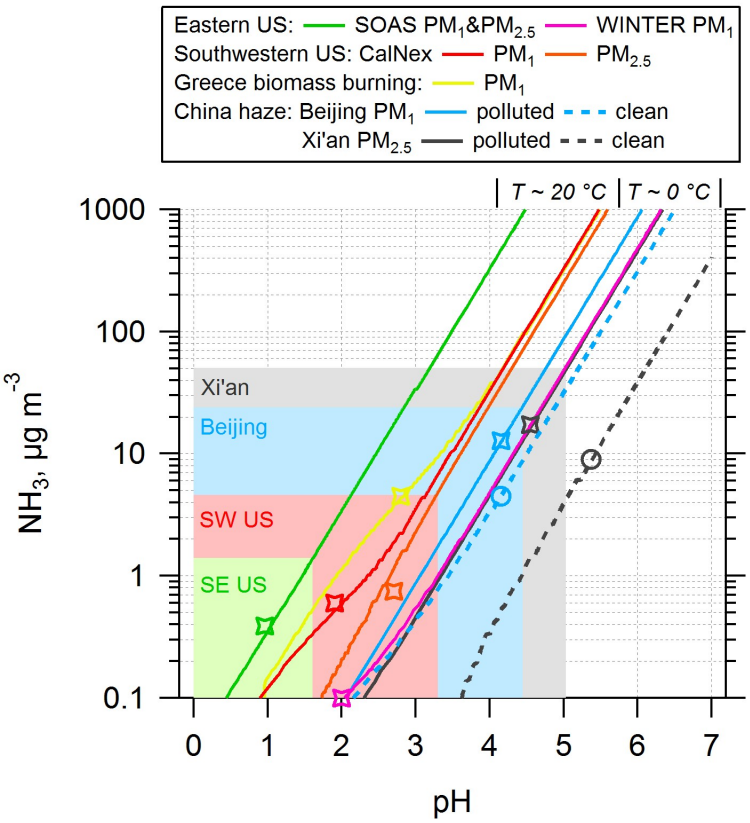

Figure 7-3 Equilibrium particle pH versus a wide range of ammonia (NH_3) based on average aerosol and meteorological conditions (RH, T) at each site. The open symbols are the study mean pH and NH_3, and shaded backgrounds show the upper limit of the pH range for each study (shading color matches color of study line given in the legend). Note that Xi'an polluted and WINTER PM_1 lines overlap showing inherent consistency between the two (also true for Beijing). For the WINTER study (the only aircraft data shown), the point represents a predicted NH_3 level 0.1 µg m^{-3} (pH = 2), whereas the reported campaign average pH (0.8 ± 1.0) is lower due to lower pH aloft.

7.5 Implications for sulfate formation mechanism

The sensitivity of pH to NH_3 is found to be similar between China and eastern US, despite the 10-fold or higher mass loadings of aerosols and gases of the former during intense haze pollution events. We show that for a given set of meteorological conditions (temperature and RH), roughly a 10-fold decrease in NH_3 concentrations is required to drop pH levels

by one unit, revealing an inherent consistency between vastly different aerosol systems. The pH levels between the eastern US, Beijing and Xi'an can indeed be related to the inherently different concentrations of NH_3 found in each environment. The average pH of Beijing PM_1 is predicted to be 4.2 (the same in clean and polluted periods), and the highest pH is about 4.5 for the maximum NH_3 levels observed. Nonvolatile cations do not appear to considerably affect $PM_{2.5}$ pH at Xi'an (12% mole fraction to total ions for the polluted period) compared to Beijing PM_1, except when these cations become a large fraction of $PM_{2.5}$ (31% mole fraction found during the clean period). Overall, Xi'an $PM_{2.5}$ may reach a slightly higher maximum pH (5.0) than Beijing, due to even higher NH_3 levels than Beijing. However, for all the pH ranges we find, none are in the range to provide consistent and sufficient alkalinity for the NO_2 oxidation pathway to overwhelm sulfate formation (Figure 7-4) based on the model of *Cheng et al.* [2016]. Given this, and that most of the sulfate forms where particles are most acidic (PM_1 or $PM_{2.5}$), it is unlikely that NO_2-mediated oxidation of SO_2 is a major SO_4^{2-} formation route. Under conditions where alkalinity is sufficient to promote NO_2 oxidation, it does not form due to the large amounts of NH_3, but rather only from the presence of nonvolatile cations, such as those found in mineral dust and sea-salt and associated carbonates that maintain pH at levels above 6. Because these species are generally limited to particles sizes larger than 1 μm diameter [*Fang et al.*, 2017], this route is highly unlikely to contribute to PM_1 sulfate production, including in Beijing [*Tian et al.*, 2014].

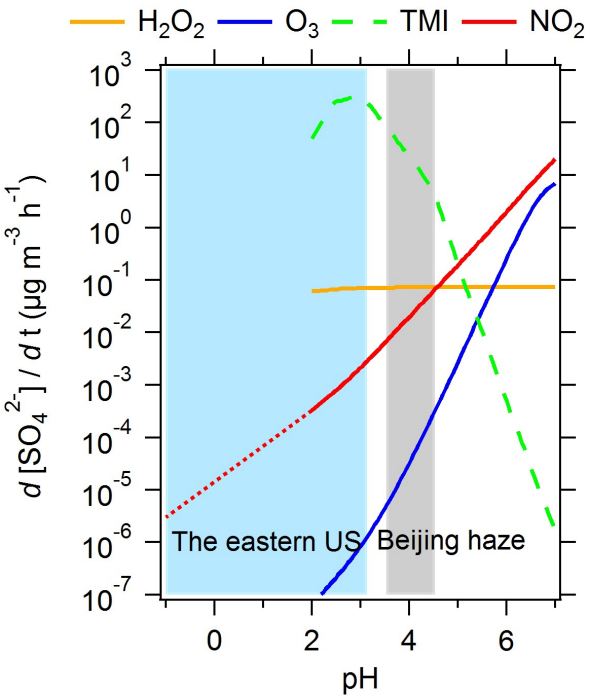

Figure 7-4 Aqueous phase sulfate production by sulfur dioxide oxidation under characteristic conditions adapted from *Cheng et al.* [2016] and plotted with pH ranges calculated in this study. Lines represent sulfate production rates calculated for different aqueous phase reaction pathways with oxidants: hydrogen peroxide (H_2O_2), ozone (O_3), transition metal ions (TMIs), and nitrogen dioxide (NO_2). The gray-shaded area indicates characteristic pH ranges for aerosols during severe haze episodes in Beijing, calculated in this study. These conditions are contrasted to the lower pH of eastern US aerosol. The plot shows the NO_2 pathway (red line) is not the main route for sulfate production.

The mildly acidic levels associated with excessive amounts of ammonia, however, could promote high rates of oxidation through transition metal chemistry, which overwhelms all other oxidation pathways for pH levels up to 4.5 (Figure 7-4). The observed high levels of soluble transition metals that coincide with sulfate at the particle level in the $PM_{2.5}$ range in US urban air masses [*Fang et al.*, 2017] and polluted air masses sampled off the coast of China [*Bougiatioti et al.*, 2017] supports that this may be an important pathway for explaining the high sulfate production rates, provided that the aerosol pH persists at the

levels predicted here for sufficient time for the slow acid dissolution process of recalcitrant species such as iron [*Meskhidze et al.*, 2003]. Our analysis shows that aerosol with neutral pH is highly unlikely to be driven by excessive amounts of NH_3; measurements of gas-phase and PM_1/$PM_{2.5}$ aerosol composition at rapid temporal resolution however are still required to show the frequency at which pH exceeds 4.5 during peak haze events, and whether it is possible to approach or exceed the pH 7.6 level in Beijing reported by *Wang et al.* [2016]. Our analysis also suggests this may not be likely, but measurements of size-resolved aerosol composition (including soluble transition metals) and gas-phase constituents at sufficient temporal resolution will provide the definitive observational constraints. We have shown that increasing NH_3 does not lead to a substantially more neutral aerosol, minimizing the importance of a proposed SO_2-NO_x sulfate formation route. An alternative explanation for the recent China winter haze events is changes in weather patterns that have strengthened stagnation conditions [*Zou et al.*, 2017].

CHAPTER 8. FUTURE WORK

The thesis presents the current most reliable method to quantify fine particle pH via a thermodynamic modeling with accurate observational aerosol and gas, RH and T data. pH is well constrained by sensitive gas-particle partitioning pairs, not completely in the gas or particle phase. The method shows agreement between predicted and observed particle liquid water, required for pH calculation. pH proxies, such as ion balance and molar ratio, have been widely used in the past analysis of particle acidity for lack of methods to retrieve particle pH. However, we have shown that those pH proxies are not reliable and don't necessarily correlate with pH. Improper use of pH proxies may lead to misunderstanding of particle acidity and its impacts on health and climate. The new pH prediction method allows a more accurate analysis either in lab or in field. The past analysis using pH proxies or measuring particle pH in dilute extracted solutions (not accurate, e.g., [*Last,* 1991]) to investigate particle acidity should be revisited. The new method also shows high potential of application in exploring unknowns, since the formation and evolution of aerosols are complex and not fully understood. For example, the haze events in China has caused severe and adverse impacts on public health and visibility but the mechanisms of haze formation have not been elucidated. The Chapter 7 presents the particle pH in China haze events and the production rate of aerosol sulfate is highly pH dependent. Therefore, pH is an important particle property that needs to be understood for effectively controlling haze in China.

We have two ongoing research projects following the thesis work. First, aerosol nitrate reduction has been a hot topic in areas with high nitrate abundance, such as Europe. Several

studies using regional or global models suggest that controlling ammonia that is mainly produced from agricultural activities is the key to reduce nitrate (e.g. [*Bauer et al.*, 2016; *Pozzer et al.*, 2017]). The conclusions require validations as the models used in those studies often have issues in predicting nitrate and nitric acid accurately. Our pH prediction method has shown the unique ability to accurately predicting HNO_3-NO_3^- partitioning and to concisely explain the interactions between the partitioning, pH, W_i, T, and activity coefficients by S curves in Chapter 3 and 4. The sensitivity of pH to ammonia has been extensively discussed in Chapter 5 and 7, showing an inherent consistency between vastly different aerosol systems: roughly 10-fold increase in ammonia is required to increase pH by one unit. Therefore, we have linked nitrate and ammonia via pH in the thesis work. We plan to look closely into the observational dataset collected in Cabauw, the Netherlands [*Schlag et al.*, 2016] and provide scientific evidence for nitrate reduction policies. Second, we focus on the gas-particle partitioning of inorganic species in the thesis and plan to investigate the organic acids that are also affected by pH and not well understood. Organic acids (e.g. formic acid and oxalic acid) are typically semivolatile and weaker than inorganic acids (e.g. sulfuric acid and nitric acid). Low particle pH in the SE US in summer time is expected to drive most organic acids into gas phase, but whether those organic acids are affected by pH and whether they are in thermodynamic equilibrium states require further investigation. The activity coefficients of organic acids are not well determined as inorganic acids, making the organic acids studies difficult, but could be constrained by S curves. Investigating organic acids may provide us insights on secondary organic aerosol formations. For example, oxalate is a product of many aqueous phase organic reactions.

One limitation with the new pH prediction method is the assumption of gas-particle equilibrium, that means it only works for fine particles that are in equilibrium but not for coarse particles that are probably not due to kinetic limitations. It also doesn't work for freshly formed fine particles that have not equilibrated with gas phase yet. The other limitation is that the new method is based on bulk aerosol properties input. Therefore, it captures the bulk (i.e., average) pH but cannot tell the pH variation range at a particle size. The new method should be compared to direct particle acidity measurements for further evaluation. However, that is not possible at the current stage due to limitation in measurement techniques. A recently developed and indirect method, that infers H^+ activity based on the ratio of SO_4^{2-} and HSO_4^- ions, is only applicable to determine pH for particles larger than 10 μm and requires activity coefficients calculated by thermodynamic modeling [*Rindelaub et al.*, 2016]. In the future, I look forward to developing new technique to directly measure single fine particle pH and comparing to thermodynamic modeling results.

SUPPORTING MATERIALS FOR CHAPTER 2

A.1 Nephelometer RH sensor calibration

The nephelometer RH sensors were calibrated by placing the sensors in a sealed container above aqueous saturated salt solutions at known temperatures for an accurate prediction of equilibrium RH [*Greenspan*, 1977]. More than 3hrs were allowed for each salt solution to reach water vapor saturation.

Table A-1 Theoretical and measured RH for saturated salt solution at 20℃.

Compound	Equilibrium RH, %	Measured RH, %
K_2CO_3	43.16 ± 0.33	40.39 ± 0.47
NaCl	75.47 ± 0.14	71.00 ± 0.00
KCl	85.11 ± 0.29	80.21 ± 0.38
KNO_3	94.62 ± 0.66	88.60 ± 0.47

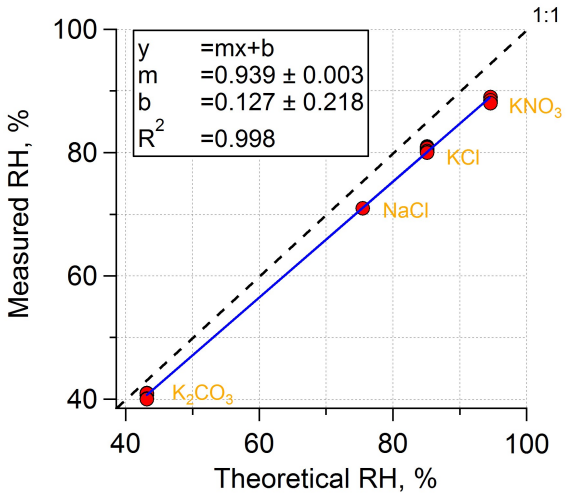

Figure A-1 A linear regression fit of measured RH vs. theoretical RH.

A.2 LWC measurement principle by nephelometers

Particle water was indirectly measured by two nephelometers. The difference between ambient and dry scattering coefficients (σ_{sp}) is assumed to be caused by the loss of water. The ratio between ambient scattering coefficient and dry scattering coefficient is referred to as $f(RH)$.

$$f(RH) = \frac{\sigma_{sp}(\mathrm{ambient})}{\sigma_{sp}(dry)} = \frac{\int \frac{\pi}{4} Q_{s,ambient} {D_{p,ambient}}^2 N(D_p) dD_p}{\int \frac{\pi}{4} Q_{s,dry} {D_{p,dry}}^2 N(D_p) dD_p} \quad \text{(A-1)}$$

where $Q_{s,ambient}$ and $Q_{s,dry}$ are scattering efficiencies in ambient and dry conditions, respectively. $N(D_p)$ is the particle number distribution function. If N_t is the total number concentration, and $\overline{D_p}$ is the diameter of average surface, and $\overline{Q_{s,ambient}}$ and $\overline{Q_{s,dry}}$ are average scattering efficiencies, then,

$$\frac{\sigma_{sp}(ambient)}{\sigma_{sp}(\mathrm{dry})} = \frac{\frac{\pi}{4} \overline{Q_{s,ambient} D_{p,ambient}}^2 N_t}{\frac{\pi}{4} \overline{Q_{s,dry}} \overline{D_{p,dry}}^2 N_t} = \frac{\overline{Q_{s,ambient} D_{p,ambient}}^2}{\overline{Q_{s,dry}} \overline{D_{p,dry}}^2} \quad \text{(A-2)}$$

$$\overline{D_{p,ambient}} = \overline{D_{p,dry}} \sqrt{f(RH) \, \overline{Q_{s,dry}} / \overline{Q_{s,ambient}}} \quad \text{(A-3)}$$

We assume:

$$\frac{\overline{Q_{s,ambient}}}{\overline{Q_{s,dry}}} \approx 1 \quad \text{(A-4)}$$

Combining Equations A-3 and A-4, we get,

$$\overline{D_{p,ambient}} = \overline{D_{p,dry}} \sqrt{f(RH)} \quad \text{(A-5)}$$

LWC is then equal to the differences between ambient particle volume and dry particle volume.

$$LWC = \left(\frac{\pi}{6}\overline{D_{p,ambient}}^3 N_t - \frac{\pi}{6}\overline{D_{p,dry}}^3 N_t\right)\rho_w \quad \text{(A-6)}$$

where ρ_w is water density (constant 1 g cm^{-3} is applied). Furthermore,

$$\overline{D_{p,dry}}^3 = \frac{m_p}{\frac{\pi}{6}\rho_p N_t} \quad \text{(A-7)}$$

where m_p is dry $PM_{2.5}$ mass concentration and ρ_p is the density of dry aerosol. For SOAS, dry $PM_{2.5}$ mass concentrations were measured by a TEOM (tapered element oscillating microbalance, 1400a, Thermo Fisher Scientific Inc., operated by Atmospheric Research & Analysis Inc.). Combining Equations A-5, A-6, and A-7 gives

$$f(RH)\_water = [f(RH)^{1.5} - 1]\, m_p \rho_w / \rho_p \quad \text{(A-8)}$$

where $f(RH)$_water refers to the particle water calculated by the above method. ρ_p was estimated from the particle composition including AMS total organics, ammonium, and sulfate, which accounted for 90% of the measure $PM_{2.5}$ dry mass (TEOM) based on the SOAS study average. A typical organic density 1.4 g cm^{-3} is assumed [*Turpin and Lim*, 2001; *King et al.*, 2007; *Engelhart et al.*, 2008; *Kuwata et al.*, 2012; *Cerully et al.*, 2014], and the density of ammonium sulfate is assumed to be 1.77 g cm^{-3} [*Sloane et al.*, 1991; *Stein et al.*, 1994]. ρ_p is calculated to be 1.49 ± 0.04 g cm^{-3} (n = 4,393) using the following relation.

$$\rho_p = \frac{1}{\varepsilon_{NH_4^+ + SO_4^{2-}}/1.77 + \varepsilon_{Org}/1.4} \quad \text{(A-9)}$$

where $\varepsilon(x)$ is the mass fraction of the species x in dry aerosol. The diurnal variation of aerosol dry density is shown in Figure A-2.

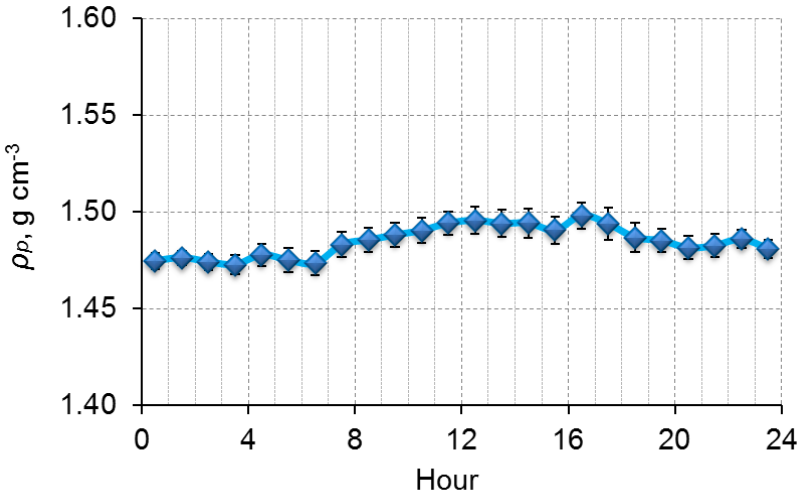

Figure A-2 Predicted $PM_{2.5}$ dry density diurnal profile. Median hourly density averages and standard error bars at local hour are plotted.

Equation A-4 is a simplified assumption that introduces error in the calculated LWC. To quantify this, we first need to determine the actual $\overline{Q_{s,ambient}}/\overline{Q_{s,dry}}$ and from the relationship of liquid water, $f(RH)$ and scattering efficiency

$$LWC = \left\{\left[\frac{f(RH)}{\overline{Q_{s,ambient}}/\overline{Q_{s,dry}}}\right]^{1.5} - 1\right\} m_p \rho_w / \rho_p \qquad \text{(A-10)}$$

we can estimate the LWC error associated with using Equation A-4 in place of the actual $\overline{Q_{s,ambient}}/\overline{Q_{s,dry}}$.

To determine the actual $\overline{Q_{s,ambient}}/\overline{Q_{s,dry}}$, we need to compute the scattering efficiency for the dry and humidified particles. For this, we need to determine the dry and wet particle size distributions and their corresponding refractive indices. Dry size distributions are obtained from in situ measurements [*Nguyen et al.*, 2014b], while the corresponding humidified distributions were calculated for predetermined values of the particle diameter-

based growth factor, $gf_D = D_{p,wet}/D_{p,dry}$, applied to the dry distribution. The mass composition of wet and dry aerosol is related to gf_D as follows:

$$gf_D = \sqrt[3]{(m_{p,wet}/\rho_{p,wet})\Big/(m_p/\rho_p)} \quad \text{(A-11)}$$

where $m_{p,wet}$ and $\rho_{p,wet}$ are particle mass concentration and density at humidified (i.e., dry aerosol + water) condition, respectively. From observations of particle dry mass (i.e. TEOM) and the liquid water content calculation outlined in the main text, we can obtain values of gf_D as a function of RH (Figure A-3). In SOAS, the observed campaign-average gf_D = 1.24 ± 0.15.

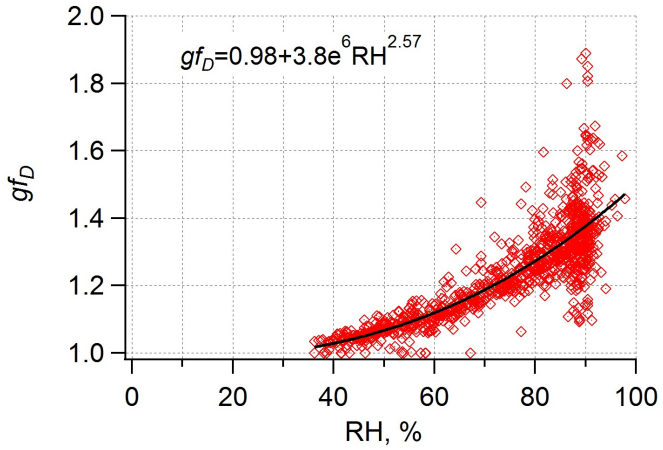

Figure A-3 gf_D plotted as a function of ambient RH based on the SOAS data set.

The particle refractive index (m_r) for wet and dry aerosol is determined as the volume-average ($\overline{m_r}$) of the refractive indices of all aerosol components [*Seinfeld and Pandis*, 2006],

$$\overline{m_r} = \sum_{i=1}^{n} m_{r,i} f_i \quad \text{(A-12)}$$

where $m_{r,i}$ is the refractive index of component *i*, and f_i is its volume fraction, and *n* is the number of constituents (including water) contained in the aerosol. The refractive indices of four major aerosol constituents in SOAS aerosol are listed in Table A-2 (NH_4^+/SO_4^{2-} molar ratio was 1.4 ± 0.5, so NH_4HSO_4 was assumed to be the dominant form of ammonium and sulfate). f_i was calculated based on the mean mass loadings with or without LWC. LWC was computed from the particle dry mass and diameter-based growth factor (gf_D).

$$m_w = \frac{m_p \rho_w}{\rho_p} (gf_D^3 - 1) \quad \text{(A-13)}$$

where m_w, ρ_w are LWC mass concentration and density, respectively; m_p, ρ_p are the dry $PM_{2.5}$ mass and density, respectively. From the above, we obtain $m_r = 1.539 - 0.023i$ ($gf_D = 1$, i.e. dry particle), $m_r = 1.488 - 0.017i$ ($gf_D = 1.1$), $m_r = 1.452 - 0.013i$ ($gf_D = 1.2$), $m_r = 1.441 - 0.012i$ ($gf_D = 1.24$), $m_r = 1.427 - 0.010i$ ($gf_D = 1.3$), and $m_r = 1.408 - 0.008i$ ($gf_D = 1.4$).

Table A-2 Refractive indices ($m_r = n + ik$), densities, and mass loadings of particle components.

species	n	k	ρ, g cm^{-3}	mean concentration, μg m^{-3}	m_r source
H_2O	1.333	0	1.0	4.50	[*Seinfeld and Pandis*, 2006]
NH_4HSO_4	1.473	0	1.77	2.19	[*Seinfeld and Pandis*, 2006]
Organics	1.55	0	1.4	3.32	[*Stelson*, 1990; *Hand and Kreidenweis*, 2002]
Black carbon	1.96	−0.66	2	0.26	[*Stelson*, 1990]

Note: m_{r,H_2O} and m_{r,NH_4HSO_4} refer to the refractive indices at λ = 589nm.

The size distributions and the refractive indices calculated as a function of gf_D are then introduced into Mie Theory [*Wiscombe*, 1980; *Graaff et al.*, 1992] and subsequently integrated over the dry and humidified size distributions via the MiePlot Version 4.4 (http://www.philiplaven.com/mieplot.htm) software to determine the respective scattering efficiencies. The light scattering calculations are carried out based on a single wavelength (λ = 530 nm) at which the nephelometer operates and assuming a temperature at the SOAS-average value of 24.7°C.

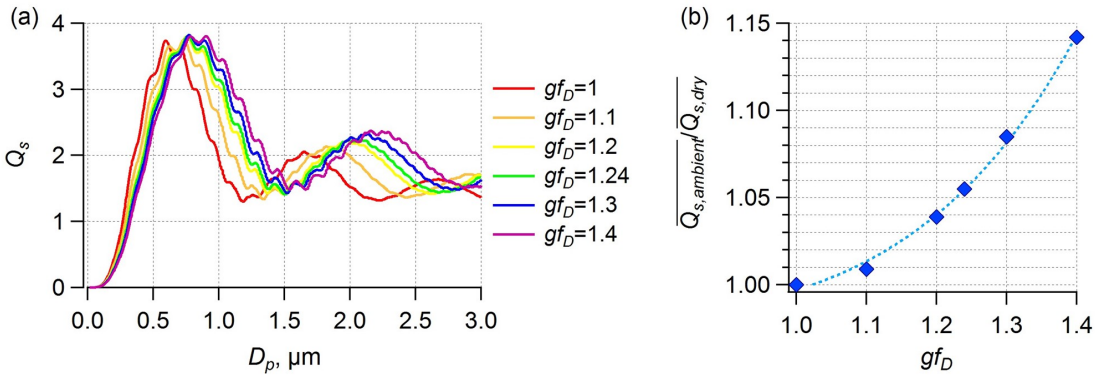

Figure A-4 (a) A single spherical particle scattering efficiency (Q_s) over $PM_{2.5}$ size range at λ = 530 nm; (b) Q_s ratio ($\overline{Q_{s,ambient}}/\overline{Q_{s,dry}}$) plotted versus gf_D for the average SOAS dry size distribution reported by *Nguyen et al.* [2014b].

On average, we find that the actual $\overline{Q_{s,ambient}}/\overline{Q_{s,dry}}$ =1.06, associated with the average SOAS gf_D of 1.24 (Figure A-4b). From the correlations between RH and gf_D (Figure A-3) and between $\overline{Q_{s,ambient}}/\overline{Q_{s,dry}}$ with gf_D (Figure A-4b), we can then apply Equation A-10 to determine the LWC. $f(RH)$_water is then compared against LWC (Figure A-5) to quantify the LWC bias associated with application of Equation A-4. From the above, the LWC error is 10% at gf_D = 1.24 (RH = 76.4%), but increases to 21% at RH = 90% (Figure A-6). Note that the particle dry size distributions from *Nguyen et al.* [2014b] ranged from 6nm to 1µm. The particles in the size range between 1µm and 2.5µm also contribute to particle scattering (as found by *Bergin et al.* [2001], but may be negligible in this case, since 90% $PM_{2.5}$ mass was found in PM_1) and make $\overline{Q_{s,ambient}}/\overline{Q_{s,dry}}$ closer to 1, because they have similar Q_s, as shown in Figure A-4a).

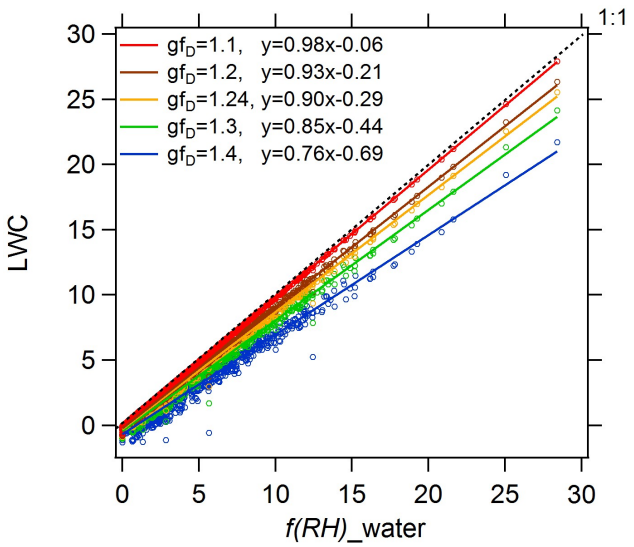

Figure A-5 Comparison between $f(RH)$_water (Equation A-8) and LWC calculated based on $\overline{Q_{s,ambient}}/\overline{Q_{s,dry}}$ at specified gf_D (Equation A-10). ODR fits are shown.

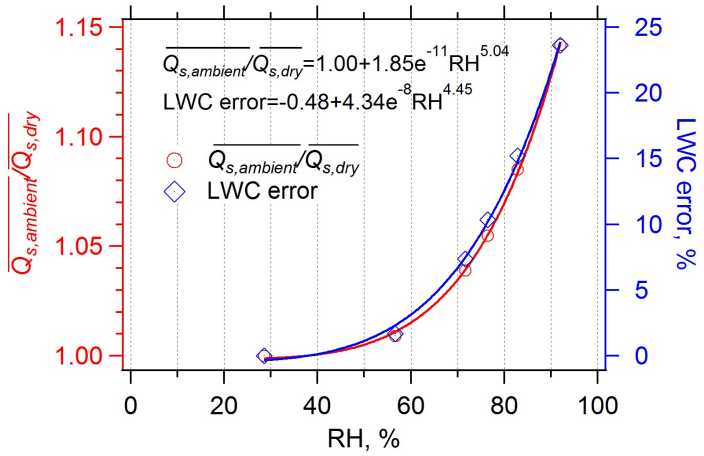

Figure A-6 $\overline{Q_{s,ambient}}/\overline{Q_{s,dry}}$ and LWC error are plotted as a function of RH. The size RH points (28.6%, 56.6%, 71.6%, 76.4%, 82.8%, 92.0%) noted on the graph corresponds to gf_D = 1, 1.1, 1.2, 1.24, 1.3, and 1.4, respectively.

A.3 Particulate organic hygroscopic parameter, κ_{org}

Overall κ_{org} had a study mean (± SD) of 0.126 ± 0.059 [*Cerully et al.*, 2014]. However, κ_{org} data were not available during the first 20 days of SOAS field study. Therefore,

diurnal hourly average κ_{org} was calculated and median values are plotted in Figure A-7. Because κ_{org} median averages were scattered, 3-hr running averages were used to calculate W_o.

The uncertainty of κ at 0.4% supersaturation, which was used to determine the values of κ_{org} (representative of SOAS ambient particles), was 0.033, mentioned in Section 3.2.1 in *Cerully et al.* [2014]. Thus, dividing the absolute uncertainty of 0.033 by the mean κ_{org} gives a relative κ_{org} uncertainty of 26%.

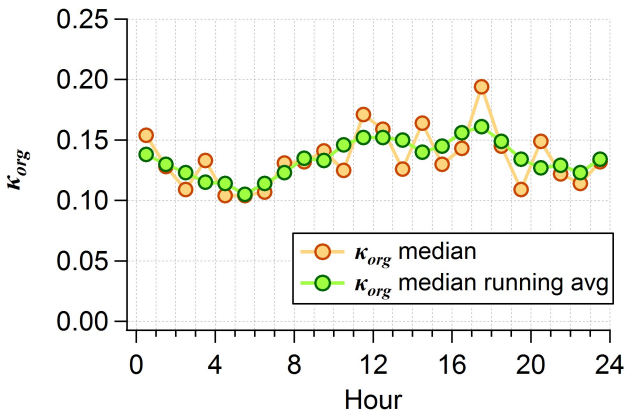

Figure A-7 κ_{org} diurnal variation. Median averages are plotted at local hours.

A.4 Filter based IC analysis at all sites

High-volume $PM_{2.5}$ filters, sampled in parallel to the AMS measurement, were analyzed by a DIONEX IC (UTAC-ULP1 concentrator column, AG11 guard column and AS11 anion column) to provide chemical information of the refractory ions (Na^+, K^+, Mg^{2+}, Ca^{2+}, PO_4^{3-}). Filter-based nitrate is excluded due to potential artifacts [*Hering and Cass*, 1999;

Chang et al., 2000]. The $PM_{2.5}$ inorganic compositions at various sites were similar, all dominated by SO_4 (64-74%) and NH_4^+ (22-31%). We found that less than 5% of the total $PM_{2.5}$ inorganic mass was refractory ions, except RS had the highest fraction as 9%.

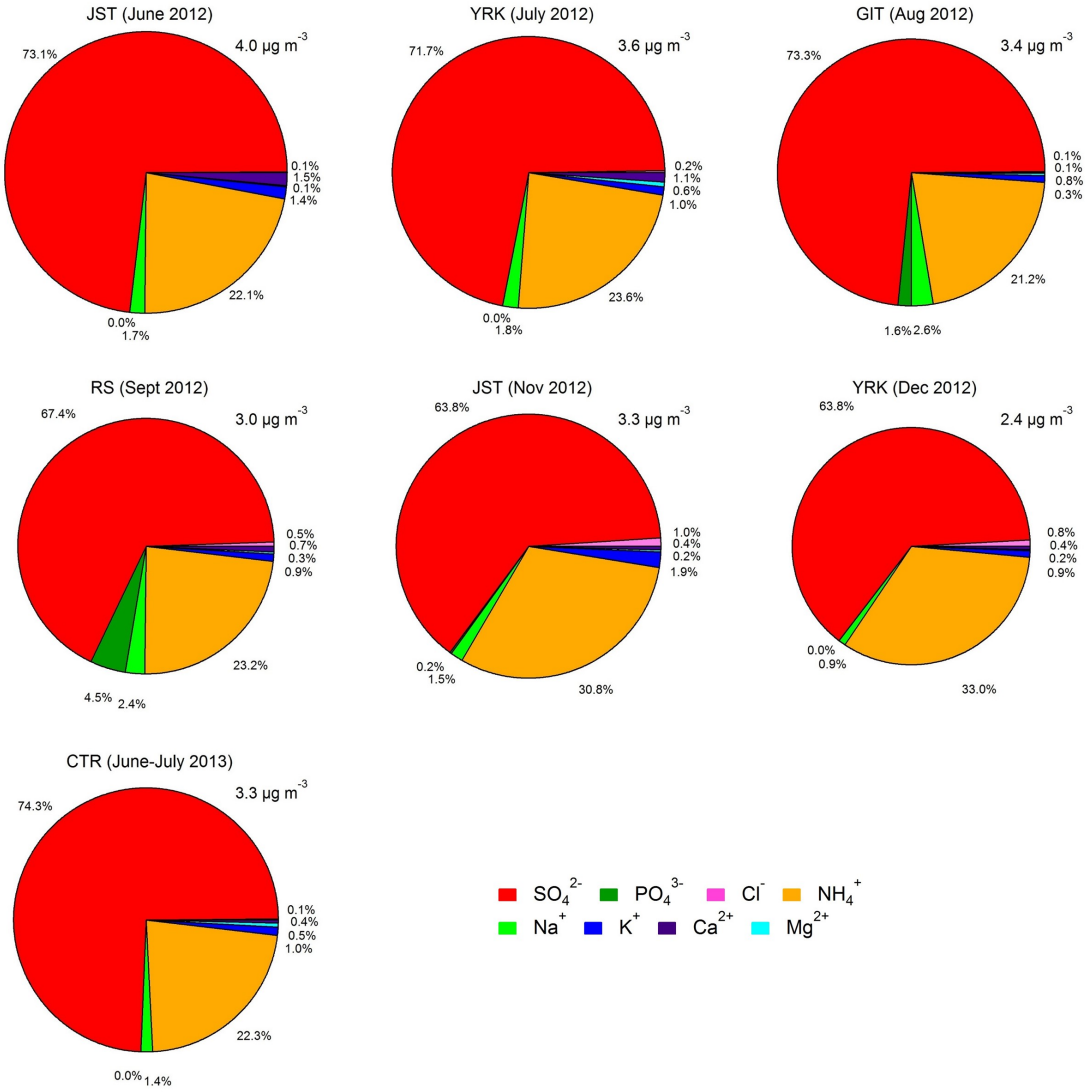

Figure A-8 Filter-based campaign averaged inorganic composition in $PM_{2.5}$ at SCAPE and SOAS sampling sites. The mean total concentrations of the listed ions are labeled to the right top of each PI chart. Filter sampling, each 23hrs, was parallel to AMS measurement. JST June 2012 is plotted instead of May 2012 due to lack of filter data during this period.

SUPPORTING MATERIALS FOR CHAPTER 3

B.1 Instrument intercomparison for measurement of particle ionic composition

The PILS-IC and AMS methods are explained in the main text; the other two particle ionic composition measurement techniques onboard the C-130 are as follows:

PILS with a fraction collector and off-line analysis by IC for PM_1: This PILS set-up was similar to the PILS-IC, except with a higher liquid flow rate of 0.72 mL min^{-1} over the impactor to allow collection of the PILS liquid sample into 2 mL polypropylene fraction collector vials. The principle of the PILS fraction collector can be found in *Sorooshian et al.* [2006]. A vial was collected every 2 min continuously during each flight. The vials were analyzed for carbohydrates following the method of *Sullivan et al.* [2014]. Inorganic ions were analyzed using two Dionex DX-500 ICs with a gradient pump, conductivity detector, and self-regenerating anion or cation SRS-ULTRA suppressor. Anion separation was performed using a Dionex AS-11HC analytical (4×250 mm) column using a sodium hydroxide gradient at a flowrate of 1.5 mL min^{-1}. The injection volume was 600 µL and analysis time was 65 min. A Dionex IonPac CS12A analytical column (3×150 mm) using 20 mM methanesulfonic acid at a flowrate of 0.5 mL min^{-1} was used for the cation separation. The injection volume and analysis time were 50 µL and 17 minutes, respectively.

Filters: Fine and coarse mode water-soluble inorganic chemical species were collected via 9 cm diameter and 1 mm thick Millipore Fluoropore Teflon filters. Filters were

subsequently processed using procedures described by *Dibb et al.* [1999; 2000]. Concentrations of chloride, nitrate, sulfate, oxalate, sodium, ammonium, potassium, magnesium, and calcium in the aqueous extracts of the teflon filters were determined by IC. The cut size for the filter aerosol sampling is ~ PM_4.

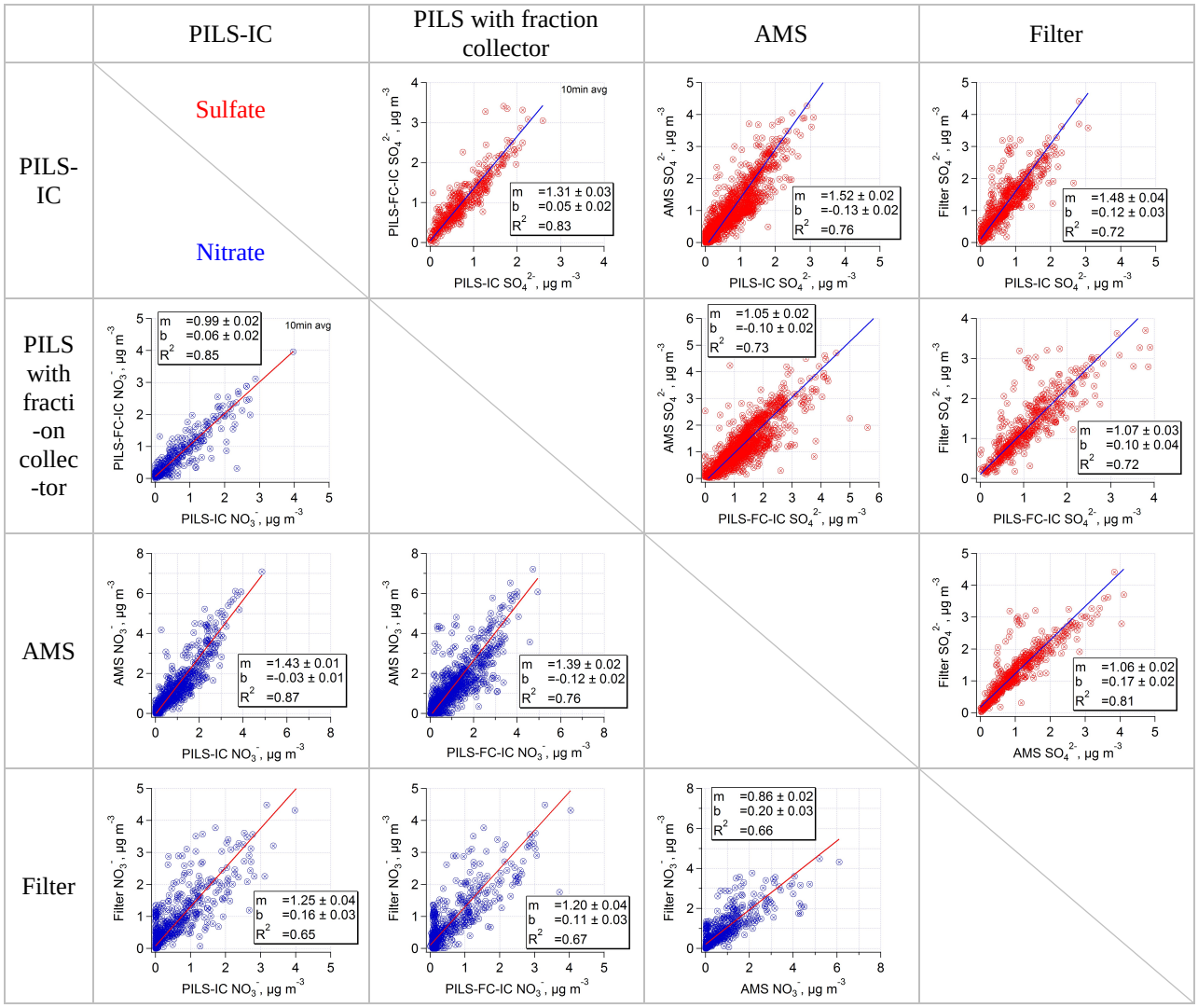

Figure B-1 Sulfate and nitrate comparisons between PM_1 PILS-IC, PM_1 PILS with fraction collector, PM_1 AMS, and PM_4 filters for the complete WINTER study. Orthogonal distance regression fits are shown.

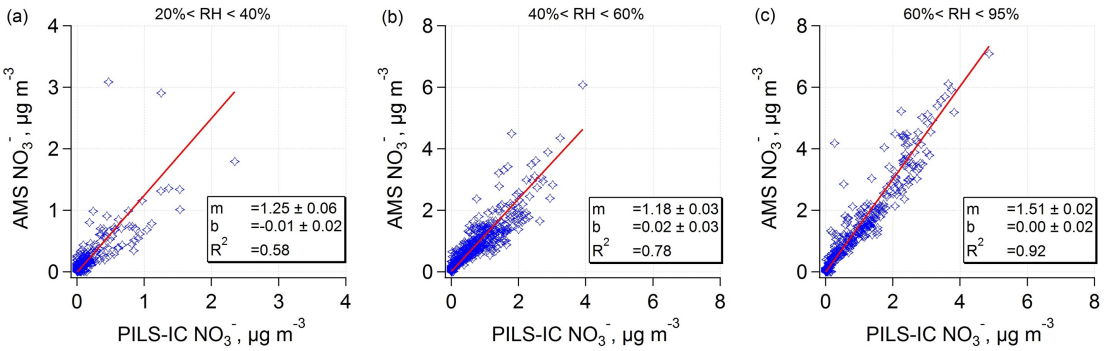

Figure B-2 Comparison between AMS and PILS-IC NO_3^- for the complete WINTER study at three RH ranges: (a) 20-40%; (b) 40-60%; (c) 60-95%. Orthogonal distance regression fits are shown. Note that, the axis range in figure (a) is smaller.

B.2 Predicted HNO_3-NO_3^- partitioning for semi-solid versus liquid phase aerosol states

The ISORROPIA-II calculation presented in the main text is based on the assumption of "metastable" aerosols; no solid precipitate is allowed to form. Since semi-solid aerosols are more likely to form at low RH and T, a comparison between predicted allowing a semi-solid phase state (ISORROPIA-II runs in stable mode) and predicted only allowing liquid phase state HNO_3/NO_3^- is shown below. Note that, all of the ISORROPIA-II input are kept the same as the metastable phase state calculations (show in Figure 3-2).

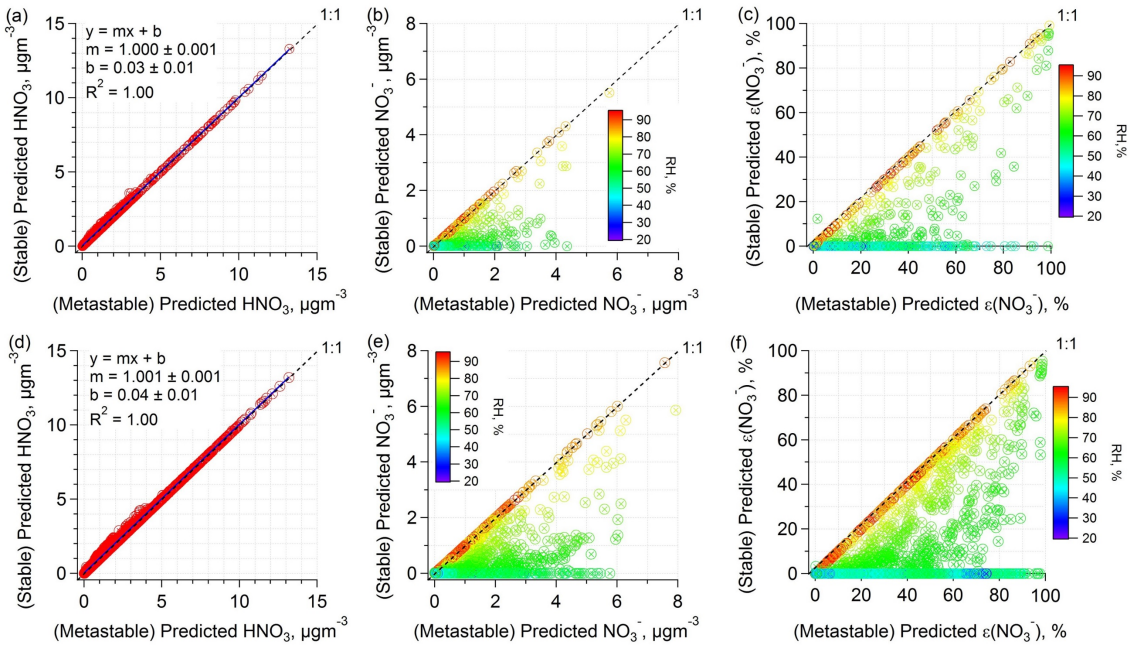

Figure B-3 Comparisons of stable (solid+liquid) aerosols vs. metastable (liquid) aerosol assumptions for predicted HNO_3 (nitric acid), (NO_3^-) (nitrate), and $\varepsilon(NO_3^-)$ (particle nitrate fraction of total nitrate) with data from the complete WINTER study: (a-c) PILS-IC anion with scaled AMS NH_4^+ input; (d-f) AMS input.

B.3 Predicted versus measured $\varepsilon(NO_3^-)$ colored by temperature and total nitrate

Figure B-4 is identical to Figure 3-3c, f and i in the main text, other than the color wave. Figure 3-3c, 3f and 3i are colored by O:C ratio, whereas Figure B-4 is colored by T. No conclusive dependence of a temperature effect on the discrepancy between predicted and measured $\varepsilon(NO_3^-)$ is observed.

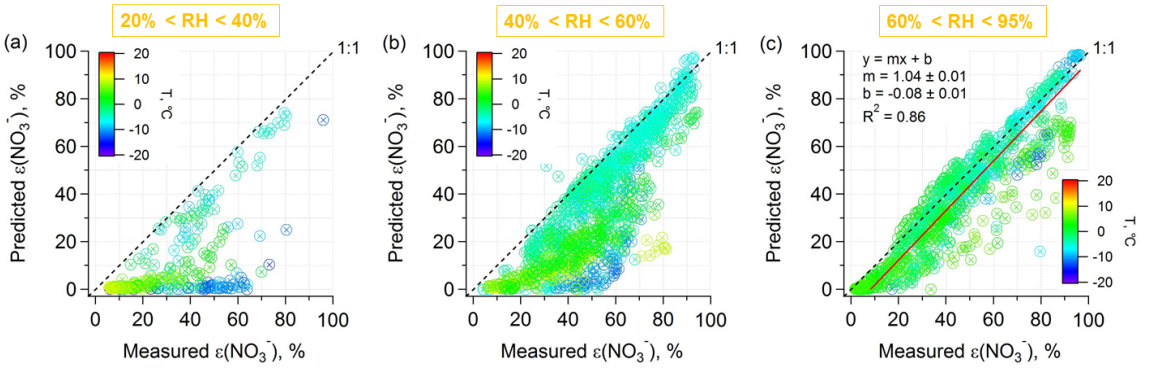

Figure B-4 Comparisons between predicted and measured $\varepsilon(NO_3^-)$ with data from the complete WINTER study (AMS aerosol data only) for different ambient RH ranges: (a) 20-40%; (b) 40-60%; (c) 60-95%.

Figure B-5 shows that greater discrepancy is generally associated with lower total nitrate mass loading.

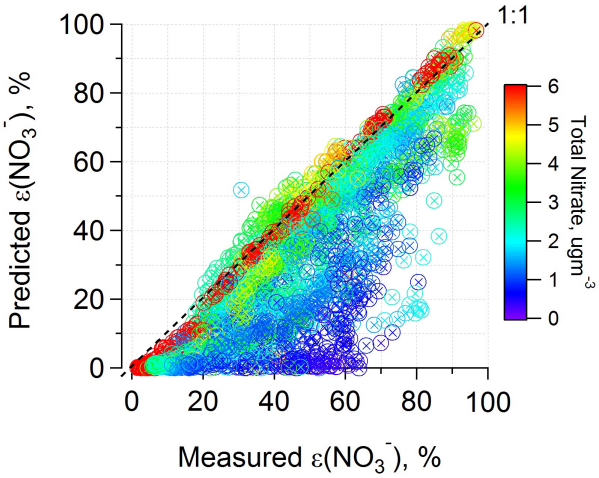

Figure B-5 Predicted versus measured partitioning of nitrate as a function of total nitrate concentration (HNO_3 + NO_3^-) from the complete WINTER study. This figure can be contrasted with Figure 2f in the main text, which is similar, but shows the RH dependence.

B.4 Thermodynamic simulations based on AMS inorgNO_3^-

The AMS inorgNO_3^- was determined by scaling AMS NO_3^- (i.e., AMS total nitrate, which may include some nitrite, organonitrate, and sodium nitrate) to PILS-IC NO_3^- concentrations on a flight-by-flight basis.

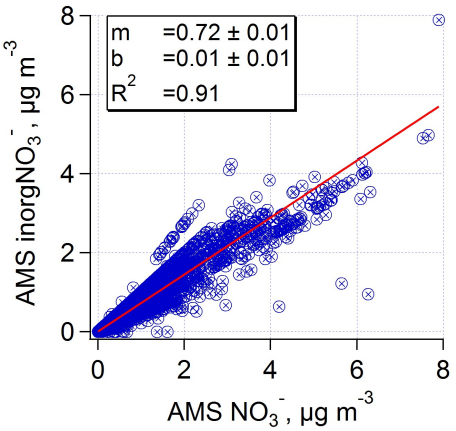

Figure B-6 Comparison between "AMS inorgNO_3^-" and "AMS NO_3^-" (i.e. complete WINTER data set). ODR fit is shown.

The input is kept the same as the AMS input in the text, other than using AMS inorgNO_3^- instead of AMS NO_3^-. Figure B-6 shows that AMS inorgNO_3^- is on average 72% of AMS NO_3^-. ISORROPIA-II was again run in "Metastable" mode with the results summarized in Figure B-7.

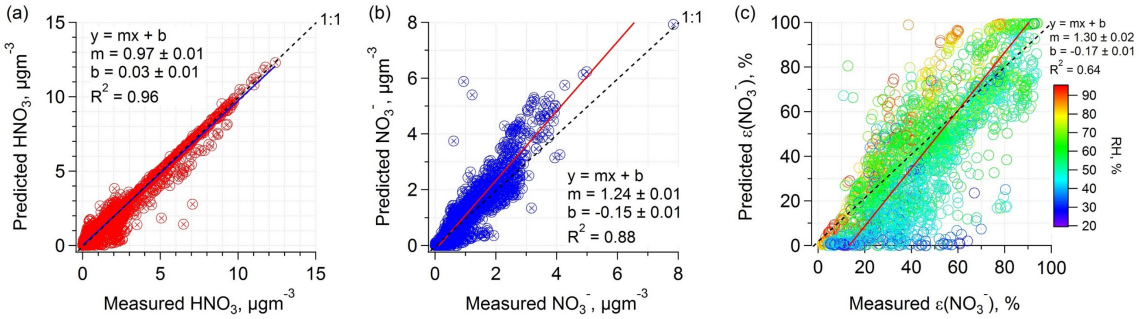

Figure B-7 Comparisons of predicted and measured HNO_3, NO_3^-, and $\varepsilon(NO_3^-)$ with data from the complete WINTER study using AMS inorgNO_3^-. ODR fits are shown. This plot is compared to Figure 3-2 in the text.

B.5 Thermodynamic simulations with refractory ions

PM_1 refractory species, such as Na^+, K^+, Ca^{2+}, Mg^{2+}, were not detected by the AMS, but were measured by the PILS-fraction collector with subsequent off-line analysis by IC. Comparing the model simulations with and without the ions shows their impacts on HNO_3-NO_3^- partitioning and particle pH. To start, we ran ISORROPIA-II with AMS NH_4^+, NO_3^-, SO_4^{2-} and PILS fraction collector Na^+, Cl^- for periods where the data was above the LOD (0.01 µg m^{-3}). 68% of Na^+ and 93% of Cl^- were above detection limits. For the complete WINTER campaign, the mean ± SD concentrations were Na^+ = 0.23 ± 0.36 µg m^{-3} and Cl^- = 0.34 ± 0.38 µg m^{-3}. Most NaCl were likely from sea-salt recorded during periods when the C-130 flew within and near coastal regions.

With the assumption of internally mixing, including NaCl in the ISORROPIA-II input doesn't shift particle pH until NaCl concentrations are comparable or higher than sulfate. This is shown in Figure B-8 for data from WINTER Flight 6. Particle pH increases more

than two units only when the sulfate concentration drops dramatically and NaCl levels increase, as the aerosol changes to mainly Na^+-containing salts (e.g., Na_2SO_4, $NaNO_3$). When sulfate (or nitrate) is low, a small amount of refractory cations can have large impacts on the particle pH. However, when sulfate (or nitrate) is high, a small amount of refractory cations (up to 50% mole fraction) do not significantly modify the particle pH.

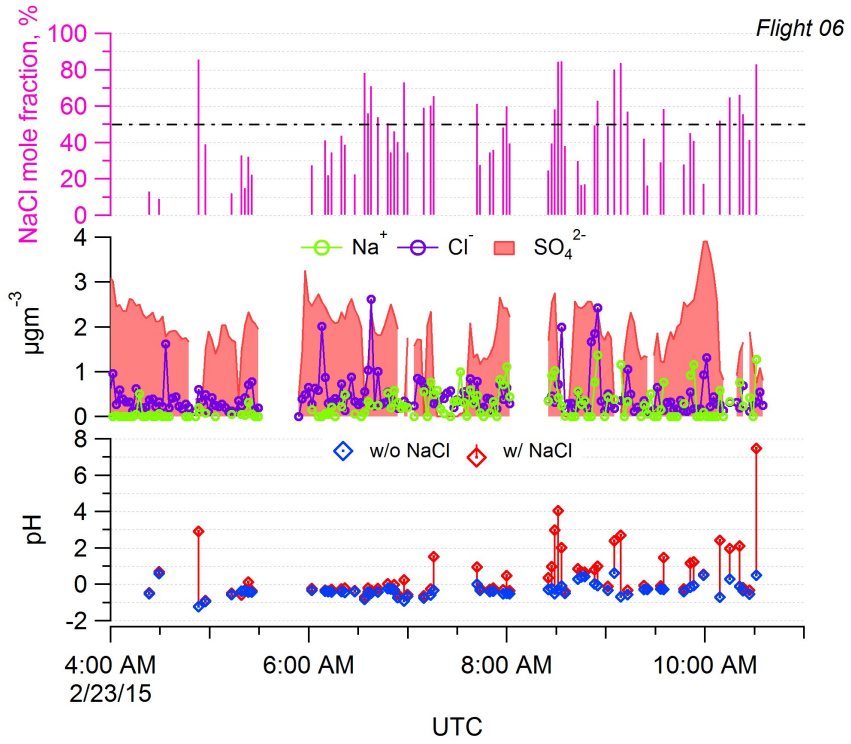

Figure B-8 Times series of WINTER Flight 6 PILS fraction collector NaCl mole fraction (NaCl to total input moles), Na^+, Cl^-, SO_4^{2-}, and predicted pH with and without NaCl.

Sensitivity of pH to cations: If the nonvolatile cations (Na^+, Ca^{2+}, etc.) get fully dissolved and internally mixed with other aerosol components, given enough time, the equilibrated particle pH will increase (Figure B-9). The simulation was run based on WINTER average condition of SO_4^{2-}, NH_4^+, total NO_3^-, RH, and T with varying Na^+ and Cl^- mass loadings.

The concentrations of Ca^{2+}, Mg^{2+}, K^+ are assumed to be zero, because the roles of these nonvolatile cations can be roughly represented by Na^+. Figure B-9 shows that if the filter measured PM_4 NaCl (Na^+ = 0.50 ± 0.88 µg m^{-3}, Cl^- = 0.69 ± 1.60 µg m^{-3}) becomes internally mixed, the particle pH would increase from 1.1 to 2.2. More pH increase is expected with higher nonvolatile cations being dissolved. For WINTER campaign, PM_1 pH is largely not affected by NaCl, because of very low PM_1 Cl^- mass loadings and probably low Na^+ (PILS-IC Cl^- 0.07 ± 0.11 µg m^{-3} and AMS Cl^- 0.02 ± 0.04 µg m^{-3}).

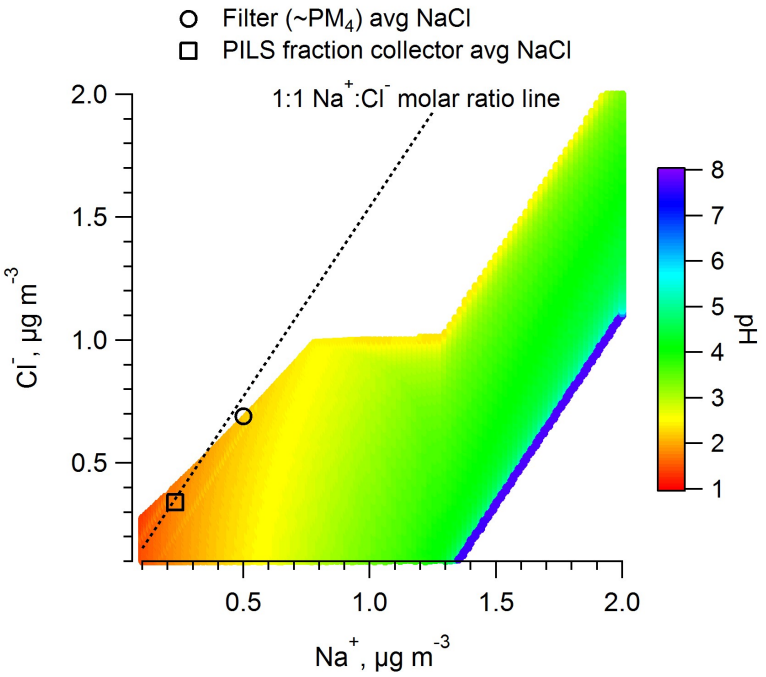

Figure B-9 Predicted particle pH as a function of assumed Na^+ and Cl^- mass loadings at the WINTER average condition of SO_4^{2-} = 1.02 µg m^{-3}, NH_4^+ = 0.50 µg m^{-3}, (NO_3^- + HNO_3) = 2.21 µg m^{-3}, K^+ = Ca^{2+} = Mg^{2+} = 0 µg m^{-3}, RH = 57.5%, T = 272.1 K. ISORROPIA-II was run in forward mode. The field campaign average Na^+ and Cl^- mass loadings from PILS fraction collector and filter are labeled in the graph. Note that, PILS-IC Cl^- (0.07 ± 0.11 µg m^{-3}) and AMS Cl^- (0.02 ± 0.04 µg m^{-3}) are much smaller than filter Cl^- (0.69 ± 1.60 µg m^{-3}).

Figure B-10 shows that adding NaCl makes the predicted vs. measured HNO_3/NO_3^- more scattered, but the slopes are nearly the same, except for $\varepsilon(NO_3^-)$. Larger NaCl mass and mole fraction are consistently observed with larger discrepancies between predicted and measured HNO_3-NO_3^- partitioning, indicating PM_1 NaCl are probably not internally mixed.

In conclusion, the effects of refractory ions on the pH prediction can be significant when these ions contribute significantly to the aerosol moles and are internally mixed. However, larger discrepancy observed in reproducing HNO_3-NO_3^- partitioning when NaCl is included in the thermodynamic calculations suggests that these refractory ions are probably not internal mixed with PM_1 nitrate, sulfate and ammonium. Thus, the predicted particle pH presented in this study is largely accurate despite not including these cations, but may be biased at very low sulfate concentrations if some fraction of refractory ions become internally mixed and the dominant ions.

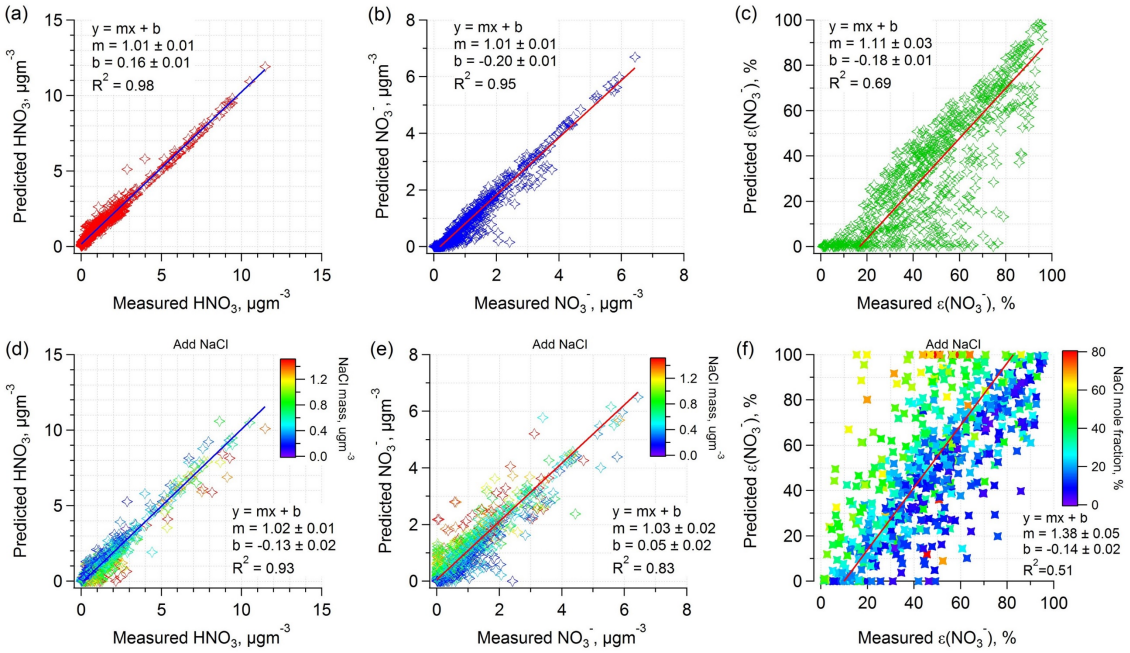

Figure B-10 Comparisons of predicted and measured HNO_3, NO_3^-, and $\varepsilon(NO_3^-)$ with the complete WINTER data when both Na^+ and Cl^- were above LOD: (a-c) AMS input (NH_4^+, NO_3^-, SO_4^{2-}); (d-f) AMS input with PILS fraction collector Na^+ and Cl^- added. Orthogonal distance regression fits are shown.

B.6 Predicted Particle Water versus AMS Total Ionic Mass

The following graph is similar to Figure 3-9 in the main text. The difference is that x-axis was changed to the AMS total ionic mass.

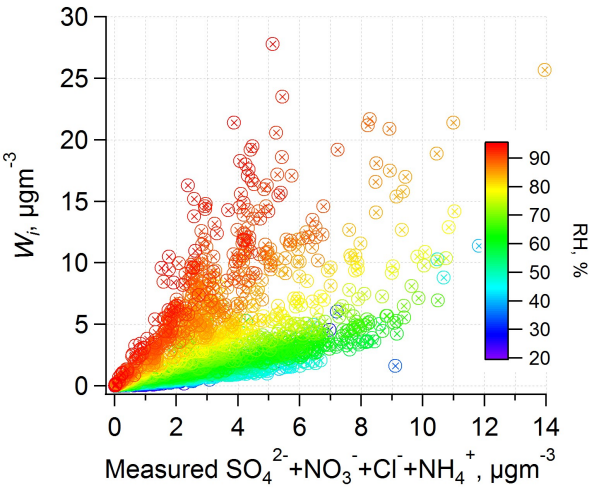

Figure B-11 Predicted W_i versus AMS "sulfate + nitrate + chloride + ammonium" mass concentrations.

B.7 HYSPLIT back trajectories of Flights 6 and 8

Flight tracks of Flights 6 and 8 are shown in Figure 3-10 in the main text. The transport of the observed plumes were calculated using the NOAA HYSPLIT model (http://ready.arl.noaa.gov/HYSPLIT_traj.php), shown as Figure B-12 below. The selected back-trajectory analysis area covers the majority of the flight routes, where back trajectories are calculated at 2 hour intervals. Starting heights are set at 500 m (Flight 6) and 100 m (Flight 8), respectively, close to the C-130 pressure altitudes for each flight. Figure B-12 shows that the plumes encountered by Flight 6 passed over a wide region of the east coast, from Pennsylvania in the north to North Carolina in the south. Flight 8 encountered plumes from a narrower region that mainly included the greater New York City area.

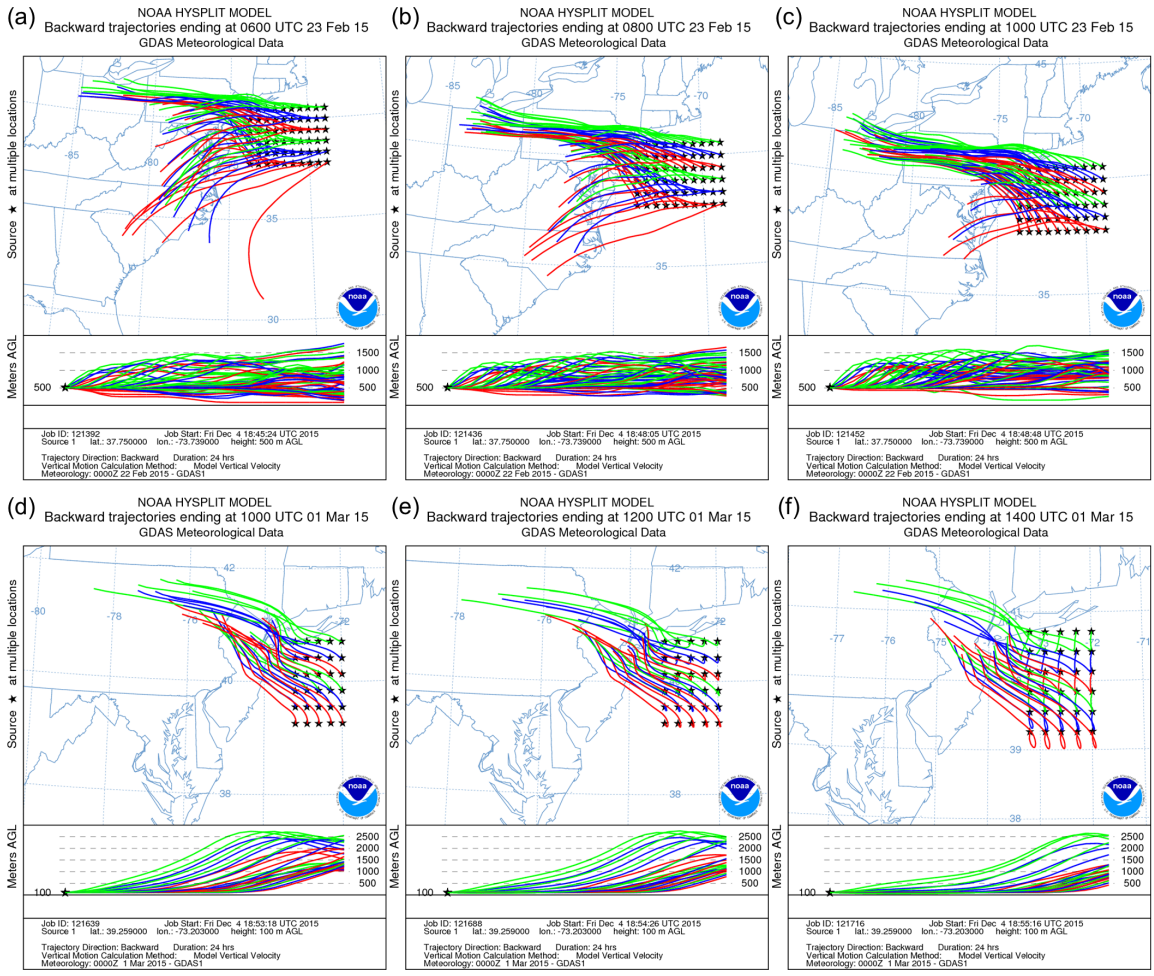

Figure B-12 HYSPLIT 24 hours air mass back trajectory matrix at 0600 (a), 0800 (b), 1000 (c) UTC time for WINTER Flight 6 and at 1000 (d), 1200 (e), 1400 (f) UTC time for WINTER Flight 8. Starting heights are set to be 500 m for Flight 6 and 100 m for Flight 8.

B.8 Nitric Acid to Coarse Mode Nitrate Partitioning

The overall good agreement between ISORROPIA-II predications and observations indicates that PM_1 nitrate was in a thermodynamic equilibrium state with nitric acid. However, during the WINTER study there were at times significant amounts of coarse mode ions (NO_3^-, Na^+, Cl^-, etc.). Figure B-13 shows a 5-hour time series of AMS and Filter

NO_3^-, as well as coarse mode NO_3^- fraction, which was on average 76 ± 18%, more than four times the campaign average of 18 ± 17%. To investigate the partitioning between nitric acid and coarse mode particles, we compare the ISORROPIA-II thermodynamic results between fine mode coarse mode inputs (Figure B-14).

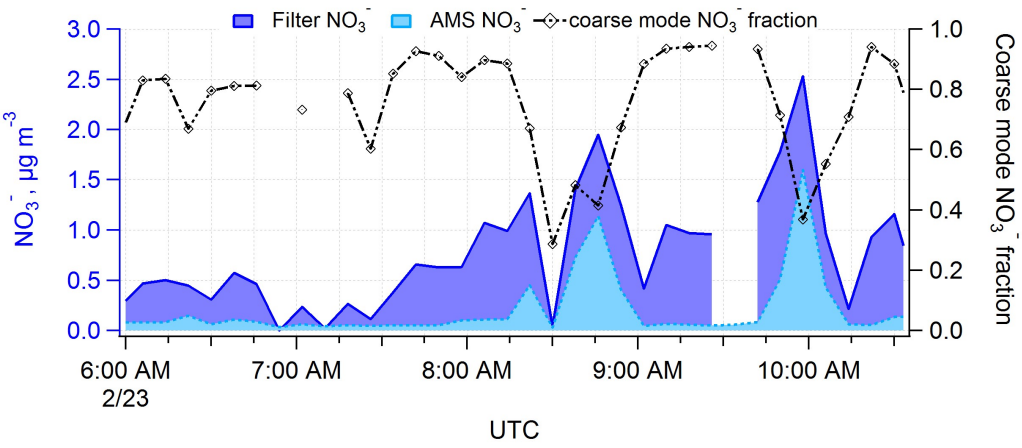

Figure B-13 Times series of WINTER Flight 6 AMS and filter NO_3^-, and the coarse mode NO_3^- fraction (1 − AMS NO_3^-/Filter NO_3^-).

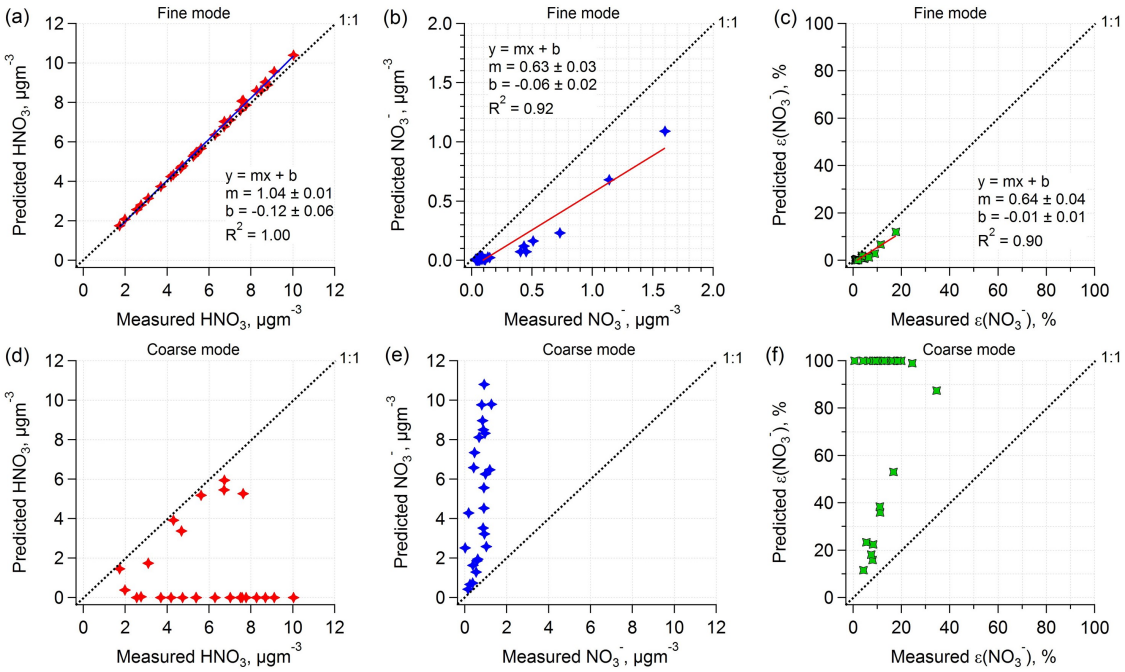

Figure B-14 Comparisons of predicted and measured HNO_3, NO_3^-, and $\varepsilon(NO_3^-)$ for a 5-hour period in Flight 6. Aerosol phase ISORROPIA-II inputs are: (a-c) AMS SO_4^{2-}, NO_3^-, NH_4^+ with $Na^+ = Cl^- = Ca^{2+} = Mg^{2+} = K^+ = 0$; (d-f) Filter minus AMS (coarse mode) SO_4^{2-}, NO_3^-, NH_4^+ with filter Na^+, Cl^-, Ca^{2+}, Mg^{2+}, K^+ (assuming all of the Na^+, Cl^-, Ca^{2+}, Mg^{2+}, K^+ is in the coarse mode). HNO_3, T, and RH are the same for (a-c) and (d-f). Orthogonal distance regression fits are shown. Note that, the axis range is smaller in (c) compared to (e).

SUPPORTING MATERIALS FOR CHAPTER 4

C.1 Comparisons of inorganic species measurements between AMS (PM_1) and PILS-IC ($PM_{2.5}$)

Consistency ($R^2 \geq 0.8$) between AMS and PILS-IC are observed. AMS measured nominally PM_1, whereas PILS-IC measured $PM_{2.5}$. These results are consistent with similar inter-comparisons reported elsewhere [*Hayes et al.*, 2013]. A larger difference in slope for nitrate than sulfate is thought to be due to higher nitrate concentrations in the 1 to 2.5 µm size range. $PM_1/PM_{2.5}$ mass ratios, reported in the main text, differ from slopes shown below due to differences in contributions of lower concentrations to these parameters (ratio vs. slope).

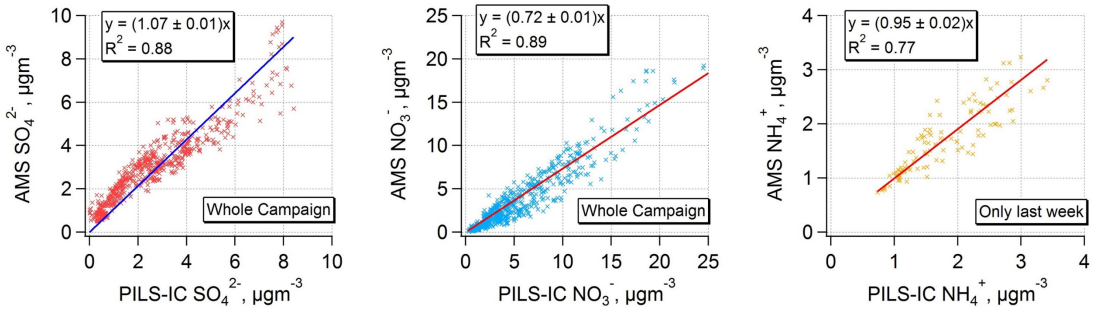

Figure C-1 Sulfate and nitrate comparisons between PM_1 PILS-IC, PM_1 PILS with fraction collector, PM_1 AMS, and PM_4 filters for the complete WINTER study. Orthogonal distance regression fits are shown.

C.2 The dependencies of nitrate, ammonium, and chloride on pH, W_i, and T (S curve equation derivations)

C.2.1 HNO_3-NO_3^- partitioning

The S curve of $\varepsilon(NO_3^-)$ has been discussed explicitly and compared to observations from WINTER aircraft campaign in *Guo et al.* [2016]. Here we show the detailed derivation of Equation 3 in that paper. Equilibrium between gaseous HNO_3 and particle-phase NO_3^- involves two processes, first dissolution of HNO_3 into aqueous phase (assuming particles are liquids) and second dissociation of dissolved HNO_3 into H^+ and NO_3^-. The two processes are reversible and often reach thermodynamic equilibriums at ambient conditions (RH, T) for fine particles.

$$1^{st} \quad HNO_{3(g)} \leftrightarrow HNO_3, \quad H_{HNO_3}$$
$$2^{nd} \quad HNO_3 \leftrightarrow {NO_3}^- + H^+, \quad K_{n1}$$

for which reaction equilibriums are expressed as follows,

$$H_{HNO_3} = \gamma_{HNO_3}[HNO_3]/p_{HNO_3} \tag{C-1}$$

$$K_{n1} = \frac{\gamma_{NO_3^-}[{NO_3}^-]\gamma_{H^+}[H^+]}{\gamma_{HNO_3}[HNO_3]} \tag{C-2}$$

where H_{HNO_3} is HNO_3 Henry's law constant, K_{n1} is HNO_3 acid dissociation constant, γ represents activity coefficient, p_{HNO_3} is partial pressure of HNO_3 in atmosphere, and [x] represents aqueous concentrations (mole L^{-1}). From Equations C-1 and C-2 we get the total dissolved HNO_3 or total particle-phase nitrate ($[{NO_3}^T]$) as

$$[{NO_3}^T] = [HNO_3] + [{NO_3}^-] = H_{HNO_3} p_{HNO_3} \left(\frac{1}{\gamma_{HNO_3}} + \frac{K_{n1}}{\gamma_{NO_3^-}\gamma_{H^+}[H^+]} \right) \tag{C-3}$$

Ideal gas law gives

$$c(HNO_3) = \frac{p_{HNO_3}}{RT} \tag{C-4}$$

where $c(x)$ represents concentration per volume of air (mole m^{-3}). Therefore, the particle-phase fraction of nitrate is

$$\varepsilon(NO_3{}^{\mathrm{T}}) = \frac{c(NO_3^T)}{c(HNO_3) + c(NO_3^T)} = \frac{[NO_3^T]W_i}{c(HNO_3) + [NO_3^T]W_i} \tag{C-5}$$

where W_i is the particle liquid water content associated with inorganic species (μg m^{-3}; mass per volume of air) (here the organics associated liquid water is not considered). Taking Equations C-3 and C-4 into C-5, we get $\varepsilon(NO_3{}^{\mathrm{T}})$ as

$$\varepsilon(NO_3{}^{\mathrm{T}}) = \frac{\left(\frac{\gamma_{NO_3^-}\gamma_{H^+}}{\gamma_{HNO_3}}[H^+] + K_{n1}\right) H_{HNO_3} W_i RT}{\gamma_{NO_3^-}\gamma_{H^+}[H^+] + \left(\frac{\gamma_{NO_3^-}\gamma_{H^+}}{\gamma_{HNO_3}}[H^+] + K_{n1}\right) H_{HNO_3} W_i RT} \tag{C-6}$$

At 298 K, K_{n1}=12 mole L^{-1} [*Fountoukis and Nenes*, 2007] often >> $\frac{\gamma_{NO_3^-}\gamma_{H^+}}{\gamma_{HNO_3}}[H^+]$, so we assume $\left(\frac{\gamma_{NO_3^-}\gamma_{H^+}}{\gamma_{HNO_3}}[H^+] + K_{n1}\right) \approx K_{n1}$. Thus, a simplified equation is

$$\varepsilon\left(NO_3{}^{\mathrm{T}}\right) \cong \frac{K_{n1} H_{HNO_3} W_i RT}{\gamma_{NO_3^-}\gamma_{H^+}[H^+] + K_{n1} H_{HNO_3} W_i RT} \tag{C-7}$$

$H_{HNO_3}K_{n1}$ is denoted as $H^*_{HNO_3}$ (mole^2 kg^{-2} atm^{-1}) hereafter, which is equilibrium constant of the combined dissolution and deprotonation processes as,

$$HNO_{3(g)} \leftrightarrow NO_3{}^- + H^+, \;\; H^*_{HNO_3}$$

$H^*_{HNO_3}$ can be easily calculated by Equation 40 in *Clegg and Brimblecombe* [1990] for T dependence and converted from unit atm^{-1} (mole fraction based) to mole^2 kg^{-2} atm^{-1}

(molality based) by Equation 5 also in that paper. To be consistent with SI units, we have the following equation ready for users' input,

$$\varepsilon\left(NO_3{}^{\mathrm{T}}\right) \cong \frac{H^*_{HNO_3} W_i RT \times 0.987 \times 10^{-14}}{\gamma_{NO_3^-}\gamma_{H^+}[H^+] + H^*_{HNO_3} W_i RT \times 0.987 \times 10^{-14}} = \frac{H^*_{HNO_3} W_i RT \times 0.987 \times 10^{-14}}{\gamma_{NO_3^-}\gamma_{H^+} 10^{-pH} + H^*_{HNO_3} W_i RT \times 0.987 \times 10^{-14}} \quad \text{(C-8)}$$

Note that 0.987 comes from the conversion from 1 atm to 1 psi and W_i unit is μg m^{-3}. Equation C-8 describes the dependence of HNO_3-NO_3^- partitioning on pH, T, and W_i (determined by RH and aerosol composition). Based on ideal and non-ideal aqueous particles, several $\varepsilon(NO_3{}^-)$ S curves at atmosphere relevant conditions are plotted together with $\varepsilon(Cl^-)$ and $\varepsilon(NH_4{}^+)$ in Figure C-3 and Figure C-4, respectively.

$\varepsilon\left(NO_3{}^{\mathrm{T}}\right)$ is equivalent to $\varepsilon(NO_3{}^-)$ in the main text, since NO_3^- is practically 100% of $NO_3{}^{\mathrm{T}}$ based on $K_{n1} \gg \frac{\gamma_{NO_3^-}\gamma_{H^+}}{\gamma_{HNO_3}}[H^+]$ (also under atmospheric condition). The fraction of NO_3^- over $NO_3{}^{\mathrm{T}}$ can be given as

$$\frac{[NO_3{}^-]}{\left[NO_3{}^{\mathrm{T}}\right]} = \frac{K_{n1}}{K_{n1} + \frac{\gamma_{NO_3^-}\gamma_{H^+}}{\gamma_{HNO_3}}[H^+]} \quad \text{(C-9)}$$

C.2.2 HCl-Cl^- partitioning

Following the same derivation procedure as HNO_3-NO_3^- partitioning, we have ε(Cl^-) as

$$\varepsilon(Cl^-) \cong \frac{H^*_{HCl} W_i RT \times 0.987 \times 10^{-14}}{\gamma_{Cl^-}\gamma_{H^+}[H^+] + H^*_{HCl} W_i RT \times 0.987 \times 10^{-14}} = \frac{H^*_{HCl} W_i RT \times 0.987 \times 10^{-14}}{\gamma_{Cl^-}\gamma_{H^+}10^{-pH} + H^*_{HCl} W_i RT \times 0.987 \times 10^{-14}} \quad \text{(C-10)}$$

where H^*_{HCl} (mole^2 kg^{-2} atm^{-1}) is the equilibrium constant and is equal to the "conventional" Henry's law constant multiplied by the acid dissociation constant of hydrochloric acid. H^*_{HCl} can be calculated by Equation 22 in *Carslaw et al.* [1995] to account for T's variation.

$$HCl_{(g)} \leftrightarrow Cl^- + H^+, \quad H^*_{HCl}$$

A comparison of $\varepsilon(Cl^-)$ S curve with a subset of CalNex data is shown in Figure C-2. The selected CalNex data are all in a small range of T 15.5 to 19.5 ºC (around campaign average T) and W_i 10 to 20 µgm^{-3}, while the S curve is calculated based on the average condition of these data as T = 17.5 ºC, W_i = 15 µgm^{-3}, $\gamma_{Cl^-}\gamma_{H^+}$ = 0.66. The distribution of the $\varepsilon(Cl^-)$ points close to S curve validates the $PM_{2.5}$ pH prediction and demonstrates the usage of S curve.

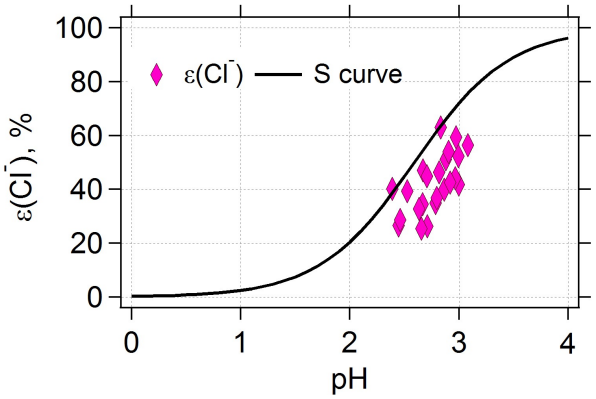

Figure C-2 The comparison of S curve and measured ε(Cl$^-$) with predicted particle pH by ISORROPIA-II. Cl$^-$ is from $PM_{2.5}$ PILS-IC measurements.

C.2.3 NH_3-NH_4^+ partitioning

The derivation of NH_3-NH_4^+ partitioning is a bit different from the above two acidic gases. Equilibrium between gaseous NH_3 and NH_4^+ can be described simply as

$$NH_{3(g)} + H^+ \leftrightarrow NH_4^+, \quad H^*_{NH_3}$$

($H^*_{NH_3}$ is equivalent to the "conventional" Henry's law constant of NH_3 divided by the acid dissociation constant of NH_4^+) or described by the follow two reversible reactions assuming water activity as unity.

$$1^{st} \quad NH_{3(g)} \leftrightarrow NH_3, \qquad H_{NH_3}$$
$$2^{nd} \quad NH_3 + H^+ \leftrightarrow NH_4^+, \quad 1/K_a$$

for which reaction equilibriums are described as

$$H_{NH_3} = \gamma_{NH_3}[NH_3]/p_{NH_3} \tag{C-11}$$

$$1/K_a = \frac{\gamma_{NH_4^+}[NH_4^+]}{\gamma_{NH_3}[NH_3]\gamma_{H^+}[H^+]} \tag{C-12}$$

where H_{NH_3} is NH_3 Henry's law constant, K_a is NH_4^+ acid dissociation constant, γ represents activity coefficient, p_{NH_3} is partial pressure of NH_3 in atmosphere, and [x] represents aqueous concentrations (mole L^{-1}). Please note that the 2nd reaction is usually written in another form [*Fountoukis and Nenes*, 2007] as

$$2^{nd} \quad NH_3 + H_2O \leftrightarrow NH_4^+ + OH^-, \quad K_w/K_a$$

where K_w is water dissociation constant. Equations C-11 and C-12 give the total dissolved NH_3 or total particle-phase ammonium (NH_4^T) as

$$[NH_4^T] = [NH_3] + [NH_4^+] = H_{NH_3}p_{NH_3}\left(\frac{1}{\gamma_{NH_3}} + \frac{\gamma_{H^+}[H^+]}{\gamma_{NH_4^+}K_a}\right) \tag{C-13}$$

Combining with ideal gas law, that is

$$c(NH_3) = \frac{p_{NH_3}}{RT} \tag{C-14}$$

where $c(x)$ represents concentration per volume of air (mole m^{-3}). We have the particle-phase fraction of ammonium as

$$(NH_4{}^{\mathrm{T}}) = \frac{c(NH_4^T)}{c(NH_3) + c(NH_4^T)} = \frac{[NH_4^T]W_i}{c(NH_3) + [NH_4^T]W_i} \tag{C-15}$$

With Equations C-13 and C-14, the above equation is transformed into

$$\varepsilon(NH_4{}^{\mathrm{T}}) = \frac{\left(\frac{\gamma_{H^+}[H^+]}{\gamma_{NH_4{}^+}} + \frac{K_a}{\gamma_{NH_3}}\right)\frac{H_{NH_3}}{K_a}W_iRT}{1 + \left(\frac{\gamma_{H^+}[H^+]}{\gamma_{NH_4{}^+}} + \frac{K_a}{\gamma_{NH_3}}\right)\frac{H_{NH_3}}{K_a}W_iRT} \tag{C-16}$$

At 298 K, K_a = 5.69×10^{-10} mole L^{-1} [*Clegg et al.*, 1998] results in $\frac{K_a}{\gamma_{NH_3}} \ll \frac{\gamma_{H^+}[H^+]}{\gamma_{NH_4{}^+}}$ as long as the solution is not too basic. Neglecting $\frac{K_a}{\gamma_{NH_3}}$ part and taking $\frac{H_{NH_3}}{K_a} = H^*_{NH_3}$, we have

$$\varepsilon(NH_4{}^{\mathrm{T}}) \cong \frac{\frac{\gamma_{H^+}[H^+]}{\gamma_{NH_4{}^+}}H^*_{NH_3}W_iRT}{1 + \frac{\gamma_{H^+}[H^+]}{\gamma_{NH_4{}^+}}H^*_{NH_3}W_iRT} \tag{C-17}$$

To be consistent with SI units, the Equation C-17 is then presented as

$$\begin{aligned}\varepsilon\left(NH_4{}^{\mathrm{T}}\right) &\cong \frac{\frac{\gamma_{H^+}[H^+]}{\gamma_{NH_4{}^+}}H^*_{NH_3}W_iRT\times 0.987\times 10^{-14}}{1 + \frac{\gamma_{H^+}[H^+]}{\gamma_{NH_4{}^+}}H^*_{NH_3}W_iRT\times 0.987\times 10^{-14}} \\ &= \frac{\frac{\gamma_{H^+}10^{-pH}}{\gamma_{NH_4{}^+}}H^*_{NH_3}W_iRT\times 0.987\times 10^{-14}}{1 + \frac{\gamma_{H^+}10^{-pH}}{\gamma_{NH_4{}^+}}H^*_{NH_3}W_iRT\times 0.987\times 10^{-14}}\end{aligned} \tag{C-18}$$

where the 0.987 comes from the conversion from 1 atm to 1 psi and W_i unit is μg m^{-3}. $H^*_{NH_3}$(atm^{-1}) can be calculated from Equation 12 in *Clegg et al.* [1998]. Note that, the mole fraction based $H^*_{NH_3}$ has the same numerical value as its molality based form. ε(NH_4^T) is equivalent to ε(NH_4^+) presented in the main text, since NH_4^+ is the dominant form of dissolved NH_3 based on $\frac{K_a}{\gamma_{NH_3}} \ll \frac{\gamma_{H^+}[H^+]}{\gamma_{NH_4^+}}$ and under atmospheric conditions.

Summary: with the equations of ε(NO_3^-), ε(Cl^-), and ε(NH_4^+), S-shaped curves of these three gas-particle partitioning can be easily calculated with pH, T, W_i, and activity coefficients. We simulate two set of results, Figure C-3 assuming activity coefficients to be one (ideal solution) and Figure C-4 with practical activity coefficients from CalNex, WINTER, and SOAS.

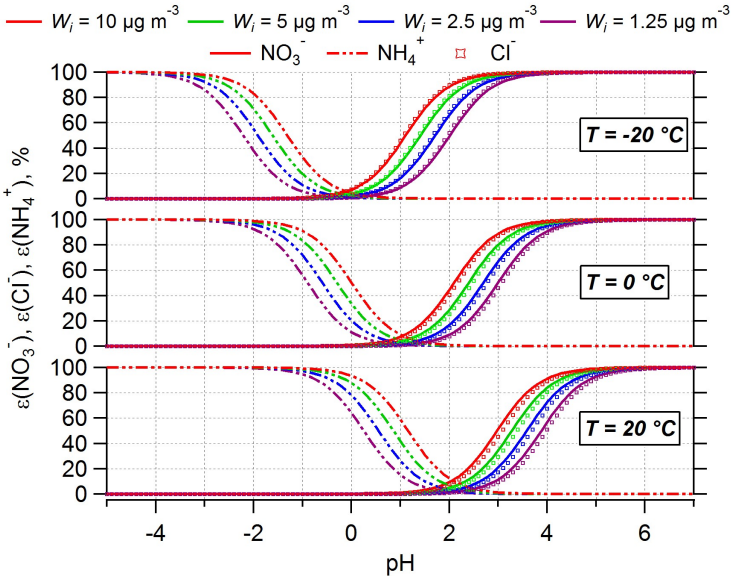

Figure C-3 Simulated $\varepsilon(NO_3^-)$, $\varepsilon(NH_4^+)$, $\varepsilon(Cl^-)$ at −20 °C, 0 °C, 20 °C and various particle liquid waterlevels (1.25, 2.5, 5, 10 µg m^{-3}) assuming ideal solutions.

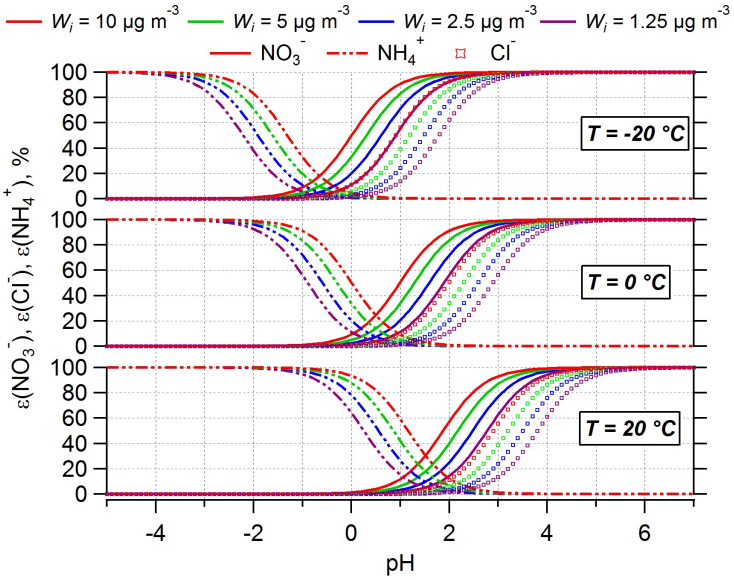

Figure C-4 Simulated $\varepsilon(NO_3^-)$, $\varepsilon(NH_4^+)$, $\varepsilon(Cl^-)$ at −20 °C, 0 °C, 20 °C and various particle liquid water levels (1.25, 2.5, 5, 10 µg m^{-3}) with activity coefficients obtained from CalNex campaign. $\gamma_{H^+}\gamma_{NO_3^-}$ = 0.078, $\gamma_{H^+}\gamma_{Cl^-}$ = 0.66, and $\gamma_{H^+}/\gamma_{NH_4^+}$ assumed to be 1. Note that, $\gamma_{H^+}\gamma_{NO_3^-}$ is calculated from ISORROPIA-predicted ionic pair activity coefficient, $\gamma_{H^+-NO_3^-}$, by $\gamma_{H^+}\gamma_{NO_3^-} = \left(\gamma_{H^+-NO_3^-}\right)^2$.

C.3 Investigation of the cause for bias in ε(NO_3^-): sample line heating?

As Figure C-5 shows, NO_3^- and ε(NO_3^-**)** are both overpredicted during the nighttime and underpredicted during the daytime. The deviations from measurements are anti-correlated with nitric acid. The deviation between predicted and measured HNO_3 also has a diurnal pattern, reverse to that of NO_3^-.

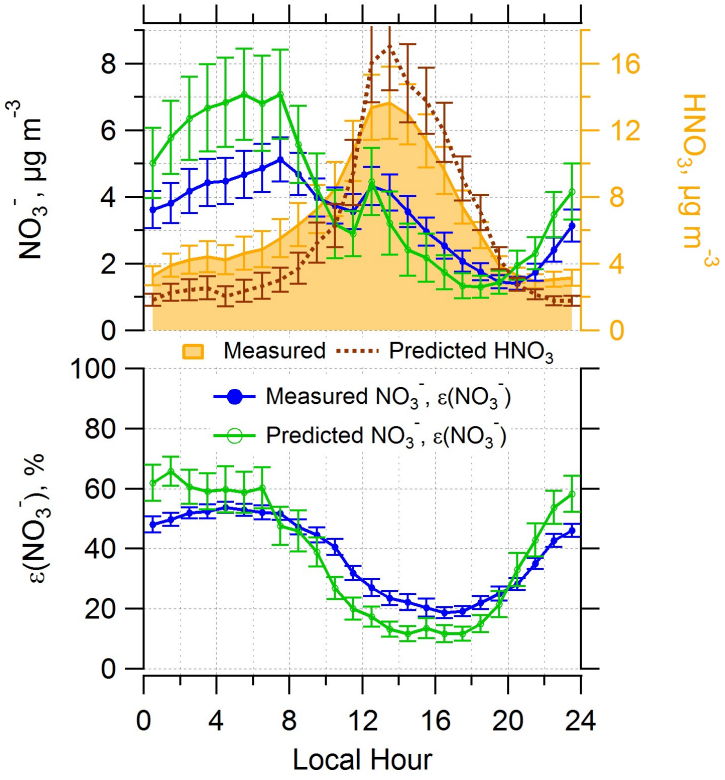

Figure C-5 Diurnal profiles of measured and predicted HNO_3, NO_3^-, and ε(NO_3^-). Data shown above are for the complete CalNex study and particle-phase data is AMS PM_1. Mean hourly averages are shown and standard errors are plotted as error bars.

Table C-1 Summary of temperature differences in sample lines and ambient and sample line residence time for the AMS and CIMS. AMS indoor T was 25°C. CIMS inlet was heated to 75°C.

Instrument	Inlet residence time, sec	Time of the day	Temperature differences, °C
AMS	2.1	Day	~0
		Night	~ +10
CIMS	0.32	Day	~ +50
		Night	~ +60

For the AMS sample line located indoors, particle heating was most likely to occur at night (indoor T > ambient T), which may cause semivolatile NO_3^- loss. There were no temperature differences during the day (Table C-1). To examine the possible sample line heating/cooling effect, we first determined sample line RH (Equation C-19) by conservation of water vapor under isobaric condition and following saturated water vapor pressure equation $e_s = 6.11\times10^{\left(\frac{7.5T}{237.5+T}\right)}$ (T unit as °C) [*Alduchov and Eskridge*, 1996]. The inferred sample line RH is plotted with measured ambient RH in Figure C-6b. Sample line RH was lower (~50%) than ambient (~90%) at midnight and close to ambient (~60%) in the afternoon since temperatures were similar.

$$RH_2 = RH_1 10^{\left[\left(\frac{7.5T_1}{237.5+T_1}\right)-\left(\frac{7.5T_2}{237.5+T_2}\right)\right]} \quad \text{(C-19)}$$

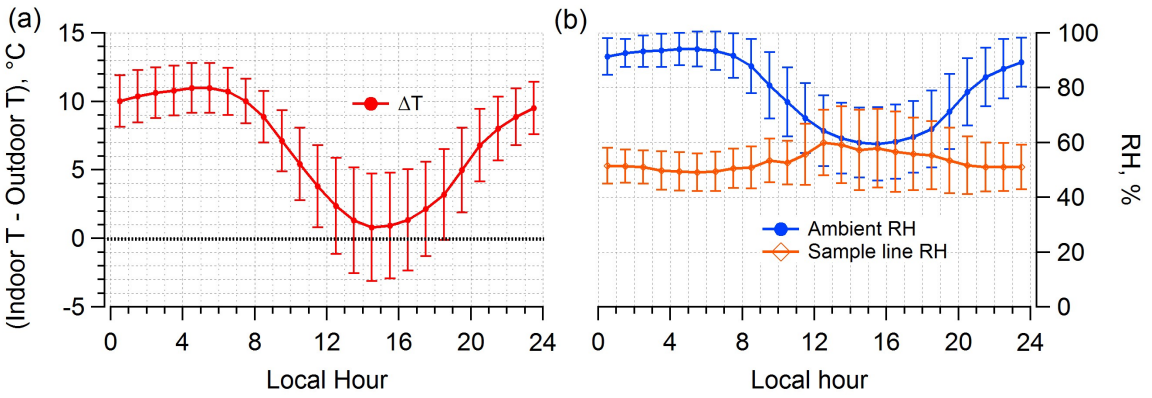

Figure C-6 Diurnal profiles of (a) temperature difference between AMS indoor and outdoor and (b) corresponding ambient and RH predicted in the sample line due to the T difference. Mean hourly averages and standard deviations are shown.

ISORROPIA-II was run with aerosol and gas-phase species at the AMS sample line T and RH and compared to predictions from ambient T and RH and measurements. Figure C-7 is discussed in the main text section 4.5.1.

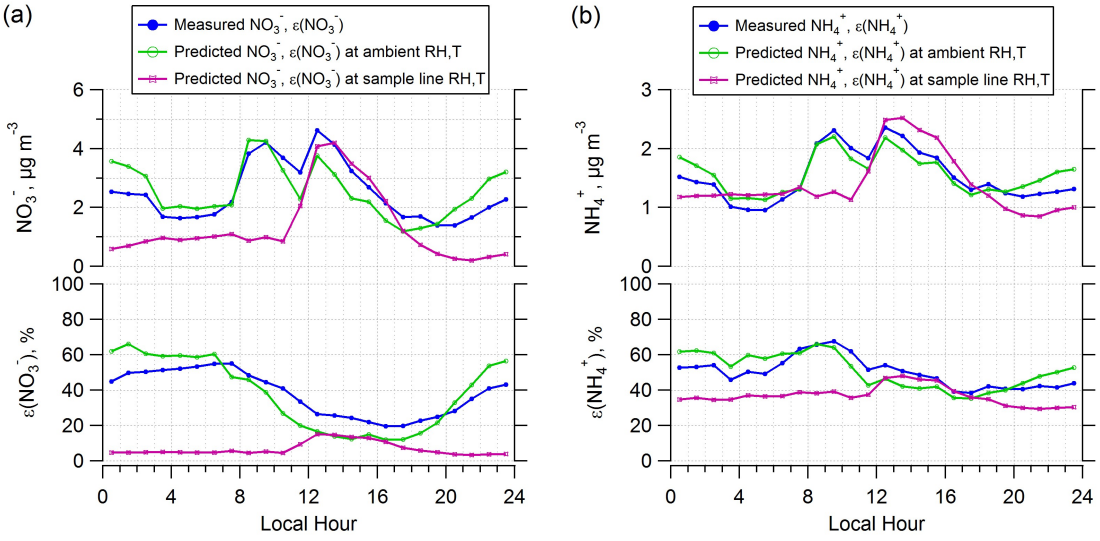

Figure C-7 Diurnal profiles of measured and predicted (a) NO_3^-, $\varepsilon(NO_3^-)$ and (b) NH_4^+, $\varepsilon(NH_4^+)$. Predictions are based on ambient or sample line RH and T for AMS inlet. Data shown above are for the complete CalNex study in the 20-95% RH range and particle-phase data is AMS PM_1. Mean hourly averages are shown. ISORROPIA run with ambient

data show that the predicted partitioning between the particle and gas phase is in better agreement with observations than runs using sample line T and RH. Note that in both runs, only T and RH differ since total nitrate and ammonium input are the same.

CIMS inlet heating is similar for day (~50°C) and night (~60°C). Potential bias in the HNO_3 or HCl then mainly depends on the mass loadings of NO_3^- or Cl^-. Here we focus only on the possible bias due to over-measurement of HNO_3. ISORROPIA-II was run at ambient RH and T with a "corrected" HNO_3 at three assumed lower levels of HNO_3 to compensate for an assumed positive nitrate artifact of 10%, 20%, 30% (i.e., assuming 10, 20 or 30% of the nitrate measured by the AMS or PILS was evaporated in the CIMS inlet leading to an over-measurement of HNO_3. 10% to 30% particle NO_3^- was subtracted from the measured CIMS HNO_3). Only HNO_3 is modified, all other inputs are kept the same. Results are shown in Figure C-8. Evaporation of 30% of the measured nitrate is expected to be an extreme upper limit. For instance, 66% of PM_1 nitrate evaporated at a temperature of 75°C in a thermal denuder upstream of the AMS at the CalNex site, consistent with previous results at other urban sites in the LA area and elsewhere [*Huffman et al.*, 2009]. The residence time on the thermal denuder was ~ 12 sec, while that of the CIMS inlet was ~0.32 sec, so the extent of evaporation in the CIMS inlet assumed to be substantially lower than that in the thermal denuder.

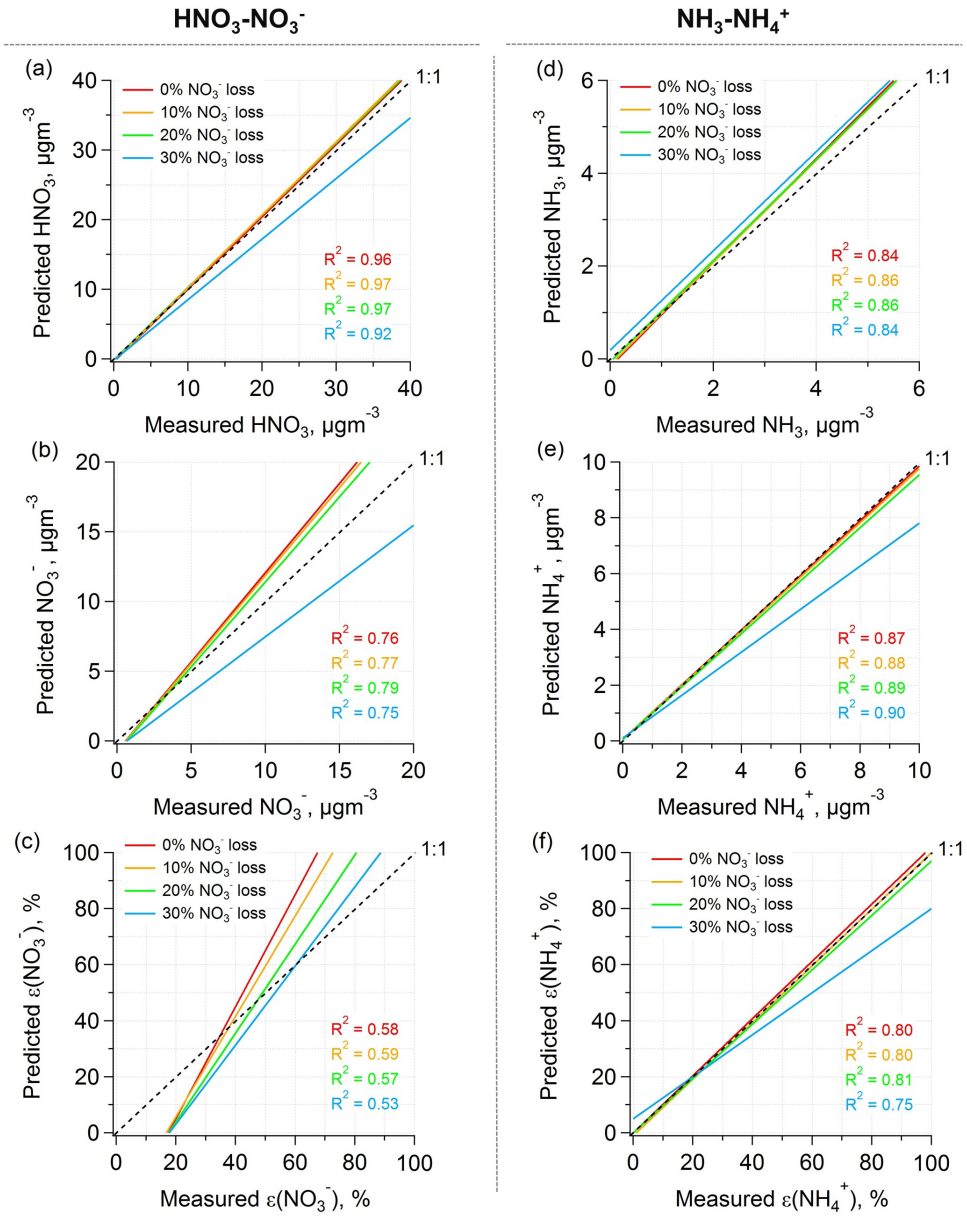

Figure C-8 Comparisons of predicted and measured HNO_3, NO_3^-, and $\varepsilon(NO_3^-)$ (a, b, c) and NH_3, NH_4^+, and $\varepsilon(NH_4^+)$ (d, e, f) for data from the complete CalNex study based on "corrected" HNO_3 data due to assumed PM_1 nitrate evaporation in the heated CIMS inlet. The other inputs are kept the same. Only the ODR fits are shown. "0% NO_3^- loss" condition is the same as Figure 4-2 in the main text.

REFERENCES

Alduchov, O. A., and R. E. Eskridge (1996), Improved magnus form approximation of saturation vapor pressure, *Journal of Applied Meteorology*, *35*(4), 601-609, doi:10.1175/1520-0450(1996)035<0601:Imfaos>2.0.Co;2.

Allen, H. M., et al. (2015), Influence of crustal dust and sea spray supermicron particle concentrations and acidity on inorganic NO_3^- aerosol during the 2013 Southern Oxidant and Aerosol Study, *Atmospheric Chemistry and Physics*, *15*(18), 10669-10685, doi:10.5194/acp-15-10669-2015.

Ansari, A. S., and S. N. Pandis (2000), The effect of metastable equilibrium states on the partitioning of nitrate between the gas and aerosol phases, *Atmospheric Environment*, *34*(1), 157-168, doi:10.1016/s1352-2310(99)00242-3.

Attwood, A. R., et al. (2014), Trends in sulfate and organic aerosol mass in the Southeast U.S.: Impact on aerosol optical depth and radiative forcing, *Geophysical Research Letters*, *41*(21), 7701-7709, doi:10.1002/2014gl061669.

Bacarella, A. L., E. Grunwald, H. P. Marshall, and E. L. Purlee (1955), The Potentiometric Measurement of Acid Dissociation Constants and *p*H in the System Methanol-Water. pK_a Values for Carboxylic Acids and Anilinium Ions, *Journal of Organic Chemistry*, *20*(6), 747-762, doi:10.1021/Jo01124a007.

Bahreini, R., E. J. Dunlea, B. M. Matthew, C. Simons, K. S. Docherty, P. F. DeCarlo, J. L. Jimenez, C. A. Brock, and A. M. Middlebrook (2008), Design and Operation of a Pressure-Controlled Inlet for Airborne Sampling with an Aerodynamic Aerosol Lens, *Aerosol Science and Technology*, *42*(6), 465-471, doi:10.1080/02786820802178514.

Bahreini, R., et al. (2009), Organic aerosol formation in urban and industrial plumes near Houston and Dallas, Texas, *Journal of Geophysical Research*, *114*, D00F16, doi:10.1029/2008jd011493.

Bauer, S. E., K. Tsigaridis, and R. Miller (2016), Significant atmospheric aerosol pollution caused by world food cultivation, *Geophysical Research Letters*, *43*(10), 5394-5400, doi:10.1002/2016gl068354.

Bellouin, N., J. Rae, A. Jones, C. Johnson, J. Haywood, and O. Boucher (2011), Aerosol forcing in the Climate Model Intercomparison Project (CMIP5) simulations by HadGEM2-ES and the role of ammonium nitrate, *Journal of Geophysical Research*, *116*, D20206, doi:10.1029/2011jd016074.

Bergin, M. H., et al. (2001), Aerosol radiative, physical, and chemical properties in Beijing during June 1999, *Journal of Geophysical Research*, *106*(D16), 17969-17980, doi:10.1029/2001jd900073.

Bertram, A. K., S. T. Martin, S. J. Hanna, M. L. Smith, A. Bodsworth, Q. Chen, M. Kuwata, A. Liu, Y. You, and S. R. Zorn (2011), Predicting the relative humidities of liquid-liquid phase separation, efflorescence, and deliquescence of mixed particles of ammonium sulfate, organic material, and water using the organic-to-sulfate mass ratio of the particle and the oxygen-to-carbon elemental ratio of the organic component, *Atmospheric Chemistry and Physics*, *11*(21), 10995-11006, doi:10.5194/acp-11-10995-2011.

Bertram, T. H., and J. A. Thornton (2009), Toward a general parameterization of N_2O_5 reactivity on aqueous particles: the competing effects of particle liquid water, nitrate and chloride, *Atmospheric Chemistry and Physics*, *9*(21), 8351-8363, doi:10.5194/acp-9-8351-2009.

Blanchard, C. L., G. M. Hidy, S. Tanenbaum, E. S. Edgerton, and B. E. Hartsell (2013), The Southeastern Aerosol Research and Characterization (SEARCH) study: Spatial variations and chemical climatology, 1999–2010, *Journal of the Air & Waste Management Association*, *63*(3), 260-275, doi:10.1080/10962247.2012.749816.

Bones, D. L., J. P. Reid, D. M. Lienhard, and U. K. Krieger (2012), Comparing the mechanism of water condensation and evaporation in glassy aerosol, *Proceedings of the National Academy of Sciences of the United States of America*, *109*(29), 11613-11618, doi:10.1073/pnas.1200691109.

Bougiatioti, A., A. Nenes, D. Paraskevopoulou, L. Fourtziou, I. Stavroulas, E. Liakakou, R. Weber, E. Gerasopoulo, P. Nikolaou, and N. Mihalopoulos (2017), The unappreciated effects of biomass burning on fine mode aerosol acidity, water and nitrogen partitioning, *In review*.

Bougiatioti, A., P. Nikolaou, I. Stavroulas, G. Kouvarakis, R. Weber, A. Nenes, M. Kanakidou, and N. Mihalopoulos (2016), Particle water and pH in the Eastern Mediterranean: Sources variability and implications for nutrients availability, *Atmospheric Chemistry and Physics*, *16*(7), 4579-4591, doi:10.5194/acp-16-4579-2016.

Budisulistiorini, S. H., et al. (2013), Real-time continuous characterization of secondary organic aerosol derived from isoprene epoxydiols in downtown Atlanta, Georgia, using the Aerodyne Aerosol Chemical Speciation Monitor, *Environmental science & technology*, *47*(11), 5686-5694, doi:10.1021/es400023n.

Budisulistiorini, S. H., et al. (2015), Examining the effects of anthropogenic emissions on isoprene-derived secondary organic aerosol formation during the 2013 Southern Oxidant and Aerosol Study (SOAS) at the Look Rock, Tennessee ground site, *Atmospheric Chemistry and Physics*, *15*(15), 8871-8888, doi:10.5194/acp-15-8871-2015.

Cabada, J. C., S. Rees, S. Takahama, A. Khlystov, S. N. Pandis, C. I. Davidson, and A. L. Robinson (2004), Mass size distributions and size resolved chemical composition of fine particulate matter at the Pittsburgh supersite, *Atmospheric Environment*, *38*(20), 3127-3141, doi:10.1016/j.atmosenv.2004.03.004.

Canagaratna, M. R., et al. (2007), Chemical and microphysical characterization of ambient aerosols with the aerodyne aerosol mass spectrometer, *Mass spectrometry reviews*, *26*(2), 185-222, doi:10.1002/mas.20115.

Capps, S. L., D. K. Henze, A. Hakami, A. G. Russell, and A. Nenes (2012), ANISORROPIA: the adjoint of the aerosol thermodynamic model ISORROPIA, *Atmospheric Chemistry and Physics*, *12*(1), 527-543, doi:10.5194/acp-12-527-2012.

Carlton, A. G., and B. J. Turpin (2013), Particle partitioning potential of organic compounds is highest in the Eastern US and driven by anthropogenic water, *Atmospheric Chemistry and Physics*, *13*(20), 10203-10214, doi:10.5194/acp-13-10203-2013.

Carrico, C. M., M. J. Rood, and J. A. Ogren (1998), Aerosol light scattering properties at Cape Grim, Tasmania, during the First Aerosol Characterization Experiment (ACE 1), *Journal of Geophysical Research*, *103*(D13), 16565, doi:10.1029/98jd00685.

Carrico, C. M., M. J. Rood, J. A. Ogren, C. Neususs, A. Wiedensohler, and J. Heintzenberg (2000), Aerosol optical properties at Sagres, Portugal during ACE-2, *Tellus Series B-Chemical and Physical Meteorology*, *52*(2), 694-715, doi:10.1034/j.1600-0889.2000.00049.x.

Carslaw, K. S., S. L. Clegg, and P. Brimblecombe (1995), A Thermodynamic Model of the System HCl-HNO_3-H_2SO_4-H_2O, Including Solubilities of Hbr, from <200 to 328 K, *Journal of physical Chemistry*, *99*(29), 11557-11574, doi:10.1021/j100029a039.

Cerully, K. M., A. Bougiatioti, J. R. Hite, H. Guo, L. Xu, N. L. Ng, R. Weber, and A. Nenes (2015), On the link between hygroscopicity, volatility, and oxidation state of ambient and water-soluble aerosols in the southeastern United States, *Atmospheric Chemistry and Physics*, *15*(15), 8679-8694, doi:10.5194/acp-15-8679-2015.

Cerully, K. M., A. Bougiatioti, J. R. Hite Jr, H. Guo, L. Xu, N. L. Ng, R. Weber, and A. Nenes (2014), On the link between hygroscopicity, volatility, and oxidation state of ambient and water-soluble aerosol in the Southeastern United States, *Atmospheric Chemistry and Physics Discussions*, *14*(22), 30835-30877, doi:10.5194/acpd-14-30835-2014.

Chang, M. C., C. Sioutas, S. Kim, H. Gong, and W. S. Linn (2000), Reduction of nitrate losses from filter and impactor samplers by means of concentration enrichment, *Atmospheric Environment*, *34*(1), 85-98, doi:Doi 10.1016/S1352-2310(99)00308-8.

Cheng, Y., et al. (2016), Reactive nitrogen chemistry in aerosol water as a source of sulfate during haze events in China, *Science Advances*, *2*(12), e1601530, doi:10.1126/sciadv.1601530.

Chu, S.-H. (2004), $PM_{2.5}$ episodes as observed in the speciation trends network, *Atmospheric Environment*, *38*(31), 5237-5246, doi:10.1016/j.atmosenv.2004.01.055.

Chung, S. H., and J. H. Seinfeld (2002), Global distribution and climate forcing of carbonaceous aerosols, *Journal of Geophysical Research*, *107*(D19), doi:10.1029/2001jd001397.

Clegg, S. L., and P. Brimblecombe (1990), Equilibrium partial pressures and mean activity and osmotic coefficients of 0-100% nitric acid as a function of temperature, *Journal of physical Chemistry*, *94*(13), 5369-5380, doi:10.1021/j100376a038.

Clegg, S. L., P. Brimblecombe, and A. S. Wexler (1998), Thermodynamic model of the system H^+-NH_4^+-SO_4^{2-}-NO_3^--H_2O at tropospheric temperatures, *Journal of Physical Chemistry A*, *102*(12), 2137-2154, doi:10.1021/Jp973042r.

Clegg, S. L., J. H. Seinfeld, and E. O. Edney (2003), Thermodynamic modelling of aqueous aerosols containing electrolytes and dissolved organic compounds. II. An extended Zdanovskii–Stokes–Robinson approach, *Journal of Aerosol Science*, *34*(6), 667-690, doi:10.1016/s0021-8502(03)00019-3.

Cohen, A. J., et al. (2017), Estimates and 25-year trends of the global burden of disease attributable to ambient air pollution: an analysis of data from the Global Burden of Diseases Study 2015, *The Lancet*, *389*(10082), 1907-1918, doi:10.1016/s0140-6736(17)30505-6.

Craig, L., A. Moharreri, D. C. Rogers, B. Anderson, and S. Dhaniyala (2014), Aircraft-Based Aerosol Sampling in Clouds: Performance Characterization of Flow-Restriction Aerosol Inlets, *Journal of Atmospheric and Oceanic Technology*, *31*(11), 2512-2521, doi:10.1175/jtech-d-14-00022.1.

Craig, L., A. Moharreri, A. Schanot, D. C. Rogers, B. Anderson, and S. Dhaniyala (2013a), Characterizations of Cloud Droplet Shatter Artifacts in Two Airborne Aerosol Inlets, *Aerosol Science and Technology*, *47*(6), 662-671, doi:10.1080/02786826.2013.780648.

Craig, L., A. Schanot, A. Moharreri, D. C. Rogers, and S. Dhaniyala (2013b), Design and Sampling Characteristics of a New Airborne Aerosol Inlet for Aerosol Measurements in Clouds, *Journal of Atmospheric and Oceanic Technology*, *30*(6), 1123-1135, doi:10.1175/jtech-d-12-00168.1.

Cruz, C. N., K. G. Dassios, and S. N. Pandis (2000), The effect of dioctyl phthalate films on the ammonium nitrate aerosol evaporation rate, *Atmospheric Environment*, *34*(23), 3897-3905, doi:10.1016/S1352-2310(00)00173-4.

Czoschke, N. M., and M. Jang (2006), Acidity effects on the formation of α-pinene ozone SOA in the presence of inorganic seed, *Atmospheric Environment*, *40*(23), 4370-4380, doi:10.1016/j.atmosenv.2006.03.030.

Dassios, K. G., and S. N. Pandis (1999), The mass accommodation coefficient of ammonium nitrate aerosol, *Atmospheric Environment*, *33*(18), 2993-3003, doi:10.1016/S1352-2310(99)00079-5.

DeCarlo, P. F., et al. (2006), Field-deployable, high-resolution, time-of-flight aerosol mass spectrometer, *Analytical chemistry*, *78*(24), 8281-8289, doi:10.1021/ac061249n.

DeCarlo, P. F., J. G. Slowik, D. R. Worsnop, P. Davidovits, and J. L. Jimenez (2004), Particle Morphology and Density Characterization by Combined Mobility and Aerodynamic Diameter Measurements. Part 1: Theory, *Aerosol Science and Technology*, *38*(12), 1185-1205, doi:10.1080/027868290903907.

Dibb, J. E., R. W. Talbot, and E. M. Scheuer (2000), Composition and distribution of aerosols over the North Atlantic during the Subsonic Assessment Ozone and Nitrogen Oxide Experiment (SONEX), *Journal of Geophysical Research*, *105*(D3), 3709, doi:10.1029/1999jd900424.

Dibb, J. E., R. W. Talbot, E. M. Scheuer, D. R. Blake, N. J. Blake, G. L. Gregory, G. W. Sachse, and D. C. Thornton (1999), Aerosol chemical composition and distribution during the Pacific Exploratory Mission (PEM) Tropics, *Journal of Geophysical Research*, *104*(D5), 5785, doi:10.1029/1998jd100001.

Dockery, D. W., J. Cunningham, A. I. Damokosh, L. M. Neas, J. D. Spengler, P. Koutrakis, J. H. Ware, M. Raizenne, and F. E. Speizer (1996), Health effects of acid aerosols on North American children: respiratory symptoms, *Environmental Health Perspectives*, *104*(5), 500-505, doi:10.2307/3432990.

Duce, R. A., and N. W. Tindale (1991), Atmospheric transport of iron and its deposition in the ocean, *Limnology and Oceanography*, *36*(8), 1715-1726, doi:10.4319/lo.1991.36.8.1715.

Dunlea, E. J., et al. (2009), Evolution of Asian aerosols during transpacific transport in INTEX-B, *Atmospheric Chemistry and Physics*, *9*(19), 7257-7287, doi:10.5194/acp-9-7257-2009.

Duyzer, J. (1994), Dry deposition of ammonia and ammonium aerosols over heathland, *Journal of Geophysical Research-Atmospheres*, *99*(D9), 18757-18763, doi:10.1029/94jd01210.

Eddingsaas, N. C., D. G. VanderVelde, and P. O. Wennberg (2010), Kinetics and Products of the Acid-Catalyzed Ring-Opening of Atmospherically Relevant Butyl Epoxy Alcohols, *Journal of Physical Chemistry A*, *114*(31), 8106-8113, doi:10.1021/Jp103907c.

Edney, E. O., T. E. Kleindienst, M. Jaoui, M. Lewandowski, J. H. Offenberg, W. Wang, and M. Claeys (2005), Formation of 2-methyl tetrols and 2-methylglyceric acid in secondary organic aerosol from laboratory irradiated isoprene/NO_X/SO_2/air mixtures and their detection in ambient $PM_{2.5}$ samples collected in the eastern United States, *Atmospheric Environment*, *39*(29), 5281-5289, doi:10.1016/j.atmosenv.2005.05.031.

Ellis, R. A., J. G. Murphy, E. Pattey, R. van Haarlem, J. M. O'Brien, and S. C. Herndon (2010), Characterizing a Quantum Cascade Tunable Infrared Laser Differential Absorption Spectrometer (QC-TILDAS) for measurements of atmospheric ammonia, *Atmospheric Measurement Techniques*, *3*(2), 397-406, doi:10.5194/amt-3-397-2010.

Enami, S., M. R. Hoffmann, and A. J. Colussi (2008), Acidity enhances the formation of a persistent ozonide at aqueous ascorbate/ozone gas interfaces, *Proceedings of the National Academy of Sciences of the United States of America*, *105*(21), 7365-7369, doi:10.1073/pnas.0710791105.

Engelhart, G. J., A. Asa-Awuku, A. Nenes, and S. N. Pandis (2008), CCN activity and droplet growth kinetics of fresh and aged monoterpene secondary organic aerosol, *Atmospheric Chemistry and Physics*, *8*(14), 3937-3949, doi:10.5194/acp-8-3937-2008.

Ervens, B., B. J. Turpin, and R. J. Weber (2011), Secondary organic aerosol formation in cloud droplets and aqueous particles (aqSOA): a review of laboratory, field and model studies, *Atmospheric Chemistry and Physics*, *11*(21), 11069-11102, doi:10.5194/acp-11-11069-2011.

Fang, T., H. Guo, V. Verma, R. E. Peltier, and R. J. Weber (2015), $PM_{2.5}$ water-soluble elements in the southeastern United States: automated analytical method development, spatiotemporal distributions, source apportionment, and implications for heath studies, *Atmospheric Chemistry and Physics*, *15*(20), 11667-11682, doi:10.5194/acp-15-11667-2015.

Fang, T., H. Guo, L. Zeng, V. Verma, A. Nenes, and R. J. Weber (2017), Highly Acidic Ambient Particles, Soluble Metals, and Oxidative Potential: A Link between Sulfate and Aerosol Toxicity, *Environmental science & technology*, *51*(5), 2611-2620, doi:10.1021/acs.est.6b06151.

Fountoukis, C., and A. Nenes (2007), ISORROPIA II: a computationally efficient thermodynamic equilibrium model for K^+-Ca^{2+}-Mg^{2+}-NH_4^+-Na^+-SO_4^{2-}-NO_3^--Cl^--H_2O aerosols, *Atmospheric Chemistry and Physics*, *7*(17), 4639-4659, doi:10.5194/acp-7-4639-2007.

Fountoukis, C., A. Nenes, A. Sullivan, R. Weber, T. Van Reken, M. Fischer, E. Matias, M. Moya, D. Farmer, and R. C. Cohen (2009), Thermodynamic characterization of Mexico City aerosol during MILAGRO 2006, *Atmospheric Chemistry and Physics*, *9*(6), 2141-2156, doi:10.5194/acp-9-2141-2009.

Frosch, M., M. Bilde, P. F. DeCarlo, Z. Jurányi, T. Tritscher, J. Dommen, N. M. Donahue, M. Gysel, E. Weingartner, and U. Baltensperger (2011), Relating cloud condensation nuclei activity and oxidation level of α-pinene secondary organic aerosols, *Journal of Geophysical Research: Atmospheres*, *116*(D22), doi:10.1029/2011jd016401.

Froyd, K. D., D. M. Murphy, P. Lawson, D. Baumgardner, and R. L. Herman (2010), Aerosols that form subvisible cirrus at the tropical tropopause, *Atmospheric Chemistry and Physics*, *10*(1), 209-218, doi:10.5194/acp-10-209-2010.

Fry, J. L., et al. (2013), Observations of gas- and aerosol-phase organic nitrates at BEACHON-RoMBAS 2011, *Atmospheric Chemistry and Physics*, *13*(17), 8585-8605, doi:10.5194/acp-13-8585-2013.

Gao, S., M. Keywood, N. L. Ng, J. Surratt, V. Varutbangkul, R. Bahreini, R. C. Flagan, and J. H. Seinfeld (2004), Low-molecular-weight and oligomeric components in secondary organic aerosol from the ozonolysis of cycloalkenes and α-pinene, *Journal of Physical Chemistry A*, *108*(46), 10147-10164, doi:10.1021/Jp047466e.

Gard, E. E., et al. (1998), Direct Observation of Heterogeneous Chemistry in the Atmosphere, *Science*, *279*(5354), 1184-1187, doi:10.1126/science.279.5354.1184.

Gauderman, W. J., et al. (2004), The effect of air pollution on lung development from 10 to 18 years of age, *New England Journal of Medicine*, *351*(11), 1057-1067, doi:10.1056/NEJMoa040610.

Ghio, A. J., M. S. Carraway, and M. C. Madden (2012), Composition of air pollution particles and oxidative stress in cells, tissues, and living systems, *Journal of toxicology and environmental health. Part B, Critical reviews*, *15*(1), 1-21, doi:10.1080/10937404.2012.632359.

Graaff, R., J. G. Aarnoudse, J. R. Zijp, P. M. A. Sloot, F. F. M. de Mul, J. Greve, and M. H. Koelink (1992), Reduced light-scattering properties for mixtures of spherical particles: a simple approximation derived from Mie calculations, *Applied Optics*, *31*(10), 1370-1376, doi:10.1364/AO.31.001370.

Greenspan, L. (1977), Humdity Fixed Points of Binary Saturated Aqueous Solutions, *Journal of Research of the National Bureau of Standards, 81A*(1), 8, doi:10.6028/jres.081A.011.

Guo, H., J. Liu, K. D. Froyd, J. M. Roberts, P. R. Veres, P. L. Hayes, J. L. Jimenez, A. Nenes, and R. J. Weber (2017a), Fine particle pH and gas–particle phase partitioning of inorganic species in Pasadena, California, during the 2010 CalNex campaign, *Atmospheric Chemistry and Physics*, *17*(9), 5703-5719, doi:10.5194/acp-17-5703-2017.

Guo, H., et al. (2016), Fine particle pH and the partitioning of nitric acid during winter in the northeastern United States, *Journal of Geophysical Research: Atmospheres*, *121*(17), 10355-10376, doi:10.1002/2016jd025311.

Guo, H., R. Weber, and A. Nenes (2017b), The sensitivity of particle pH to NH_3: Can high NH_3 cause London Fog conditions?, *In review*.

Guo, H., et al. (2015), Fine-particle water and pH in the southeastern United States, *Atmospheric Chemistry and Physics*, *15*(9), 5211-5228, doi:10.5194/acp-15-5211-2015.

Gwynn, R. C., R. T. Burnett, and G. D. Thurston (2000), A time-series analysis of acidic particulate matter and daily mortality and morbidity in the Buffalo, New York, region, *Environmental Health Perspectives*, *108*(2), 125-133, doi:10.2307/3454510.

Han, Y., C. A. Stroud, J. Liggio, and S.-M. Li (2016a), The effect of particle acidity on secondary organic aerosol formation from α-pinene photooxidation under atmospherically relevant conditions, *Atmospheric Chemistry and Physics*, *16*(21), 13929-13944, doi:10.5194/acp-16-13929-2016.

Han, Y., C. A. Stroud, J. Liggo, and S.-M. Li (2016b), The effect of particle acidity on secondary organic aerosol formation from α-pinene photooxidation under atmospherically relevant conditions, *Atmospheric Chemistry and Physics Discussions*, 1-26, doi:10.5194/acp-2016-301.

Hand, J. L., and S. M. Kreidenweis (2002), A New Method for Retrieving Particle Refractive Index and Effective Density from Aerosol Size Distribution Data, *Aerosol Science and Technology*, *36*(10), 1012-1026, doi:10.1080/02786820290092276.

Hand, J. L., B. A. Schichtel, W. C. Malm, and M. L. Pitchford (2012a), Particulate sulfate ion concentration and SO_2 emission trends in the United States from the early 1990s through 2010, *Atmospheric Chemistry and Physics*, *12*(21), 10353-10365, doi:10.5194/acp-12-10353-2012.

Hand, J. L., B. A. Schichtel, M. Pitchford, W. C. Malm, and N. H. Frank (2012b), Seasonal composition of remote and urban fine particulate matter in the United States, *Journal of Geophysical Research: Atmospheres*, *117*(D5), D05209, doi:10.1029/2011jd017122.

Hanisch, F., and J. N. Crowley (2001), The heterogeneous reactivity of gaseous nitric acid on authentic mineral dust samples, and on individual mineral and clay mineral components, *Physical Chemistry Chemical Physics*, *3*(12), 2474-2482, doi:10.1039/b101700o.

Hansen, D. A., et al. (2006), Air Quality Measurements for the Aerosol Research and Inhalation Epidemiology Study, *Journal of the Air & Waste Management Association*, *56*(10), 1445-1458, doi:10.1080/10473289.2006.10464549.

Hansen, D. A., E. S. Edgerton, B. E. Hartsell, J. J. Jansen, N. Kandasamy, G. M. Hidy, and C. L. Blanchard (2003), The Southeastern Aerosol Research and Characterization Study: Part 1—Overview, *Journal of the Air & Waste Management Association*, *53*(12), 1460-1471, doi:10.1080/10473289.2003.10466318.

Hayes, P. L., et al. (2015), Modeling the formation and aging of secondary organic aerosols in Los Angeles during CalNex 2010, *Atmospheric Chemistry and Physics*, *15*(10), 5773-5801, doi:10.5194/acp-15-5773-2015.

Hayes, P. L., et al. (2013), Organic aerosol composition and sources in Pasadena, California, during the 2010 CalNex campaign, *Journal of Geophysical Research: Atmospheres*, *118*(16), 9233-9257, doi:10.1002/jgrd.50530.

Haywood, J., and O. Boucher (2000), Estimates of the direct and indirect radiative forcing due to tropospheric aerosols: A review, *Reviews of Geophysics*, *38*(4), 513-543, doi:10.1029/1999rg000078.

Heald, C. L., et al. (2012), Atmospheric ammonia and particulate inorganic nitrogen over the United States, *Atmospheric Chemistry and Physics*, *12*(21), 10295-10312, doi:10.5194/acp-12-10295-2012.

Heintzenberg, J. (1989), Fine particles in the global troposphere A review, *Tellus B: Chemical and Physical Meteorology*, *41*(2), 149-160, doi:10.3402/tellusb.v41i2.15064.

Hennigan, C. J., M. H. Bergin, J. E. Dibb, and R. J. Weber (2008a), Enhanced secondary organic aerosol formation due to water uptake by fine particles, *Geophysical Research Letters*, *35*(18), L18801, doi:10.1029/2008gl035046.

Hennigan, C. J., J. Izumi, A. P. Sullivan, R. J. Weber, and A. Nenes (2015), A critical evaluation of proxy methods used to estimate the acidity of atmospheric particles, *Atmospheric Chemistry and Physics*, *15*(5), 2775-2790, doi:10.5194/acp-15-2775-2015.

Hennigan, C. J., S. Sandholm, S. Kim, R. E. Stickel, L. G. Huey, and R. J. Weber (2006), Influence of Ohio River valley emissions on fine particle sulfate measured from aircraft over large regions of the eastern United States and Canada during INTEX-NA, *Journal of Geophysical Research: Atmospheres*, *111*(D24), D24S04, doi:10.1029/2006/Jd007282.

Hennigan, C. J., et al. (2008b), On the volatility and production mechanisms of newly formed nitrate and water soluble organic aerosol in Mexico City, *Atmospheric Chemistry and Physics*, *8*(14), 3761-3768, doi:10.5194/acp-8-3761-2008.

Hering, S., and G. Cass (1999), The Magnitude of Bias in the Measurement of $PM_{2.5}$ Arising from Volatilization of Particulate Nitrate from Teflon Filters, *Journal of the Air & Waste Management Association*, *49*(6), 725-733, doi:10.1080/10473289.1999.10463843.

Hidy, G. M., C. L. Blanchard, K. Baumann, E. Edgerton, S. Tanenbaum, S. Shaw, E. Knipping, I. Tombach, J. Jansen, and J. Walters (2014), Chemical climatology of the southeastern United States, 1999-2013, *Atmospheric Chemistry and Physics*, *14*(21), 11893-11914, doi:10.5194/acp-14-11893-2014.

Hildebrandt Ruiz, L., A. L. Paciga, K. M. Cerully, A. Nenes, N. M. Donahue, and S. N. Pandis (2015), Formation and aging of secondary organic aerosol from toluene: changes in chemical composition, volatility, and hygroscopicity, *Atmospheric Chemistry and Physics*, *15*(14), 8301-8313, doi:10.5194/acp-15-8301-2015.

Huebert, B. J., and C. H. Robert (1985), The Dry Deposition of Nitric-Acid to Grass, *Journal of Geophysical Research: Atmospheres*, *90*(D1), 2085-2090, doi:10.1029/JD090iD01p02085.

Huffman, J. A., et al. (2009), Chemically-resolved aerosol volatility measurements from two megacity field studies, *Atmospheric Chemistry and Physics*, *9*(18), 7161-7182, doi:10.5194/acp-9-7161-2009.

Iinuma, Y., O. Böge, T. Gnauk, and H. Herrmann (2004), Aerosol-chamber study of the α-pinene/O_3 reaction: influence of particle acidity on aerosol yields and products, *Atmospheric Environment*, *38*(5), 761-773, doi:10.1016/j.atmosenv.2003.10.015.

IPCC (2013), Climate Change 2013: The Physical Science Basis. Contribution of Working Group I to the Fifth Assessment Report of the Intergovernmental Panel on Climate Change [Stocker, T.F., D. Qin, G.-K. Plattner, M. Tignor, S.K. Allen, J. Boschung, A. Nauels, Y. Xia, V. Bex and P.M. Midgley (eds.)].*Rep.*, 1535 pp, Cambridge, United Kingdom and New York, NY, USA.

Ito, A., and L. Xu (2014), Response of acid mobilization of iron-containing mineral dust to improvement of air quality projected in the future, *Atmospheric Chemistry and Physics*, *14*(7), 3441-3459, doi:10.5194/acp-14-3441-2014.

Ito, T., A. Nenes, M. S. Johnson, N. Meskhidze, and C. Deutsch (2016), Acceleration of oxygen decline in the tropical Pacific over the past decades by aerosol pollutants, *Nature Geoscience*, *9*(6), 443-447, doi:10.1038/ngeo2717.

Jang, M., N. M. Czoschke, S. Lee, and R. M. Kamens (2002), Heterogeneous atmospheric aerosol production by acid-catalyzed particle-phase reactions, *Science*, *298*(5594), 814-817, doi:10.1126/science.1075798.

Jayne, J. T., D. C. Leard, X. F. Zhang, P. Davidovits, K. A. Smith, C. E. Kolb, and D. R. Worsnop (2000), Development of an aerosol mass spectrometer for size and composition analysis of submicron particles, *Aerosol Science and Technology*, *33*(1-2), 49-70, doi:10.1080/027868200410840.

Jimenez, J. L., et al. (2009), Evolution of organic aerosols in the atmosphere, *Science*, *326*(5959), 1525-1529, doi:10.1126/science.1180353.

Kanakidou, M., et al. (2005), Organic aerosol and global climate modelling: a review, *Atmospheric Chemistry and Physics*, *5*, 1053-1123, doi:10.5194/acp-5-1053-2005.

Karambelas, A., H. O. T. Pye, S. H. Budisulistiorini, J. D. Surratt, and R. W. Pinder (2014), Contribution of Isoprene Epoxydiol to Urban Organic Aerosol: Evidence from Modeling and Measurements, *Environmental Science & Technology Letters*, *1*(6), 278-283, doi:10.1021/ez5001353.

Katoshevski, D., A. Nenes, and J. H. Seinfeld (1999), A study of processes that govern the maintenance of aerosols in the marine boundary layer, *Journal of Aerosol Science*, *30*(4), 503-532, doi:10.1016/S0021-8502(98)00740-X.

Katsouyanni, K., et al. (2001), Confounding and effect modification in the short-term effects of ambient particles on total mortality: Results from 29 European cities within the APHEA2 project, *Epidemiology*, *12*(5), 521-531, doi:10.1097/00001648-200109000-00011.

Keene, W. C., R. Sander, A. A. P. Pszenny, R. Vogt, P. J. Crutzen, and J. N. Galloway (1998), Aerosol pH in the marine boundary layer: A review and model evaluation, *Journal of Aerosol Science*, *29*(3), 339-356, doi:10.1016/s0021-8502(97)10011-8.

Keene, W. C., and D. L. Savoie (1998), The pH of deliquesced sea-salt aerosol in polluted marine air, *Geophysical Research Letters*, *25*(12), 2181-2184, doi:10.1029/98gl01591.

Kim, J., S.-C. Yoon, A. Jefferson, and S.-W. Kim (2006), Aerosol hygroscopic properties during Asian dust, pollution, and biomass burning episodes at Gosan, Korea in April 2001, *Atmospheric Environment*, *40*(8), 1550-1560, doi:10.1016/j.atmosenv.2005.10.044.

Kim, P. S., et al. (2015), Sources, seasonality, and trends of southeast US aerosol: an integrated analysis of surface, aircraft, and satellite observations with the GEOS-Chem chemical transport model, *Atmospheric Chemistry and Physics*, *15*(18), 10411-10433, doi:10.5194/acp-15-10411-2015.

Kimmel, J. R., D. K. Farmer, M. J. Cubison, D. Sueper, C. Tanner, E. Nemitz, D. R. Worsnop, M. Gonin, and J. L. Jimenez (2011), Real-time aerosol mass spectrometry with millisecond resolution, *International Journal of Mass Spectrometry*, *303*(1), 15-26, doi:10.1016/j.ijms.2010.12.004.

King, S. M., T. Rosenoern, J. E. Shilling, Q. Chen, and S. T. Martin (2007), Cloud condensation nucleus activity of secondary organic aerosol particles mixed with sulfate, *Geophysical Research Letters*, *34*(24), L24806, doi:10.1029/2007gl030390.

Kleindienst, T. E., E. O. Edney, M. Lewandowski, J. H. Offenberg, and M. Jaoui (2006), Secondary organic carbon and aerosol yields from the irradiations of isoprene and α-pinene in the presence of NO_x and SO_2, *Environmental science & technology*, *40*(12), 3807-3812, doi:10.1021/Es052446r.

Kleinstreuer, C., and Z. Zhang (2010), Airflow and Particle Transport in the Human Respiratory System, *Annual Review of Fluid Mechanics*, *42*(1), 301-334, doi:10.1146/annurev-fluid-121108-145453.

Kotchenruther, R. A., and P. V. Hobbs (1998), Humidification factors of aerosols from biomass burning in Brazil, *Journal of Geophysical Research*, *103*(D24), 32081, doi:10.1029/98jd00340.

Koutrakis, P., J. M. Wolfson, and J. D. Spengler (1988), An improved method for measuring aerosol strong acidity: Results from a nine-month study in St Louis, Missouri and Kingston, Tennessee, *Atmospheric Environment (1967)*, *22*(1), 157-162, doi:10.1016/0004-6981(88)90308-3.

Kuwata, M., S. R. Zorn, and S. T. Martin (2012), Using elemental ratios to predict the density of organic material composed of carbon, hydrogen, and oxygen, *Environmental science & technology*, *46*(2), 787-794, doi:10.1021/es202525q.

Lance, S., A. Nenes, J. Medina, and J. N. Smith (2006), Mapping the Operation of the DMT Continuous Flow CCN Counter, *Aerosol Science and Technology*, *40*(4), 242-254, doi:10.1080/02786820500543290.

Langer, S., R. S. Pemberton, and B. J. Finlayson-Pitts (1997), Diffuse Reflectance Infrared Studies of the Reaction of Synthetic Sea Salt Mixtures with NO_2: A Key Role for Hydrates in the Kinetics and Mechanism, *The Journal of Physical Chemistry A*, *101*(7), 1277-1286, doi:10.1021/jp962122c.

Last, J. A. (1991), Global atmospheric change: potential health effects of acid aerosol and oxidant gas mixtures, *Environmental Health Perspectives*, *96*, 151-157, doi:10.1289/ehp.9196151.

Lee, B. H., F. D. Lopez-Hilfiker, C. Mohr, T. Kurten, D. R. Worsnop, and J. A. Thornton (2014), An iodide-adduct high-resolution time-of-flight chemical-ionization mass spectrometer: application to atmospheric inorganic and organic compounds, *Environmental science & technology*, *48*(11), 6309-6317, doi:10.1021/es500362a.

Lelieveld, J., J. S. Evans, M. Fnais, D. Giannadaki, and A. Pozzer (2015), The contribution of outdoor air pollution sources to premature mortality on a global scale, *Nature*, *525*(7569), 367-371, doi:10.1038/nature15371.

Lewandowski, M., M. Jaoui, T. E. Kleindienst, J. H. Offenberg, and E. O. Edney (2007), Composition of $PM_{2.5}$ during the summer of 2003 in Research Triangle Park, North

Carolina, *Atmospheric Environment*, *41*(19), 4073-4083, doi:10.1016/j.atmosenv.2007.01.012.

Li, W., et al. (2017), Air pollution-aerosol interactions produce more bioavailable iron for ocean ecosystems, *Science Advances*, *3*(3), e1601749, doi:10.1126/sciadv.1601749.

Liao, H., and J. H. Seinfeld (2005), Global impacts of gas-phase chemistry-aerosol interactions on direct radiative forcing by anthropogenic aerosols and ozone, *Journal of Geophysical Research: Atmospheres*, *110*(D18), D18208, doi:10.1029/2005jd005907.

Lim, S. S., et al. (2012), A comparative risk assessment of burden of disease and injury attributable to 67 risk factors and risk factor clusters in 21 regions, 1990–2010: a systematic analysis for the Global Burden of Disease Study 2010, *The Lancet*, *380*(9859), 2224-2260, doi:10.1016/S0140-6736(12)61766-8.

Lin, Y. H., et al. (2012), Isoprene epoxydiols as precursors to secondary organic aerosol formation: acid-catalyzed reactive uptake studies with authentic compounds, *Environmental science & technology*, *46*(1), 250-258, doi:10.1021/es202554c.

Liu, J., et al. (2012), On the gas-particle partitioning of soluble organic aerosol in two urban atmospheres with contrasting emissions: 2. Gas and particle phase formic acid, *Journal of Geophysical Research*, *117*, D00V21, doi:10.1029/2012jd017912.

Lohmann, U., and J. Feichter (2005), Global indirect aerosol effects: a review, *Atmospheric Chemistry and Physics*, *5*(3), 715-737, doi:10.5194/acp-5-715-2005.

Longo, A. F., Y. Feng, B. Lai, W. M. Landing, R. U. Shelley, A. Nenes, N. Mihalopoulos, K. Violaki, and E. D. Ingall (2016), Influence of Atmospheric Processes on the Solubility and Composition of Iron in Saharan Dust, *Environmental science & technology*, *50*(13), 6912-6920, doi:10.1021/acs.est.6b02605.

Lopez-Hilfiker, F. D., K. Constantin, J. P. Kercher, and J. A. Thornton (2012), Temperature dependent halogen activation by N_2O_5 reactions on halide-doped ice surfaces, *Atmospheric Chemistry and Physics*, *12*(11), 5237-5247, doi:10.5194/acp-12-5237-2012.

Lopez-Hilfiker, F. D., et al. (2016), Molecular Composition and Volatility of Organic Aerosol in the Southeastern U.S.: Implications for IEPOX Derived SOA, *Environmental science & technology*, *50*(5), 2200-2209, doi:10.1021/acs.est.5b04769.

Losey, D. J., R. G. Parker, and M. A. Freedman (2016), pH Dependence of Liquid-Liquid Phase Separation in Organic Aerosol, *Journal of Physical Chemistry Letters*, *7*(19), 3861-3865, doi:10.1021/acs.jpclett.6b01621.

Magi, B. I., and P. V. Hobbs (2003), Effects of humidity on aerosols in southern Africa during the biomass burning season, *Journal of Geophysical Research*, *108*(D13), 8495, doi:10.1029/2002jd002144.

Makkonen, U., A. Virkkula, J. Mäntykenttä, H. Hakola, P. Keronen, V. Vakkari, and P. P. Aalto (2012), Semi-continuous gas and inorganic aerosol measurements at a Finnish urban site: comparisons with filters, nitrogen in aerosol and gas phases, and aerosol acidity, *Atmospheric Chemistry and Physics*, *12*(12), 5617-5631, doi:10.5194/acp-12-5617-2012.

Malm, W. C., and D. E. Day (2001), Estimates of aerosol species scattering characteristics as a function of relative humidity, *Atmospheric Environment*, *35*(16), 2845-2860, doi:10.1016/S1352-2310(01)00077-2.

Marion, G. M., F. J. Millero, M. F. Camões, P. Spitzer, R. Feistel, and C. T. A. Chen (2011), pH of seawater, *Marine Chemistry*, *126*(1-4), 89-96, doi:10.1016/j.marchem.2011.04.002.

Marple, V. A., K. L. Rubow, and S. M. Behm (1991), A Microorifice Uniform Deposit Impactor (MOUDI): Description, Calibration, and Use, *Aerosol Science and Technology*, *14*(4), 434-446, doi:10.1080/02786829108959504.

McNaughton, C. S., et al. (2007), Results from the DC-8 Inlet Characterization Experiment (DICE): Airborne Versus Surface Sampling of Mineral Dust and Sea Salt Aerosols, *Aerosol Science and Technology*, *41*(2), 136-159, doi:10.1080/02786820601118406.

Mei, F., P. L. Hayes, A. Ortega, J. W. Taylor, J. D. Allan, J. Gilman, W. Kuster, J. de Gouw, J. L. Jimenez, and J. Wang (2013), Droplet activation properties of organic aerosols observed at an urban site during CalNex-LA, *Journal of Geophysical Research: Atmospheres*, *118*(7), 2903-2917, doi:10.1002/jgrd.50285.

Meier, P. C. (1982), Two-parameter debye-hückel approximation for the evaluation of mean activity coefficients of 109 electrolytes, *Analytica Chimica Acta*, *136*, 363-368, doi:10.1016/s0003-2670(01)95397-8.

Meissner, H. P., and J. W. Tester (1972), Activity Coefficients of Strong Electrolytes in Aqueous Solutions, *Industrial & Engineering Chemistry Process Design and Development*, *11*(1), 128-133, doi:10.1021/i260041a025.

Menz, F. C., and H. M. Seip (2004), Acid rain in Europe and the United States: an update, *Environmental Science & Policy*, *7*(4), 253-265, doi:10.1016/j.envsci.2004.05.005.

Meskhidze, N., W. L. Chameides, and A. Nenes (2005), Dust and pollution: A recipe for enhanced ocean fertilization?, *Journal of Geophysical Research*, *110*(D3), D03301, doi:10.1029/2004jd005082.

Meskhidze, N., W. L. Chameides, A. Nenes, and G. Chen (2003), Iron mobilization in mineral dust: Can anthropogenic SO_2 emissions affect ocean productivity?, *Geophysical Research Letters*, *30*(21), 2085, doi:10.1029/2003gl018035.

Middlebrook, A. M., R. Bahreini, J. L. Jimenez, and M. R. Canagaratna (2012), Evaluation of Composition-Dependent Collection Efficiencies for the Aerodyne Aerosol Mass Spectrometer using Field Data, *Aerosol Science and Technology*, *46*(3), 258-271, doi:10.1080/02786826.2011.620041.

Mitchell, R. M., S. K. Campbell, Y. Qin, and J. L. Gras (2009), Performance Characteristics of Integrating Nephelometers in the Australian Outback, *Journal of Atmospheric and Oceanic Technology*, *26*(5), 984-995, doi:10.1175/2008jtecha1187.1.

Moharreri, A., L. Craig, P. Dubey, D. C. Rogers, and S. Dhaniyala (2014), Aircraft testing of the new Blunt-body Aerosol Sampler (BASE), *Atmospheric Measurement Techniques*, *7*(9), 3085-3093, doi:10.5194/amt-7-3085-2014.

Murphy, D. M., D. J. Cziczo, K. D. Froyd, P. K. Hudson, B. M. Matthew, A. M. Middlebrook, R. E. Peltier, A. Sullivan, D. S. Thomson, and R. J. Weber (2006), Single-particle mass spectrometry of tropospheric aerosol particles, *Journal of Geophysical Research-Atmospheres*, *111*(D23), D23S32, doi:10.1029/2006jd007340.

Myriokefalitakis, S., N. Daskalakis, N. Mihalopoulos, A. R. Baker, A. Nenes, and M. Kanakidou (2015), Changes in dissolved iron deposition to the oceans driven by human activity: a 3-D global modelling study, *Biogeosciences*, *12*(13), 3973-3992, doi:10.5194/bg-12-3973-2015.

Myriokefalitakis, S., A. Nenes, A. R. Baker, N. Mihalopoulos, and M. Kanakidou (2016), Bioavailable atmospheric phosphorous supply to the global ocean: a 3-D global modeling study, *Biogeosciences*, *13*(24), 6519-6543, doi:10.5194/bg-13-6519-2016.

Nemesure, S., R. Wagener, and S. E. Schwartz (1995), Direct shortwave forcing of climate by the anthropogenic sulfate aerosol: Sensitivity to particle size, composition, and relative humidity, *Journal of Geophysical Research: Atmospheres*, *100*(D12), 26105-26116, doi:10.1029/95jd02897.

Nenes, A., M. D. Krom, N. Mihalopoulos, P. Van Cappellen, Z. Shi, A. Bougiatioti, P. Zarmpas, and B. Herut (2011), Atmospheric acidification of mineral aerosols: a source of bioavailable phosphorus for the oceans, *Atmospheric Chemistry and Physics*, *11*(13), 6265-6272, doi:10.5194/acp-11-6265-2011.

Nenes, A., S. N. Pandis, and C. Pilinis (1998), ISORROPIA: A new thermodynamic equilibrium model for multiphase multicomponent inorganic aerosols, *Aquatic Geochemistry*, *4*(1), 123-152, doi:10.1023/A:1009604003981.

Nguyen, T. B., M. M. Coggon, K. H. Bates, X. Zhang, R. H. Schwantes, K. A. Schilling, C. L. Loza, R. C. Flagan, P. O. Wennberg, and J. H. Seinfeld (2014a), Organic aerosol formation from the reactive uptake of isoprene epoxydiols (IEPOX) onto non-acidified inorganic seeds, *Atmospheric Chemistry and Physics*, *14*(7), 3497-3510, doi:10.5194/acp-14-3497-2014.

Nguyen, T. B., M. M. Coggon, R. C. Flagan, and J. H. Seinfeld (2013), Reactive uptake and photo-Fenton oxidation of glycolaldehyde in aerosol liquid water, *Environmental science & technology*, *47*(9), 4307-4316, doi:10.1021/es400538j.

Nguyen, T. K. V., M. D. Petters, S. R. Suda, H. Guo, R. J. Weber, and A. G. Carlton (2014b), Trends in particle-phase liquid water during the Southern Oxidant and Aerosol Study, *Atmospheric Chemistry and Physics*, *14*(20), 10911-10930, doi:10.5194/acp-14-10911-2014.

Northcross, A. L., and M. Jang (2007), Heterogeneous SOA yield from ozonolysis of monoterpenes in the presence of inorganic acid, *Atmospheric Environment*, *41*(7), 1483-1493, doi:10.1016/j.atmosenv.2006.10.009.

Nowak, J. B., et al. (2006), Analysis of urban gas phase ammonia measurements from the 2002 Atlanta Aerosol Nucleation and Real-Time Characterization Experiment (ANARChE), *Journal of Geophysical Research*, *111*(D17), D17308, doi:10.1029/2006jd007113.

Oakes, M., E. D. Ingall, B. Lai, M. M. Shafer, M. D. Hays, Z. G. Liu, A. G. Russell, and R. J. Weber (2012), Iron solubility related to particle sulfur content in source emission and ambient fine particles, *Environmental science & technology*, *46*(12), 6637-6644, doi:10.1021/es300701c.

Orsini, D. A., Y. Ma, A. Sullivan, B. Sierau, K. Baumann, and R. J. Weber (2003), Refinements to the particle-into-liquid sampler (PILS) for ground and airborne measurements of water soluble aerosol composition, *Atmospheric Environment*, *37*(9-10), 1243-1259, doi:10.1016/s1352-2310(02)01015-4.

Pathak, R. K., P. K. K. Louie, and C. K. Chan (2004), Characteristics of aerosol acidity in Hong Kong, *Atmospheric Environment*, *38*(19), 2965-2974, doi:10.1016/j.atmosenv.2004.02.044.

Pathak, R. K., T. Wang, K. F. Ho, and S. C. Lee (2011), Characteristics of summertime $PM_{2.5}$ organic and elemental carbon in four major Chinese cities: Implications of high acidity for water-soluble organic carbon (WSOC), *Atmospheric Environment*, *45*(2), 318-325, doi:10.1016/j.atmosenv.2010.10.021.

Paulot, F., and D. J. Jacob (2014), Hidden cost of U.S. agricultural exports: particulate matter from ammonia emissions, *Environmental science & technology*, *48*(2), 903-908, doi:10.1021/es4034793.

Peltier, R. E., A. P. Sullivan, R. J. Weber, C. A. Brock, A. G. Wollny, J. S. Holloway, J. A. de Gouw, and C. Warneke (2007a), Fine aerosol bulk composition measured on WP-3D research aircraft in vicinity of the Northeastern United States - results from NEAQS, *Atmospheric Chemistry and Physics*, *7*(12), 3231-3247, doi:10.5194/acp-7-3231-2007.

Peltier, R. E., A. P. Sullivan, R. J. Weber, A. G. Wollny, J. S. Holloway, C. A. Brock, J. A. de Gouw, and E. L. Atlas (2007b), No evidence for acid-catalyzed secondary organic aerosol formation in power plant plumes over metropolitan Atlanta, Georgia, *Geophysical Research Letters*, *34*(6), L06801, doi:10.1029/2006gl028780.

Petters, M. D., and S. M. Kreidenweis (2007), A single parameter representation of hygroscopic growth and cloud condensation nucleus activity, *Atmospheric Chemistry and Physics*, *7*(8), 1961-1971, doi:10.5194/acp-7-1961-2007.

Pilinis, C., S. N. Pandis, and J. H. Seinfeld (1995), Sensitivity of Direct Climate Forcing by Atmospheric Aerosols to Aerosol-Size and Composition, *Journal of Geophysical Research: Atmospheres*, *100*(D9), 18739-18754, doi:10.1029/95jd02119.

Pinder, R. W., P. J. Adams, and S. N. Pandis (2007), Ammonia Emission Controls as a Cost-Effective Strategy for Reducing Atmospheric Particulate Matter in the Eastern United States, *Environmental science & technology*, *41*(2), 380-386, doi:10.1021/es060379a.

Pinder, R. W., A. B. Gilliland, and R. L. Dennis (2008), Environmental impact of atmospheric NH_3 emissions under present and future conditions in the eastern United States, *Geophysical Research Letters*, *35*(12), L12808, doi:10.1029/2008gl033732.

Pitzer, K. S., and G. Mayorga (1973), Thermodynamics of electrolytes. II. Activity and osmotic coefficients for strong electrolytes with one or both ions univalent, *The Journal of Physical Chemistry*, *77*(19), 2300-2308, doi:10.1021/j100638a009.

Pope, C. A., III, R. T. Burnett, G. D. Thurston, M. J. Thun, E. E. Calle, D. Krewski, and J. J. Godleski (2004), Cardiovascular mortality and long-term exposure to particulate air pollution: epidemiological evidence of general pathophysiological pathways of disease, *Circulation*, *109*(1), 71-77, doi:10.1161/01.CIR.0000108927.80044.7F.

Pope, C. A., III, M. J. Thun, M. M. Namboodiri, D. W. Dockery, J. S. Evans, F. E. Speizer, and C. W. Heath, Jr. (1995), Particulate air pollution as a predictor of mortality in a prospective study of U.S. adults, *American Journal of Respiratory and Critical Care Medicine*, *151*(3 Pt 1), 669-674, doi:10.1164/ajrccm/151.3_Pt_1.669.

Pozzer, A., A. P. Tsimpidi, V. A. Karydis, A. de Meij, and J. Lelieveld (2017), Impact of agricultural emission reductions on fine particulate matter and public health, *Atmospheric Chemistry and Physics Discussions*, 1-19, doi:10.5194/acp-2017-390.

Puchalski, M. A., C. M. Rogers, R. Baumgardner, K. P. Mishoe, G. Price, M. J. Smith, N. Watkins, and C. M. Lehmann (2015), A statistical comparison of active and passive ammonia measurements collected at Clean Air Status and Trends Network (CASTNET) sites, *Environmental Science Processes & Impacts*, *17*(2), 358-369, doi:10.1039/c4em00531g.

Pye, H. O., et al. (2013), Epoxide pathways improve model predictions of isoprene markers and reveal key role of acidity in aerosol formation, *Environmental science & technology*, *47*(19), 11056-11064, doi:10.1021/es402106h.

Raizenne, M., L. M. Neas, A. I. Damokosh, D. W. Dockery, J. D. Spengler, P. Koutrakis, J. H. Ware, and F. E. Speizer (1996), Health effects of acid aerosols on North American children: pulmonary function, *Environmental Health Perspectives*, *104*(5), 506-514, doi:10.2307/3432991.

Rindelaub, J. D., R. L. Craig, L. Nandy, A. L. Bondy, C. S. Dutcher, P. B. Shepson, and A. P. Ault (2016), Direct Measurement of pH in Individual Particles via Raman Microspectroscopy and Variation in Acidity with Relative Humidity, *Journal of Physical Chemistry A*, *120*(6), 911-917, doi:10.1021/acs.jpca.5b12699.

Robbins, R. C., R. D. Cadle, and D. L. Eckhardt (1959), The Conversion of Sodium Chloride to Hydrogen Chloride in the Atmosphe, *Journal of Meteorology*, *16*(1), 53-56, doi:10.1175/1520-0469(1959)016<0053:tcosct>2.0.co;2.

Roberts, G. C., and A. Nenes (2005), A Continuous-Flow Streamwise Thermal-Gradient CCN Chamber for Atmospheric Measurements, *Aerosol Science and Technology*, *39*(3), 206-221, doi:10.1080/027868290913988.

Rostami, A. A. (2009), Computational modeling of aerosol deposition in respiratory tract: a review, *Inhalation toxicology*, *21*(4), 262-290, doi:10.1080/08958370802448987.

Rumsey, I. C., et al. (2014), An assessment of the performance of the Monitor for AeRosols and GAses in ambient air (MARGA): a semi-continuous method for soluble compounds, *Atmospheric Chemistry and Physics*, *14*(11), 5639-5658, doi:10.5194/acp-14-5639-2014.

Ryerson, T. B., et al. (2013), The 2010 California Research at the Nexus of Air Quality and Climate Change (CalNex) field study, *Journal of Geophysical Research: Atmospheres*, *118*(11), 5830-5866, doi:10.1002/jgrd.50331.

Sardar, S. B., P. M. Fine, and C. Sioutas (2005), Seasonal and spatial variability of the size-resolved chemical composition of particulate matter (PM_{10}) in the Los Angeles Basin, *Journal of Geophysical Research-Atmospheres*, *110*(D7), D07S08, doi:10.1029/2004jd004627.

Saylor, R., L. Myles, D. Sibble, J. Caldwell, and J. Xing (2015), Recent trends in gas-phase ammonia and PM2.5 ammonium in the Southeast United States, *Journal of the Air & Waste Management Association*, *65*(3), 347-357, doi:10.1080/10962247.2014.992554.

Schill, G. P., and M. A. Tolbert (2013), Heterogeneous ice nucleation on phase-separated organic-sulfate particles: effect of liquid vs. glassy coatings, *Atmospheric Chemistry and Physics*, *13*(9), 4681-4695, doi:10.5194/acp-13-4681-2013.

Schlag, P., A. Kiendler-Scharr, M. J. Blom, F. Canonaco, J. S. Henzing, M. Moerman, A. S. H. Prévôt, and R. Holzinger (2016), Aerosol source apportionment from 1-year measurements at the CESAR tower in Cabauw, the Netherlands, *Atmospheric Chemistry and Physics*, *16*(14), 8831-8847, doi:10.5194/acp-16-8831-2016.

Schrader, F., and C. Brummer (2014), Land Use Specific Ammonia Deposition Velocities: a Review of Recent Studies (2004-2013), *Water, air, and soil pollution*, *225*(10), 2114, doi:10.1007/s11270-014-2114-7.

Seinfeld, J. H., and S. N. Pandis (2006), *Atmospheric Chemistry and Physics: from Air Pollution to Climate Change 2nd Edition*, John Wiley & Sons, Inc., Hoboken, New Jersey.

Sheridan, P. J., A. Jefferson, and J. A. Ogren (2002), Spatial variability of submicrometer aerosol radiative properties over the Indian Ocean during INDOEX, *Journal of Geophysical Research*, *107*(D19), 8011, doi:10.1029/2000jd000166.

Shingler, T., et al. (2016), Airborne characterization of subsaturated aerosol hygroscopicity and dry refractive index from the surface to 6.5 km during the SEAC4RS campaign, *Journal of Geophysical Research: Atmospheres*, *121*(8), 4188-4210, doi:10.1002/2015jd024498.

Shiraiwa, M., and J. H. Seinfeld (2012), Equilibration timescale of atmospheric secondary organic aerosol partitioning, *Geophysical Research Letters*, *39*(24), L24801, doi:10.1029/2012gl054008.

Silvern, R. F., D. J. Jacob, P. S. Kim, E. A. Marais, J. R. Turner, P. Campuzano-Jost, and J. L. Jimenez (2017), Inconsistency of ammonium–sulfate aerosol ratios with thermodynamic models in the eastern US: a possible role of organic aerosol, *Atmospheric Chemistry and Physics*, *17*(8), 5107-5118, doi:10.5194/acp-17-5107-2017.

Sloane, C. S., J. Watson, J. Chow, L. Pritchett, and L. W. Richards (1991), Size-Segregated Fine Particle Measurements by Chemical-Species and Their Impact on Visibility Impairment in Denver, *Atmospheric Environment. Part A. General Topics*, *25*(5-6), 1013-1024, doi:10.1016/0960-1686(91)90143-U.

Slusher, D. L., L. G. Huey, D. J. Tanner, F. M. Flocke, and J. M. Roberts (2004), A thermal dissociation–chemical ionization mass spectrometry (TD-CIMS) technique for the simultaneous measurement of peroxyacyl nitrates and dinitrogen pentoxide, *Journal of Geophysical Research: Atmospheres*, *109*(D19), D19315, doi:10.1029/2004JD004670.

Song, M., P. F. Liu, S. J. Hanna, Y. J. Li, S. T. Martin, and A. K. Bertram (2015), Relative humidity-dependent viscosities of isoprene-derived secondary organic material and atmospheric implications for isoprene-dominant forests, *Atmospheric Chemistry and Physics*, *15*(9), 5145-5159, doi:10.5194/acp-15-5145-2015.

Song, M., C. Marcolli, U. K. Krieger, A. Zuend, and T. Peter (2012), Liquid-liquid phase separation and morphology of internally mixed dicarboxylic acids/ammonium sulfate/water particles, *Atmospheric Chemistry and Physics*, *12*(5), 2691-2712, doi:10.5194/acp-12-2691-2012.

Sorooshian, A., F. J. Brechtel, Y. L. Ma, R. J. Weber, A. Corless, R. C. Flagan, and J. H. Seinfeld (2006), Modeling and characterization of a particle-into-liquid sampler (PILS), *Aerosol Science and Technology*, *40*(6), 396-409, doi:10.1080/02786820600632282.

Sorooshian, A., S. Hersey, F. J. Brechtel, A. Corless, R. C. Flagan, and J. H. Seinfeld (2008), Rapid, Size-Resolved Aerosol Hygroscopic Growth Measurements: Differential Aerosol Sizing and Hygroscopicity Spectrometer Probe (DASH-SP), *Aerosol Science and Technology*, *42*(6), 445-464, doi:10.1080/02786820802178506.

Spracklen, D. V., et al. (2011), Aerosol mass spectrometer constraint on the global secondary organic aerosol budget, *Atmospheric Chemistry and Physics*, *11*(23), 12109-12136, doi:10.5194/acp-11-12109-2011.

Stein, S. W., B. J. Turpin, X. P. Cai, C. P. F. Huang, and P. H. Mcmurry (1994), Measurements of Relative Humidity-Dependent Bounce and Density for Atmospheric Particles Using the DMA-Impactor Technique, *Atmospheric Environment*, *28*(10), 1739-1746, doi:10.1016/1352-2310(94)90136-8.

Stelson, A. W. (1990), Urban aerosol refractive index prediction by partial molar refraction approach, *Environmental science & technology*, *24*(11), 1676-1679, doi:10.1021/es00081a008.

Stith, J. L., et al. (2009), An overview of aircraft observations from the Pacific Dust Experiment campaign, *Journal of Geophysical Research*, *114*(D5), doi:10.1029/2008jd010924.

Stockdale, A., M. D. Krom, R. J. Mortimer, L. G. Benning, K. S. Carslaw, R. J. Herbert, Z. Shi, S. Myriokefalitakis, M. Kanakidou, and A. Nenes (2016), Understanding the nature of atmospheric acid processing of mineral dusts in supplying bioavailable phosphorus to the oceans, *Proceedings of the National Academy of Sciences of the United States of America*, *113*(51), 14639-14644, doi:10.1073/pnas.1608136113.

Stokes, R. H., and R. A. Robinson (1966), Interactions in Aqueous Nonelectrolyte Solutions .I. Solute-Solvent Equilibria, *Journal of physical Chemistry*, *70*(7), 2126-2130, doi:10.1021/J100879a010.

Stumm, W., and J. J. Morgan (1996), *Aquatic Chemistry: Chemical Equilibria and Rates in Natural Waters 3rd Edition*, John Wiley & Sons, Inc.

Sullivan, A. P., A. A. May, T. Lee, G. R. McMeeking, S. M. Kreidenweis, S. K. Akagi, R. J. Yokelson, S. P. Urbanski, and J. L. Collett Jr (2014), Airborne characterization of smoke

marker ratios from prescribed burning, *Atmospheric Chemistry and Physics*, *14*(19), 10535-10545, doi:10.5194/acp-14-10535-2014.

Sullivan, A. P., R. E. Peltier, C. A. Brock, J. A. de Gouw, J. S. Holloway, C. Warneke, A. G. Wollny, and R. J. Weber (2006), Airborne measurements of carbonaceous aerosol soluble in water over northeastern United States: Method development and an investigation into water-soluble organic carbon sources, *Journal of Geophysical Research*, *111*(D23), D23S46, doi:10.1029/2006jd007072.

Surratt, J. D., A. W. Chan, N. C. Eddingsaas, M. Chan, C. L. Loza, A. J. Kwan, S. P. Hersey, R. C. Flagan, P. O. Wennberg, and J. H. Seinfeld (2010), Reactive intermediates revealed in secondary organic aerosol formation from isoprene, *Proceedings of the National Academy of Sciences of the United States of America*, *107*(15), 6640-6645, doi:10.1073/pnas.0911114107.

Surratt, J. D., M. Lewandowski, J. H. Offenberg, M. Jaoui, T. E. Kleindienst, E. O. Edney, and J. H. Seinfeld (2007), Effect of acidity on secondary organic aerosol formation from isoprene, *Environmental science & technology*, *41*(15), 5363-5369, doi:10.1021/es0704176.

Takahama, S., C. I. Davidson, and S. N. Pandis (2006), Semicontinuous measurements of organic carbon and acidity during the Pittsburgh Air Quality Study: implications for acid-catalyzed organic aerosol formation, *Environmental science & technology*, *40*(7), 2191-2199, doi:10.1021/es050856+.

Tang, I. N. (1976), Phase transformation and growth of aerosol particles composed of mixed salts, *Journal of Aerosol Science*, *7*(5), 361-371, doi:10.1016/0021-8502(76)90022-7.

Tang, I. N., and H. R. Munkelwitz (1993), Composition and Temperature-Dependence of the Deliquescence Properties of Hygroscopic Aerosols, *Atmospheric Environment. Part A. General Topics*, *27*(4), 467-473, doi:10.1016/0960-1686(93)90204-C.

Tang, I. N., and H. R. Munkelwitz (1994), Water Activities, Densities, and Refractive-Indexes of Aqueous Sulfates and Sodium-Nitrate Droplets of Atmospheric Importance, *Journal of Geophysical Research-Atmospheres*, *99*(D9), 18801-18808, doi:10.1029/94jd01345.

Tanner, R. L., K. J. Olszyna, E. S. Edgerton, E. Knipping, and S. L. Shaw (2009), Searching for evidence of acid-catalyzed enhancement of secondary organic aerosol formation using ambient aerosol data, *Atmospheric Environment*, *43*(21), 3440-3444, doi:10.1016/j.atmosenv.2009.03.045.

Thurston, G. D., K. Ito, C. G. Hayes, D. V. Bates, and M. Lippmann (1994), Respiratory hospital admissions and summertime haze air pollution in Toronto, Ontario: consideration

of the role of acid aerosols, *Environmental Research*, *65*(2), 271-290, doi:10.1006/enrs.1994.1037.

Tian, S., Y. Pan, Z. Liu, T. Wen, and Y. Wang (2014), Size-resolved aerosol chemical analysis of extreme haze pollution events during early 2013 in urban Beijing, China, *Journal of Hazardous Materials*, *279*, 452-460, doi:10.1016/j.jhazmat.2014.07.023.

Tolocka, M. P., M. Jang, J. M. Ginter, F. J. Cox, R. M. Kamens, and M. V. Johnston (2004), Formation of oligomers in secondary organic aerosol, *Environmental science & technology*, *38*(5), 1428-1434, doi:10.1021/es035030r.

Tong, H. J., J. P. Reid, D. L. Bones, B. P. Luo, and U. K. Krieger (2011), Measurements of the timescales for the mass transfer of water in glassy aerosol at low relative humidity and ambient temperature, *Atmospheric Chemistry and Physics*, *11*(10), 4739-4754, doi:10.5194/acp-11-4739-2011.

Tsimpidi, A. P., V. A. Karydis, and S. N. Pandis (2007), Response of Inorganic Fine Particulate Matter to Emission Changes of Sulfur Dioxide and Ammonia: The Eastern United States as a Case Study, *Journal of the Air & Waste Management Association*, *57*(12), 1489-1498, doi:10.3155/1047-3289.57.12.1489.

Turpin, B. J., and H.-J. Lim (2001), Species Contributions to PM2.5 Mass Concentrations: Revisiting Common Assumptions for Estimating Organic Mass, *Aerosol Science and Technology*, *35*(1), 602-610, doi:10.1080/02786820119445.

Vasilakos, P., A. G. Russell, R. J. Weber, and A. Nenes (2017), Understanding nitrate formation in a world with less sulfate, *In review*.

Veres, P., J. M. Roberts, C. Warneke, D. Welsh-Bon, M. Zahniser, S. Herndon, R. Fall, and J. de Gouw (2008), Development of negative-ion proton-transfer chemical-ionization mass spectrometry (NI-PT-CIMS) for the measurement of gas-phase organic acids in the atmosphere, *International Journal of Mass Spectrometry*, *274*(1-3), 48-55, doi:10.1016/j.ijms.2008.04.032.

Veres, P. R., et al. (2011), Evidence of rapid production of organic acids in an urban air mass, *Geophysical Research Letters*, *38*(17), L17807, doi:10.1029/2011gl048420.

Verma, V., T. Fang, H. Guo, L. King, J. T. Bates, R. E. Peltier, E. Edgerton, A. G. Russell, and R. J. Weber (2014), Reactive oxygen species associated with water-soluble $PM_{2.5}$ in the southeastern United States: spatiotemporal trends and source apportionment, *Atmospheric Chemistry and Physics*, *14*(23), 12915-12930, doi:10.5194/acp-14-12915-2014.

Villani, P., K. Sellegri, M. Monier, and P. Laj (2013), Influence of semi-volatile species on particle hygroscopic growth, *Atmospheric Environment*, *79*, 129-137, doi:10.1016/j.atmosenv.2013.05.069.

Wagner, N. L., et al. (2013), N_2O_5 uptake coefficients and nocturnal NO_2 removal rates determined from ambient wintertime measurements, *Journal of Geophysical Research: Atmospheres*, *118*(16), 9331-9350, doi:10.1002/jgrd.50653.

Wahner, A., T. F. Mentel, M. Sohn, and J. Stier (1998), Heterogeneous reaction of N_2O_5 on sodium nitrate aerosol, *Journal of Geophysical Research: Atmospheres*, *103*(D23), 31103-31112, doi:10.1029/1998jd100022.

Wang, G., et al. (2016), Persistent sulfate formation from London Fog to Chinese haze, *Proceedings of the National Academy of Sciences of the United States of America*, *113*(48), 13630-13635, doi:10.1073/pnas.1616540113.

Washenfelder, R. A., et al. (2011), The glyoxal budget and its contribution to organic aerosol for Los Angeles, California, during CalNex 2010, *Journal of Geophysical Research: Atmospheres*, *116*(D21), D00V02, doi:10.1029/2011jd016314.

Waugh, A., and A. Grant (2014), *Anatomy and Physiology in Health and Illness 12th Edition*, Elsevier Ltd.

Weber, R. J., H. Guo, A. G. Russell, and A. Nenes (2016), High aerosol acidity despite declining atmospheric sulfate concentrations over the past 15 years, *Nature Geoscience*, *9*(4), 282-285, doi:10.1038/ngeo2665.

West, J. J., A. S. Ansari, and S. N. Pandis (1999), Marginal PM25: Nonlinear Aerosol Mass Response to Sulfate Reductions in the Eastern United States, *Journal of the Air & Waste Management Association*, *49*(12), 1415-1424, doi:10.1080/10473289.1999.10463973.

Wexler, A. S., and S. L. Clegg (2002), Atmospheric aerosol models for systems including the ions H^+, NH_4^+, Na^+, SO_4^{2-}, NO_3^-, Cl^-, Br^-, and H_2O, *Journal of Geophysical Research*, *107*(D14), 4207, doi:10.1029/2001jd000451.

Wexler, A. S., and J. H. Seinfeld (1991), Second-generation inorganic aerosol model, *Atmospheric Environment. Part A. General Topics*, *25*(12), 2731-2748, doi:10.1016/0960-1686(91)90203-J.

Wiscombe, W. J. (1980), Improved Mie scattering algorithms, *Applied Optics*, *19*(9), 1505-1509, doi:10.1364/AO.19.001505.

Xing, J., J. Pleim, R. Mathur, G. Pouliot, C. Hogrefe, C. M. Gan, and C. Wei (2013), Historical gaseous and primary aerosol emissions in the United States from 1990 to 2010, *Atmospheric Chemistry and Physics*, *13*(15), 7531-7549, doi:10.5194/acp-13-7531-2013.

Xu, L., et al. (2015a), Effects of anthropogenic emissions on aerosol formation from isoprene and monoterpenes in the southeastern United States, *Proceedings of the National Academy of Sciences of the United States of America*, *112*(1), 37-42, doi:10.1073/pnas.1417609112.

Xu, L., et al. (2016), Enhanced formation of isoprene-derived organic aerosol in sulfur-rich power plant plumes during Southeast Nexus, *Journal of Geophysical Research: Atmospheres*, *121*(18), 11137-11153, doi:10.1002/2016jd025156.

Xu, L., S. Suresh, H. Guo, R. J. Weber, and N. L. Ng (2015b), Aerosol characterization over the southeastern United States using high-resolution aerosol mass spectrometry: spatial and seasonal variation of aerosol composition and sources with a focus on organic nitrates, *Atmospheric Chemistry and Physics*, *15*(13), 7307-7336, doi:10.5194/acp-15-7307-2015.

Ye, Q., E. S. Robinson, X. Ding, P. Ye, R. C. Sullivan, and N. M. Donahue (2016), Mixing of secondary organic aerosols versus relative humidity, *Proceedings of the National Academy of Sciences of the United States of America*, *113*, 12649-12654, doi:10.1073/pnas.1604536113.

Yin, L., Z. Niu, X. Chen, J. Chen, F. Zhang, and L. Xu (2014), Characteristics of water-soluble inorganic ions in $PM_{2.5}$ and $PM_{2.5-10}$ in the coastal urban agglomeration along the Western Taiwan Strait Region, China, *Environmental Science and Pollution Research*, *21*(7), 5141-5156, doi:10.1007/s11356-013-2134-7.

You, Y., and A. K. Bertram (2015), Effects of molecular weight and temperature on liquid–liquid phase separation in particles containing organic species and inorganic salts, *Atmospheric Chemistry and Physics*, *15*(3), 1351-1365, doi:10.5194/acp-15-1351-2015.

You, Y., et al. (2014a), Atmospheric amines and ammonia measured with a chemical ionization mass spectrometer (CIMS), *Atmospheric Chemistry and Physics*, *14*(22), 12181-12194, doi:10.5194/acp-14-12181-2014.

You, Y., L. Renbaum-Wolff, and A. K. Bertram (2013), Liquid–liquid phase separation in particles containing organics mixed with ammonium sulfate, ammonium bisulfate, ammonium nitrate or sodium chloride, *Atmospheric Chemistry and Physics*, *13*(23), 11723-11734, doi:10.5194/acp-13-11723-2013.

You, Y., et al. (2012), Images reveal that atmospheric particles can undergo liquid-liquid phase separations, *Proceedings of the National Academy of Sciences of the United States of America*, *109*(33), 13188-13193, doi:10.1073/pnas.1206414109.

You, Y., M. L. Smith, M. Song, S. T. Martin, and A. K. Bertram (2014b), Liquid–liquid phase separation in atmospherically relevant particles consisting of organic species and inorganic salts, *International Reviews in Physical Chemistry*, *33*(1), 43-77, doi:10.1080/0144235x.2014.890786.

Young, A. H., W. C. Keene, A. A. P. Pszenny, R. Sander, J. A. Thornton, T. P. Riedel, and J. R. Maben (2013), Phase partitioning of soluble trace gases with size-resolved aerosols in near-surface continental air over northern Colorado, USA, during winter, *Journal of Geophysical Research: Atmospheres*, *118*(16), 9414-9427, doi:10.1002/jgrd.50655.

Zdanovskii, A. B. (1936), Trudy Solyanoi Laboratorii Akad, *Nauk SSSR*, *2*.

Zhang, J., W. L. Chameides, R. Weber, G. Cass, D. Orsini, E. Edgerton, P. Jongejan, and J. Slanina (2002), An evaluation of the thermodynamic equilibrium assumption for fine particulate composition: Nitrate and ammonium during the 1999 Atlanta Supersite Experiment, *Journal of Geophysical Research*, *108*(D7), doi:10.1029/2001jd001592.

Zhang, Q., et al. (2007a), Ubiquity and dominance of oxygenated species in organic aerosols in anthropogenically-influenced Northern Hemisphere midlatitudes, *Geophysical Research Letters*, *34*(13), L13801, doi:10.1029/2007gl029979.

Zhang, Q., J. L. Jimenez, D. R. Worsnop, and M. Canagaratna (2007b), A case study of urban particle acidity and its influence on secondary organic aerosol, *Environmental science & technology*, *41*(9), 3213-3219, doi:10.1021/es061812j.

Zhang, X., A. Hecobian, M. Zheng, N. H. Frank, and R. J. Weber (2010), Biomass burning impact on $PM_{2.5}$ over the southeastern US during 2007: integrating chemically speciated FRM filter measurements, MODIS fire counts and PMF analysis, *Atmospheric Chemistry and Physics*, *10*(14), 6839-6853, doi:10.5194/acp-10-6839-2010.

Zhang, X., Z. Liu, A. Hecobian, M. Zheng, N. H. Frank, E. S. Edgerton, and R. J. Weber (2012), Spatial and seasonal variations of fine particle water-soluble organic carbon (WSOC) over the southeastern United States: implications for secondary organic aerosol formation, *Atmospheric Chemistry and Physics*, *12*(14), 6593-6607, doi:10.5194/acp-12-6593-2012.

Zhuang, H., C. K. Chan, M. Fang, and A. S. Wexler (1999), Size distributions of particulate sulfate, nitrate, and ammonium at a coastal site in Hong Kong, *Atmospheric Environment*, *33*(6), 843-853, doi:10.1016/S1352-2310(98)00305-7.

Zobrist, B., C. Marcolli, D. A. Pedernera, and T. Koop (2008), Do atmospheric aerosols form glasses?, *Atmospheric Chemistry and Physics*, *8*(17), 5221-5244, doi:10.5194/acp-8-5221-2008.

Zou, Y., Y. Wang, Y. Zhang, and J. H. Koo (2017), Arctic sea ice, Eurasia snow, and extreme winter haze in China, *Science Advances*, *3*(3), e1602751, doi:10.1126/sciadv.1602751.

Zuend, A., C. Marcolli, T. Peter, and J. H. Seinfeld (2010), Computation of liquid-liquid equilibria and phase stabilities: implications for RH-dependent gas/particle partitioning of organic-inorganic aerosols, *Atmospheric Chemistry and Physics*, *10*(16), 7795-7820, doi:10.5194/acp-10-7795-2010.

Zuend, A., and J. H. Seinfeld (2012), Modeling the gas-particle partitioning of secondary organic aerosol: the importance of liquid-liquid phase separation, *Atmospheric Chemistry and Physics*, *12*(9), 3857-3882, doi:10.5194/acp-12-3857-2012.